UNIVERSITY OF CALIFORNIA,
IRVINE

Advancement in the modeling of electron beam devices and ultrasensitive circuits

DISSERTATION

submitted in partial satisfaction of the requirements
for the degree of

DOCTOR OF PHILOSOPHY

in Electrical and Computer Engineering

by

Kasra Rouhi

Dissertation Committee:
Professor Filippo Capolino, Chair
Professor Alexander Figotin, Co-chair
Assistant Professor Hamidreza Aghasi

2024

DEDICATION

To my father, mother, sister, and wife—thank you for your unwavering love and support.

TABLE OF CONTENTS

LIST OF FIGURES

LIST OF TABLES

ACKNOWLEDGMENTS

First and foremost, I wish to express my gratitude to my advisor, Professor Filippo Capolino, for his support, insightful guidance, and exceptional mentorship throughout my doctoral studies. His profound knowledge, patience, and encouragement have shaped my research and academic growth. I am equally indebted to my co-advisor, Professor Alexander Figotin, whose expertise and thoughtful advice have greatly enriched my work and broadened my perspectives. Our inspiring weekly discussions were not only intellectually stimulating but also a constant source of motivation and encouragement throughout my journey. I would also like to extend my sincere appreciation to Professor Hamidreza Aghasi for serving on my committee and providing invaluable feedback that has significantly enhanced the quality of this dissertation.

I am profoundly grateful to Dr. Hamidreza Kazemi for his invaluable assistance during the initial six months of my Ph.D. journey and for our collaborative efforts on Chapter 6. My sincere thanks extend to Dr. Alireza Nikzamir for his continuous support and collaboration throughout my doctoral studies, particularly in Chapters 2, 3, and 5. I am thankful to Robert Marosi for our joint work on the traveling-wave tube (TWT) projects encompassed in Chapters 7, 8, and 9, and to Dr. Tarek Mealy for his significant contributions to these projects and chapters. I also wish to acknowledge Dr. Ahmed Abdelshafy for our collaboration on Chapter 7, Amin Hakimi for his contributions to the graphene project, and Miguel Saavedra-Melo for our collaborative work on metasurface projects and publications. Additionally, I am grateful to my lab mates—Dr. Mohamed Y. Nada, Dr. Farshad Yazdi, Dr. Dmitry Oshmarin, Dr. Mina Hanifeh, Nathaniel Furman, Albert Herrero-Parareda, Benjamin Bradshaw and Vanessa Yao—for their friendship, support, and for creating the perfect environment that greatly enhanced my research experience.

I am deeply appreciative of the financial support that made this research possible. I acknowledge the Air Force Office of Scientific Research (AFOSR) under Grant No. FA9550-19-1-0103, the National Science Foundation (NSF) under Grant No. ECCS-1711975, and the AFOSR Multidisciplinary Research Program of the University Research Initiative (MURI) administered through the University of New Mexico under Grant FA9550-20-1-0409. Their generous funding not only supported my Ph.D. research but also facilitated the publication of my work.

Words cannot convey the depth of my gratitude to my father, mother, and sister. Their unconditional love, endless encouragement, and unwavering belief in me are the bedrock of my life. My parents' sacrifices and dedication have inspired me to pursue my dreams with passion and determination. My sister's support and understanding have been a constant source of strength and comfort, reminding me of the importance of family in all of life's endeavors.

To my beloved wife, whose support transcended the miles between us during my Ph.D. journey, I express my heartfelt thanks. Her patience, love, and encouragement have been an inspiration of hope and motivation. Despite the distance, her firm belief in me provided the

strength and inspiration I needed to persevere and succeed.

I would also like to express my sincere appreciation to the University of California, Irvine, and the Department of Electrical Engineering and Computer Science for providing me with the opportunity and resources to pursue my doctoral degree. The enriching academic environment and faculty and staff support have been pivotal in my development as a researcher and scholar.

Finally, I extend my deepest gratitude to the Iran University of Science and Technology for laying the foundational knowledge that has been critical to my academic career. The education and experiences I gained there prepared me to embark on this journey and have been integral to reaching the position I hold today.

- The text of Chapter 2 of this dissertation is a reprint of the material as it appears in K. Rouhi, A. Nikzamir, A. Figotin, and F. Capolino, "Exceptional point in a degenerate system made of a gyrator and two unstable resonators," Physical Review A, vol. 105, no. 3, Mar. 2022. The coauthors listed in this publication are Alireza Kazemi, Alexander Figotin, and Filippo Capolino. Alexander Figotin and Filippo Capolino directed and supervised research which forms the basis for the dissertation.

- The text of Chapter 3 of this dissertation is a reprint of the material as it appears in K. Rouhi, A. Nikzamir, A. Figotin, and F. Capolino, "High-sensitivity in various gyrator-based circuits with exceptional points of degeneracy," EPJ Applied Metamaterials, vol. 9, p. 8, 2022. The coauthors listed in this publication are Alireza Nikzamir, Alexander Figotin, and Filippo Capolino. Alexander Figotin and Filippo Capolino directed and supervised research which forms the basis for the dissertation.

- The text of Chapter 4 of this dissertation is a reprint of the material as it appears in K. Rouhi, F. Capolino, and A. Figotin, "Simple reciprocal electric circuit exhibiting exceptional point of degeneracy," Journal of Physics A: Mathematical and Theoretical, vol. 57, no. 45, Sep. 2024. The coauthors listed in this publication are Alexander Figotin, and Filippo Capolino. Alexander Figotin and Filippo Capolino directed and supervised research which forms the basis for the dissertation.

- The text of Chapter 5 of this dissertation is a reprint of the material as it appears in A. Nikzamir, K. Rouhi, A. Figotin, and F. Capolino, "Time modulation to manage and increase the power harvested from external vibrations," Applied Physics Letters, vol. 123, no. 21, Nov. 2023. The coauthors listed in this publication are Alireza Nikzamir, Alexander Figotin, and Filippo Capolino. Alexander Figotin and Filippo Capolino directed and supervised research which forms the basis for the dissertation.

- The text of Chapter 6 of this dissertation is a reprint of the material as it appears in A. Nikzamir, K. Rouhi, A. Figotin, and F. Capolino, "Time modulation to manage and increase the power harvested from external vibrations," Applied Physics Letters, vol. 123, no. 21, Nov. 2023. The coauthors listed in this publication are Alireza

Nikzamir, Alexander Figotin, and Filippo Capolino. Alexander Figotin and Filippo Capolino directed and supervised research which forms the basis for the dissertation.

- The text of Chapter 7 of this dissertation is a reprint of the material as it appears in K. Rouhi, R. Marosi, T. Mealy, A. F. Abdelshafy, A. Figotin, and F. Capolino, "Exceptional degeneracies in traveling wave tubes with dispersive slow-wave structure including space-charge effect," Applied Physics Letters, vol. 118, no. 26, p. 263506, Jun. 2021. The coauthors listed in this publication are Robert Marosi, Tarek Mealy, Ahmed F. Abdelshafy, Alexander Figotin, and Filippo Capolino. Alexander Figotin and Filippo Capolino directed and supervised research which forms the basis for the dissertation.

- The text of Chapter 8 of this dissertation is a reprint of the material as it appears in K. Rouhi, R. Marosi, T. Mealy, A. Figotin, and F. Capolino, "Parametric Modeling of Serpentine Waveguide Traveling Wave Tubes," IEEE Transactions on Plasma Science, vol. 52, no. 4, pp. 1247–1263, Apr. 2024. The coauthors listed in this publication are Robert Marosi, Tarek Mealy, Alexander Figotin, and Filippo Capolino. Alexander Figotin and Filippo Capolino directed and supervised research which forms the basis for the dissertation.

VITA

Kasra Rouhi

EDUCATION

Doctor of Philosophy in Electrical and Computer Engineering **2019-2024**
University of California, Irvine *Irvine, California, USA*

Masters of Science in Electrical Engineering **2015-2018**
Iran University of Science and Technology *Tehran, Tehran, Iran*

Bachelor of Science in Electrical Engineering **2011-2015**
Iran University of Science and Technology *Tehran, Tehran, Iran*

INTERNSHIP

Summer Intern **Summer 2024**
Apple Inc. *San Diego, California*

LIST OF PUBLICATIONS

- **Journals**

[1] **K. Rouhi**, H. Kazemi, A. Figotin, and F. Capolino, "Exceptional Points of Degeneracy Directly Induced by Space–Time Modulation of a Single Transmission Line," *IEEE Antennas and Wireless Propagation Letters*, vol. 19, no. 11, pp. 1906–1910, Nov. 2020.

[2] **K. Rouhi**, R. Marosi, T. Mealy, A. F. Abdelshafy, A. Figotin, and F. Capolino, "Exceptional Degeneracies in Traveling Wave Tubes with Dispersive Slow-Wave Structure Including Space-Charge Effect," *Applied Physics Letters*, vol. 118, no. 26, p. 263506, Jun. 2021.

[3] **K. Rouhi**, A. Nikzamir, A. Figotin, and F. Capolino, "Exceptional point in a degenerate system made of gyrator and two unstable resonators," *Physical Review A*, vol. 105, no. 3, p. 032214, Mar. 2022.

[4] **K. Rouhi**, A. Nikzamir, A. Figotin, and F. Capolino, "High-Sensitivity in Various Gyrator-Based Circuits with Exceptional Points of Degeneracy," *EPJ Applied Metamaterials*, vol. 9, p. 8, 2022.

[5] **K. Rouhi**, R. Marosi, T. Mealy, A. Figotin and F. Capolino, "Parametric Modeling of Serpentine Waveguide Traveling Wave Tubes," *IEEE Transactions on Plasma Science*, pp. 1247-1263, 2024.

[6] A. Nikzamir*, **K. Rouhi***, A. Figotin, and F. Capolino, "Time modulation to manage and increase the power harvested from external vibrations," *Applied Physics Letters*, vol. 123, no. 21, p. 211701, 2023. (** These authors contributed equally to the work.*)

[7] **K. Rouhi**, F. Capolino, and A. Figotin, "Simple reciprocal electric circuit exhibiting exceptional point of degeneracy," *Journal of Physics A: Mathematical and Theoretical*, Sep. 2024.

[8] A. Nikzamir, **K. Rouhi**, A. Figotin, and F. Capolino, "How to Achieve Exceptional Points in Coupled Resonators Using a Gyrator or PT-symmetry, and in a Time-Modulated Single Resonator: High Sensitivity to Perturbations," *EPJ Applied Metamaterials*, vol. 9, p. 14, 2022.

[9] T. Mealy, R. Marosi, **K. Rouhi**, and F. Capolino, "Analytical Solution for Space-Charge Waves in a Two-Stream Cylindrical Electron Beam," *IEEE Transactions on Plasma Science*, vol. 51, no. 3, pp. 675–686, Mar. 2023.

[10] A. Hakimi, **K. Rouhi**, T. G. Rappoport, M. G. Silveirinha, and F. Capolino, "Chiral terahertz lasing with Berry-curvature dipoles," *Physical Review Applied*, vol. 22, no. 4, p. 041003, Oct. 2024.

[11] R. Marosi, **K. Rouhi**, T. Mealy, A. Figotin, and F. Capolino, "Small-Signal Model for

Inhomogeneous Helix Traveling-Wave Tubes using Transfer Matrices," *Physics of Plasmas*, Dec 2024.

- **Preprints**

[1] A. Nikzamir, **K. Rouhi**, A. Figotin, and F. Capolino, "Demonstration of Exceptional Points of Degeneracy in Gyrator-Based Circuit for High-Sensitivity Applications," *arXiv preprint* arXiv:2107.00639, Jul. 2021.

[2] **K. Rouhi**, A. Nikzamir, A. Figotin, and F. Capolino, "Enhanced Sensitivity of Degenerate System Made of Two Unstable Resonators Coupled by Gyrator Operating at an Exceptional Point," *arXiv preprint* arXiv:2110.01860, Oct. 2021.

- **Conferences**

[1] **K. Rouhi**, H. Kazemi, A. Figotin, and F. Capolino, "Investigation of Exceptional Point of Degeneracy in Space-Time Modulated Transmission Line," 2021 United States National Committee of URSI National Radio Science Meeting (USNC-URSI NRSM), Boulder, CO, USA, 2021.

[2] A. Nikzamir, **K. Rouhi**, A. Figotin, and F. Capolino, "Exceptional Points of Degeneracy in Gyrator-Based Coupled Resonator Circuit," 2021 United States National Committee of URSI National Radio Science Meeting (USNC-URSI NRSM), Boulder, CO, USA, 2021.

[3] Nikzamir, **K. Rouhi**, A. Figotin and F. Capolino, "Exceptional Points of Degeneracy in Gyrator-Based Coupled Resonator Circuit," 2021 Fifteenth International Congress on Artificial Materials for Novel Wave Phenomena (Metamaterials), NYC, NY, USA, 2021, pp. 302-304.

[4] **K. Rouhi**, A. Nikzamir, A. Figotin and F. Capolino, "Enhanced Sensitivity of Gyrator-based Circuit at Exceptional Point Composed of Unstable Resonators," 2022 United States National Committee of URSI National Radio Science Meeting (USNC-URSI NRSM), Boulder, CO, USA, 2022, pp. 66-67.

[5] **K. Rouhi**, R. Marosi, T. Mealy, A. F. Abdelshafy, A. Figotin and F. Capolino, "Model of Helix Traveling Wave Tube Including the Slow-Wave Structure Dispersion Characteristics and Space-Charge Effect," 2022 23rd International Vacuum Electronics Conference (IVEC), Monterey, CA, USA, 2022, pp. 478-479.

[6] **K. Rouhi**, A. Nikzamir, A. Figotin and F. Capolino, "Two resonators with negative and positive reactive components to achieve an exceptional point of degeneracy," 2022 Sixteenth International Congress on Artificial Materials for Novel Wave Phenomena (Metamaterials), Siena, Italy, 2022, pp. 374-376.

[7] **K. Rouhi**, R. Marosi, T. Mealy, A. Figotin and F. Capolino, "Modeling of Serpentine Waveguide Traveling Wave Tube to Calculate Gain Diagram," 2023 24th International Vacuum Electronics Conference (IVEC), Chengdu, China, 2023, pp. 1-2.

[8] T. Mealy, R. Marosi, **K. Rouhi**, and F. Capolino, "Analytical Solution for Space-Charge Waves in a Two-Stream Cylindrical Electron Beam," 2023 IEEE International Conference on Plasma Science (ICOPS), Santa Fe, NM, USA, 2023, pp. 1-1.

[9] H. Kazemi, A. Nikzamir, **K. Rouhi**, and F. Capolino, "Breaking Physical Bound on Absorbers Bandwidth Using Linear Time Varying Periodic Systems," 2023 URSI International Symposium on Electromagnetic Theory (EMTS), Vancouver, BC, Canada, 2023.

[10] M. Saavedra-Melo, **K. Rouhi**, and F. Capolino, "Wave-Controlled RIS: A Novel Method for Reconfigurable Elements Biasing," 2023 IEEE International Symposium on Antennas and Propagation and USNC-URSI Radio Science Meeting (USNC-URSI), Portland, OR, USA, 2023, pp. 979-980.

[11] **K. Rouhi**, A. Nikzamir, A. Figotin and F. Capolino, "Exceptional Points of Degeneracy Induced by Time-Periodic Modulation," 2023 Seventeenth International Congress on Artificial Materials for Novel Wave Phenomena (Metamaterials), Chania, Greece, 2023, pp. 312-314.

[12] **K. Rouhi**, R. Marosi, T. Mealy, A. Figotin, and F. Capolino, "Modeling of Sever in Two-stage Serpentine Waveguide Traveling Wave Tubes," 2024 25th International Conference on Vacuum Electronics (IVEC), Monterey, CA, USA, 2024.

[13] A. Hakimi, **K. Rouhi** and F. Capolino, "Electromagnetic Wave Propagation and Amplification in Anisotropic Material Made of Stacking Layers of Two-Dimensional Material and Dielectric," 2024 United States National Committee of URSI National Radio Science Meeting (USNC-URSI NRSM), Boulder, CO, USA, 2024, pp. 408-408.

[14] **K. Rouhi**, A. Nikzamir, A. Figotin and F. Capolino, "Second-Order Exceptional Point of Degeneracy in Two Directly Coupled Resonator," 2024 United States National Committee of URSI National Radio Science Meeting (USNC-URSI NRSM), Boulder, CO, USA, 2024, pp. 263-263.

[15] M. A. Saavedra-Melo, **K. Rouhi**, B. Bradshaw and F. Capolino, "Full RIS-domain Standing Waves for Elements' Biasing," 2024 United States National Committee of URSI National Radio Science Meeting (USNC-URSI NRSM), Boulder, CO, USA, 2024, pp. 93-93.

[16] M. Saavedra-Melo, **K. Rouhi**, B. Bradshaw, and F. Capolino, "Wave-Controlled Biasing of RIS for Multi-beam Scattering Pattern Generation," 2024 18th European Conference on Antennas and Propagation (EuCAP), Glasgow, Scotland, 2024.

[17] **K. Rouhi**, M. Saavedra-Melo, and F. Capolino, "Wave-Controlled RIS as Reconfigurable Reflective Lens for Focusing in the Fresnel Zone," 2024 IEEE International Sym-

posium on Antennas and Propagation and INC/USNC-URSI Radio Science Meeting (AP-S/INC-USNC-URSI), Firenze, Italy, 2024, pp. 259-260.

[18] M. Saavedra-Melo, V. Yao, B. Bradshaw, **K. Rouhi**, A. De Leon, A. Nikzamir, R. Marosi, and F. Capolino, " Progress in Wave-Controlled RIS: Experimental Demonstration of Biasing Voltage Generation," 2024 IEEE International Symposium on Antennas and Propagation and INC/USNC-URSI Radio Science Meeting (AP-S/INC-USNC-URSI), Firenze, Italy, 2024, pp. 1963-1964.

[19] A. Nikzamir, **K. Rouhi** and F. Capolino, "Exceptional Points of Degeneracy in Nonlinear Systems: Two Coupled Oscillators and Arrays of Oscillators," 2024 Eighteenth International Congress on Artificial Materials for Novel Wave Phenomena (Metamaterials), Chania, Greece, 2024, pp. 1-3.

LIST OF ACRONYMS

1D	One dimensional
2D	Two dimensional
3D	Three dimensional
ADS	Advanced Design System
CC	Coupled cavity
DBE	Degenerate band edge
e-beam	Electron beam
EM	Electromagnetic
EPD	Exceptional point of degeneracy
FFT	Fast Fourier transform
FW	Folded waveguide
LTP	Linear time-periodic
MEMS	Micro-electromechanical systems
Opamp	Operational amplifier
PIC	Particle in cell
PT	Parity-time
RBE	Regular band edge
RF	Radio frequency
SI	International system of units
SIP	Stationary inflection point
STM	Space-time modulated
SWS	Slow-wave structure
TE	Transverse electric
TL	Transmission line
TWT	Traveling wave tube

ABSTRACT OF THE DISSERTATION

Advancement in the modeling of electron beam devices and ultrasensitive circuits

By

Kasra Rouhi

Doctor of Philosophy in Electrical and Computer Engineering

University of California, Irvine, 2024

Professor Filippo Capolino, Chair

This dissertation explores the advancement of exceptional points of degeneracy (EPDs) in electrical circuits and their applications in highly sensitive devices, alongside the modeling of traveling wave tubes (TWTs) for microwave amplification. The EPD phenomenon, where two or more eigenmodes coalesce at a critical point, results in systems with heightened sensitivity to perturbations. This work illustrates how EPDs can be achieved using a gyrator-based and simpler circuit without the use of nonreciprocal components. A detailed analysis of various circuit configurations, including series and parallel LC resonators coupled via a gyrator, reveals the potential of these systems to exhibit second- and third-order EPDs. These systems demonstrate exceptional sensitivity, where small changes in capacitance, inductance, or other parameters lead to significant shifts in the resonance frequency, enabling applications such as material characterization and high-performance signal processing.

This dissertation investigates time-modulated systems and their ability to obtain EPDs. Time modulation introduces an additional degree of freedom to systems by periodically varying system parameters, such as damping or capacitance. A dual analogy between mechanical and electrical systems is presented to better understand how energy is dynamically redistributed within these modulated systems. By applying this approach to a mechanical system equipped with a time-modulated damper, the results demonstrate increases in

harvested power, making this technique highly advantageous for applications like wireless sensors, remote monitoring devices, and energy-autonomous systems. This dissertation also explores the use of space-time modulation in transmission lines (TL) as a method to directly induce EPDs, a novel approach that can significantly impact microwave circuits and telecommunication systems. By modulating the per-unit-length capacitance of a single transmission line in both space and time, two propagating eigenmodes coalesce at EPD. This research highlights the advantages of this approach, demonstrating how small variations in modulation parameters can lead to large shifts in system behavior, thus providing a powerful tool for next-generation electronic and communication devices.

In the second part of the thesis, the focus shifts to TWTs, which are essential devices for high-power microwave amplification based on linear electron beams. TWTs are widely used in telecommunications, radar, and satellite communication due to their ability to amplify RF signals over a broad frequency range. This research focuses on the inclusion of dispersive slow-wave structures (SWS) and the space-charge effect to better understand and optimize TWT performance. A critical aspect of this work is the introduction of EPD in TWTs by carefully tuning the dispersive properties of the SWS and accounting for electron beam (e-beam) and electromagnetic (EM) wave interactions.

Parametric modeling of serpentine waveguide TWTs is presented as a key advancement in understanding wave propagation and amplification in TWTs. We developed a model for TWTs and applied it to helix TWT and serpentine TWT which are well-known types of TWTs in the industry. This model provides insight into optimizing beam-wave interactions for maximum gain without dealing with the high burden of PIC simulation. Furthermore, the dissertation explores multi-stage TWT designs, introducing the concept of severs—components that stop RF wave propagation at the middle of TWT to prevent back reflections and improve stability. Additionally, the work investigates the small-signal behavior of TWTs, examining how small perturbations in beam current, phase velocity, or input power affect the overall amplifica-

tion process. Numerical simulations and theoretical models are provided to compare various TWT configurations, offering a clear pathway to design improvements that maximize gain while minimizing energy loss. By bridging the gap between theoretical modeling and practical implementation, this dissertation contributes to the development of more efficient, and high-performing TWTs, making them well-suited to next-generation communication where power, efficiency, and bandwidth are paramount importance.

Chapter 1

Introduction

1.1 Exceptional Point of Degeneracy

Exceptional points of degeneracy (EPDs) represent a profound physical phenomenon where two or more eigenvalues and their corresponding eigenvectors coalesce into a single eigenmode under certain conditions [3, 4, 5, 6, 7, 8]. We denote these points as EPD, and the degeneracy order represents the number of coalescing eigenmodes. This point of coalescence occurs in the parameter space of a system and is distinctly different from conventional degeneracy, which often refers to the matching of eigenvalues without the simultaneous merging of eigenvectors. Such a condition is also simply referred to as "EP" in various works [9, 10]; here, the "D" is used to stress the importance of the degeneracy [11]. The concept of EPDs has received significant attention due to its wide range of applications across various domains, including electromagnetics, optics, and quantum mechanics [12, 13, 14, 15, 16, 17]. A general description of possible electromagnetic (EM) structures that may exhibit EPDs is shown in Figure 1.1. The structures were categorized into four main categories.

It is possible to observe the EPD phenomenon in EM systems, waveguides, and circuits.

In multimodal waveguides, for instance, eigenvectors may coalesce into a single eigenvector as parameters such as frequency or geometrical properties of the structure are varied [18]. This condition leads to unique behaviors such as diverging waves in time and space, as explored in time-varying structures [19]. In such cases, the system matrix is defective and non-diagonalizable, a characteristic that distinguishes EPD from typical degeneracies where the system matrix is diagonalizable [20, 21]. However, EPDs are not common in nature but can be engineered into various structures for significant performance enhancements in devices such as sensors, amplifiers, and oscillators [15]. For example, periodic guiding structures can exhibit EPDs at the band edges where group velocity approaches zero. This class of EPDs is known as the Regular Band Edge (RBE), where two Floquet-Bloch eigenwaves coalesce at the Brillouin zone edge [22]. Higher-order EPDs, such as the Degenerate Band Edge (DBE), can also be found in more complex periodic systems. These higher-order degeneracy are particularly advantageous in microwave and photonic applications, allowing for the creation of high-power and highly efficient devices [23]. Also, an EPD occurs in systems where the evolution of the system vector, in space or time, is described by a non-Hermitian matrix which can be imposed by periodicity [24, 20, 19] or by having losses and gain in the system [6, 7, 25, 26, 27]. EPDs of second order may occur with asymmetric distributions of gain and loss in uniform CTLs [25, 28]. Also, in [28] second order EPDs in uniform CTLs with loss and gain have been investigated from the bifurcation theory point of view. Forth order EPDs have been demonstrated in [29] using waveguides without loss and gain, and also with loss and gain.

Another intriguing aspect of EPDs arises in Parity-Time (PT)-symmetric systems, where the system's refractive index obeys the condition $n(x) = n^*(-x)$, where the asterisk means complex conjugation, leading to a symmetric balance of gain and loss [30, 31, 7]. PT-symmetric systems are known for having a real-valued spectrum when the PT symmetry is unbroken, and a transition from real to complex eigenvalues occurs at the EPD, also known as the bifurcation point [32, 33, 28]. This transition is critical in systems such as coupled

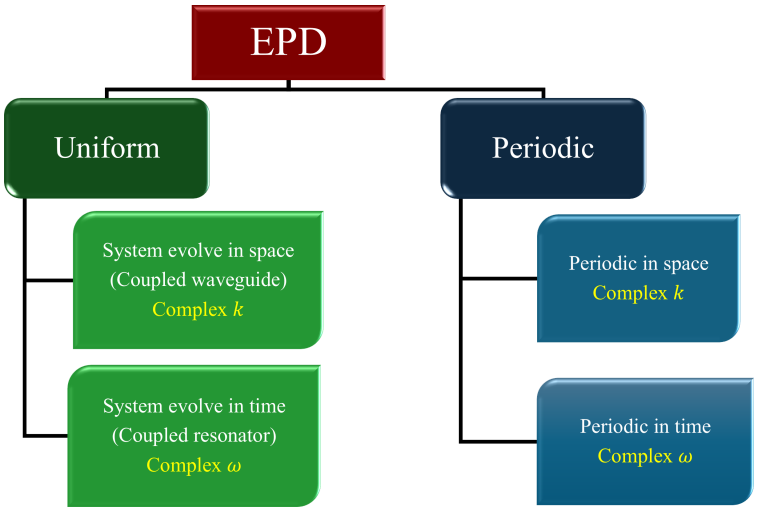

Figure 1.1: Classification of the different structure and topologies that can exhibit EPDs.

waveguides and resonators, where the interplay between gain and loss leads to fascinating phenomena like low-threshold lasing and enhanced sensitivity in sensors [34, 35].

The occurrence of EPDs is not limited to systems with PT-symmetry. EPDs can also be found in systems with periodic spatial or temporal variations, even in the absence of gain and loss. In periodic structures, for instance, EPDs manifest at the cut-off frequencies or zero frequencies in waveguides, leading to interesting degeneracy related to EM band gaps [18, 36, 24]. Time-varying systems, on the other hand, can exhibit EPDs when the system parameters, such as frequency or gain and loss, are periodically changed. Under such conditions, the eigenvalues and eigenvectors coalesce, resulting in unique resonance behaviors.

In summary, the exploration of EPD offers a rich and versatile framework for advancing the design and performance of various electromagnetic and waveguide devices. Through careful engineering of system parameters, EPDs can be exploited to achieve superior device functionalities, making them a key focus of ongoing research in high-power microwave, RF systems, and beyond.

1.2 Applications of EPD

EPDs hold significant potential in various applications due to their ability to enhance system performance through careful parameter design. EPDs are implemented in systems such as sensors, oscillators, and amplifiers to achieve remarkable properties like ultra-sensitivity, high efficiency, and enhanced nonlinear effects. This section explores the wide-ranging applications of EPDs and how their presence improves system functionality.

1.2.1 Sensors

EPDs play a crucial role in developing sensors with ultra-sensitivity to small perturbations. In optical microcavity systems, for instance, traditional sensing methods depend on changes in linewidth, frequency shift, or splitting of a resonance, which scales proportionally to perturbation strength. However, by operating at EPDs, sensors can achieve significantly enhanced sensitivity.

In PT-symmetric systems, EPDs are obtained by carefully balancing gain and loss parameters. Such systems exhibit real eigenfrequencies, leading to sharp resonances, which enhance spectral resolution beyond what passive systems can achieve. This improvement in spectral resolution directly impacts the sensor's ability to detect minor changes in the environment [37, 38].

For example, the study in [37] reports the observation of EPDs in a coupled-cavity photonic laser, where a precisely tailored gain-loss distribution enabled the system to operate at an EPD. In this configuration, the frequency response follows a cube-root dependence on refractive index perturbations, highlighting the sensitivity of such a system to structural changes. Similarly, another study in [38] demonstrates a sensor design based on a whispering-gallery mode microtoroid cavity, where nanoscale scatterers introduced EPDs that led to

enhanced sensitivity. Due to the frequency splitting resulting from the perturbation strength, the system is much more sensitive than traditional sensors.

1.2.2 Oscillators

EPD-based oscillators offer significant efficiency improvements, especially for radio-frequency (RF) and microwave sources. The key advantage of these oscillators lies in their ability to utilize modal degeneracy, which allows for reduced oscillation thresholds, frequency independence from load variations, and the elimination of active output buffer stages.

For example, the degeneracy condition can be exploited in spatially periodic coupled transmission lines (TLs), where multiple Bloch eigenmodes coalesce into a single eigenmode at the band edge. This results in high-Q resonances and improved efficiency. Various oscillator designs based on EPDs have been proposed, including the DBE oscillator made from a double-ladder resonant circuit. This design shows enhanced performance, such as lower oscillation thresholds and improved output loading robustness.

Another oscillator design uses a periodically-loaded circular waveguide structure to support slow-wave electromagnetic modes that coupled with a linear electron beam. Here, the coalescence of four degenerate modes (in the "cold" structure) results in the so called "multi-mode synchronization regime" resulting in low beam current requirements for oscillation initiation, further improving efficiency [39, 40, 41]. Analogously, microstrip-based oscillators achieve EPDs through spatial periodicity in coupled microstrip lines leading to a DBE in the lossless waveguides; the system oscillates at the DE frequency when small gain is introduced [42, 43].

Finally, a new class of array oscillators have been proposed using waveguides where gain elements compensate for radiation loss of arrayed antennas, paving the way to high power highly-synchronous directive radiation [44, 45].

1.2.3 Amplifiers

EPD-based amplifiers have been proposed as a solution to exceeding the performance limits of conventional amplification techniques. These amplifiers, operating under degeneracy conditions, can achieve higher gain and greater efficiency [17].

The core principle behind these amplifiers lies in the electromagnetic eigenmode degeneracy in periodic slow-wave structures (SWS). The third-order degeneracy, known as stationary inflection points (SIPs), coalesces three Floquet-Bloch eigenmodes, leading to amplified performance. When synchronized with an electron beam (e-beam), a periodic structure operating at an SIP offers possible advantages, such as gain enhancement, improved gain-bandwidth products, and higher power efficiency [23].

1.3 Traveling Wave Tubes

Traveling wave tubes (TWTs) are high-gain, high-frequency amplifiers that play a crucial role in various communication and radar systems [46]. Since their invention in the 1940s, TWTs have remained indispensable due to their unique ability to amplify microwave signals over a broad range of frequencies, which cannot be easily achieved with conventional amplifiers. The operational principle of a TWT relies on the interaction between an electron beam (e-beam) and an RF signal traveling along an SWS, which allows for continuous energy transfer between them [47]. This continuous interaction ensures that even weak signals can be amplified significantly without being limited by resonance frequency bands.

In the TWTs, amplification is achieved through the interaction between an e-beam and EM wave traveling along the SWS. A typical TWT is shown in Figure 1.2. The e-beam is typically generated by an electron gun, accelerated through a vacuum tube, and directed along the SWS, where it interacts with the RF signal [48, 49]. As the EM wave propagates along

the structure at nearly the same velocity as the e-beam, synchronism is established, allowing electrons to transfer energy efficiently to the EM wave, leading to signal amplification. This process relies on electron bunching, where the EM field influences the e-beam, causing electrons to cluster and create a space-charge wave that further amplifies the RF field by inducing additional current back into the RF circuit, enhancing the electron bunching effect. This positive feedback amplifies the EM field as the RF signal travels down the structure where the large RF signal is collected at the output. The SWS plays a crucial role by providing slow-wave modes that match the electron velocity, which is typically a fraction of the speed of light, ensuring in-phase interaction and efficient extraction of kinetic energy from the e-beam. This mechanism enables TWTs to operate across a wide frequency spectrum, from several GHz up to millimeter-wave frequencies, and allows for high power output and linearity, making TWTs ideal for applications that require both high efficiency and minimal signal distortion, such as satellite communications, radar, scientific research, and electronic warfare [47].

1.4 Applications of TWTs

There are several variants of TWTs, each designed with specific applications and performance characteristics in mind.

1.4.1 Helix TWTs

The helix TWT is one of the earliest and most commonly used types. It features a helix-shaped slow-wave structure that enables wideband amplification [50]. The helix serves to slow down the RF wave to match the velocity of the e-beam, facilitating continuous energy transfer across a broad frequency range. Helix TWTs can operate at frequencies from a

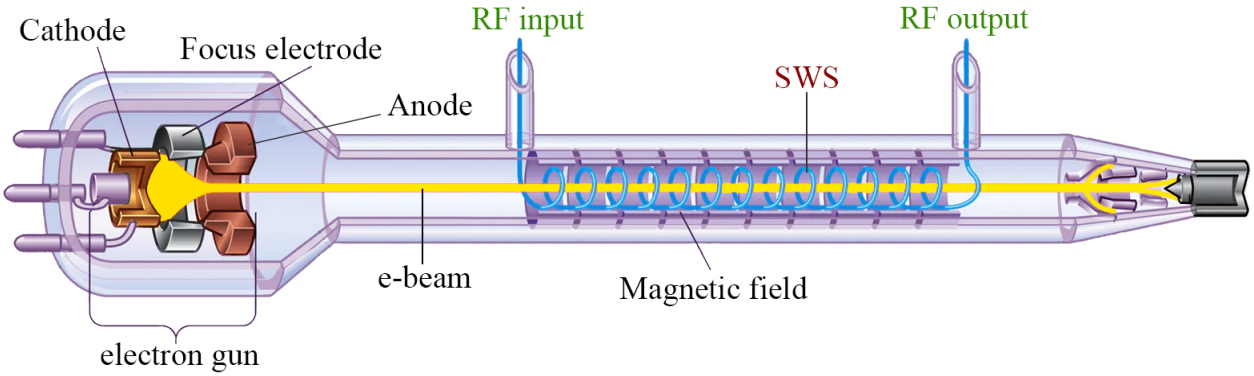

Figure 1.2: Schematic representation of a TWT with the required components. As the input RF signal enters the input port on the left, the amplified output signal is extracted from the output port on the right. The original illustration is adapted from *Encyclopedia Britannica*, and the colors and composition were modified by the author.

few GHz up to millimeter-wave bands, typically offering wide bandwidths and moderate power output [51]. These characteristics make them ideal for use in satellite communication systems, terrestrial microwave links, and telemetry systems, where broad frequency coverage and consistent amplification are required.

1.4.2 Coupled-Cavity TWTs

Coupled-cavity (CC) TWTs use a series of resonant cavities instead of continuous SWS [52, 53]. The EM wave interacts with the e-beam at specific intervals determined by cavity spacing. This design allows CCTWTs to achieve higher power output than helix TWTs, though typically at the expense of bandwidth [54, 55]. These TWTs are most suitable for applications requiring high-power amplification in a narrow frequency range, such as military radar systems and electronic warfare devices. The precise tuning of CCTWTs makes them well-suited to environments where signal integrity and power are critical.

1.4.3 Folded Waveguide TWTs / Serpentine Waveguide TWTs

Folded waveguide (FW) TWTs represent an evolution in TWT design, offering improved efficiency and compactness for high-frequency applications [56, 57]. In this design, the SWS consists of a waveguide that is "folded" into a series of tight, parallel sections, which significantly slows the phase velocity of the RF signal to match the e-beam. This allows the device to operate at higher frequencies than helix TWTs while providing efficient amplification over a moderately wide bandwidth [58]. The FW structure is inherently robust and compact, reducing losses and enhancing thermal performance. These characteristics make FWTWTs ideal for use in applications such as millimeter-wave radar, electronic warfare, and space-borne communication systems, where both high power and efficient heat dissipation are crucial.

FWTWTs also offer the advantage of high gain and lower noise levels, making them a preferred choice in situations where signal integrity is paramount [46]. For instance, in high-resolution radar systems and satellite transponders, the folded waveguide design ensures that the amplified signal remains clear and precise, even at high frequencies where other TWT types may introduce more distortion or signal degradation. Additionally, these TWTs are valued for their long operational lifetimes and reliability in harsh environments, making them well-suited to aerospace and defense applications.

The primary difference between serpentine waveguide (SW) TWTs and FWTWTs lies in the design and geometry of their SWS, which directly affects their performance characteristics. SWTWTs use a meandering or serpentine path for the waveguide, where the wave travels through multiple bends, slowing the phase velocity of the RF signal to match that of the e-beam. In other words, an SW has a winding, snake-like path, whereas an FW is essentially a flat waveguide that is folded back and forth on itself to slow down the EM wave, allowing for better interaction with the e-beam. This design offers a compact form factor

and is typically used for moderate power applications, where the primary goal is to achieve wideband operation in a relatively small package. On the other hand, FWTWTs feature a more tightly folded or zigzag structure that compresses the waveguide into even smaller, parallel sections. This design is optimized for high-frequency operation and better thermal management, allowing the FWTWT to handle higher power and maintain efficiency in more demanding environments. While both types offer advantages in terms of bandwidth and compactness, FWTWTs are generally preferred for high-power, high-frequency applications, where efficiency and power output are crucial, whereas SWTWTs are often used when size constraints are more critical.

1.5 Classification of Different Types of TWTs

TWTs can be classified based on several factors, including their SWSs, the application they are designed for, and their operating frequency range. In the following classification, TWTs are divided into a number of categories.

1.5.1 Based on SWS

- **Helix TWT:** Characterized by a helix-shaped SWS, these TWTs offer wide bandwidth and are commonly used in communication systems such as satellite transponders and microwave links.
- **CCTWT:** Utilizing a series of resonant cavities, this type of TWT is suited for high-power applications with narrow bandwidth, typically used in radar and military systems.
- **FWTWT:** Featuring a folded or zigzag waveguide structure, FWTWTs are compact and provide high-efficiency amplification at millimeter-wave frequencies. They are used

in space-borne systems, radar, and electronic warfare.

- **SWTWT:** These TWTs use a meandering waveguide path to slow down the RF wave. They are compact, provide moderate power, and are suitable for wideband applications where space is limited.

1.5.2 Based on Applications

- **Communication TWTs:** Primarily helix TWTs are used due to their wide bandwidth, making them ideal for satellite communications, television broadcasting, and telemetry systems.

- **Radar and Electronic Warfare TWTs:** CCTWTs and FWTWTs are used in applications requiring high power and precision, such as military radar, air traffic control, and electronic warfare systems.

- **Scientific and Medical TWTs:** These TWTs are designed for high precision and power output, used in particle accelerators, plasma research, and medical devices like linear accelerators for cancer treatment.

- **Space Exploration TWTs:** TWTs are employed in deep-space communication systems, providing reliable, high-power amplification for signals transmitted over vast distances. They are essential for spacecraft communications and data relay on interplanetary missions.

- **Industrial Processing TWTs:** Used in industrial processing applications requiring high energy, such as microwave heating, drying, and material processing, where precision and controlled power are crucial.

- **Instrumentation and Test TWTs:** These TWTs are used in laboratory and industrial test equipment, enabling accurate signal generation and amplification for testing

various electronic and communication components.

- **Security and Surveillance TWTs:** TWTs provide high-power amplification in security and surveillance radar systems, including those used in perimeter monitoring, maritime patrol, and border security.

1.5.3 Based on Frequency Range

- **Low-Frequency TWTs (GHz Range):** These TWTs operate in the GHz frequency range and typically include helix TWTs for communication applications.

- **High-Frequency TWTs (Millimeter-Wave Range):** FWTWTs and SWTWTs are commonly employed at millimeter-wave frequencies, where high power and efficient amplification are needed.

1.6 Application of TWTs

TWTs are integral to a vast array of high-frequency systems, thanks to their ability to offer high-power amplification over a wide frequency range with excellent linearity [46]. In satellite communications, TWTs are used as the primary amplifiers in satellite transponders, where they are responsible for boosting signals transmitted from Earth to space and vice versa. The wide bandwidth of TWTs allows for the simultaneous transmission of numerous communication channels, enabling a variety of services including television broadcasting, internet access, and secure communications. Their high power output ensures that signals can be transmitted over long distances with minimal loss of fidelity, a critical requirement for maintaining reliable satellite links.

In radar systems, particularly in military and air traffic control applications, TWTs provide

the power needed to transmit radar signals over great distances and to detect objects with high precision [51]. TWTs are essential for both continuous-wave and pulsed radar systems, where their high efficiency and ability to operate at microwave and millimeter-wave frequencies allow for superior detection capabilities. In military radar systems, TWTs enhance the ability to track fast-moving objects, while in air traffic control, they help ensure aircraft safety by providing real-time data on their positions.

TWTs are also widely used in electronic warfare systems, where their broad bandwidth enables the generation of powerful jamming signals that can disrupt communication and radar systems across a wide spectrum. The ability to generate high-power, wideband signals is particularly valuable in modern electronic warfare, where adversaries may employ various communication methods over a wide range of frequencies.

In scientific research, TWTs are used in fields such as particle physics and plasma research [59]. They are integral components of particle accelerators, where they provide the microwave energy needed to accelerate charged particles to near-light speeds. TWTs are also employed in plasma heating systems for nuclear fusion research, where their high-frequency output is used to heat and sustain plasma for experiments aimed at developing sustainable fusion energy.

Additionally, TWTs find application in medical devices like linear accelerators, which are used for radiation therapy in cancer treatment. In these systems, TWTs amplify the microwave signals that generate high-energy x-rays used to target and destroy cancerous cells while sparing surrounding healthy tissue. TWT reliability and precision in these medical applications are critical to ensuring patient safety and treatment efficacy.

TWT amplifiers offer several advantages over semiconductor amplifiers, particularly in applications requiring high power and wide bandwidth. TWTs can operate at much higher power levels than typical semiconductor amplifiers, making them suitable for systems such

as satellite communications and radar, where substantial signal strength is essential over long distances [60]. Additionally, TWTs provide a broader frequency range, often covering multiple GHz, which supports a wider array of channels or signals simultaneously—critical in both communication and scientific applications. Their inherent linearity is another significant advantage, enabling TWTs to handle complex modulation schemes with minimal signal distortion, a key factor in maintaining fidelity for data transmission. Moreover, TWTs tend to have better thermal stability in high-power operations, whereas semiconductor amplifiers can suffer from heat dissipation challenges at similar power outputs [60]. These characteristics make TWT amplifiers especially advantageous in demanding environments and applications where reliability, power, and bandwidth are prioritized.

In summary, traveling wave tubes are versatile and powerful devices that have been essential in advancing technology in communications, radar, electronic warfare, and scientific research. Their ability to amplify signals over a wide range of frequencies with high efficiency and linearity makes them invaluable for both commercial and military applications. As technology continues to demand higher frequencies, greater bandwidth, and more powerful signals, TWTs will remain a critical component in the evolution of high-frequency electronic systems.

1.7 Organization of the Dissertation and Contents

Chapter 2: This chapter focuses on a system comprising a gyrator and two unstable resonators, which is designed to exhibit EPD. The gyrator is a non-reciprocal element and couples two LC resonators, both intentionally designed with negative inductances or capacitances, creating instability. These instabilities are key to achieving the desired degenerate state. We further explore various configurations, such as when both inductances are negative or when both capacitances are negative, to demonstrate how the system reaches EPD.

A significant portion of the analysis is dedicated to frequency-domain analysis, where the resonance frequencies are examined in both lossless and lossy circuits. The role of loss is also considered, showing how EPDs can still occur in circuits that experience damping, though with different sensitivity characteristics. The practical implications of this are explored in a liquid level sensing application, where the extremely high sensitivity near the EPD is utilized to measure changes in liquid content by detecting shifts in resonance frequencies. This chapter concludes by illustrating the potential of this system to serve as a high-precision sensor, especially in applications that require detecting small environmental changes.

Chapter 3: This chapter extends the work from Chapter 2 by investigating various configurations of gyrator-based circuits, all of which exhibit EPDs. It discusses both series and parallel configurations of LC resonators connected via a gyrator. The first part of the chapter provides an in-depth review of the theoretical background, explaining how second-order and third-order EPDs occur in these circuits. A second-order EPD occurs when two eigenmodes merge, while third-order EPDs involve the coalescence of three eigenmodes, leading to even greater sensitivity. The chapter then details the mathematical framework for analyzing the eigenfrequencies of these circuits, with a focus on how small perturbations in system parameters, such as capacitance or inductance, affect the eigenfrequencies near the EPD. This characteristic makes these systems ideal candidates for high-sensitivity sensors. Additionally, the chapter discusses the physical realization of both stable and unstable EPD frequencies, and how these can be controlled by adjusting the circuit components. The ability to manipulate the order of the EPDs, as well as the sensitivity of the circuit to parameter changes, is highlighted as a major advantage in designing precision sensors or oscillators.

Chapter 4: In this chapter, the focus shifts to a simple, reciprocal circuit that still exhibits an EPD. This system consists of two LC resonators (series and parallel) coupled via a shared capacitor. The circuit is reciprocal, meaning it does not require a gyrator, yet it achieves a similar Jordan canonical form to that of more complex nonreciprocal systems. This is

significant because it shows that a simpler, more easily realizable system can still demonstrate the desirable properties of EPD, including enhanced sensitivity to perturbations. The chapter delves into the mathematical formulation of the circuit, providing a detailed analysis of its eigenvalues and the conditions under which it reaches EPD. The coalescence of eigenmodes is discussed in terms of the system's Lagrangian and Hamiltonian structures, which further illuminate how symmetry plays a role in the circuit's behavior. This theoretical framework is complemented by numerical simulations, which show excellent agreement with analytical results. Given its simplicity and ease of implementation, this reciprocal circuit offers a more accessible pathway to designing high-sensitivity systems without the need for complex nonreciprocal elements.

Chapter 5: This chapter introduces the concept of time modulation as a means of enhancing energy harvesting from external vibrations. The primary focus is on mechanical systems that convert vibrational energy into electrical energy, a process that is often limited by the efficiency of the energy conversion mechanism. By introducing time-periodic modulation of certain system parameters, such as the damping coefficient, the energy harvested can be increased significantly. The time modulation creates a dynamic EPD in the system, which allows it to resonate more efficiently with external vibrations and thus extract more energy. The chapter begins by explaining the underlying physics of time modulation and its effect on system eigenmodes. It then presents a mathematical derivation of the EPD condition in a time-modulated mechanical system, followed by a dual circuit analog that clarifies the electrical equivalent of the mechanical process. Detailed simulations show how different modulation frequencies affect power output. A key result is that time modulation at specific frequencies can increase harvested power by an order of magnitude compared to systems without modulation.

Chapter 6: This chapter explores the use of space-time modulation in a single TL to induce EPDs. Unlike previous chapters, which rely on circuit components like inductors and

capacitors, this chapter demonstrates how the distributed parameters of a TL—such as its capacitance—can be modulated in time and space to achieve an EPD. This approach is particularly promising for applications in microwave circuits and telecommunications, where modulated TLs can be used. The chapter begins with a background on space-time modulation and its effects on wave propagation in TLs. It then presents a detailed mathematical analysis of how periodic modulation of per-unit-length capacitance leads to eigenmode coalescence. This phenomenon creates a second-order EPD, where the system's wavenumbers exhibit a square-root dependence on small perturbations. The practical significance of this result lies in the fact that such systems can be used to design highly sensitive sensors or amplifiers, with the TL acting as both the signal propagation medium and the sensor element. This dual functionality makes the space-time modulated TL a highly efficient and compact design for next-generation electronic devices.

Chapter 7: This chapter serves to bridge the gap between the two main concepts explored in this thesis, namely, EPD and TWT. This chapter discusses the occurrence of EPDs in TWTs with dispersive SWS and accounts for space-charge effects. TWTs are widely used in high-power microwave amplification, and this chapter explores how introducing dispersive media and space-charge effects can lead to exceptional degeneracy. The chapter begins with an overview of how TWTs operate, followed by a detailed mathematical formulation of the conditions required for an EPD in such systems. By carefully tuning the SWS parameters, such as its phase velocity and impedance, it is possible to achieve an EPD, which leads to enhanced gain and efficiency in the TWT. The chapter provides a practical example using a realistic helix TWT, showing how theoretical predictions align with simulation results. This work has significant implications for the design of more efficient high-power amplifiers, especially in applications where compact size and high performance are critical.

Chapter 8: This chapter delves into the parametric modeling of SWTWTs, a type of SWS commonly used in microwave amplification. The chapter provides a comprehensive analysis

of SW, beginning with an equivalent circuit model that describes cold (unpowered) SWS. This model is used to study the wave propagation characteristics in SW, including its dispersion and interaction impedance. The chapter also introduces the concept of a cascaded circuit model, where each segment of SW is modeled as a TL. In addition to the cold SWS, the chapter discusses the interaction between the e-beam and the EM wave in the hot (powered) SWS. This interaction is key to understanding the gain and efficiency of the TWT. The chapter also presents a detailed analysis of the on-axis electric field distribution within the beam tunnel and how it affects the interaction impedance. The theoretical findings are validated through simulations, which show excellent agreement with the circuit model. This work provides valuable insights into the design of SWTWTs, particularly in optimizing their gain and efficiency.

Chapter 9: This chapter presents a small-signal model for multi-stage SWTWTs, with a particular focus on the use of severs. A sever is a device used to interrupt EM wave in a multi-stage TWT, which improves stability by reducing reflections. The chapter begins by outlining the theoretical background for modeling small-signal interactions in TWTs and then applies this model to a two-stage SWTWT with ideal and realistic severs. The model is used to predict the TWT gain at different frequencies, and the results are compared with simulations. The chapter also explores the design of a wedge-shaped sever, which introduces losses in a controlled manner to attenuate the wave. By comparing theoretical predictions with simulation results, we demonstrate how severs can be optimized to mitigate instability and better performance in multi-stage TWTs. This work has important implications for the design of high-power microwave amplifiers with multiple stages.

Chapter 10: The final chapter provides an in-depth analysis of wavepacket propagation in TWTs. Wavepackets are short bursts of EM waves that propagate through the SWS of a TWT, and their behavior is critical to understanding the device's performance. The chapter begins by reviewing the fundamental equations of wavepacket propagation in dispersive

media, followed by a detailed analysis of how different design parameters, such as the SWS geometry and the beam-wave interaction, affect wavepacket propagation. One of the key findings is that wavepacket propagation is highly sensitive to the signal frequency near the EPD. When the pulse frequency composition is close to the transition point between stable and unstable modes, the propagated wavepacket can distort dramatically. The chapter provides several examples of wavepacket behavior in realistic TWTs, showing how these phenomena can be used to analyze the device's performance.

Chapter 2

Exceptional Point in Degenerate System Made of Gyrator and Two Unstable Resonators

We demonstrate that a circuit comprising two unstable LC resonators coupled via a gyrator supports an EPD with purely real eigenfrequency. Each of the two resonators includes either a capacitor or an inductor with a negative value, showing a purely imaginary resonance frequency when not coupled to the other via the gyrator. With external perturbation imposed on the system, we show analytically that the resonance frequency response of the circuit follows the square-root dependence on perturbation, leading to possible sensor applications. Furthermore, the effect of small losses in the resonators has been investigated, and we show that losses lead to instability. In addition, the EPD occurrence and sensitivity are demonstrated by showing that the relevant Puiseux fractional power series expansion describes the eigenfrequency bifurcation near the EPD. The EPD has the great potential to enhance the sensitivity of a sensing system by orders of magnitude.

2.1 Background, Motivation, and State of the Art

An EPD is a point in parameter space at which the eigenmodes of the circuit, namely the eigenvalues and the eigenvectors, coalesce simultaneously [3, 61, 4, 62, 63, 18, 64, 24, 65]. As the remarkable feature of an EPD is the strong full degeneracy of at least two eigenmodes, as mentioned in [11], the significance of referring to it as a "degeneracy" is here emphasized, hence including "D" in the EPD. An EPD in the system is reached when the system matrix is similar to a matrix that contains a non-trivial Jordan block. EPD-induced sensitivity according to the concept of PT-symmetry in multiple coupled resonators has been studied [66, 67, 12]. Also, the electronic circuits with EPD based on PT-symmetry have been expressed in [9, 33] and then more developed in [68, 69] where the circuits are made of two coupled resonators with gain-loss symmetry and a proper combination of parameters leads to an EPD. Primarily, it has been confirmed that the eigenvalues bifurcation feature at EPD can significantly increase the effect of external perturbation; namely, the sensitivity of resonance frequency to component value perturbations can be enhanced. Moreover, frequency splitting happens at degenerate frequencies of the system where eigenmodes coalesce, and this feature at EPDs has been investigated to conceive a new generation of sensors [70, 71, 72, 15]. The resulting perturbation leads to a shift in the system resonance frequency that can be recognized and measured using the proper measurement setup [70]. When a second-order EPD at which specifically two eigenstates coalesce is subjected to a small external perturbation, the resulting eigenvalue splitting is proportional to the square root of the external perturbation value, which is bigger than the case of linear splitting for conventional degeneracies [73]. The concept of EPD has been employed in various sensing schemes such as optical microcavities [12], optical microdisk [74], e-beam devices [75], mass sensors [76], and bending curvature sensors [77].

The gyrator is a two-terminal network in which the transmission phase shift in one direction differs by π from the transmission phase shift in the reverse direction [78]. Another property

of the gyrator network is that of impedance inversion. The inductance at the output of the gyrator is observed as capacitance at the input port, and a voltage source is transformed to a current source. A relevant alias for the gyrator might be the "dualizer" since it can interchange current and voltage roles and turns an impedance into its dual [79]. Gyrators could be designed directly as integrated circuits [80, 81]. Also, many opamp-based gyrator circuits have been proposed [82, 83, 84], which can be classified into two types. First, 3-terminal gyrator circuits in which both ports are grounded [82]; second, 4-terminal gyrator circuits in which the output port is floating [83, 84]. Because of the availability of different realizable circuits for gyrators and their versatility as practical circuit devices, gyrator-based circuits may form an essential part of integrated circuit technology in a wide range of applications.

In this chapter, we study the second-order EPDs in a gyrator-based sensing circuit as Figure 2.1 and explore its enhanced sensitivity (variation in the sensor's resonance frequencies to external perturbations) and its potential for sensing devices in the vicinity of the EPD. At the EPD, the degeneracy is in both the real and imaginary parts of the eigenvalues, as well as in the eigenvectors. Two series LC resonators are coupled in the utilized circuit via an ideal gyrator, as explained in [85]. Contrary to the study in [85], this chapter demonstrates the conditions to get the EPD with real eigenfrequency by using unstable resonators. In other words, we study the case of two unstable resonators coupled via an ideal gyrator. A general mathematical approach for constructing lossless circuits for any conceivable Jordan structure has been developed in [86], including the simplest possible circuit as in Figure 2.1 and other circuits related to the Jordan blocks of higher dimensions. In addition, important issues related to operational stability, perturbation analysis, and sensitivity analysis are studied in [87], whereas analysis of stability or instability by adding losses to the circuit is not discussed. We show that the gyrator-based circuit can achieve EPD with real eigenfrequency even when two unstable resonators are used in the circuit. Hence, dispersion diagrams corresponding to perturbations in the circuit's parameters show the eigenfrequencies split. Then, we show examples for different cases and analyze the voltage signals by

using time-domain simulations. We then study the impact of small losses in the circuit and explain how they can make it unstable. Besides, we look at the sensitivity of circuit eigenfrequencies to component variations, and we show that the Puiseux fractional power series expansion well approximates the bifurcation of the eigenfrequency diagram near the EPD [4]. The sensitivity enhancement is attributed to the second root topology of the eigenvalues in parameter space, peculiar to the second-order EPD. Lastly, we examine the gyrator-based circuit's enhanced sensitivity and provide a practical scenario to detect physical parameter variations and material characteristics changes. This work is important for understanding the instability in the coupled resonators circuit, in addition to exploring EPD physics in gyrator-based circuits. The given analysis and circuit show promising potential in novel ultra high-sensitive sensing applications.

2.2 Gyrator Characteristic

A gyrator is a two-port component that couples an input port to an output port by a gyration resistance value. It is a lossless and storage-less two-port network that converts circuits at the gyrator output into their duals, with respect to the gyration resistance value [88]. For instance, this component can make a capacitive circuit behave inductively, a series LC resonator behave like a parallel LC resonator, and so on. This device allows network realizations of two-port devices, which cannot be realized by just the basic components, i.e., resistors, inductors, capacitors, and transformers. In addition, the gyrator could be considered a more fundamental circuit component than the ideal transformer because an ideal transformer can be made by cascading two ideal gyrators, but a gyrator cannot be made from transformers [78]. The circuit symbol for the ideal gyrator is represented in Figure 2.1 (red dashed box), and the defining equations are [78, 89]

$$\begin{cases} v_2 = R_{\mathrm{g}} i_1 \\ v_1 = -R_{\mathrm{g}} i_2 \end{cases} \tag{2.1}$$

where R_{g} is called gyration resistance and has a unit of Ohm. A gyrator is a nonreciprocal two-port network represented by an asymmetric impedance matrix $\underline{\mathbf{Z}}_{\mathrm{g}}$ as [89]

$$\underline{\mathbf{Z}}_{\mathrm{g}} = \begin{bmatrix} 0 & -R_{\mathrm{g}} \\ R_{\mathrm{g}} & 0 \end{bmatrix}. \tag{2.2}$$

2.3 EPD Condition in The Lossless Gyrator-based Circuit

This section provides an analysis of a gyrator-based circuit in which two series LC resonators are coupled via an ideal gyrator as illustrated in Figure 2.1. In the first step, we consider the circuit's components to be lossless. The circuit resembles the one in [85], but here the two resonance angular frequencies $\omega_{01} = 1/\sqrt{C_1 L_1}$ and $\omega_{02} = 1/\sqrt{C_2 L_2}$ of the two uncoupled resonators are imaginary with a negative sign (also the counterpart with the positive sign is a resonance), since we consider three cases: (i) both L_1 and L_2 are negative while the capacitors have positive values, (ii) both C_1 and C_2 are negative while the inductors have positive values, and (iii) $L_1(C_1)$ and $C_2(L_2)$ are negative while other elements have positive values. Then, we investigate the conditions for an EPD to occur in the three cases just mentioned. In realistic sensing devices, various sensor types are used. For instance, capacitive sensors are used to sense humidity, temperature, and distance. Proximity sensors and distance measurement sensors are available on the market, which operate based on electromagnetic induction, hence

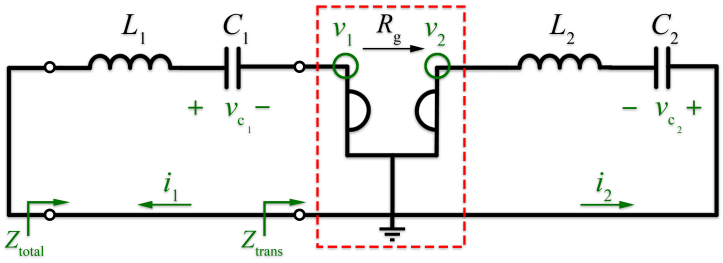

Figure 2.1: The schematic illustration of the proposed gyrator-based circuit with the ideal gyrator is indicated by the red dashed box. In this circuit, two different (unstable) LC resonators are embedded in a series configuration, coupled via an ideal gyrator.

the variation of inductance mutual coupling. Some other sensors are based on a perturbation of the inductance. Therefore, both the inductance and capacitance can be used as sensing components, and we will investigate both cases in two separate subsections.

In the past years, EPDs have been found by using balanced loss and gain in a PT-symmetry scheme [33, 12]. More recently, EPDs have also been found in systems with time-periodic modulation [19, 90]. Here, we obtain EPDs by using a negative inductance and a negative capacitance in the gyrator-based circuit, constituting a new class of EPD-based circuits.

We consider the Kirchhoff voltage law equations in the time-domain for two loops of the circuit in Figure 2.1. In order to find the solution of the circuit differential equations, it is convenient to define the state vector as $\mathbf{\Psi}(t) \equiv [Q_1, Q_2, \dot{Q}_1, \dot{Q}_2]^{\mathrm{T}}$, where T denotes the transpose operator. The state vector consists of stored charges in the capacitors $Q_n = \int i_n dt = C_n v_{c_n}$, and their time derivative (currents) $\dot{Q}_n = i_n$, $n = 1, 2$. We utilize the Liouvillian formalism for this circuit as [85]

$$\frac{\mathrm{d}\mathbf{\Psi}(\mathrm{t})}{\mathrm{dt}} = \underline{\mathbf{M}}\mathbf{\Psi}(\mathrm{t}), \underline{\mathbf{M}} = \begin{pmatrix} 0 & 0 & 1 & 0 \\ 0 & 0 & 0 & 1 \\ -\omega_{01}^2 & 0 & 0 & \frac{R_\mathrm{g}}{L_1} \\ 0 & -\omega_{02}^2 & -\frac{R_\mathrm{g}}{L_2} & 0 \end{pmatrix}, \tag{2.3}$$

where $\underline{\mathbf{M}}$ is the 4×4 circuit matrix. Assuming time harmonic dependence of the form $Q_n \propto e^{j\omega t}$, we obtain the characteristic equation allowing us to find the eigenfrequencies by solving $\det(\underline{\mathbf{M}} - j\omega\underline{\mathbf{I}}) = 0$, where $\underline{\mathbf{I}}$ is the identity matrix. The corresponding characteristic equation of the circuit is

$$\omega^4 - \omega^2\left(\omega_{01}^2 + \omega_{02}^2 + \frac{R_\mathrm{g}^2}{L_1 L_2}\right) + \omega_{01}^2\omega_{02}^2 = 0, \tag{2.4}$$

where any solution ω is an eigenfrequency of the circuit. In the case of $R_\mathrm{g} = 0$, the two resonators are uncoupled, and the circuit has two eigenfrequency pairs of $\omega_{1,3} = \pm\omega_{01}$, and $\omega_{2,4} = \pm\omega_{02}$, that are purely imaginary (in contrast to the case studies in [85], where the resonance frequencies have real values). All the ω's coefficients of the characteristic equation are real, so ω and ω^* are both roots of the characteristic equation, where * indicates the complex conjugate operator. Moreover, it is a quadratic equation in ω^2; therefore, ω and $-\omega$ are both solutions of the Equation (2.4). As we mentioned before, we only consider unstable resonators, i.e., resonators with an imaginary resonance frequency. Therefore, only one circuit element in each resonator should have a negative value, leading to ω_{01}^2 and ω_{02}^2 with negative values. After finding the solutions of the characteristic equation, the angular eigenfrequencies (resonance frequencies) of the circuit are expressed as

$$\omega_{1,3} = \pm\sqrt{a+b},\ \omega_{2,4} = \pm\sqrt{a-b}, \tag{2.5}$$

where

$$a = \frac{1}{2}\left(\omega_{01}^2 + \omega_{02}^2 + \omega_{\mathrm{g}}^2\right), \tag{2.6}$$

$$b^2 = a^2 - \omega_{01}^2\omega_{02}^2\ , \tag{2.7}$$

where it has been convenient to define $\omega_{\mathrm{g}}^2 = R_{\mathrm{g}}^2/(L_1L_2)$, that may be positive or negative depending on the considered case. According to Equation (2.5), the EPD condition requires

$$b = 0, \tag{2.8}$$

leading to an EPD angular frequency $\omega_{\mathrm{e}} = \sqrt{a}$ (with its negative pair $-\omega_{\mathrm{e}}$). According to Equation (2.7), the EPD condition is rewritten as $a^2 = \omega_{01}^2\omega_{02}^2$. As in [85], we consider positive values for a to have a real EPD angular frequency ω_{e} , so we have

$$\omega_{01}^2 + \omega_{02}^2 + \omega_{\mathrm{g}}^2 > 0. \tag{2.9}$$

Finally, the EPD frequency is calculated by using Equations (2.6), (2.7), and (2.8) as

$$\omega_{\mathrm{e}} = \sqrt{\tfrac{1}{2}\left(\omega_{01}^2 + \omega_{02}^2 + \omega_{\mathrm{g}}^2\right)}. \tag{2.10}$$

The last equation can also be rewritten as $\omega_e = \sqrt[4]{\omega_{01}^2\omega_{02}^2}$, with the quartic square root defined by taking the positive value; in other words, if we consider that the two unstable frequencies have the following purely imaginary expression, $\omega_{01} = -j/\sqrt{|C_1L_1|}$ and $\omega_{02} = -j/\sqrt{|C_2L_2|}$, the EPD frequency can be expressed as $\omega_e = \sqrt{-\omega_{01}\omega_{02}}$. We obtain the desired value of a real EPD frequency by optimizing the values of the components in the circuit. Theoretically, the employed optimization method is not critical, and we need to find the solutions of Equation (2.8). Obviously, practical limitations also affect the selection of suitable constraints for optimization. In the particular case the two circuits are identical, one has $\omega_0^2 \equiv \omega_{01}^2 = \omega_{02}^2 = 1/(LC) < 0$, and the EPD condition reduces to $4\omega_0^2 = -\omega_g^2$,that in turns leads to the EPD angular frequency $\omega_e = \sqrt{-\omega_0^2}$. In the following subsections, we analyze the circuit in three different cases, i.e., the three different assumptions mentioned earlier.

2.3.1 Negative Inductances L_1 and L_2

As a first case, we consider a negative value for both inductances and a positive value for both capacitances; hence, in this case $\omega_g^2 > 0$. According to the required condition for EPD expressed in Equation (2.8) and by using Equation (2.7), the first and second terms in Equation (2.6) are negative and the third term is positive. Equation (2.10) shows that, if $|\omega_{01}^2 + \omega_{02}^2| < \omega_g^2$ we obtain a real value for EPD frequency, and if $|\omega_{01}^2 + \omega_{02}^2| > \omega_g^2$, the EPD frequency yields an imaginary value.

We explain the procedure for obtaining an EPD in this circuit by presenting an example. We select L_1, L_2, and C_2 to have standard commercial values. Then, the calculated value for C_1 can be realized by a combination of the standard capacitors values and a trimmer capacitor. Various combinations of values for the circuit's components can satisfy the EPD condition demonstrated in Equation (2.8), and here as an example, we consider this set of values:

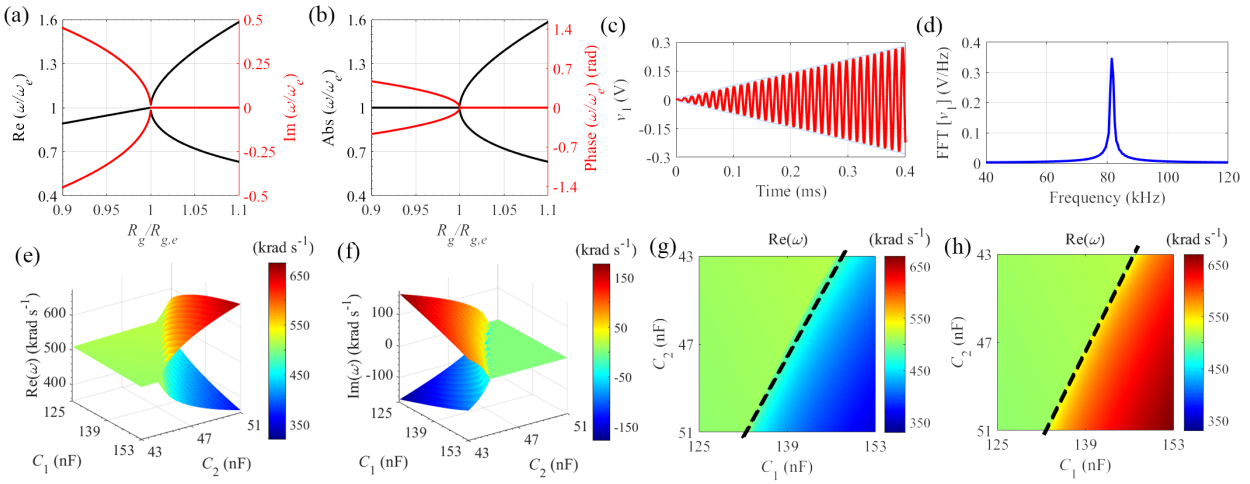

Figure 2.2: The sensitivity of the (a) real/imaginary parts and (b) magnitude/phase of the eigenfrequencies to gyration resistance perturbation, while inductances are negative. Voltage $v_1(t)$ under the EPD condition in the (c) time-domain, and (d) frequency-domain. The frequency-domain result is calculated from 40 kHz to 120 kHz by applying an FFT with 10^6 samples in the time window of 0 ms to 0.4 ms. The three-dimensional plot of the (e) real and (f) imaginary parts of the eigenfrequencies to C_1 and C_2 perturbation. The real part of eigenfrequencies for (g) higher and (h) lower value of resonance frequencies which colormap show the resonance frequency value. The black dashed line in these plots shows the EPD.

$L_1 = -47\,\mu$H, $L_2 = -47\,\mu$H, $C_2 = 47$ nF, and $R_\mathrm{g} = 50\,\Omega$. Then, the capacitance of the first resonator is determined by solving the resulting quadratic equation from the EPD condition demonstrated in Equation (2.8). In this example, we consider C_1 as a sensing capacitance of the circuit, which has a positive value and it can detect variations in environmental parameters and transform them into electrical quantities. According to Equation (2.8), after solving the quadratic equation, two different values for capacitance in the first resonator are calculated, and we consider $C_{1,\mathrm{e}} = 139.17$ nF for the presented example. In this example, both ω_{01}^2 and ω_{02}^2 have negative values, with $\omega_{01} = -j391$ krad/s, and $\omega_{02} = -j672.82$ krad/s, leading to a positive result for a in Equation (2.6) and real EPD angular frequency $\omega_\mathrm{e} = 512.9$ krad/s. The results in Figures 2.2(a), and (b) show the real/imaginary parts and magnitude/phase of perturbed eigenfrequencies obtained from the eigenvalue problem when R_g of the ideal gyrator is perturbed, revealing the high sensitivity to perturbations. An EPD occurs when both eigenvalues and eigenvectors coalesce. Therefore, the eigenvalues coalesce

in both the real and imaginary parts.

To investigate the time-domain behavior of the circuit under EPD conditions, we use the Keysight ADS circuit simulator. The transient behavior of the coupled resonators with the ideal gyrator is simulated using the time-domain solver with an initial condition $v_{c_1}(0) = 1\text{mV}$, where $v_{c_1}(t)$ is the voltage of the capacitor in the left resonator. Figure 2.2(c) shows the time-domain simulation results of the voltage $v_1(t)$, where $v_1(t)$ is the voltage at the gyrator input port (see Figure 2.1). The extracted result is obtained in the time span of 0 ms to 0.4 ms. The solution of the eigenvalue problem in the Equation (2.3) and at the EPD is different from any other regular frequency in the dispersion diagram since the system matrix contains repeated eigenvalues associated with one eigenvector. Thus, the time-domain response of the circuit at the second-order EPD is expected to be in the form of $\mathbf{\Psi}(t) \propto te^{j\omega_e t}$, as it is indeed shown in Figure 2.2(c). The envelope of the voltage signal grows linearly with increasing time, whereas the oscillation frequency is constant. This remarkable feature is peculiar to an EPD, and it is the result of coalescing eigenvalues and eigenvectors that also correspond to a double pole in the circuit (or zero, depending on what is observed). We take an FFT of the voltage $v_1(t)$ to show the frequency spectrum, and the calculated result is illustrated in Figure 2.2(d). The result is calculated from 40 kHz to 120 kHz by applying an FFT with 10^6 samples in the time window of 0 ms to 0.4 ms. The numerically observed oscillation frequency is $f_o = \omega_o/(2\pi) = 81.63\,\text{kHz}$, which shows the frequency corresponds to the maximum value in Figure 2.2(d). The numerically obtained value is in good agreement with the theoretical value calculated above.

So far, we have used the gyrator-based circuit to measure the perturbation near EPD by varying the gyrator resistance. Next, we analyze the circuit's sensitivity to independent perturbations in the positive values of *both* capacitances. We change the capacitance value on each resonator independently and calculate the eigenfrequencies' real and imaginary parts. The three-dimensional result for the calculated eigenfrequencies is illustrated in Figures

2.2(e), and (f). The elevation value of any point on the surface shows the eigenfrequency, and the associated color helps to recognize it conveniently. In these figures, only the two solutions with $\mathrm{Re}(\omega) > 0$ are illustrated. Although the resonance frequency of each resonator in this chapter is imaginary, in the specific range of C_1 and C_2, the EPD frequency is purely real. To utilize these calculated results, the flat version of the three-dimensional diagram for the real part is provided in Figures 2.2(g), and (h) for higher and lower eigenfrequency. These figures can help designers in the design procedure to select the proper value for components to achieve the desired real resonance frequency. The intersection of two surfaces (eigenfrequencies surface and surface of constant z plane) is a one-dimensional curve. Therefore, there is a different set of values for capacitances to produce oscillation at a certain frequency. Moreover, the intersection of the higher eigenfrequencies surface and lower eigenfrequencies surface indicates the possible EPD that various combinations of capacitances values can yield. Designers can use these figures to pick the proper value in the design steps according to their practical limitations.

2.3.2 Negative Capacitances C_1 and C_2

In the following section, we consider another condition in which negative capacitances are used on both resonators; so $\omega_g^2 > 0$. Using the mentioned presumption, the first and second terms in Equation (2.6) are negative because of the imaginary value of the resonance frequencies of resonators, and the third term is positive. So, if the EPD condition is met, the sign of a in Equation (2.6) indicates whether the eigenfrequency is real or imaginary. According to Equation (2.5), if $|\omega_{01}^2 + \omega_{02}^2| < \omega_g^2$ we get a real value for the EPD frequency, and if $|\omega_{01}^2 + \omega_{02}^2| > \omega_g^2$, the EPD frequency is imaginary.

Different combinations of values for the circuit's components can satisfy the EPD condition demonstrated in Equation (2.8), and here as an example, we use this set of values: $C_1 =$

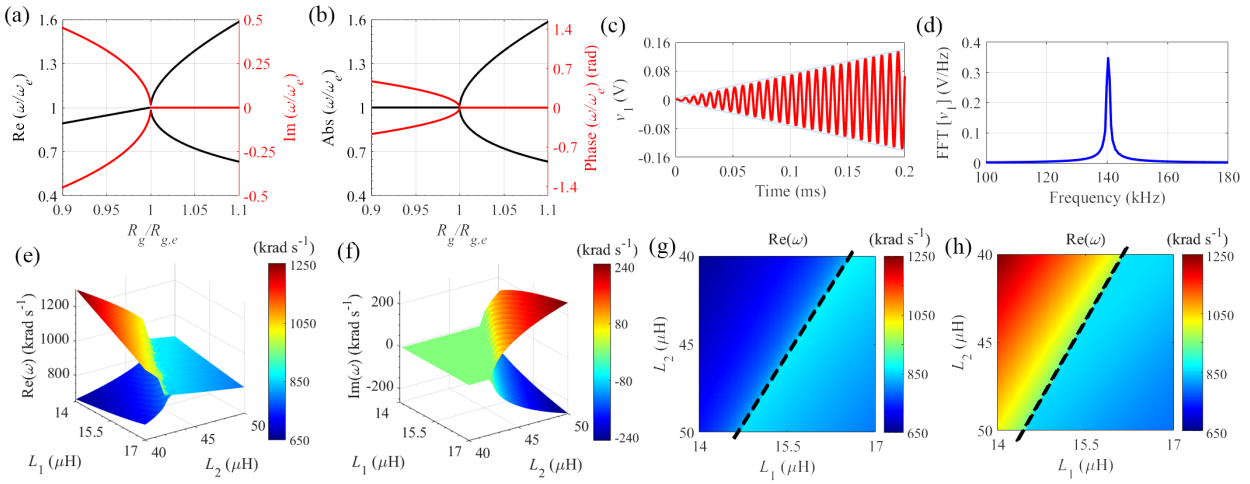

Figure 2.3: The sensitivity of the (a) real/imaginary parts and (b) magnitude/phase of the eigenfrequencies to gyration resistance perturbation, while capacitances are negative. Voltage $v_1(t)$ under the EPD condition in the (c) time-domain, and (d) frequency-domain. The frequency-domain result is calculated from 100 kHz to 180 kHz by applying an FFT with 10^6 samples in the time window of 0 ms to 0.2 ms. The three-dimensional plot of the (e) real and (f) imaginary parts of the eigenfrequencies to L_1 and L_2 perturbation. The real part of eigenfrequencies for (g) higher and (h) lower value of resonance frequencies which colormap show the resonance frequency value. The black dashed line in these plots shows the EPD.

-47 nF, $C_2 = -47$ nF, $L_2 = 47\,\mu$H, and $R_\mathrm{g} = 50\,\Omega$. The inductance value on the left resonator is calculated by solving the resulting quadratic equation from Equation (2.8). In the presented example, L_1 can be a sensing inductor in a system. According to Equation (2.8), two different values for inductance in the first resonator are calculated after solving the quadratic equation. We consider $L_{1,\mathrm{e}} = 15.87\,\mu$H for this example, so both ω_{01}^2 and ω_{02}^2 have negative values, with $\omega_{01} = -j1.16$ Mrad/s, and $\omega_{02} = -j672.82$ krad/s. Then, we obtain a positive value for a in Equation (2.6), leading to a real EPD angular frequency of $\omega_\mathrm{e} = 881.6$ krad/s. The results in Figures 2.3(a), and (b) shows the the real/imaginary parts and magnitude/phase of eigenfrequencies obtained by perturbing R_g near the value that made the EPD.

The time-domain simulation result by using the Keysight ADS with an initial condition $v_1(0) = 1$mV is presented in Figure 2.3(c). The voltage $v_1(t)$ is calculated in the time interval of 0 ms to 0.2 ms. Figure 2.3(c) shows the envelope of $v_1(t)$ is growing linearly with increasing

time. The growing signal demonstrates that the circuit eigenvalues coalesce, and the output envelope rises linearly at the second-order EPD frequency. In order to evaluate the oscillation frequency from the time-domain simulation, we take an FFT of voltage $v_1(t)$ from 100 kHz to 180 kHz using 10^6 samples in the time window of 0 ms to 0.2 ms. The calculated spectrum is shown in Figure 2.3(d), showing an oscillation frequency of $f_o = \omega_o/(2\pi) = 140.31$ kHz, which is in good agreement with the calculated theoretical value obtained from Equation (2.10).

In the following step, we investigate the circuit's sensitivity to independent perturbations in the value of both inductances. The real and imaginary parts of the eigenfrequencies are calculated when the values of the inductances are changed. The three-dimensional eigenfrequencies map of the two solutions with $\mathrm{Re}(\omega) > 0$ is shown in Figures 2.3(e), and (f). In order to provide a better representation, the flat view of the three-dimensional diagram for the real part is shown in Figures 2.3(g), and (h) for higher and lower eigenfrequencies.

2.3.3 Negative Inductance on One Side and Negative Capacitance on the Other Side

In this last case, different constraints for components value are considered. We assume a component with a negative value on one side (capacitance/inductance) and the other component with a negative value on the other side (inductance/capacitance); hence, in this case $\omega_g^2 < 0$. For instance, we consider a negative inductance on the right resonator and a negative capacitance on the left resonator. So, we have two unstable resonators when they are uncoupled. When two resonators are coupled, EPD should satisfy Equation (2.7). According to Equation (2.10), all terms inside the square root are negative, and the sum of negative values is always negative. As a result, it is impossible to achieve an EPD with a real eigenfrequency under the assumption mentioned above. Since we focus on cases with

real EPD frequency in this chapter, we will skip considering this condition in the rest of the chapter.

2.4 Frequency-Domain Analysis of the Resonances in Lossless Gyrator-Based Circuit

We demonstrate how the EPD regime is associated with a special kind of circuit's resonance, directly observed in frequency-domain circuit analysis. First, we calculate the transferred impedance on the left port of the gyrator in Figure 2.1, which is

$$Z_{\text{trans}}(\omega) = \frac{R_{\text{g}}^2}{Z_2(\omega)}, \tag{2.11}$$

where $Z_2(\omega) = j\omega L_2 + 1/(j\omega C_2)$ is the impedance of LC tank on the right side of the gyrator. The total impedance observed from the input port (see Figure 2.1) is

$$Z_{\text{total}}(\omega) \triangleq Z_1(\omega) + Z_{\text{trans}}(\omega) = Z_1(\omega) + \frac{R_{\text{g}}^2}{Z_2(\omega)}, \tag{2.12}$$

where $Z_1(\omega) = j\omega L_1 + 1/(j\omega C_1)$ is the impedance of LC tank on the left side of the gyrator. The complex-valued resonance frequencies of the circuit are calculated by imposing $Z_{\text{total}}(\omega) = 0$. Figure 2.4 shows the zeros of such total impedance $Z_{\text{total}}(\omega)$ for various gyration resistance values (arrows represent growing R_{g} values). When considering the EPD gyrator resistance $R_{\text{g}} = R_{\text{g,e}} = 50\,\Omega$, one has $Z_{\text{total}}(\omega) \propto (\omega - \omega_{\text{e}})^2$, i.e., the two zeros coincide with the EPD angular frequency ω_{e}, that is also the point where the two curves in Figure 2.4 meet. For gyrator resistances $R_{\text{g}} < R_{\text{g,e}}$, the two resonance angular frequencies are complex conjugate, consistent with the result in Figure 2.4. Also, for gyrator resistances

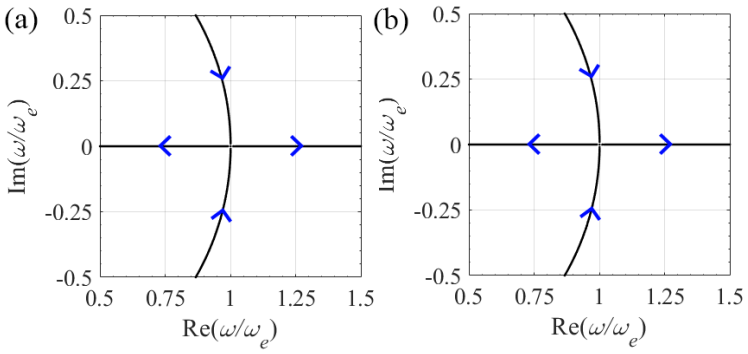

Figure 2.4: Root locus of zeros of $Z_{\text{total}}(\omega) = 0$ shows the real and imaginary parts of the resonance frequencies of the circuit when varying gyration resistance (arrows represent growing R_{g} values). In these figures, we consider two cases with a negative value of (a) both inductances and (b) both capacitances, discussed in Section 2.3. At the EPD, the system's total impedance is $Z_{\text{total}}(\omega) \propto (\omega - \omega_{\text{e}})^2$; hence it exhibits a double zero at ω_{e}.

such that $R_{\text{g}} > R_{\text{g,e}}$, the two resonance angular frequencies are purely real. In other words, the EPD frequency coincides with the double zeros of the frequency spectrum, or double poles, depending on the way the circuit is described.

2.5 EPD in the Lossy Gyrator-Based Circuit

The following section analyzes the EPD condition in the gyrator-based circuit by accounting for series resistors R_1 and R_2 in resonators as illustrated in Figure 2.5. A procedure analogous to the one discussed earlier, using the same state vector $\mathbf{\Psi} \equiv [Q_1, Q_2, \dot{Q}_1, \dot{Q}_2]^{\text{T}}$, leads to [85]

$$\frac{\mathrm{d}\mathbf{\Psi}}{\mathrm{dt}} = \underline{\mathbf{M}}\mathbf{\Psi}, \;\; \underline{\mathbf{M}} = \begin{pmatrix} 0 & 0 & 1 & 0 \\ 0 & 0 & 0 & 1 \\ -\omega_{01}^2 & 0 & -\gamma_1 & \frac{R_{\text{g}}}{L_1} \\ 0 & -\omega_{02}^2 & -\frac{R_{\text{g}}}{L_2} & -\gamma_2 \end{pmatrix}. \tag{2.13}$$

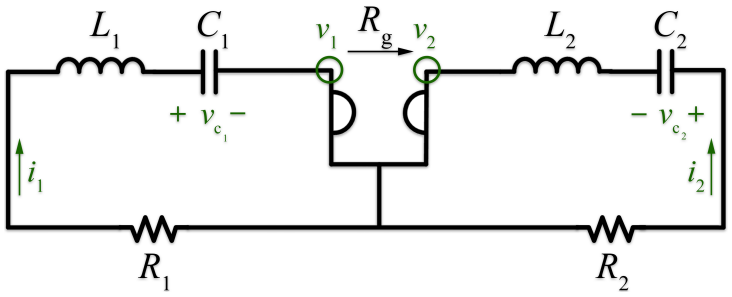

Figure 2.5: Schematic view of the lossy gyrator-based circuit, with a resistor in each resonator.

In the presented lossy circuit matrix, $\gamma_1 = R_1/L_1$, and $\gamma_2 = R_2/L_2$ determine losses in each resonator. These eigenfrequencies of the circuit are calculated by solving the below characteristic equation,

$$\omega^4 - j\omega^3(\gamma_1 - \gamma_2) - \omega^2\left(\omega_{01}^2 + \omega_{02}^2 + \gamma_1\gamma_2 + \tfrac{R_g^2}{L_1L_2}\right) + j\omega(\gamma_1\omega_{02}^2 + \gamma_2\omega_{01}^2) + \omega_{01}^2\omega_{02}^2 = 0. \tag{2.14}$$

The coefficients of the odd-power terms of the angular eigenfrequency in the characteristic equation are imaginary; therefore, ω and $-\omega^*$ are both roots of the characteristic equation. In order to obtain a stable circuit with real-valued eigenfrequencies, the coefficients of the odd-power terms in the characteristic equation of Equation (2.14), $-j(\gamma_1 - \gamma_2)$ and $j(\gamma_1\omega_{02}^2 + \gamma_2\omega_{01}^2)$, should vanish, otherwise a complex eigenfrequency is needed to satisfy the characteristic equation. The coefficient of the ω^3 term is zero when $\gamma_1 = \gamma_2$, but according to this condition, the coefficient of the ω term is non-zero because ω_{01}^2 and ω_{02}^2 are both negative. Moreover, the coefficient of the ω term never vanishes when both resonators are lossy because both ω_{01}^2 and ω_{02}^2 have the same sign. Consequently, it is not possible to have all real-valued coefficients in the characteristic polynomials, except when $\gamma_1 = \gamma_2 = 0$, which corresponds to a lossless circuit.

2.5.1 RLC Resonators With Negative Inductances L_1 and L_2

In the first case, we assume inductances with negative values. In Figures 2.6(a) and (b), γ_1 is perturbed while we assume $\gamma_2 = 0$, whereas in Figures 2.6(c), and (d), γ_2 is perturbed while $\gamma_1 = 0$. These four figures present the real/imaginary parts and magnitude/phase of eigenfrequencies when the resistances R_1 and R_2 are perturbed individually. We use the same values for the circuit components as already used in the lossless circuit presented in Subsection 2.3.1. The normalization term ω_e is the EPD angular frequency obtained when $\gamma_1 = \gamma_2 = 0$, which is the same EPD frequency as the lossless circuit. In this case, losses in the circuit are represented by negative γ_1 and γ_2 since L_1, and L_2 are negative, so the right half side of the figure axes show the loss and the left half side of the axes represent the gain in the circuit through a negative resistance. In Figures 2.6(a)-(d), we recognize the bifurcations of the real/imaginary parts and magnitude/phase of the eigenfrequencies, so the circuit is extremely sensitive to variations of resistances in the vicinity of EPD. By perturbing γ_1 or γ_2 away from $\gamma_1 = \gamma_2 = 0$, the circuit becomes unstable, and it begins to self oscillate at a frequency associated with the real part of the unstable angular eigenfrequency. In addition, we show the real and imaginary parts of the eigenfrequencies by separately perturbing the resistances on both sides in Figures 2.6(e)-(f). The black contour lines in these three-dimensional figures show constant real and imaginary parts of the eigenfrequencies. We observe that by adding either loss or gain, the circuit becomes unstable. Instability in the circuit is not due to the instability of the uncoupled resonators, but rather it is unstable because of the addition of losses, as was the case in [85] for different configurations. When γ_1 or γ_2 is perturbed from the EPD, the oscillation frequency is shifted from the EPD frequency, and it could be measured for sensing applications. The eigenfrequency with a negative imaginary part is associated with an exponentially growing signal (instability). Considering the existence of instability, there are a few possible ways of operation: preventing the system from reaching saturation by switching off the circuit, partially compensating for losses, or

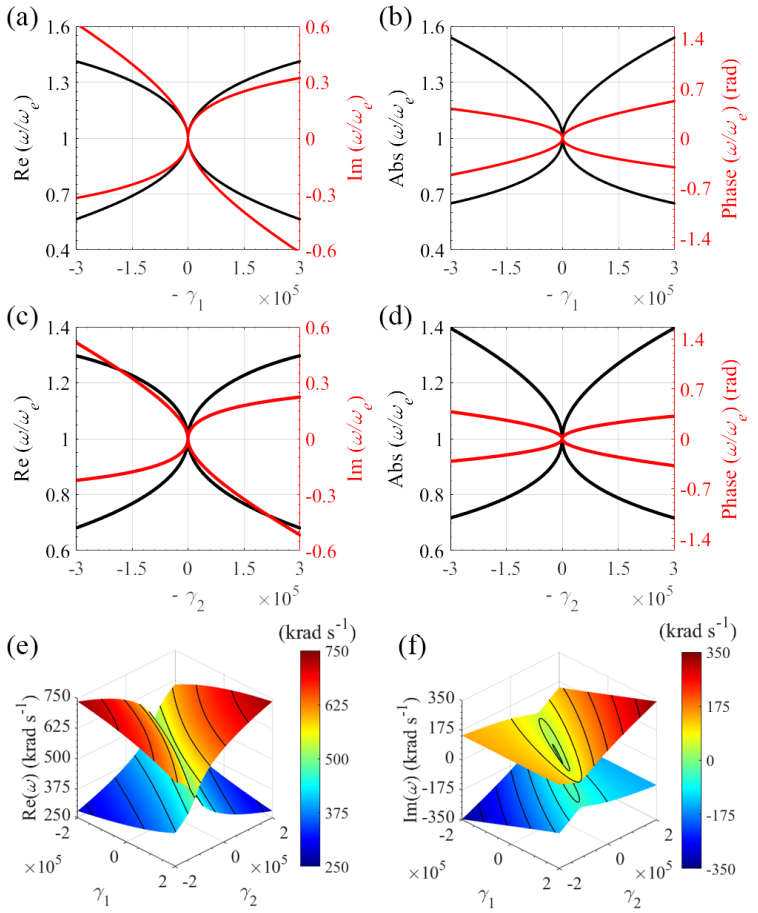

Figure 2.6: Case with negative value of the inductances on both resonators. Variation of (a) real/imaginary parts and (b) magnitude/phase of the angular eigenfrequencies to a resistor perturbation on the left resonator, i.e., when $-\gamma_1$ changes and $\gamma_2 = 0$. (c) and (d), as in (a) and (b), but the resistor perturbation is on the right resonator, i.e., $-\gamma_2$ changes and $\gamma_1 = 0$. Variation of (e) real and (f) imaginary parts of the angular eigenfrequencies to independent resistor perturbation on the both sides.

making the circuit an oscillator. In the partial compensation scheme, the instability effect due to losses in the circuit can be counterbalanced by adding an independent series gain to each resonator. A negative resistance can be easily implemented using the same opamp-based circuit designed to achieve negative inductance and capacitance. This issue is beyond the scope of this chapter, and it seems a complicated strategy for stability. We believe that exploiting the system's instability may be an excellent strategy to design sensitive oscillators that work as sensors; this could be the subject of future investigations.

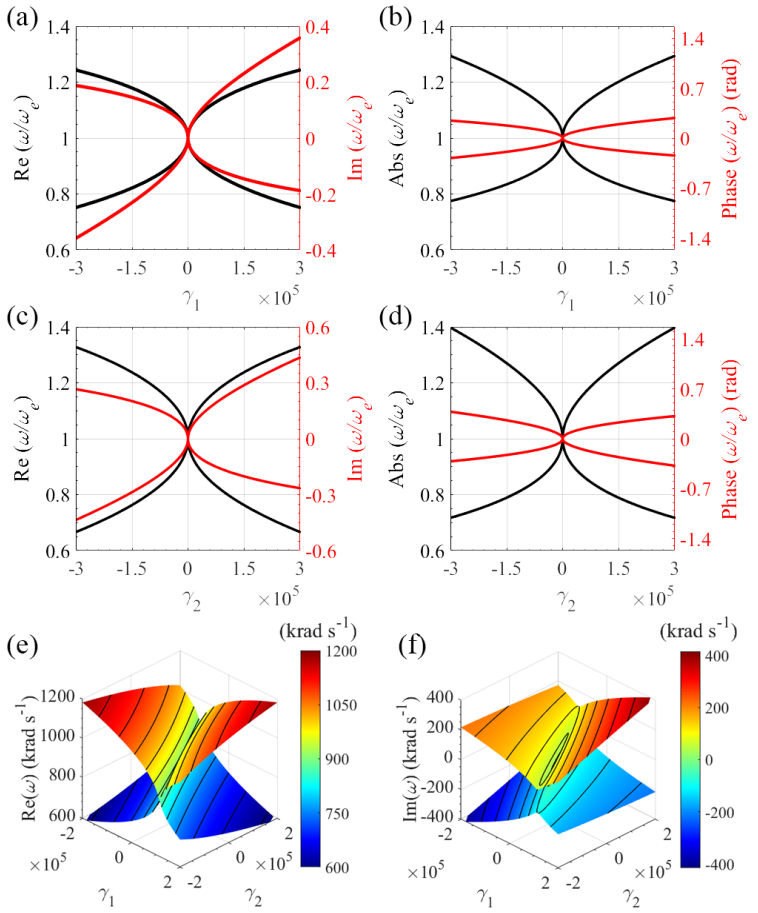

Figure 2.7: Case with negative value of the capacitances on both resonators. Variation of (a) real/imaginary parts and (b) magnitude/phase of the angular eigenfrequencies to a resistor perturbation on the left resonator, i.e., when $-\gamma_1$ changes and $\gamma_2 = 0$. (c) and (d), as in (a) and (b), but the resistor perturbation is on the right resonator, i.e., $-\gamma_2$ changes and $\gamma_1 = 0$. Variation of (e) real and (f) imaginary parts of the angular eigenfrequencies to independent resistor perturbation on the both sides.

2.5.2 RLC Resonators With Negative Capacitances C_1 and C_2

In the second case, we consider the negative value for capacitances. In Figures 2.7(a) and (b), γ_1 is perturbed while we consider $\gamma_2 = 0$ and in Figures 2.7(c), and (d), γ_2 is perturbed while $\gamma_1 = 0$. These figures show the real and imaginary parts of the eigenfrequencies when each resistor is perturbed individually. We use the same values for the circuit components as used earlier in the lossless circuit shown in Subsection 2.3.2, and the EPD angular frequency is obtained for these circuit parameters when $\gamma_1 = \gamma_2 = 0$, which is the same EPD frequency as

the lossless circuit. In Figures 2.7(a)-(d), we observe the bifurcations of the real/imaginary parts and magnitude/phase of the eigenfrequencies, so the circuit exhibits extreme sensitivity to resistance value variations in the vicinity of EPD. We show the real and imaginary parts of the eigenfrequencies by independently changing the resistances in both sides in Figures 2.7(e)-(f). The black contour lines in these three-dimensional figures show constant real and imaginary parts of the eigenfrequencies. Angular eigenfrequencies are complex-valued when perturbing γ_1 and γ_2 away from $\gamma_1 = \gamma_2 = 0$; hence the circuit gets unstable and it starts to oscillate at a fundamental frequency associated with the real part of the unstable angular eigenfrequency. In Figures 2.7(a)-(f), both conditions $\gamma_1 > 0$ and $\gamma_2 > 0$ represent loss, whereas the conditions $\gamma_1 < 0$ and $\gamma_2 < 0$ represent gain in the circuit through a negative resistance.

2.6 High-Sensitivity and Puiseux Fractional Power Series Expansion

Eigenfrequencies at EPDs are extremely sensitive to perturbations of the circuit elements, a property that is peculiar to the EPD condition. We study the circuit under EPD perturbation to investigate the circuit's sensitivity near the EPD. We demonstrate how small perturbations in a component's value perturb the eigenfrequencies of the circuit. In order to do this analysis, the relative circuit perturbation Δ_{X} is defined as

$$\Delta_{\mathrm{X}} = \frac{X - X_{\mathrm{e}}}{X_{\mathrm{e}}}, \tag{2.15}$$

where X is the perturbed parameter value, and X_{e} is its unperturbed value that provides the EPD. The perturbation in Δ_{X} value leads to a perturbed circuit matrix $\underline{\mathbf{M}}(\Delta_{\mathrm{X}})$. We demonstrate the extreme sensitivity to extrinsic perturbation by resorting to the general

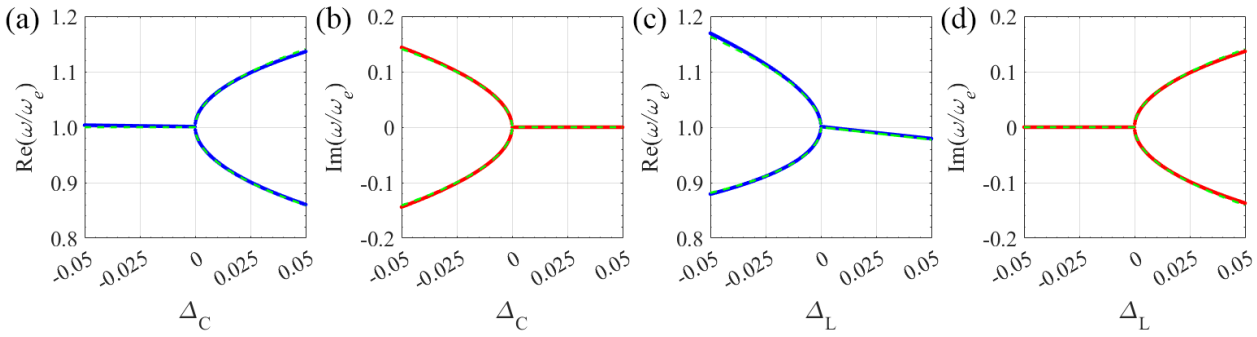

Figure 2.8: Sensitivity of (a) real and (b) imaginary parts of the eigenfrequencies to a capacitance perturbation (solid lines), $\Delta_{\mathrm{C}} = (C_1 - C_{1,\mathrm{e}})/C_{1,\mathrm{e}}$, while the inductances values on both sides are negative. Dashed lines show the perturbed eigenfrequencies according to the Puiseux expansion up to its first order. Sensitivity of (c) real and (d) imaginary parts of the eigenfrequencies to an inductance perturbation (solid lines), $\Delta_{\mathrm{L}} = (L_1 - L_{1,\mathrm{e}})/L_{1,\mathrm{e}}$, while the capacitances values on both sides are negative. Dashed lines show the perturbed eigenfrequencies according to Puiseux expansion up to its second order.

theory of EPD and utilizing the Puiseux fractional power series expansion [4]. Accordingly, when a small relative perturbation in component value Δ_{X} is applied, the resulting two different eigenfrequencies $\omega_p(\Delta_{\mathrm{X}})$, with $p = 1, 2$ are estimated using the convergent Puiseux series. Here, we provide the first two terms to estimate the eigenfrequencies near an EPD, using the explicit formulas given in [91],

$$\omega_p(\Delta_{\mathrm{X}}) \approx \omega_{\mathrm{e}} + (-1)^p \alpha_1 \sqrt{\Delta_{\mathrm{X}}} + \alpha_2 \Delta_{\mathrm{X}}, \tag{2.16}$$

$$\alpha_1 = \sqrt{\left. -\frac{\frac{\partial H(\Delta_{\mathrm{X}},\omega)}{\partial \Delta_{\mathrm{X}}}}{\frac{1}{2!}\frac{\partial^2 H(\Delta_{\mathrm{X}},\omega)}{\partial \omega^2}} \right|_{\Delta_{\mathrm{X}}=0,\,\omega=\omega_e}}, \tag{2.17}$$

$$\alpha_2 = -\left. \frac{\alpha_1^2 \frac{1}{3!}\frac{\partial^3 H(\Delta_{\mathrm{X}},\omega)}{\partial \omega^3} + \frac{\partial^2 H(\Delta_{\mathrm{X}},\omega)}{\partial \omega \partial \Delta_{\mathrm{X}}}}{\frac{\partial^2 H(\Delta_{\mathrm{X}},\omega)}{\partial \omega^2}} \right|_{\Delta_{\mathrm{X}}=0,\,\omega=\omega_e}, \tag{2.18}$$

where $H(\Delta_{\mathrm{X}}, \omega) = \det[\underline{\mathbf{M}}(\Delta_{\mathrm{X}}) - j\omega\underline{\mathbf{I}}]$, and α_1, and α_2 are first- and second-order coefficients respectively. Equation (2.16) indicates that for a tiny perturbation in component value

$\Delta_X \ll 1$ the eigenvalues change sharply from their original degenerate value due to the square root function, which is an essential characteristic of second-order EPD.

Typically, the inductor or capacitor changes in response to an external perturbation of the parameter of interest, leading to a shift in resonance frequency. We consider variations of L_1, or C_1, one at the time, and the calculated real and imaginary parts of the eigenfrequencies near the EPD is shown in Figures 2.8. In the first case, the perturbation parameter is the capacitance, $\Delta_C = (C_1 - C_{1,e})/C_{1,e}$, and a negative value for both inductances is assumed, so the first-order Puiseux expansion coefficient is calculated as $\alpha_1 = 3.228 \times 10^5$ rad/s. To calculate the coefficients, we use the components value utilized in Subsection 2.3.1. Figures 2.8(a) and (b) exhibit the real and imaginary parts of the perturbed eigenfrequencies ω obtained from the eigenvalue problem after perturbing Δ_C. Furthermore, green dashed lines in these figures demonstrate that such perturbed eigenfrequencies are well estimated with high accuracy by using the Puiseux expansion truncated at its first order. For a negative but small value of Δ_C, the imaginary part of the eigenfrequencies experiences a rapid change, and its real part remains constant. On the other hand, a very small positive value of Δ_C causes a sharp change in the real part of the eigenfrequencies while its imaginary part remains unchanged.

In the second example, the inductance value in the left resonator is considered as a perturbed parameter, $\Delta_L = (L_1 - L_{1,e})/L_{1,e}$, whereas capacitances values are both negative. By using Equations (2.17), and (2.18) and using the components values utilized in Subsection 2.3.2, the coefficients of the Puiseux expansion are calculated as $\alpha_1 = j5.548 \times 10^5$ rad/s and $\alpha_2 = -3.960 \times 10^5$ rad/s. The calculated results in Figures 2.8(c), and (d) show the two branches (solid lines) of the exact perturbed eigenfrequencies evaluated from the eigenvalue problem when the external perturbation is applied to the circuit. This figure shows that the perturbed eigenfrequencies are estimated accurately by applying the Puiseux expansion truncated at its second order (dashed lines). For a tiny value of positive perturbation, the

imaginary part of the eigenfrequencies undergoes sharp changes, while its real part remains approximately unchanged. However, a small negative perturbation in the inductance value rapidly changes the real part of the two eigenfrequencies away from the EPD eigenfrequency. The bifurcation in the diagram, described by a square root, is the most exceptional physical property associated with the EPD. It can be employed to devise ultra-sensitive sensors for various applications [37, 68, 92, 93].

2.7 Sensing Scenario for Liquid Content Measurement

In recent years various well-established techniques have been proposed to measure the liquid level, such as light-reflection sensors [94], chirped fiber Bragg grating [95, 96], fiber optic sensors [97, 98, 99], ultrasonic Lamb waves [100], and capacitive sensors [101, 102, 103, 104]. The use of a capacitive sensor is a well-known method for liquid level measurement [105]. This kind of sensor has been proven to be stable, can be assembled using various materials, and can provide high resolution [106]. The principle of operation of capacitive sensors is that they converts a variation in position, or material characteristics, into measurable electrical signals [107]. Capacitive sensors are operated by changing any of the three main parameters: relative dielectric constant, area of capacitive plates, and distance between the plates. In conventional methods, a capacitive liquid level detector can sense the fluid level by measuring variations in capacitance made between two conducting plates embedded outside a non-conducting tank or immersed in the liquid [108, 105]. The same concept applies when the liquid occupies a varying volume percentage of a mixture's components.

In order to compare the advantages of the EPD-based sensors with conventional sensors based on a single LC circuit, we use a simple ideal scheme for liquid content measurement. We demonstrate the sensitivity of a gyrator-based circuit by operating near the EPD is much higher than the one of a conventional LC resonator circuit. We provide the required

setup and the measurement procedure to measure the liquid volume. Here, we use the following set of values for the components in the gyrator-based circuit: $L_1 = -4.7\,\text{nH}$, $L_2 = -4.7\,\text{nH}$, $C_2 = 47\,\text{pF}$, and $R_\text{g} = 50\,\Omega$. Consider a cylindrical glass with top and bottom metal plates. This structure can serve as a variable capacitor in which the volume of filled liquid (or a percentage of a mixture) can change the total capacitance. A schematic structure for this scenario is illustrated in Figure 2.9(a). The designed device includes the gyrator-based circuit (see Figure 2.1) where the positive capacitor on the left side is the cylindrical container with height $d_2 = 3.0142\,\text{cm}$, of which a height d_1 is filled with water and the area of metal plates are $A = 100\,\text{cm}^2$. Pure water is assumed to have a relative permittivity of $\varepsilon_\text{r} = 78.7$ at $T = 22.0^\text{o}\,\text{C}$, and we neglect losses in this simple case [109]. Two series variable capacitors model the structure, that the bottom one has a capacitance $C_\text{filled} = \varepsilon_0\varepsilon_r A/d_1$,and the top one has a capacitance $C_\text{empty} = \varepsilon_0 A/(d_2 - d_1)$. The total capacitance is $C_\text{total} = C_\text{filled}C_\text{empty}/(C_\text{filled} + C_\text{empty})$, which changes when varying the water level. By opening the top inlet, the height of the water will increase, so the capacitance value will be increased. On the contrary, the water's height decreases when opening the bottom outlet, and the total capacitance value will be decreased. In summary, the level of water is related to the capacitance, and the perturbation in the value of capacitance will change a circuit's eigenfrequencies. Using the steps explained in Section 2.3 and by solving the eigenvalue problem, the plot of resonance frequency versus water level percentage for this specific example is illustrated in Figure 2.9(b) by the solid blue line. The measuring scheme is very sensitive near 0 water content. The EPD can be designed for different water contents, so the frequency variation caused by changes in the water level around that mentioned level would be very sensitive. We now compare the sensitivity of the EPD-based scheme with that of a single LC resonator. We consider an LC resonator with the resonance frequency of $\omega_0 = \omega_\text{e}$, i.e., coincident with one of the EPD systems. We assume that the sensing capacitor is the same as the one in Figure 2.9, i.e., the same as that considered in the EPD system. The variation in the resonance frequency by perturbing the capacitance as described above,

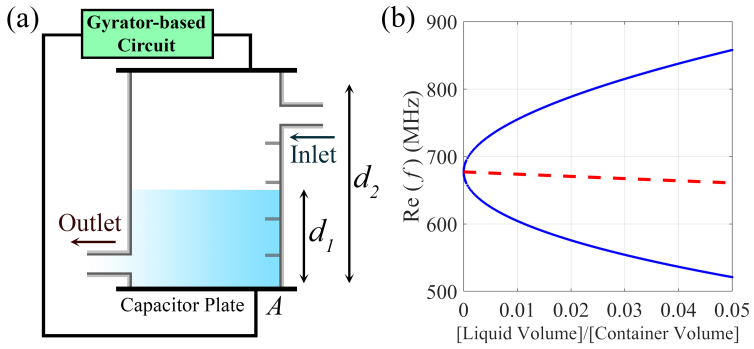

Figure 2.9: (a) Schematic illustration of a device for liquid level measurement. (b) The EPD is designed at a given level of water content (0 in the figure). The solid blue line in the plot shows the two resonance frequencies of the gyrator-based circuit versus water level variation with very high sensitivity near 0. Also, the red dashed line shows the resonance frequency of a single resonator when the water content changes. The EPD-based circuit and the single LC resonator have the same resonance frequency at 0. It is clear that the EPD-based circuit provides much higher sensitivity to the capacitance perturbation than the single LC resonator.

i.e., the level of water content, is shown in Figure 2.9(b) by the red dashed line. It is clear that the EPD-based bifurcation in the dispersion diagram, characterized by a square root, dramatically enhances the circuit's sensitivity compared to the sensitivity of the single LC resonator to the same capacitance perturbation.

In the proposed scheme for liquid content measurement, we assume that the gyrator-based circuit works in the stable region where eigenfrequencies are purely real. However, when considering the instabilities generated by losses, one eigenfrequency has a negative imaginary value, as explained in Section 2.5. Consequently, the circuit starts having growing oscillations. The exponential growth rate can be controlled in two ways: either by stopping (switching off) the circuit to reach saturation or by letting it saturate. In this latter case, the gyrator-based circuit should be designed as a sensor that oscillates. The circuit can be used to sense physical or chemical parameters changes by measuring the oscillation frequency variations.

2.8 Conclusions

A second-order EPD with a real (degenerate) eigenfrequency in a gyrator-based circuit is achieved using two unstable series LC resonators coupled via a gyrator. Each unstable resonator has either a negative capacitance or a negative inductance; hence, the resonance frequency of each resonator is purely imaginary when they are uncoupled. We have demonstrated that coupling the two unstable resonators can make the overall circuit marginally stable with a purely real-valued EPD frequency. We have also shown that the system becomes unstable when small losses or gains are considered in the circuit. We investigated and demonstrated the enhanced sensitivity to perturbations when operating at the EPD. In particular, we have considered the perturbation of the gyration resistance, capacitance, and inductance. The perturbation in physical or chemical parameters affects the circuit component's value in realistic applications. Such a perturbation could be estimated by measuring the shift of resonance frequencies that follow the square root behavior typical of an EPD perturbation. The presented results may impact sensing technology, security systems, particle monitoring, and motion sensors. Future studies using resonators with purely imaginary frequencies like waveguides below cutoff may help miniaturize microwave sensing devices.

Acknowledgments

- I would like to thank Alireza Nikzamir for collaboration on this chapter.
- This material is based upon work supported by the National Science Foundation (NSF) under Grant No. ECCS-1711975 and by Air Force Office of Scientific Research (AFOSR) Grant No. FA9550-19-1-0103.
- The text of Chapter 2 of this dissertation is a reprint of the material as it appears in K. Rouhi, A. Nikzamir, A. Figotin, and F. Capolino, "Exceptional point in a degenerate

system made of a gyrator and two unstable resonators," Physical Review A, vol. 105, no. 3, Mar. 2022. The coauthors listed in this publication are Alireza Kazemi, Alexander Figotin, and Filippo Capolino. Alexander Figotin and Filippo Capolino directed and supervised research which forms the basis for the dissertation.

- The results of this chapter have been published in the journal paper of [110] and in the arXiv preprint of [111] and in the conference papers of [112].

Chapter 3

High-Sensitivity in Various Gyrator-Based Circuits With Exceptional Points of Degeneracy

EPD can enhance the sensitivity of circuits by orders of magnitude. We show various configurations of coupled LC resonators via a gyrator that support EPDs of second and third-order. Each resonator includes a capacitor and inductor with a positive or negative value, and the corresponding EPD frequency could be real or imaginary. When a perturbation occurs in the second-order EPD gyrator-based circuit, we show that there are two real-valued frequencies shifted from the EPD one, following a square root law. This is contrary to what happens in a PT-symmetric circuits where the two perturbed resonances are complex valued. We show how to get a stable EPD by coupling two unstable resonators, how to get an unstable EPD with an imaginary frequency, and how to get an EPD with a real frequency using an asymmetric gyrator. The relevant Puiseux fractional power series expansion shows the EPD occurrence and the circuit's sensitivity to perturbations. Our findings pave the way for new types of high-sensitive devices that can be used to sense physical, chemical, or biological

changes.

3.1 Background, Motivation, and State of the Art

The presence of at least one nontrivial Jordan block in the Jordan canonical form of the system matrix shows an EPD [3, 61, 4, 113], as was demonstrated in PT-symmetric systems [114, 64, 115, 116, 117, 71, 15, 72]. Analogous concepts were discovered in the area of slow light in propagation in photonic crystals by Figotin and Vitebskiy in [118, 18, 24, 20] even though they did not use the term "exceptional point". The strong sensitivity of the degenerate eigenvalues (i.e., degenerate resonance frequencies) to perturbations is a remarkable feature of EPDs [4]. We emphasize the necessity of referring to it as a "degeneracy", hence, incorporating the D in EPD, because the defining feature of an exceptional point is the strong full degeneracy of at least two eigenmodes, as implied in [11]. When a second-order EPD with two coalesced eigenstates is subject to a small perturbation Δ, the eigenvalue splitting is proportional to the square root of Δ, which is larger than the linear splitting of conventional sensors without degeneracy [73]. Moreover, the sensitivity increases by increasing the order of the degeneracy, whereas a more complex system is needed. The physics of operating near an EPD may improve a sensor response to a perturbation by an amount that grows with the proximity of the sensor's operating point to the EPD [71, 119, 38]. Noise may also play a critical role in the performance of these kinds of sensing applications based on EPD, also depending on the chosen circuit configuration [72]. Although this topic requires further investigation, some discussion can be seen in [120, 121, 122, 123]. The concept of EPD has been investigated in lossless, spatially [18, 124, 29] or temporally [19, 125] periodic structures and in circuits with loss and/or gain under PT-symmetry [33, 9]. The EPD-based principle of higher sensitivity has been proposed in various sensing systems, including optical microcavities [12], e-beam devices [75, 126], optomechanical mass sensors [76], and ring laser

gyroscopes [127].

Previously, most of the published EPDs circuits were based on coupled resonators with gain and loss, satisfying PT-symmetry [114, 64, 115, 116, 117, 71, 15, 72]. This paper shows and discusses a new way developed at UC Irvine to obtain EPDs based on coupling LC circuits by gyrators. A gyrator is a two-port and nonreciprocal component invented by Tellegen in 1948 and proposed as a fifth fundamental network element, alongside the resistor, capacitor, inductor, and transformer [78]. Numerous publications on the development and deployment of the gyrator have been written since its invention. Gyrators have been designed using vacuum tubes, transistors [89, 80, 81, 128, 129, 130, 131, 132], and opamps [82, 84, 133, 134, 135, 136, 137, 138] due to their nonreciprocal property. In addition, a brief review of various methods and electronic circuits to realize the gyrator is summarized in Appendix A. In addition, the gyrator concept is not restricted to a two-port network, and it can be extended to various complex models such as the three-port gyrator [139]. A gyrator loaded with a capacitor is used to realize an effective inductance, so passive RLC networks can be synthesized using only resistors, capacitors, and gyrators [82]. Also, RLC filters can be constructed utilizing gyrators without using inductances [82]. More details on important features and specific characteristics of the gyrator are presented in Section 3.2.

In this paper, we study various schemes to get EPDs in gyrator-based sensing circuits, as well as their enhanced sensitivity when operating near an EPD. First, two series LC resonators are coupled via a gyrator, as explained in [86, 87, 110, 85], leading to a second-order EPD. Next, we extend our study to a third-order EPD obtained using three LC resonators and two gyrators. In this case, the circuit's sensitivity is enhanced, although the circuit is always unstable. The second part of this paper investigates gyrator circuits with parallel LC resonators, a dual version of the series configuration. It covers various cases leading to (i) stable EPDs by coupling two unstable resonators, (ii) EPDs with imaginary frequency, and (iii) EPDs using two LC circuits and an asymmetric gyrator. We show examples for all

the cases and analyze the second-order circuits' signal using time-domain simulations. In addition, the sensitivity of circuit eigenfrequencies to component variations is investigated. We demonstrate that the Puiseux fractional power series expansion closely approximates the eigenfrequency diagram bifurcation near the EPD [4]. This paper explores and reviews specific cases, whereas a mathematical framework for constructing lossless circuits for any conceivable Jordan structure using a gyrator has been presented in [86]. In addition, we consider lossless components in our study, and the analysis of stability or instability in some circuit configurations by adding small losses to the circuits is discussed in [110, 85]. The analysis and circuit presented in this paper have great potential applications in novel ultra-high-sensitive schemes.

3.2 Gyrator

A gyrator is a two-port component defined by its gyration resistance value that connects an input port to an output port. This two-port network converts circuits at the gyrator output into their dual regarding the gyration resistance value [136, 88, 140]. This component can cause a capacitive circuit to behave inductively and a parallel LC resonator to act like a series LC resonator. Gyrator enables the development of two-port devices that would otherwise be impossible to build with only the basic components, i.e., resistors, capacitors, inductors, and transformers. The gyrator, unlike the other four conventional elements, is nonreciprocal. Moreover, the gyrator could be considered a more fundamental circuit component than the ideal transformer because an ideal transformer can be made by cascading two ideal gyrators, but transformers cannot make a gyrator. The circuit symbol for this component is illustrated in Figure 3.1(a). The voltage on one port is linked to the current on the other in an ideal gyrator and vice versa. So, the voltages and currents are converted by [89]

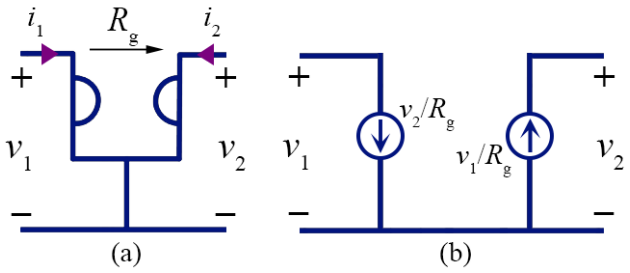

Figure 3.1: (a) Gyrator schematic circuit symbol and corresponding voltages, currents, and gyration resistance direction. (b) Equivalent circuit for an ideal gyrator by using two dependent current sources.

$$\begin{cases} v_2(t) = R_g i_1(t) \\ \\ v_1(t) = -R_g i_2(t) \end{cases} \tag{3.1}$$

The gyration resistance R_g is the crucial parameter of the gyrator, which has a unit of ohm, and it has a gyration direction shown by an arrow in the circuit symbol. Although a gyrator is defined by its gyration resistance value, an ideal gyrator is a lossless element. A gyrator is a nonreciprocal component that can be determined by an antisymmetric impedance matrix as

$$\underline{\mathbf{Z}}_g = \begin{bmatrix} 0 & -R_g \\ \\ R_g & 0 \end{bmatrix}. \tag{3.2}$$

Also, we can characterize it by admittance matrix as

$$\underline{\mathbf{Y}}_{\mathrm{g}} = \begin{bmatrix} 0 & G_{\mathrm{g}} \\ -G_{\mathrm{g}} & 0 \end{bmatrix}, \tag{3.3}$$

where $G_{\mathrm{g}} = 1/R_{\mathrm{g}}$ is gyration conductance. The aforementioned equations show that the gyration impedance and direction may be determined by connecting a voltage source to one port and measuring the current through a short circuit to another [141]. Therefore, we can model the gyrator using two dependent current sources, as shown in Figure 3.1.

3.3 EPD in Series Configuration

This section reviews various series configurations with gyrators to obtain an EPD. We provide the required circuit equations to get the EPD conditions based on a Liouvillian formalism. We build the eigenvalue problem to find a secondorder EPD, leading to two resonant frequencies, and demonstrate the condition for obtaining EPD at the desired frequency. Moreover, we show the circuit's perturbation effects on the eigenfrequencies. Besides the theoretical calculations, we also perform time-domain circuit simulations. We estimate the eigenfrequencies by using the Puiseux fractional power series expansion. The first part summarizes the analysis provided in [85] but later is cast in a more general way to include all cases. Next, we demonstrate a third-order EPD in three LC series resonators coupled via two gyrators. In this latter case, the circuit's sensitivity increases dramatically because of the higher EPD order. However, a more complex circuit with more components is needed, and the circuit is unstable.

3.3.1 Second-Order EPD

In the first circuit, shown in Figure 3.2(a), two series LC tanks are connected via an ideal gyrator. All of the components in the circuit are assumed to be ideal, so there is no resistance in the circuit. The Kirchhoff voltage law equations are written in two loops [85]

$$\begin{cases} \ddot{Q}_1 = -\frac{1}{C_1 L_1} Q_1 + \frac{R_g}{L_1} \dot{Q}_2 \\ \ddot{Q}_2 = -\frac{1}{C_2 L_2} Q_2 - \frac{R_g}{L_2} \dot{Q}_1 \end{cases} \tag{3.4}$$

In the above equations, Q_n is the stored charge in the capacitor C_n, where $n = 1$ indicates the left resonator and $n = 2$ indicates the right resonator. It is convenient to define a state vector as $\Psi \equiv \left[Q_1, Q_2, \dot{Q}_1, \dot{Q}_2\right]^{\mathrm{T}}$, which consists of a combination of stored charges and their time derivative on both sides, and the superscript T denotes the transpose operation. Finally, we express the equations in Liouvillian form as [85]

$$\frac{\mathrm{d}\Psi}{\mathrm{d}t} = \underline{\mathbf{M}}\Psi, \quad \underline{\mathbf{M}} = \begin{bmatrix} 0 & 0 & 1 & 0 \\ 0 & 0 & 0 & 1 \\ -\omega_{01}^2 & 0 & 0 & -\frac{R_g}{L_1} \\ 0 & -\omega_{02}^2 & -\frac{R_g}{L_2} & 0 \end{bmatrix}. \tag{3.5}$$

Here, $\omega_{01} = 1/\sqrt{C_1 L_1}$, and $\omega_{02} = 1/\sqrt{C_2 L_2}$ are resonance angular frequencies of two isolated resonators, i.e., without coupling. We will assume that both resonators have a real resonance frequency in this section, so the inductance and capacitance in each resonator have the same sign. Considering signals of the form $Q_n \propto e^{j\omega t}$, where ω is the angular eigenfrequency. We

write the eigenvalue problem associated with the circuit equations, and the characteristic equation is obtained from $\det(\underline{\mathbf{M}} - j\omega\underline{\mathbf{I}}) = 0$, where $\underline{\mathbf{I}}$ is the identity matrix, leading to [85]

$$\omega^4 - \omega^2\left(\omega_{01}^2 + \omega_{02}^2 + \frac{R_{\mathrm{g}}^2}{L_1 L_2}\right) + \omega_{01}^2\omega_{02}^2 = 0. \tag{3.6}$$

In the characteristic equation, all the ω 's coefficients are real, so both ω and ω^* are roots of the equation, where * represents the complex conjugate operation. In addition, the characteristic equation is quadratic in ω^2; so, ω and $-\omega$ are both solutions. When $R_{\mathrm{g}} = 0$, the two resonators are uncoupled, and the two independent circuits have two angular eigenfrequency pairs of $\omega_{1,3} = \pm\omega_{01}$, and $\omega_{2,4} = \pm\omega_{02}$. In the gyrator-based circuit, the angular eigenfrequencies are determined as [85]

$$\omega_{1,3} = \pm\sqrt{a+b}, \omega_{2,4} = \pm\sqrt{a-b}, \tag{3.7}$$

$$a = \frac{1}{2}\left(\omega_{01}^2 + \omega_{02}^2 + \frac{R_{\mathrm{g}}^2}{L_1 L_2}\right), \tag{3.8}$$

$$b^2 = a^2 - \omega_{01}^2\omega_{02}^2. \tag{3.9}$$

Based on Equation (3.7), the EPD can be obtained when $b = 0$ and the corresponding EPD angular frequency is $\omega_{\mathrm{e}} = \sqrt{a}$. Here we consider EPD with real eigenfrequency, so a is a positive value. The condition for real EPD frequency is expressed as [85]

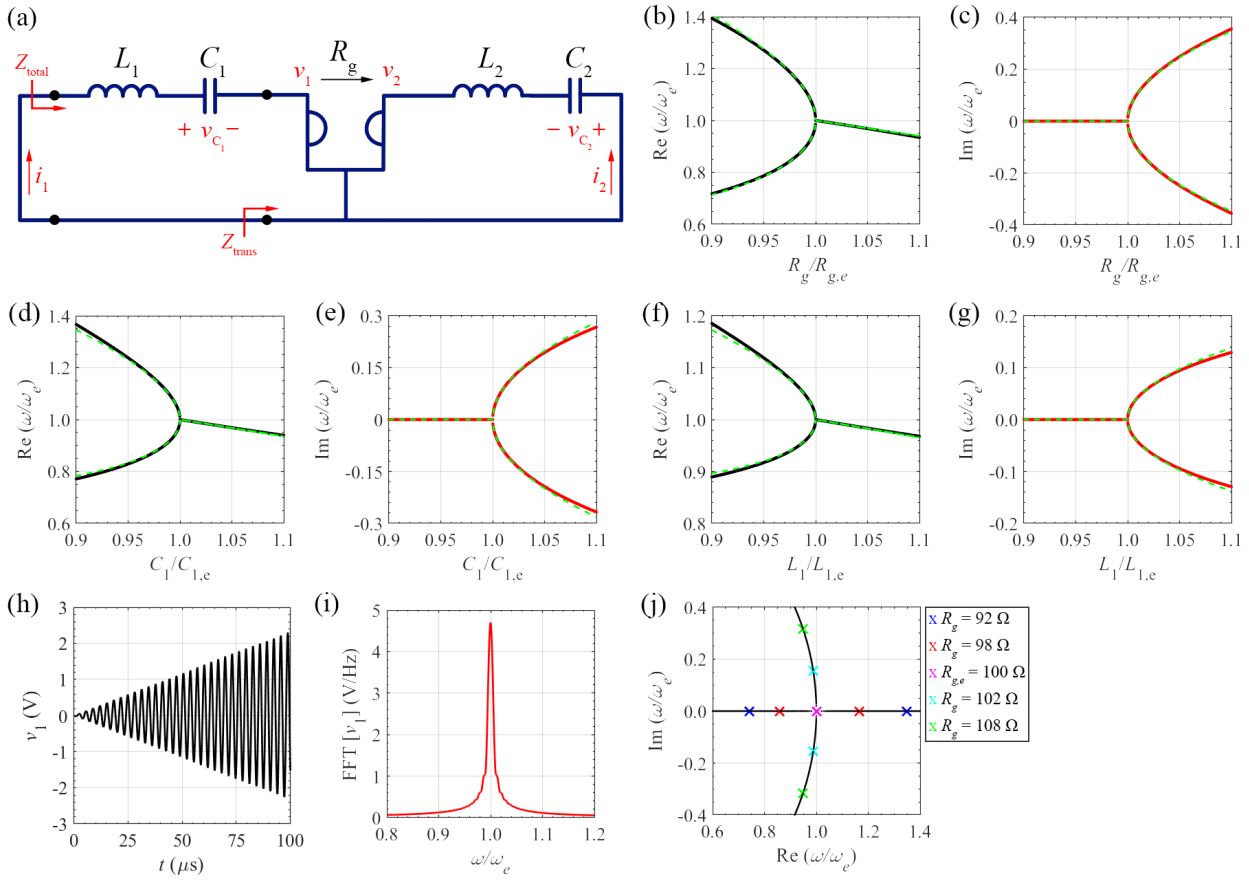

Figure 3.2: (a) The schematic illustration of the gyrator-based circuit with the ideal gyrator in series configuration. In this circuit, two different LC resonators are used in a series configuration, coupled via an ideal gyrator. The sensitivity of the (b), (d), (f) real and (c),(e),(g) imaginary parts of the eigenfrequencies to (b), (c) gyration resistance, (d), (e) positive capacitance C_1 (f), (g) positive inductance L_1 perturbation. Solid lines: solution of eigenvalue problem of Equation (3.5); green-dashed lines: Puiseux series approximation truncated to its second term. Voltage $v_1(t)$ under the EPD condition in the (h) time-domain, and (i) frequency-domain. The frequency-domain result is calculated by applying an FFT with 10^6 samples in the time window of $0\,\mu$s to $100\,\mu$s. (j) Root locus of zeros of $Z_{\text{total}}(\omega) = 0$ showing the real and imaginary parts of resonance frequencies of the circuit when perturbing gyration resistance. At the EPD, the system's total impedance is $Z_{\text{total}}(\omega) \propto (\omega - \omega_{\text{e}})^2$; hence it shows a double zero at ω_{e}.

$$\omega_{01}^2 + \omega_{02}^2 - \omega_{\text{gs}}^2 > 0, \tag{3.10}$$

where the equivalent gyrator frequency is defined as $\omega_{\text{gs}}^2 = -R_{\text{g}}^2/(L_1 L_2)$ for the series con-

figuration [85]. To obtain an EPD in this configuration using Equations (3.8), and (3.9) the following equation should be satisfied [85],

$$(\omega_{01} - \omega_{02})^2 = \omega_{\mathrm{gs}}^2. \tag{3.11}$$

First, if ω_{01} and ω_{02} are purely real, the value of either L_1 or L_2 should be negative to have the same sign on both sides of Equation (3.11). Thus, one of the resonators should have a negative inductance to have a pure real ω_{01} or ω_{02}.

Second, if both ω_{01} and ω_{02} have imaginary values, the selected values for L_1 and L_2 should have the same sign. When L_1 and L_2 are positive, C_1 and C_2 should be negative, or vice versa.

Finally, if only one of the ω_{01} or ω_{02} has imaginary value and the other one has a real value, there are no conditions to obtain an EPD [85]. In this section, we consider the first case in which only one inductor and one capacitor in the same resonator have a negative value so ω_{gs}^2 is positive. The required circuit to synthesize the negative components is described in Appendix B.

The EPD frequency is calculated by using Equations (3.7), (3.8), and (3.9) as

$$\omega_{\mathrm{e}} = \sqrt{\frac{1}{2}\left(\omega_{01}^2 + \omega_{02}^2 - \omega_{\mathrm{gs}}^2\right)} = \sqrt{\omega_{01}\omega_{02}}. \tag{3.12}$$

The EPD condition can be satisfied by many different combinations of component values, and we will use this set of values for components as an example: $L_1 = 33\ \mu\mathrm{H}, L_2 = -33\ \mu\mathrm{H}, C_2 = -33\ \mathrm{nF}$, and $R_{\mathrm{g}} = 100\ \Omega$. Then, the capacitance C_1 is determined by solving the quadratic equation from the EPD condition, i.e., $b = 0$. There are two different values

of the capacitance C_1 in the first resonator that satisfies the EPD condition, and we select $C_1 = 1.90\,\text{nF}$ for this example. The real and imaginary parts of eigenfrequencies calculated from the eigenvalue problem by perturbing the gyrator resistance R_g near the EPD value of 100Ω are shown in Figures 3.2(b) and (c). In this example, we have $\omega_\text{e} = 1.95 \times 10^6\,\text{rad/s}$ and the calculated eigenvalues are normalized to ω_e. In addition, the calculated results in Figures 3.2(d) and (e) show the real and imaginary parts of eigenvalue by perturbing the positive capacitance C_1 in the left resonator. Finally, by changing the positive inductance, the real and imaginary parts of eigenfrequencies are shown in Figures 3.2(f) and (g). To confirm the calculated results and show the sensitivity of the eigenvalues to external perturbation, the eigenfrequencies are also calculated by the Puiseux fractional power series expansion. More details about this method are in Section 3.5. The approximated results calculated by the Puiseux series are shown by the green dashed lines in Figures 3.2(b)-(g), which show a good agreement with the solutions of the eigenvalue problem in Equation (3.5). In the approximated results, the coefficients of the Puiseux series are calculated as, $\alpha_1 = j2.14 \times 10^6\,\text{rad/s}$, and $\alpha_2 = -1.17 \times 10^6\,\text{rad/s}$ when perturbing $R_\text{g}, \alpha_1 = j1.74 \times 10^6\,\text{rad/s}$, and $\alpha_2 = -1.26 \times 10^6\,\text{rad/s}$ when perturbing C_1, and $\alpha_1 = j8.52 \times 10^2\,\text{rad/s}$, and $\alpha_2 = -6.74 \times 10^5\,\text{rad/s}$ when perturbing L_1. The results in Figures 3.2(b)-(g) demonstrate that by perturbing R_g, C_1, and L_1, the eigenfrequencies in the gyrator-based circuit always show an analogous behavior. So, by individual variation of the components value, the real parts of the eigenfrequencies split when the value is smaller than the EPD value, and the imaginary parts of the eigenfrequencies split when the value is bigger than the EPD value.

Furthermore, Figures 3.2(h) and (i) show the time-domain and frequency-domain simulation results obtained with the Keysight ADS time-domain circuit simulator. The calculated results in these two plots are the voltage $v_1(t)$ in the left gyrator port and its frequency spectrum, where we use 1 mV as an initial voltage on the left capacitor C_1. According to Figure 3.2(h), the voltage increases linearly, which is an important aspect peculiar to an

EPD. This typical signal is the inverse Laplace transform of a double pole, i.e., the result of coalescing circuit eigenvalues and eigenvectors corresponds to a double pole (or a double zero of the total circuit admittance). A linear growth demonstrates a second-order EPD with real frequency in the circuit. We take the FFT of the voltage $v_1(t)$ to calculate the frequency spectrum, with 10^6 samples in the time window of 0μs to 100μs, and the calculated spectrum is illustrated in Figure 3.2(i). According to the frequency spectrum of the signal, the oscillation angular frequency corresponds to $\omega_{\mathrm{e}} = 1.95 \times 10^6$ rad/s, that is the same as the one obtained from solving the eigenvalue problem. In this example, we used lossless components in the circuit. A complete investigation showing the effect of losses in the series configuration is presented in [85].

The following part demonstrates how the EPD regime is related to a specific type of circuit's resonance, which can be found directly in a frequency-domain analysis of the circuit. The transferred impedance on the left side of the gyrator is expressed as (see Figure 3.2(a))

$$Z_{\mathrm{trans}}\left(\omega\right) = \frac{R_{\mathrm{g}}^2}{Z_2}. \tag{3.13}$$

In the above equation, $Z_2(\omega) = j\omega L_2 + 1/\left(j\omega C_2\right)$ is the series impedance on the right side of the gyrator. The total impedance observed from the circuit input port (see Figure 3.2(a)) is calculated by

$$Z_{\mathrm{total}}(\omega) = Z_1(\omega) + Z_{\mathrm{trans}}(\omega), \tag{3.14}$$

where $Z_1(\omega) = j\omega L_1 + 1/\left(j\omega C_1\right)$ is the series impedance connected to the left side of the gyrator. The complexvalued resonant frequencies are obtained by imposing $Z_{\mathrm{total}}\left(\omega\right) = 0$. The real and imaginary parts of calculated resonance frequency by finding the zeros of such

total impedance $Z_{\text{total}}(\omega)$ for various gyration resistance values are shown in Figure 3.2(j). When the gyration resistance is equal to the corresponding EPD value, the two zeros coincide with the EPD angular frequency ω_{e}, that is also the point where the two curves in Figure 3.2(j) meet where $Z_{\text{total}}(\omega) \propto (\omega - \omega_{\text{e}})^2$. For gyrator resistances such that $R_{\text{g}} < R_{\text{g,e}}$, two resonance angular frequencies are purely real. Instead, for $R_{\text{g}} > R_{\text{g,e}}$, the two resonance angular frequencies are complex conjugate. In other words, depending on how the circuit is defined, the EPD frequency coincides with double zeros (or double poles, depending on what we look at) of the frequency spectrum.

3.3.2 Third-Order EPD

In this section, we investigate the third-order EPD in the gyrator-based circuit. Three series LC tanks are coupled via two ideal gyrators to obtain third-order EPD, as shown in Figure 3.3(a). We write the Kirchhoff voltage law equations in three loops as

$$\begin{cases} \ddot{Q}_1 = -\frac{1}{C_1 L_1} Q_1 + \frac{R_{\text{g1}}}{L_1} \dot{Q}_2 \\ \ddot{Q}_2 = -\frac{1}{C_2 L_2} Q_2 - \frac{R_{\text{g1}}}{L_2} \dot{Q}_1 + \frac{R_{\text{g2}}}{L_2} \dot{Q}_3 \\ \ddot{Q}_3 = -\frac{1}{C_3 L_3} Q_3 - \frac{R_{\text{g2}}}{L_3} \dot{Q}_2 \end{cases} \tag{3.15}$$

In these equations, Q_n is the stored charge in the capacitor $C_n (n = 1$ for the left resonator, $n = 2$ for the middle resonator, and $n = 3$ for the right resonator). In this circuit, we consider two different values for the gyration resistance of two gyrators. The state vector for the thirdorder circuit is conveniently defined as $\Psi \equiv \left[Q_1, Q_2, Q_3, \dot{Q}_1, \dot{Q}_2, \dot{Q}_3\right]^{\text{T}}$. Finally, the circuit's equations are written in Liouvillian form as

$$\frac{\mathrm{d}\Psi}{\mathrm{d}t} = \underline{\mathbf{M}}\Psi, \quad \underline{\mathbf{M}} = \begin{bmatrix} 0 & 0 & 0 & 1 & 0 & 0 \\ 0 & 0 & 0 & 0 & 1 & 0 \\ 0 & 0 & 0 & 0 & 0 & 1 \\ -\omega_{01}^2 & 0 & 0 & 0 & \frac{R_{\mathrm{g1}}}{L_1} & 0 \\ 0 & -\omega_{02}^2 & 0 & -\frac{R_{\mathrm{g1}}}{L_2} & 0 & \frac{R_{\mathrm{g2}}}{L_2} \\ 0 & 0 & -\omega_{03}^2 & 0 & -\frac{R_{\mathrm{g2}}}{L_3} & 0 \end{bmatrix}, \tag{3.16}$$

where $\underline{\mathbf{M}}$ is the six-by-six circuit matrix for the third-order circuit. Moreover, $\omega_{01} = 1/\sqrt{C_1 L_1}, \omega_{02} = 1/\sqrt{C_2 L_2}$, and $\omega_{03} = 1/\sqrt{C_3 L_3}$ are resonance angular frequencies of three isolated resonators (without coupling). The characteristic equation is expressed by

$$\begin{aligned} &\omega^6 - \omega^4 \left(\frac{R_{\mathrm{g2}}^2}{L_2 L_3} - \frac{R_{\mathrm{g1}}^2}{L_1 L_2} + \omega_{01}^2 + \omega_{02}^2 + \omega_{03}^2 \right) \\ &+ \omega^2 \left(\frac{R_{\mathrm{g2}}^2 \omega_{01}^2}{L_2 L_3} - \frac{R_{\mathrm{g1}}^2 \omega_{03}^2}{L_1 L_2} + \omega_{01}^2 \omega_{02}^2 + \omega_{01}^2 \omega_{03}^2 + \omega_{02}^2 \omega_{03}^2 \right) - \omega_{01}^2 \omega_{02}^2 \omega_{03}^2 = 0. \end{aligned} \tag{3.17}$$

For $R_{\mathrm{g1}} = 0$ and $R_{\mathrm{g2}} = 0$, the three series resonators are uncoupled, and the three circuits have three angular eigenfrequency pairs of $\omega_{1,4} = \pm\omega_{01}, \omega_{2,5} = \pm\omega_{02}$, and $\omega_{3,6} = \pm\omega_{03}$. As an example, we use the following component values to obtain third-order EPD: $L_1 = 1\ \mu\mathrm{H}$, $L_2 = -33.33\ \mu\mathrm{H}$, $L_3 = 3.33\ \mathrm{mH}$, $C_1 = 3\ \mu\mathrm{F}$, $C_2 = -30\ \mathrm{nF}$, $C_3 = 0.1\ \mathrm{nF}$, $R_{\mathrm{g1}} = 3.33\ \Omega$ and $R_{\mathrm{g2}} = 333.33\ \Omega$. The obtained EPD frequency that corresponds to the mentioned component values is $\omega_{\mathrm{e}} = 10^6\ \mathrm{rad/s}$. The calculated results in Figures 3.3(b) and (c) show the real and imaginary parts of perturbed eigenfrequencies by solving the eigenvalue problem presented in Equation (3.16). In these two plots, the first gyration resistance R_{g1} is perturbed near the EPD, and the calculated eigenfrequencies are normalized to the corre-

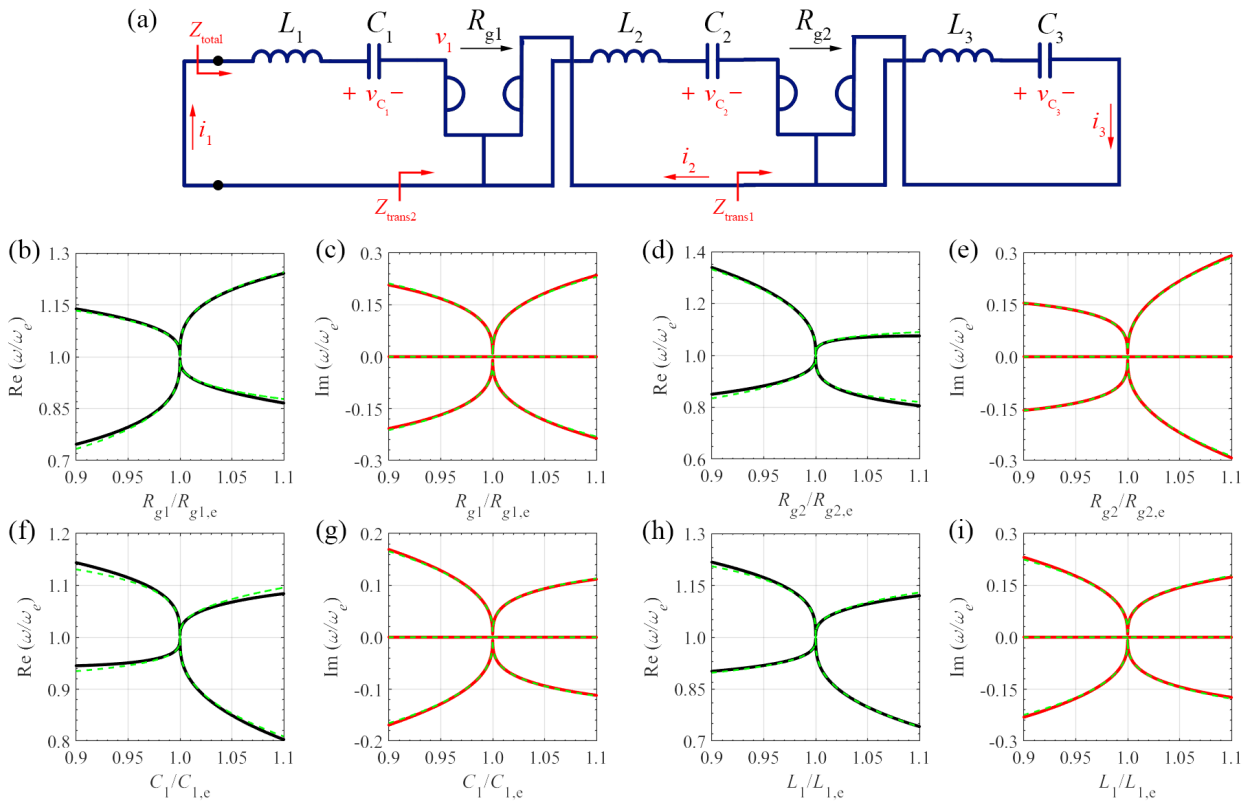

Figure 3.3: (a) The schematic illustration of the gyrator-based circuit with the ideal gyrator in third-order configuration. In this circuit, three different LC resonators are coupled via two different ideal gyrators. The sensitivity of the (b), (d), (f), (h) real and (c), (e), (g), (i) imaginary parts of the eigenfrequencies to (b), (c) gyration resistance of the first gyrator R_{g1}, (d), (e) gyration resistance of the second gyrator R_{g2},(f), (g) positive capacitance C_1 (h), (i) positive inductance L_1 perturbation. Solid lines: solution of eigenvalue problem of Equation (3.16); green-dashed lines: Puiseux series approximation truncated to its second term.

sponding EPD frequency. Also, Figures 3.3(d) and (e) show analogous results by perturbing the second gyration resistance R_{g2}. Let's consider the first resonator to be a sensing resonator. We can quantify its perturbation due to variations of external parameters in the surrounding environment by measuring the changes in the eigenfrequencies. The calculated eigenfrequencies when perturbing either the capacitance or the inductance in the first resonator are displayed in Figures 3.3(f) and (g) and Figures 3.3(h) and (i), respectively. The eigenfrequencies near the EPD are also estimated by using the Puiseux fractional power series expansion, as explained in Section 3.5. According to the computed values in

Figures 3.3(b)-(i), eigenfrequencies always have a negative imaginary part that shows instability. The green dashed lines in Figures 3.3(b)-(i) represent the estimated results by the Puiseux series, which exhibit good agreement with the eigenvalues obtained directly from the eigenvalue problem in Equation (3.16). The coefficient of the Puiseux series are calculated as, $\alpha_1 = 5.50 \times 10^5$rad/s, and $\alpha_2 = -5.05 \times 10^4$rad/s when perturbing R_{g1}, $\alpha_1 = 2.75\times10^5 + j4.77\times10^5$ rad/s and $\alpha_2 = -1.77\times10^5 + j3.06\times10^5$ rad/s when perturbing R_{g2}, $\alpha_1 = 1.73\times10^5 + j3.00\times10^5$ rad/s, and $\alpha_2 = 7.01\times 10^4 - j1.21\times10^5$ rad/s when perturbing C_1, and finally $\alpha_1 = 2.50\times10^5 + j4.33\times10^5$ rad/s, and $\alpha_2 = 6.25\times 10^4 - j1.08\times10^5$ rad/s when perturbing L_1.

3.4 EPD in Parallel Configuration

This section analyzes various types of second-order EPD in the parallel configuration. First, we show the general condition for second-order EPD in the parallel configuration and complement the theoretical calculations using time-domain circuit simulators. Second, we show how to get an EPD with real frequency by coupling two unstable resonators, i.e., imaginary resonance frequencies. Next, we show how to obtain an EPD associated with instability, i.e., where the EPD frequency is purely imaginary. Finally, we get EPD in a circuit that two stable resonators coupled via asymmetric gyrator compared to the symmetric case.

3.4.1 Second-Order EPD

In this configuration, two parallel LC tanks are coupled by an ideal gyrator, as displayed in Figure 3.4(a). We first write the Kirchhoff current law equations describing current and voltages in terms of charges [85]

$$\begin{cases} \ddot{Q}_1 = -\frac{1}{C_1 L_1} Q_1 + \frac{1}{R_g C_2} \dot{Q}_2 \\ \ddot{Q}_2 = -\frac{1}{C_2 L_2} Q_2 - \frac{1}{R_g C_1} \dot{Q}_1 \end{cases} \tag{3.18}$$

Introducing the state vector as $\Psi \equiv \left[Q_1, Q_2, \dot{Q}_1, \dot{Q}_2\right]^{\mathrm{T}}$ analogously to what was defined in the series configuration, leads to the following system of equations [85]

$$\frac{\mathrm{d}\Psi}{\mathrm{d}t} = \underline{\mathbf{M}}\Psi, \quad \underline{\mathbf{M}} = \begin{bmatrix} 0 & 0 & 1 & 0 \\ 0 & 0 & 0 & 1 \\ -\omega_{01}^2 & 0 & 0 & \frac{1}{R_g C_2} \\ 0 & -\omega_{02}^2 & -\frac{1}{R_g C_1} & 0 \end{bmatrix}, \tag{3.19}$$

The eigenfrequencies of the circuit are evaluated by solving the characteristic equation [85]

$$\omega^4 - \omega^2 \left(\omega_{01}^2 + \omega_{02}^2 + \frac{1}{C_1 C_2 R_g^2} \right) + \omega_{01}^2 \omega_{02}^2 = 0. \tag{3.20}$$

All the coefficients are real, so ω and ω^* are both roots of the equation. Also, the characteristic equation is a quadratic equation in ω^2, so both ω and $-\omega$ are solutions. The angular eigenfrequencies are determined as [85]

$$\omega_{1,3} = \pm\sqrt{a+b}, \omega_{2,4} = \pm\sqrt{a-b}, \tag{3.21}$$

$$a = \frac{1}{2}\left(\omega_{01}^2 + \omega_{02}^2 + \frac{1}{C_1 C_2 R_{\mathrm{g}}^2}\right), \tag{3.22}$$

$$b^2 = a^2 - \omega_{01}^2 \omega_{02}^2. \tag{3.23}$$

Based on Equation (3.21), the EPD can be achieved when $b = 0$ and the EPD angular frequency is $\omega_{\mathrm{e}} = \sqrt{a}$. We assume $a > 0$, so the EPD has a real angular frequency. Therefore, the condition to get EPD with real frequency is rewritten as [85]

$$\omega_{01}^2 + \omega_{02}^2 - \omega_{\mathrm{gp}}^2 > 0, \tag{3.24}$$

where the equivalent gyrator frequency for the parallel circuit is defined as $\omega_{\mathrm{gp}}^2 = -1/\left(C_1 C_2 R_{\mathrm{g}}^2\right)$. The following condition must be achieved to obtain EPD based on Equations (3.21), (3.22), and (3.23), [85]

$$\left(\omega_{01} - \omega_{02}\right)^2 = \omega_{\mathrm{gp}}^2. \tag{3.25}$$

We investigate three cases to select the components' values. First, if ω_{01} and ω_{02} are purely real, so the value of either C_1 or C_2 should be negative to have the same sign on both sides of Equation (3.25). As a result, to have a real value for ω_{01} and ω_{02}, one resonator needs to be composed of both negative C and L.

Second, if ω_{01} and ω_{02} have imaginary values, then C_1 and C_2 should have the same sign, either positive or negative. In this case, each resonator is unstable when uncoupled, and more details for this case are provided in Subsection 3.4.2.

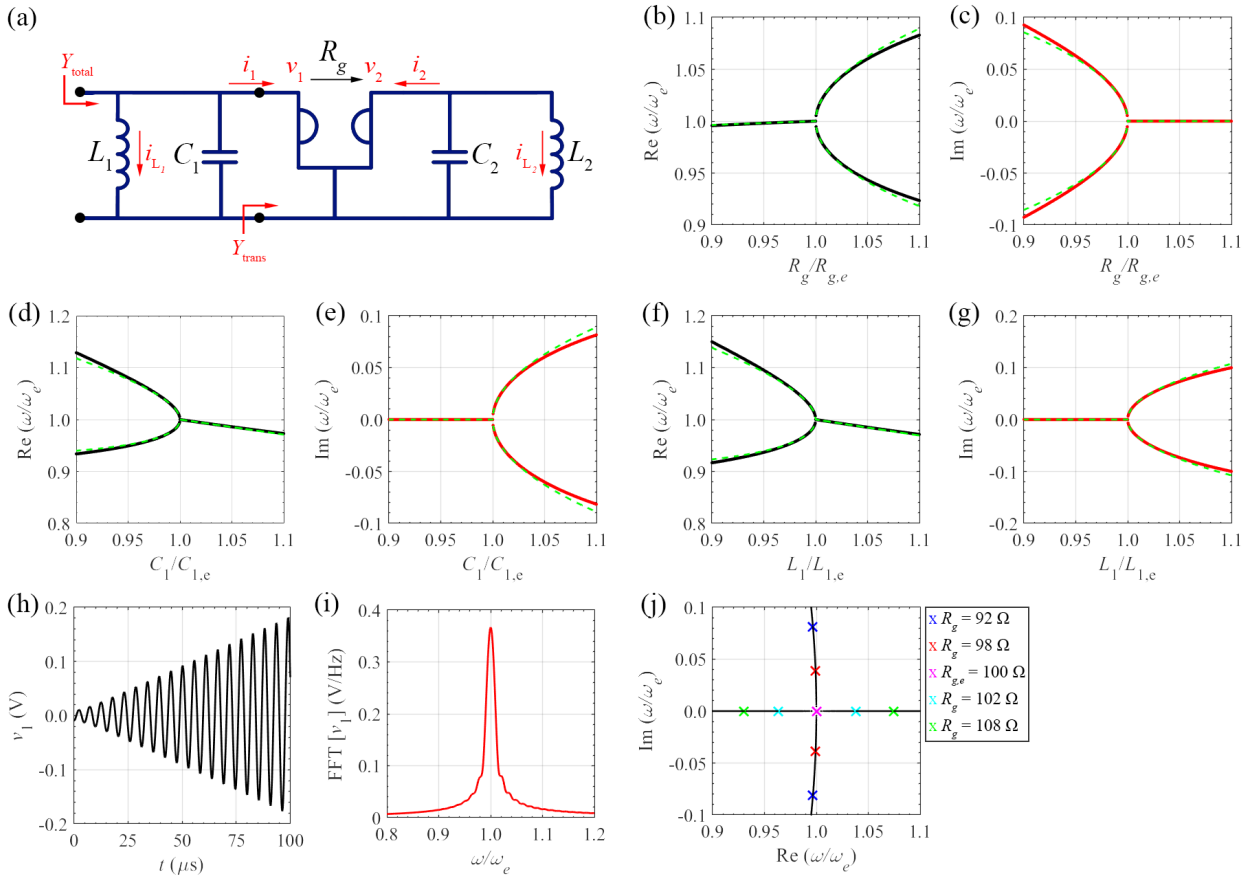

Figure 3.4: (a) The schematic illustration of the gyrator-based circuit with the ideal gyrator in parallel configuration. In this circuit, two different LC resonators are used in a parallel configuration, coupled via an ideal gyrator. The sensitivity of the (b), (d), (f) real and (c), (e), (g) imaginary parts of the eigenfrequencies to (b), (c) gyration resistance, (d), (e) positive capacitance C_1 (f), (g) positive inductance L_1 perturbation. Solid lines: solution of eigenvalue problem of Equation (3.19); green-dashed lines: Puiseux series approximation truncated to its second term. Voltage $v_1(t)$ under the EPD condition in the (h) time-domain, and (i) frequency-domain. The frequency-domain result is calculated by applying an FFT with 10^6 samples in the time window of $0\,\mu$s to $100\,\mu$s. (j) Root locus of zeros of $Y_{\text{total}}(\omega) = 0$ showing the real and imaginary parts of resonance frequencies of the circuit when perturbing gyration resistance. At the EPD, the system's total admittance is $Y_{\text{total}}(\omega) \propto (\omega - \omega_{\text{e}})^2$; hence it shows a double zero at ω_{e}.

Lastly, if only one of the ω_{01} or ω_{02} is imaginary, and the other is real; there is not any condition to obtain an EPD. In this section, we consider the first case in which one capacitor and one inductor on the same resonator have a negative value so ω_{gp}^2 is positive. When the EPD condition is satisfied, two eigenfrequencies coalesce at a real EPD angular frequency

$$\omega_{\mathrm{e}} = \sqrt{\frac{1}{2}\left(\omega_{01}^2 + \omega_{02}^2 - \omega_{\mathrm{gp}}^2\right)} = \sqrt{\omega_{01}\omega_{02}}. \tag{3.26}$$

As an example, we use the following values for the components: $L_1 = 33\,\mu$H, $L_2 = -33\,\mu$H, $C_2 = -33$ nF, and $R_{\mathrm{g}} = 50\Omega$. The capacitance C_1 is determined by solving the quadratic equation from the EPD condition. There are two possible values of the capacitance C_1 that satisfies the EPD condition, and we select $C_1 = 15.43$ nF in this example. Then the corresponding value for EPD frequency is calculated as $\omega_{\mathrm{e}} = 1.16 \times 10^6$ rad/s. The calculated results in Figures 3.4(b) and (c) show the real and imaginary parts of the angular eigenfrequencies obtained from the eigenvalue problem when varying the gyrator resistance near the EPD. Moreover, the results in Figures 3.4(d) and (e) show the real and imaginary parts of eigenfrequencies when varying the positive capacitance C_1. Then, by varying the positive inductance L_1, the real and imaginary parts of eigenfrequencies are shown in Figures 3.4(f) and (g). All the angular eigenfrequencies in the plots are normalized to the EPD angular frequency. In addition, the eigenfrequencies are also estimated using the Puiseux fractional power series expansion to show the sensitivity of angular eigenfrequencies to perturbation. Section 3.5 provides additional details on this method. The calculated eigenfrequencies using the Puiseux fractional power series expansion are shown by the green dashed lines in Figures 3.4(b)-(g). The approximated results show excellent agreement compared to the solutions of the eigenvalue problem of Equation (3.19). The coefficients of the Puiseux series up to second order are calculated as, $\alpha_1 = 3.13 \times 10^5$ rad/s, and $\alpha_2 = 4.24 \times 10^4$ rad/s when perturbing R_{g}, $\alpha_1 = j3.26 \times 10^5$ rad/s, and $\alpha_2 = -3.35 \times 10^5$ rad/s when perturbing C_1, $\alpha_1 = j3.94 \times 10^5$ rad/s, and $\alpha_2 = -3.57\times\ 10^5$rad/s when perturbing L_1. According to the obtained eigenfrequencies in Figures 3.4(b) and (c), by varying R_{g}, the real part of the eigenfrequencies split when $R_{\mathrm{g}} > R_{\mathrm{g,e}}$ and the imaginary part of the eigenfrequencies splits when $R_{\mathrm{g}} < R_{\mathrm{g,e}}$. In addition, the results in Figures 3.4(d)-(g) show that by perturbing C_1 and L_1, the dispersion diagram exhibits an analogous frequency behavior.

The time-domain simulation is provided using the Keysight ADS time-domain circuit simulator, and the voltage on the node v_1 is shown in Figure 3.4(h) . In the simulation, we use 1 mV as an initial voltage on the left capacitor C_1 and we use an ideal gyrator model. The voltage increases linearly with time, indicating that two circuit eigenfrequencies are coalescing, and the system signal is described by a double pole. The spectrum is calculated by using the FFT of the voltage $v_1(t)$ with 10^6 samples in the time window of $0\,\mu$s to $100\,\mu$s, and the result is shown in Figure 3.4(i). According to Figure 3.4(i), the oscillation frequency corresponds to $\omega_{\mathrm{e}} = 1.16 \times 10^6$ rad/s, hence there is a very good agreement with the theoretical EPD angular frequency. In this example, the components are lossless.

We demonstrate how the EPD is related to the circuit's resonance, which can be recognized directly in a frequencydomain analysis. We calculate the circuit's total input admittance $Y_{\mathrm{total}}(\omega)$ using the same method as we did for the series configuration. We define the admittances of the resonators as $Y_1 = j\omega C_1 + 1/\left(j\omega L_1\right)$, and $Y_2 = j\omega C_2 + 1/\left(j\omega L_2\right)$. Then the transferred admittance on the left side is calculated by (see Figure 3.4(a))

$$Y_{\mathrm{trans}}(\omega) = \frac{1}{R_{\mathrm{g}}^2 Y_2}. \tag{3.27}$$

The total admittance observed from the circuit input port (see Figure 3.4(a)) is calculated by

$$Y_{\mathrm{total}}(\omega) = Y_1(\omega) + Y_{\mathrm{trans}}(\omega). \tag{3.28}$$

The resonant angular frequencies are obtained by solving $Y_{\mathrm{total}}(\omega) = 0$. The resonance frequencies by perturbing gyration resistance values are calculated in Figure 3.4(j), normalized to the EPD angular frequency. Considering the gyrator resistance value at the EPD, two

zeros coincide, representing the point where the two curves meet exactly at the EPD angular frequency. According to Figure 3.4(j), for $R_{\mathrm{g}} < R_{\mathrm{g,e}}$, the resonance angular frequencies are complex conjugate pairs, and for $R_{\mathrm{g}} > R_{\mathrm{g,e}}$, the resonance angular frequencies are purely real.

3.4.2 Stable EPD Frequency via Unstable Uncoupled Resonators

This section employs unstable resonators to obtain an EPD with real eigenfrequency. In other words, we study the case of two unstable resonators coupled via an ideal gyrator. This issue can be investigated in both series and parallel configurations; here, we look at the case with the parallel configuration. A comprehensive analysis of the unstable resonators for series configuration is presented in [110]. The analysis in this section is analogous to one in Subsection 3.4.1. Each resonator should have only one component with a negative value to have an unstable resonance frequency. Without loss of generality, we consider a negative value for both inductances and a positive value for both capacitances; hence, ω_{gs}^2 has negative value. Based on the condition for EPD ($b = 0$) and by using Equation (3.23), the first and second terms in Equation (3.22) are negative, and the third term is positive. According to Equation (3.26), if $|\omega_{01}^2 + \omega_{02}^2| < \omega_{\mathrm{gp}}^2$ the calculated EPD frequency will be real, and if $|\omega_{01}^2 + \omega_{02}^2| > \omega_{\mathrm{gp}}^2$, the EPD frequency yields an imaginary value.

In order to obtain EPD with real frequency by using unstable resonators, we use the following set of values for components: $L_1 = -33\,\mu\mathrm{H}$, $L_2 = -33\,\mu\mathrm{H}$, $C_1 = 2.32\,\mathrm{nF}$, $C_2 = 33\,\mathrm{nF}$, and $R_{\mathrm{g}} = 25\,\Omega$. Therefore, both ω_{01}^2 and ω_{02}^2 have negative values, with $\omega_{01} = -j3.62 \times 10^6\,\mathrm{rad/s}$, and $\omega_{02} = -j9.58 \times 10^5\,\mathrm{rad/s}$. The used value for components leads to a real EPD angular frequency of $\omega_{\mathrm{e}} = 1.86 \times 10^6\,\mathrm{rad/s}$. The normalized eigenfrequencies by solving the eigenvalue problem of Equation (3.19) while perturbing R_{g}, C_1, and L_1 are shown in Figures 3.5(a)-(f). In addition, the eigenfrequencies are estimated using the Puiseux fractional power series

expansion to confirm the calculated results. More information for the Puiseux series is provided in Section 3.5. The calculated eigenfrequencies using the Puiseux series are drawn by the green dashed lines in Figures 3.5(a)-(f). To calculate the estimated eigenfrequencies, the coefficients of the Puiseux series are calculated as, $\alpha_1 = j3.24 \times 10^6$ rad/s, and $\alpha_2 = -2.81 \times 10^6$ rad/s when perturbing R_{g}, $\alpha_1 = j1.05\times 10^6$ rad/s, and $\alpha_2 = -7.60 \times 10^5$ rad/s when perturbing C_1, $\alpha_1 = 2.03 \times 10^6$ rad/s, and $\alpha_2 = 6.46 \times 10^5$ rad/s when perturbing L_1. The calculated results in Figures 3.5(a)-(d) demonstrate that by perturbing R_{g} and C_1, the circuit shows the analogous frequency behavior. So, when the component value is smaller than the EPD value, the real parts of the eigenfrequencies split, and when the component value is bigger than the EPD value, the imaginary parts of the eigenfrequencies split. According to the obtained eigenfrequencies in Figures 3.5(e) and (f), by varying L_1, the real part of the eigenfrequencies split when $L_1 > L_{1,\mathrm{e}}$ and the imaginary part of the eigenfrequencies split when $L_1 < L_{1,\mathrm{e}}$.

We use the Keysight ADS circuit simulator to analyze the time-domain response of the circuit under EPD conditions. The transient response of the coupled resonators with the ideal gyrator is simulated using the timedomain solver with an initial condition $v_1(0) = 1\mathrm{mV}$, where $v_1(t)$ is the voltage of the capacitor in the left resonator (see Figure 3.4(a)). Figure 3.5(g) shows the time-domain simulation results of the voltage $v_1(t)$. The voltage is obtained in the period of $0\,\mu$s to $100\,\mu$s. As previously stated, the solution of the eigenvalue problem at the EPD differs from any other regular frequency in the dispersion diagram because the circuit matrix contains repeated eigenvalues associated with one eigenvector. As a result, the voltage increases linearly with increasing time, while the oscillation frequency remains constant. It is the consequence of coalescing eigenvalues and eigenvectors, which correspond to a double pole or a zero in the circuit, depending on the observed parameter. The spectrum is calculated by using the FFT of the voltage $v_1(t)$ with 10^6 samples in the time window of 0μs to 100μs, and the calculated result is shown in Figure 3.5(h). According to Figure 3.5(h) , the oscillation frequency corresponds to $\omega_{\mathrm{e}} = 1.86 \times 10^6$ rad/s, so there is a very good agreement

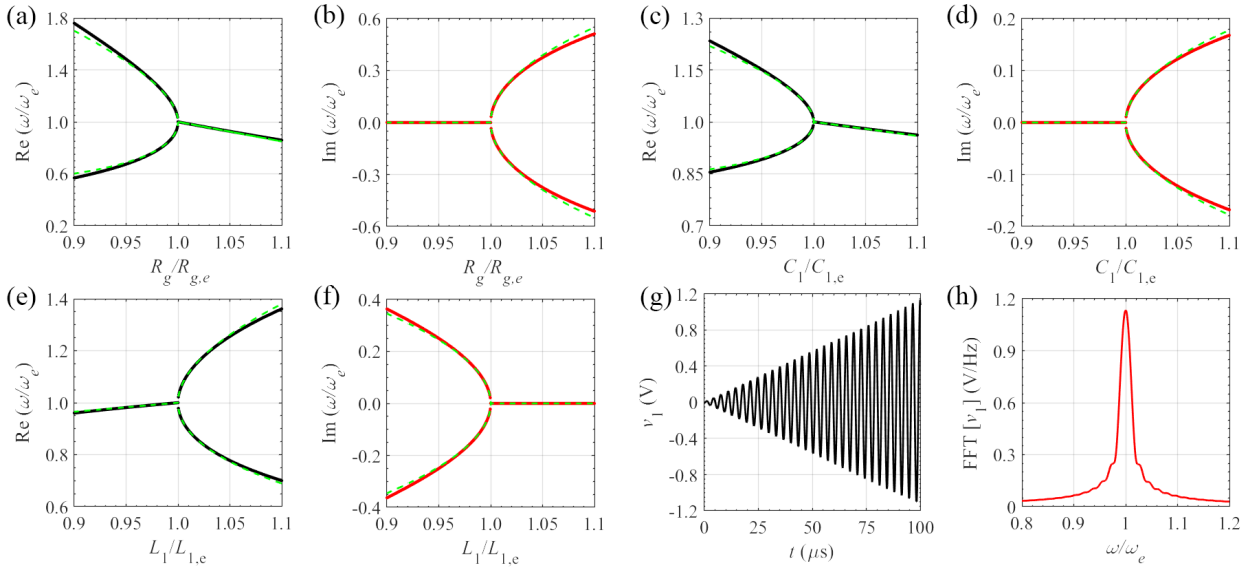

Figure 3.5: The sensitivity of the (a), (c), (e) real and (b), (d), (f) imaginary parts of the eigenfrequencies to (a), (b) gyration resistance, (c), (d) positive capacitance C_1 (e), (f) positive inductance L_1 perturbation. Solid lines: solution of eigenvalue problem of Equation (3.19); green-dashed lines: Puiseux series approximation truncated to its second term. Here, both resonators are unstable, i.e., resonance frequency of resonators is purely imaginary. Voltage $v_1(t)$ under the EPD condition in the (g) time-domain, and (h) frequency-domain. The frequency-domain result is calculated by applying an FFT with 10^6 samples in the time window of 0 μs to 100 μs.

with the theoretical EPD angular frequency. In the presented example, all components were ideal, and we did not consider any lossy element in the circuit. A comprehensive study for the effect of losses in the stability of the circuit with unstable resonators is presented in [110].

3.4.3 Unstable EPD Frequency

So far, we have focused on the EPD with real frequency, which is a practical case due to the stability of the resonance frequency. This section analyzes the case with unstable EPD frequency, i.e., EPD with imaginary frequency. Here we investigate the example for second-order EPD in the parallel configuration. The required analysis in this section is the same as the discussion presented in Subsection 3.4.1. The only difference is that the selected value for components leads to imaginary EPD frequency.

As an example, we use the following values for the components: $L_1 = 15\,\mu$H, $L_2 = -50\,\mu$H, $C_2 = -15$ nF, and $R_g = 25\,\Omega$. The capacitance C_1 is obtained by solving the quadratic equation from the EPD condition. There are two possible values for C_1 that satisfies the EPD condition, and we select $C_1 = 3.50$ nF in this example. Then the corresponding value for EPD frequency is calculated as $\omega_e = j2.24 \times 10^6$ rad/s, which shows that the circuit is unstable at EPD. The results in Figures 3.6(a) and (b) show the real and imaginary parts of perturbed eigenfrequencies calculated from the eigenvalue problem when varying the gyration resistance near the EPD. Also, the obtained results in Figures 3.6(c) and (d) show the real and imaginary parts of eigenfrequencies by perturbing the positive capacitance C_1. Then, by perturbing the positive inductance L_1, the real and imaginary parts of eigenfrequencies are shown in Figures 3.6(e) and (f). The calculated eigenfrequencies in these plots are normalized to the absolute value of imaginary EPD frequency. In addition, the eigenfrequencies are calculated using the Puiseux fractional power series expansion. Section 3.5 contains further information on this method. The obtained eigenfrequencies using the Puiseux series are shown by the green dashed lines in Figures 3.6(a)-(f). The estimated results show perfect agreement compared to the solutions of the eigenvalue problem in Equation (3.19). In the calculated estimated eigenfrequencies, the coefficients of the Puiseux series are calculated as, $\alpha_1 = 3.90 \times 10^6$ rad/s, and $\alpha_2 = -j3.39\times\ 10^6$ rad/s when perturbing R_g, $\alpha_1 = 1.26 \times 10^6$ rad/s, and $\alpha_2 = -j9.16 \times 10^5$ rad/s when perturbing $C_1, \alpha_1 = j2.45\times\ 10^6$ rad/s, and $\alpha_2 = j7.78 \times 10^5$ rad/s when perturbing L_1. Using the ideal model for the gyrator, the time-domain simulation result for the node voltage v_1 in Figure 3.6(g) is obtained using the Keysight ADS circuit simulator. We use 1 mV as an initial voltage on the capacitor C_1. The voltage exponentially increases over time without any oscillation, indicating that the circuit is unstable.

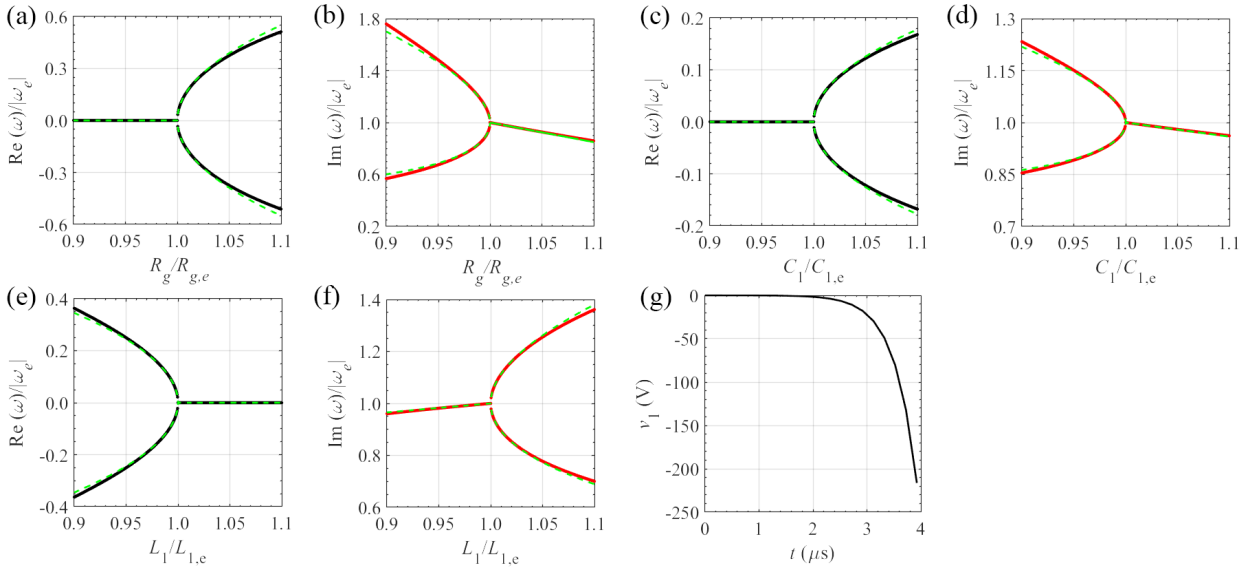

Figure 3.6: The sensitivity of the (a), (c), (e) real and (b), (d), (f) imaginary parts of the eigenfrequencies to (a), (b) gyration resistance, (c), (d) positive capacitance C_1(e), (f) positive inductance L_1 perturbation. Solid lines: solution of eigenvalue problem of Equation (3.19); green-dashed lines: Puiseux series approximation truncated to its second term. Here, the EPD frequency is unstable, i.e., EPD frequency is purely imaginary. (g) Voltage $v_1(t)$ for the unstable EPD condition in the time-domain, which increases exponentially over time.

3.4.4 Asymmetric Gyrator

In this section, two parallel LC tanks are coupled by an asymmetric gyrator with the forward gyration resistance of R_{gf} and backward gyration resistance of R_{gb}, as displayed in Figure 3.7(a). The concept of asymmetry in the gyrator is discussed in Appendix C. We find the EPD condition by writing the Kirchhoff current law equations and finding the Liouvillian matrix. As a result, the following equations are written by describing currents and voltages in terms of charges

$$\begin{cases} \ddot{Q}_1 = -\frac{1}{C_1 L_1} Q_1 + \frac{1}{R_{\text{gb}} C_2} \dot{Q}_2 \\ \ddot{Q}_2 = -\frac{1}{C_2 L_2} Q_2 - \frac{1}{R_{\text{gf}} C_1} \dot{Q}_1 \end{cases} \tag{3.29}$$

By defining the state vector as $\Psi \equiv \left[Q_1, Q_2, \dot{Q}_1, \dot{Q}_2\right]^{\mathrm{T}}$, we represent equations in Liouvillian form

$$\frac{\mathrm{d}\Psi}{\mathrm{d}t} = \underline{\mathbf{M}}\Psi, \quad \underline{\mathbf{M}} = \begin{bmatrix} 0 & 0 & 1 & 0 \\ 0 & 0 & 0 & 1 \\ -\omega_{01}^2 & 0 & 0 & \frac{1}{R_{\mathrm{gb}}C_2} \\ 0 & -\omega_{02}^2 & -\frac{1}{R_{\mathrm{gf}}C_1} & 0 \end{bmatrix}. \tag{3.30}$$

The eigenfrequencies of the circuit are calculated by solving the below characteristic equation

$$\omega^4 - \omega^2\left(\omega_{01}^2 + \omega_{02}^2 + \frac{1}{R_{\mathrm{gb}}R_{\mathrm{gf}}C_1C_2}\right) + \omega_{01}^2\omega_{02}^2 = 0. \tag{3.31}$$

Then the angular eigenfrequencies are determined as

$$\omega_{1,3} = \pm\sqrt{a+b}, \omega_{2,4} = \pm\sqrt{a-b}, \tag{3.32}$$

$$a = \frac{1}{2}\left(\omega_{01}^2 + \omega_{02}^2 + \frac{1}{C_1C_2R_{\mathrm{gb}}R_{\mathrm{gf}}}\right), \tag{3.33}$$

$$b^2 = a^2 - \omega_{01}^2\omega_{02}^2. \tag{3.34}$$

According to Equation (3.32), the EPD is achieved when $b = 0$. The following condition must be met to achieve EPD in the asymmetric configuration using Equations (3.33), and

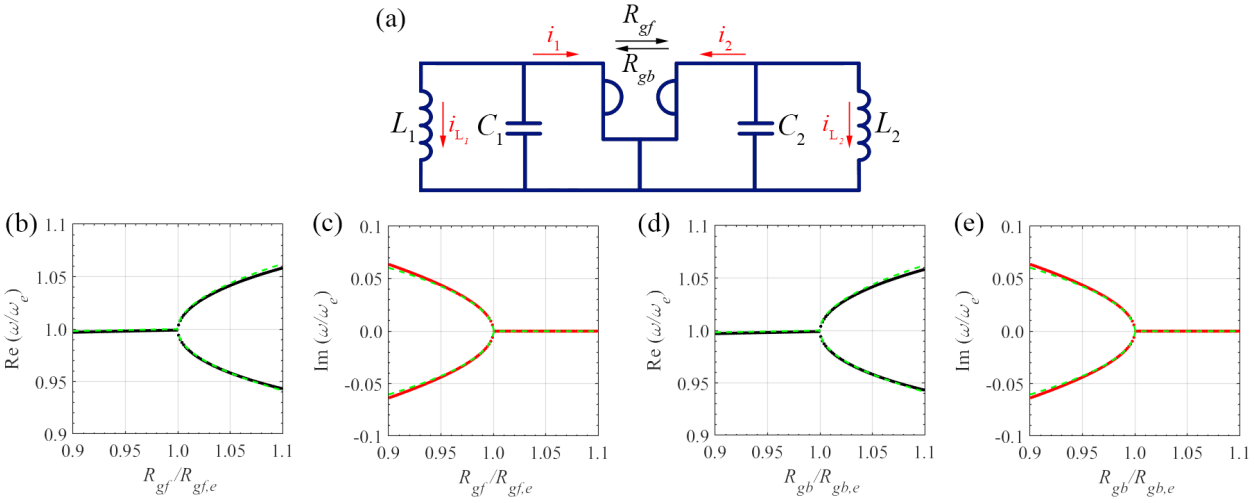

Figure 3.7: (a) The schematic illustration of the gyrator-based circuit with the assymetric gyrator in parallel configuration. The sensitivity of the (b), (d), real and (c), (e), imaginary parts of the eigenfrequencies to (b), (c) forward gyration resistance and (d), (e) backward gyration resistance. Solid lines: solution of eigenvalue problem of Equation (3.30); green-dashed lines: Puiseux series approximation truncated to its second term.

(3.34)

$$(\omega_{01} - \omega_{02})^2 = -\frac{1}{C_1 C_2 R_{\mathrm{gb}} R_{\mathrm{gf}}}. \tag{3.35}$$

When the EPD condition is satisfied, two eigenfrequencies coalesce at a real EPD angular frequency

$$\omega_{\mathrm{e}} = \sqrt{\frac{1}{2}\left(\omega_{01}^2 + \omega_{02}^2 + \frac{1}{C_1 C_2 R_{\mathrm{gb}} R_{\mathrm{gf}}}\right)} = \sqrt{\omega_{01}\omega_{02}}. \tag{3.36}$$

Here we use the values derived for parallel configuration in Subsection 3.4.1 where $L_1 = 33\mu\mathrm{H}$, $L_2 = -33\,\mu\mathrm{H}$, $C_1 = 15.43\,\mathrm{nF}$, $C_2 = -33\,\mathrm{nF}$, $R_{\mathrm{gf}} = 100\,\Omega$, and $R_{\mathrm{gb}} = 100\,\Omega$. Then the EPD frequency is calculated as $\omega_{\mathrm{e}} = 1.16\times\ 10^6\,\mathrm{rad/s}$. The results in Figures 3.7(b) and (c) show the real and imaginary parts of perturbed eigenfrequencies obtained from the eigenvalue problem of Equation (3.30) when varying the forward gyrator resistance near the EPD value

and Figures 3.7(d) and (e) are eigenfrequency evolution by varying the backward gyration resistance. All the obtained eigenfrequencies in the mentioned plots are normalized to the EPD frequency. In addition, the eigenfrequencies are calculated using the Puiseux fractional power series expansion to measure the sensitivity of the eigenfrequencies to perturbation, and the calculated eigenfrequencies are drawn by the green dashed lines. Section 3.5 provides additional information on this method. In the presented estimated result, the coefficients of the Puiseux series are calculated as, $\alpha_1 = 2.21 \times 10^5$ rad/s, and $\alpha_2 = 2.12\times\ 10^4$ rad/s when perturbing R_{gb} or R_{gf}. As we demonstrate for symmetric case in Subsection 3.4.1, by varying R_{g}, the real part of the eigenfrequencies split when $R_{\mathrm{g}} > R_{\mathrm{g,e}}$, and the imaginary part of the eigenfrequencies split when $R_{\mathrm{g}} < R_{\mathrm{g,e}}$. In addition, the calculated eigenfrequencies in Figures 3.7(b)-(e) demonstrate that by perturbing R_{gf} and R_{gb}, the gyrator-based circuit shows the analogous frequency behavior. On the other hand, we know that higher sensitivity is achieved when the bifurcation of the dispersion diagrams is wider [92]. So, by comparing the symmetric and asymmetric cases, it is clear that the symmetric case is more sensitive than the asymmetric case.

3.5 Puiseux Fractional Power Series Expansion

The sensitivity of a system to a specific parameter may be detectable where the perturbation on the system changes observable quantities such as the system's resonance frequency. Changes in the system will be detected by measuring frequency changes and determining their relationship to perturbation. Puiseux fractional power series expansion helps us to find this relation for eigenvalues in the vicinity of EPD. For EPDs, sensitivity is boosted because of the eigenvalue's degeneracy. We consider a small perturbation Δ_X of a system parameter X as

$$\Delta_X = \frac{X - X_e}{X_e}, \tag{3.37}$$

where X_e is the parameters's value at EPD, and X is the parameter's value after applying perturbation. A perturbation Δ_X to a system parameter results in a perturbed system matrix $\underline{\mathbf{M}}(\Delta_X)$, which results in perturbed eigenfrequencies $\omega_p(\Delta_X)$ with $p = 1, \ldots, n$ close to the n-th order EPD angular frequency. The perturbed eigenfrequencies near an EPD are found using a Puiseux fractional power series expansion [4]. A Puiseux series is a generalized power series with fractional and negative exponents in one variable. The Puiseux fractional power series expansion of $\omega_p(\Delta_X)$ is defined by [91]

$$\omega_p(\Delta_X) \approx \omega_{\mathrm{e}} + \sum_{k=1}^{\infty} \alpha_k \left(\left(e^{j\frac{2\pi}{n}} \right)^p \Delta_X{}^{\frac{1}{n}} \right)^k, \tag{3.38}$$

where the first two coefficients for the second-order approximation are expressed as [91]

$$\alpha_1 = \left(-\frac{\frac{\partial H(\Delta_X,\omega)}{\partial \Delta_X}}{\frac{1}{n!}\frac{\partial^n H(\Delta_X,\omega)}{\partial \omega^n}} \right)^{\frac{1}{n}}, \tag{3.39}$$

$$\alpha_2 = -\frac{\alpha_1^{n+1}\frac{1}{(n+1)!}\frac{\partial^{n+1} H(\Delta_X,\omega)}{\partial \omega^{n+1}} + \alpha_1 \frac{\partial^2 H(\Delta_X,\omega)}{\partial \omega \partial \Delta_X}}{n\alpha_1^{n-1}\left(\frac{1}{n!}\frac{\partial^n H(\Delta_X,\omega)}{\partial \omega^n}\right)}. \tag{3.40}$$

The coefficients are calculated at the EPD, where $\Delta_X = 0, \omega = \omega_{\mathrm{e}}$, and $H(\Delta_X, \omega) = \det(\underline{\mathbf{M}}(\Delta_X) - j\omega\underline{\mathbf{I}})$. In this paper, we utilize this series expansion for the second-order and third-order EPD. For second-order EPD, we express Puiseux fractional power series expansion by

$$\omega_p\left(\Delta_X\right) \approx \omega_{\mathrm{e}} + \alpha_1(-1)^p\sqrt{\Delta_X} + \alpha_2\Delta_X, \tag{3.41}$$

$$\alpha_1 = \sqrt{-2\frac{\frac{\partial H(\Delta_X,\omega)}{\partial \Delta_X}}{\frac{\partial^2 H(\Delta_X,\omega)}{\partial \omega^2}}}, \tag{3.42}$$

$$\alpha_2 = -\frac{\alpha_1^2\frac{1}{6}\frac{\partial^3 H(\Delta_X,\omega)}{\partial \omega^3} + \frac{\partial^2 H(\Delta_X,\omega)}{\partial \omega \partial \Delta_X}}{\frac{\partial^2 H(\Delta_X,\omega)}{\partial \omega^2}}. \tag{3.43}$$

Moreover, for third-order EPD, we calculate Puiseux fractional power series expansion by

$$\omega_p\left(\Delta_X\right) \approx \omega_{\mathrm{e}} + \alpha_1\left(e^{j\frac{2\pi}{3}}\right)^p \sqrt[3]{\Delta_X} + \alpha_2\left(e^{j\frac{4\pi}{3}}\right)^p \sqrt[3]{\left(\Delta_X\right)^2}, \tag{3.44}$$

$$\alpha_1 = \sqrt[3]{-6\frac{\frac{\partial H(\Delta_X,\omega)}{\partial \Delta_X}}{\frac{\partial^3 H(\Delta_X,\omega)}{\partial \omega^3}}}, \tag{3.45}$$

$$\alpha_2 = -\frac{\alpha_1^3\frac{1}{24}\frac{\partial^4 H(\Delta_X,\omega)}{\partial \omega^4} + \frac{\partial^2 H(\Delta_X,\omega)}{\partial \omega \partial \Delta_X}}{\alpha_1\left(\frac{1}{2}\frac{\partial^3 H(\Delta_X,\omega)}{\partial \omega^3}\right)}. \tag{3.46}$$

3.6 Conclusions

We have provided a comprehensive description of a new technique based on using gyrators and resonators to get EPDs. This new method opens up a new way to realize EPDs offering many new circuit configurations complementary to those satisfying PT-symmetry.

We have shown various circuits based on resonators coupled via gyrators that support an EPD, where some resonators are made of negative inductance and negative capacitance that can be realized using operational amplifiers. We have provided the theoretical conditions

for second-order EPD to exist with either purely real or imaginary frequency. We have complemented our theoretical calculations with time-domain circuit simulations, showing an excellent agreement. We have shown how to obtain a stable second-order EPD by using two unstable (when isolated) coupled resonators and also using two stable resonators coupled via an asymmetric gyrator. We have demonstrated that the eigenfrequencies are extremely sensitive to the circuit's perturbation, which may have important implications for ultrasensitive sensing technologies and RF sensors. An important feature is that when we perturb a circuit component (e.g., a capacitor), the circuit provides two shifted frequencies with real values, contrary to the case of EPD based on PT-symmetry where the two shifted frequencies are complex valued.

In this paper, the lossless circuits are analyzed, whereas the effects of additional loss or gain on each resonator for some configurations have been investigated in [85, 110]. Any loss or gain in the circuit leads to complex-valued eigenfrequencies, which cause instability and start an oscillatory regime. To prevent the circuit from saturating and still using the high sensitivity advantage, we could switch on and off the circuit and work in the transient regime as was done in [125].

Higher sensitivity is achieved using third-order EPD, with the important property that the circuit is always unstable, which is a feature that can be exploited to make an oscillator based on an EPD. Based on duality theory, all the cases mentioned above can be explored for both series and parallel resonators. Calculating the relevant Puiseux fractional power series expansion for all the cases shows the EPD's occurrence and the circuit's sensitivity when operating at the EPD. We believe that the demonstrated results pave the way for conceivable new operation strategies for boosting the overall performance of highsensitive sensors.

Acknowledgments

- I would like to thank Alireza Nikzamir for collaboration on this chapter.

- This material is based upon work supported by the National Science Foundation (NSF) under Grant No. ECCS-1711975 and the Air Force Office of Scientific Research (AFOSR) Grant No. FA9550-19-1-0103.

- The text of Chapter 3 of this dissertation is a reprint of the material as it appears in K. Rouhi, A. Nikzamir, A. Figotin, and F. Capolino, "High-sensitivity in various gyrator-based circuits with exceptional points of degeneracy," EPJ Applied Metamaterials, vol. 9, p. 8, 2022. The coauthors listed in this publication are Alireza Nikzamir, Alexander Figotin, and Filippo Capolino. Alexander Figotin and Filippo Capolino directed and supervised research which forms the basis for the dissertation.

- The results of this chapter have been published in the journal papers of [142, 143] and in the arXiv preprint of [85] and in the conference papers of [144].

Chapter 4

Simple Reciprocal Electric Circuit Exhibiting Exceptional Point of Degeneracy

An EPD occurs when both the eigenvalues and the corresponding eigenvectors of a square matrix coincide and the matrix has a nontrivial Jordan block structure. It is not easy to achieve an EPD exactly. In our prior studies, we synthesized simple conservative (lossless) circuits with evolution matrices featuring EPDs by using two LC loops coupled by a gyrator. In this chapter, we advance even a simpler circuit with an EPD consisting of only two LC loops with one capacitor shared. Consequently, this circuit involves only four elements and it is perfectly reciprocal. The shared capacitance and parallel inductance are negative with values determined by explicit formulas which lead to EPD. This circuit can have the same Jordan canonical form as the nonreciprocal circuit we introduced before. This implies that the Jordan canonical form does not necessarily manifest systems' nonreciprocity. It is natural to ask how nonreciprocity is manifested in the system's spectral data. Our analysis of this issue shows that nonreciprocity is manifested explicitly in: (i) the circuit Lagrangian and (ii)

the breakdown of certain symmetries in the set of eigenmodes. All our significant theoretical findings were thoroughly tested and confirmed by numerical simulations using commercial circuit simulator software.

4.1 Background, Motivation, and State of the Art

A key motivation for this work is an interest in systems that exhibit EPDs. EPD refers to the degeneracy of the system matrix that occurs when both the eigenvalues and the corresponding eigenvectors of the system coincide [4, 145, 114, 64, 115]. The corresponding system matrix is not diagonalizable at EPD. Also, EPD occurs when the system matrix is similar to a matrix containing a nontrivial Jordan block that is a Jordan block with a size of at least two [114]. One application of EPD systems is high-sensitivity, which has attracted a great deal of interest [70, 71, 38].

Considerable efforts are required to design an EPD system, and several methods have been proposed for achieving EPD. Those approaches are based on: (i) non-Hermitian PT-symmetric coupled systems with balanced loss and gain [66, 146, 147]; (ii) lossless and gainless structures associated with a stationary inflection point (and degenerate band edge [39, 148]; (iii) coupled resonators [9, 33, 149, 37]; and (iv) time-varying systems [19, 92, 150]. Additionally, the EPD is investigated in a nonreciprocal circuit consisting of two LC resonators without gain and loss coupled via a nonreciprocal element, i.e., a gyrator [86, 87, 110, 142]. Although one of the approaches suggests that loss and gain are essential for EPD, our recent studies indicate that an EPD can be obtained in time-varying [19, 92, 150] and gyrator-based [86, 87, 110, 142] systems without gain and losses.

Following studies in [86, 87, 110, 142] we ask whether conservative and reciprocal circuits exist such that their evolution matrices exhibit EPDs. The answer to this question is positive and

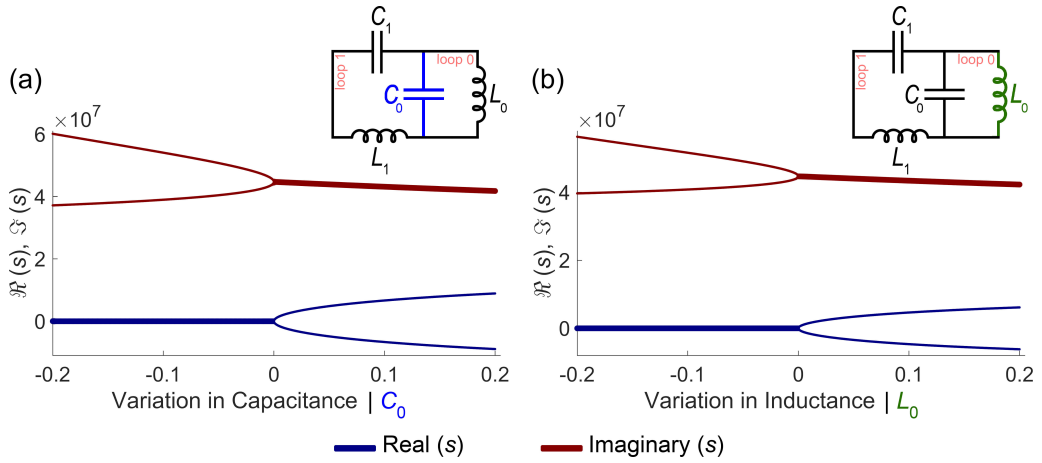

Figure 4.1: The real (dark blue solid curve) and imaginary (dark red solid curve) parts of the eigenvalues ($s = \mathrm{i}\omega$, where ω is eigenfrequency) of the circuit by varying (a) capacitance (C_0) and (b) inductance (L_0). In these plots, thicker branches indicate a multiplicity of two, and we limited the plots to eigenvalues with positive imaginary parts. Due to the bifurcation near the EPD, a second-order EPD with high sensitivity can be applied to sensing applications. The proposed reciprocal circuit is shown here where the perturbed elements are colored in blue (capacitance) and green (inductance).

we construct here a circuit with EPD that does not involve nonreciprocal or lossy elements (see circuits in Figure 4.1). One of our primary goals here is to synthesize a conservative circuit by using only reciprocal components so that its evolution matrix has the nontrivial Jordan canonical form subject to natural constraints considered later on as will be discussed in Subsection 4.5.1. The approach to achieve EPD without a gyrator, and still not relaying PT symmetry, would be useful because implementing a gyrator may be cumbersome because it may require active components or nonreciprocal elements that are usually lossy. As a result, removing the gyrator from the circuit and proposing a circuit with the Jordan canonical form without using any nonreciprocal elements is an important simplification of the earlier circuit's implementation.

In this chapter, we advance a perfectly conservative and reciprocal circuit that can be used to obtain the desired Jordan canonical form and achieve second-order EPD. Our comparative studies of reciprocal and nonreciprocal circuits suggest that circuit reciprocity information is not necessarily encoded in the relevant Jordan canonical form but rather in certain sym-

metries of the circuit eigenvectors. Nonreciprocity can manifest in various ways depending on the specific system and its Lagrangian. In terms of the Lagrangian itself, signs of nonreciprocity might include terms that explicitly depend on time or velocity (current), or terms that violate symmetries such as time-reversal symmetry. In addition, both reciprocal and nonreciprocal schemes can lead to the same eigenvalues whereas their Lagrangian equations are different. We demonstrate the conditions for equivalence between reciprocal and nonreciprocal circuits in general (i.e., when circuits are degenerate or non-degenerate) to have the same Jordan canonical form despite different Lagrangian equations. The present study includes mathematical analysis as well as time-domain numerical simulation results for verification computed by a well-known commercial circuit simulator. A number of examples with different values for elements that satisfy the EPD condition were examined. All the examples demonstrate the validity of our investigation in both the time and frequency domains. However, only one example is presented for ease of reading. The eigenvalues of the proposed circuit, which will be discussed later, are exceedingly sensitive to perturbations in circuit parameters (such as capacitance or inductance) as shown in Figure 4.1. Hence, the proposed circuit provides exceptional capabilities for applications that require high-sensitivity sensing when a component of the circuit, which is essentially a sensing component, is perturbed externally.

The structure of the chapter is as follows. The mathematical setup of the problem is presented in Section 4.2. The main achievements and results of this chapter are reviewed in Section 4.3. Then, we show our primary circuit with lossless and reciprocal elements in Section 4.4. We study the Jordan canonical form of the circuit and the condition to obtain second-order EPD in our proposed circuit in Section 4.5. Section 4.6 demonstrates the Lagrangian and Hamiltonian structures and their relation in the general case. Next, we review briefly the gyrator-based circuit introduced in our previous studies and explain the mathematical analysis behind the nonreciprocal design in Section 4.7. In Section 4.8, we analyze both reciprocal and nonreciprocal circuits to identify the signs of nonreciprocity in

the Lagrangian and eigenvectors of the circuits. Also, we provide the equivalency condition for both reciprocal and nonreciprocal circuits in Section 4.9 to have the same eigenvalues while the circuits' Lagrangian equations are different. Finally, we support our mathematical analysis and findings by giving examples that are verified by using a time-domain circuit simulator in Section 4.10 and wrapping up the chapter in Section 4.11. Also, we include many appendices for readers to provide more information and details.

4.2 Mathematical Setup of the Problem

Our primary focus here is to develop a conservative electric circuit with 2 *fundamental loops* (see circuit in Figure 4.1) that its evolution matrix $\mathscr{H}$ has a Jordan canonical form $\mathscr{J}$ subject to natural constraints considered later on. According to the definition of the Jordan canonical form, we have $\mathscr{H} = \mathscr{S}\,\mathscr{J}\,\mathscr{S}^{-1}$ where $\mathscr{S}$ is an invertible 4×4 matrix for the two-loop circuit that is a block diagonal matrix of the form

$$\mathscr{J} = \begin{bmatrix} J(\zeta_1) & 0_2 \\ 0_2 & J(\zeta_2) \end{bmatrix}, \quad J(\zeta_j) = \begin{bmatrix} \zeta_j & 1 \\ 0 & \zeta_j \end{bmatrix}, \quad j = 1, 2, \tag{4.1}$$

where 0_2 is 2×2 zero matrix, ζ_j are real or complex numbers, and $J(\zeta_j)$ are the corresponding so-called Jordan block. We assume that circuit evolution is described by the following Hamilton evolution equation

$$\partial_t \mathscr{X} = \mathscr{H}\,\mathscr{X}, \tag{4.2}$$

where $\mathscr{X}$ is 4 dimensional vector-column describing the circuit state and $\mathscr{H}$ is 4×4 matrix. The matrix $\mathscr{H}$ is going to be a Hamiltonian matrix and we will refer to it as the *circuit evolution matrix* or simply *circuit matrix* (see Section 4.6). Also, the circuit state vector is

represented by the two time-dependent charges $q_j(t)$ $(j = 1, 2)$ which are the time integrals of the corresponding loop currents $\partial_t q_k(t)$ (see the circuit in Figure 4.1).

The eigenvalue problem of Equation (4.2) can be written as

$$s\mathscr{X} = \mathscr{H}\mathscr{X}, \quad s = \mathrm{i}\omega, \tag{4.3}$$

where s is the eigenvalue and ω is the eigenfrequency. If the Jordan canonical form $\mathscr{J}$ of the circuit matrix $\mathscr{H}$ has a nontrivial Jordan block, the circuit must have at least one negative inductance and capacitance (see Section 4.5.1). The origin of the constraints is the fundamental property of a Hamiltonian matrix $\mathscr{H}$ to be similar to $-\mathscr{H}^{\mathrm{T}}$ (T is transpose operator). In addition to the Hamiltonian spectral symmetry, the Jordan structure of Hamiltonian matrices may be arbitrary. Our proposed approach for the generation of Hamiltonian and the corresponding Hamiltonian matrices is related to the Hamiltonian canonical forms (see Appendix F of [86]).

Another important mathematical point for the synthesis of the simplest possible conservative circuit with nontrivial Jordan blocks originates from the property of a square matrix $\mathscr{M}$ to be *cyclic* (see Appendix B of [86]). The matrix $\mathscr{M}$ is referred to as cyclic if the geometric multiplicity of each eigenvalue is exactly 1 which corresponds to exactly one relevant eigenvector. So, if a matrix $\mathscr{M}$ is cyclic its Jordan canonical form $\mathscr{J}_{\mathscr{M}}$ is completely determined by its *characteristic polynomial* $\chi(s) = \det\{s\mathbb{I}_4 - \mathscr{M}\}$ where $\mathbb{I}_4$ is the 4×4 identity matrix. Namely, as shown in Equation (4.1), every eigenvalue s_0 of multiplicity 2 is associated with the single Jordan block $J(s_0)$ in the Jordan canonical form $\mathscr{J}_{\mathscr{M}}$. Therefore, the characteristic polynomial of a cyclic matrix $\mathscr{M}$ encodes all of the information regarding the Jordan canonical form $\mathscr{J}_{\mathscr{M}}$.

Another important property of any cyclic matrix $\mathscr{M}$ associated with the monic polynomial χ is that it is similar to the so-called companion matrix C_χ defined by a simple explicit expression involving the coefficients of the polynomial χ (see Appendix B of [86]). The

companion matrix C_χ is directly related to the high-order differential equation $\chi(\partial_t)\, x(t) = 0$, where $x(t)$ is a complex-valued function of t (see Appendices B and D of [86]). As a result, the cyclicity property is relevant to the evolution of simpler systems described by higher order differential equations for scalar functions. Accordingly, we focus here on cyclic Hamiltonian matrices $\mathscr{H}$ because they lead to the simplest conservative circuits with evolution matrices $\mathscr{H}$ having nontrivial Jordan canonical forms $\mathscr{J}$.

Let us assume that the Jordan canonical form $\mathscr{J}$ is a matrix subject to the Hamiltonian spectral symmetry and cyclicity conditions. For the two-loop circuit we have $\chi(s) = \det\{s\mathbb{I}_4 - \mathscr{J}\}$ which is an even monic polynomial of the degree 4. Then, we consider the companion to $\chi(s)$ matrix $\mathscr{C}$ (see Appendix B of [86]), that is

$$\mathscr{C} = \mathscr{Y}\, \mathscr{J}\, \mathscr{Y}^{-1}, \tag{4.4}$$

where the columns of matrix $\mathscr{Y}$ comprise the Jordan basis of the companion matrix $\mathscr{C}$ associated with the characteristic polynomial $\chi(s)$. We introduce our principal Hamiltonian $\mathcal{H}$ and recover from it 4×4 Hamiltonian matrix $\mathscr{H}$ that governs the system evolution according to Equation (4.2). Due to our specific choice of the Hamiltonian $\mathcal{H}$ the corresponding to it Hamiltonian matrix $\mathscr{H}$ is similar to the companion matrix $\mathscr{C}$ and consequently they have exactly the same Jordan canonical form. So, we construct 4×4 matrix $\mathscr{T}$ such that

$$\mathscr{C} = \mathscr{T}^{-1}\mathscr{H}\,\mathscr{T}, \quad \mathscr{H} = \mathscr{Z}\, \mathscr{J}\, \mathscr{Z}^{-1}, \quad \mathscr{Z} = \mathscr{T}\mathscr{Y}, \tag{4.5}$$

where the columns of matrix $\mathscr{Z}$ comprise the Jordan basis of the evolution matrix $\mathscr{H}$.

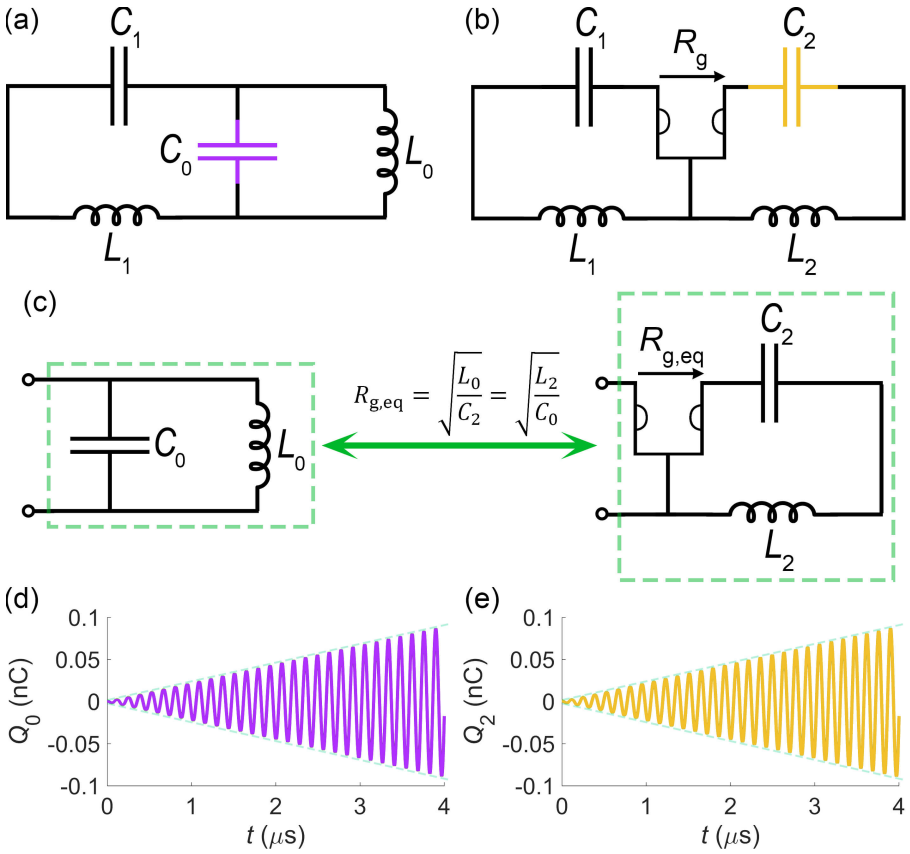

Figure 4.2: Comparison between (a) the 4-element reciprocal circuit (the focus of this chapter), also denoted as PRC, and (b) the 5-element nonreciprocal circuit that uses a gyrator as a nonreciprocal element, also denoted as GNC. (c) Equivalent resonators with the equivalency value of gyration resistance $R_{\text{g,eq}} = \sqrt{L_0/C_2} = \sqrt{L_2/C_0}$. Stored charges calculated by time-domain circuit simulator in (d) the capacitor of the PRC C_0 and (e) the capacitor of the GNC C_2 under the both EPD and equivalency conditions. Furthermore, the envelope of the charge signals shows linear growth over time, which is a distinguishing characteristic of second-order EPDs.

4.3 Review of the Main Results

We advance here a perfectly conservative circuit without a gyrator which has an EPD and consequently a nontrivial Jordan canonical form. This circuit is shown in Figure 4.2(a) and we will refer to it as a *principle reciprocal circuit* (PRC) or simply a *reciprocal circuit* in the rest of the chapter. The circuit has only four elements which are all lossless and reciprocal. The nontrivial Jordan canonical form is already obtained in the *gyrator-based nonreciprocal circuit* (GNC) which has a nonreciprocal element [86, 87, 110, 142], as shown in Figure 4.2(b).

Table 4.1: List of component and required conditions for equivalent reciprocal and nonreciprocal circuits.

	4-Element*	5-Element†	Equivalency
Capacitance - left loop	C_1	C_1	
Inductance - left loop	L_1	L_1	$L_1C_1 = L_1C_1$
Capacitance - right loop	C_0	C_2	
Inductance - right loop	L_0	L_2	$L_2C_2 = L_0C_0$
Gyrator	None	R_{g}	$R_{\mathrm{g,eq}} = \sqrt{\frac{L_0}{C_2}} = \sqrt{\frac{L_2}{C_0}}$

* 4-Element: Principal reciprocal circuit
† 5-Element: Gyrator-based nonreciprocal circuit

We define the nonreciprocity property in the Lagrangian as explained in Definition 1. The list of components for reciprocal and nonreciprocal circuits and the necessary conditions to pick the equivalency value of gyration resistance is summarized in Table 4.1. The list of our main achievements that are elaborated in the rest of the chapter is as follows:

- *Construction of a reciprocal and lossless circuit with an EPD.* We prove that the nontrivial Jordan canonical form can be obtained in a circuit without a gyrator (see Section 4.4).

- *PRC can have exactly the same Jordan canonical form as GNC and we find conditions for this to occur.* If we consider the gyration resistance value of $R_{\mathrm{g,eq}}$ (see Figure 4.2(c)), the reciprocal and nonreciprocal circuits can have the same Jordan canonical forms implying that the eigenvalues of both circuits are the same. We conducted numerical simulations of PRC and GNC using a commercial time-domain circuit simulator for comparison. In particular, we observe the charge stored in the capacitor associated with right loops as shown in Figures 4.2(d) and (e) for reciprocal (C_0) and nonreciprocal (C_2) circuits, respectively. There is excellent agreement between numerical simulations when the above condition of equivalency is satisfied (see Sections 4.9 and 4.10).

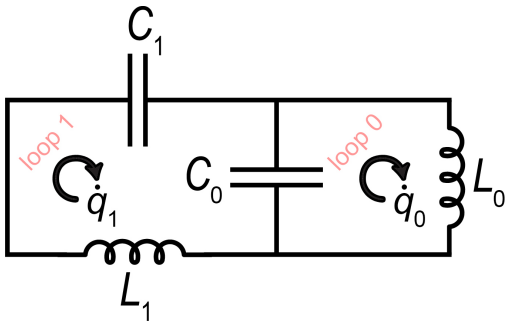

Figure 4.3: The principal two-loop circuit with reciprocal and lossless elements. For particular choices of values for quantities L_1, C_1, L_0, and C_0, the evolution matrix of the circuit develops second-order degeneracy, and its nontrivial Jordan canonical form consists of exactly two Jordan blocks of size 2. In this circuit, it is possible to replace C_0 and L_0 with each other since they are parallel. It is noteworthy that the zeroth loop and the first loop serve different purposes, with the capacitance C_0 being shared within the loops to couple them together.

- *Our analysis of the spectral data shows that nonreciprocity in the GNC is manifested in the breakdown of certain symmetries for the set of eigenvectors while this symmetry exists for PRC.* The nonreciprocity is also manifested in the circuit Lagrangian. Despite this, nonreciprocity is not captured by analyzing the eigenvalues or the Jordan canonical form of the circuit matrix (see Section 4.8).

Definition 1 (Nonreciprocity)**.** The concept of nonreciprocity has many definitions, each of which emphasizes one aspect of it. Nonreciprocity in Lagrangian equations occurs when the Lagrangian is not symmetric with respect to time [118]. The terms in the Lagrangian that depend on velocities (currents) $\partial_t \mathrm{q}$ *can* introduce nonreciprocal behavior. If the Lagrangian does not exhibit time-reversal symmetry, meaning it behaves differently when time is reversed ($t \to -t$), then the system's dynamics are nonreciprocal [118]. This can occur if there are terms in the Lagrangian that explicitly break this symmetry. It follows that if $x\,(t)$ is the solution of the nonreciprocal system, then $x\,(-t)$ is not its solution [118].

4.4 Principal Reciprocal Circuit

We advance here our proposed simple reciprocal circuit with a circuit matrix having the nontrivial Jordan canonical form without the need for gyrator. Figure 4.3 shows the PRC made of two fundamental loops connected directly. In this circuit, quantities L_j and C_j ($j = 0, 1$) are respectively inductance and capacitance of the corresponding loops. The *Lagrangian* associated with PRC displayed in Figure 4.3 is expressed by

$$\mathcal{L}_{\mathrm{r}}\left(\mathrm{q_r}, \partial_t \mathrm{q_r}\right)\big|_{\Theta_{\mathrm{r}}} = \frac{L_1\left(\partial_t q_1\right)^2}{2} + \frac{L_0\left(\partial_t q_0\right)^2}{2} - \frac{\left(q_1\right)^2}{2C_1} - \frac{\left(q_1 - q_0\right)^2}{2C_0}, \tag{4.6a}$$

$$q_j\left(t\right) = \int^t i_j\left(t'\right)\,\mathrm{d}t', \quad j = 0, 1, \tag{4.6b}$$

where q_j and i_j are the charges and the currents associated with loops of the PRC depicted in Figure 4.3 and $\Theta_{\mathrm{r}} = \{L_1, L_0, C_1, C_0\}$ is the set of circuit's parameters. We introduce a vector of charges as $\mathrm{q_r} = \left[q_1, q_0\right]^{\mathrm{T}}$ (T denotes the transpose operator) that composed of the charges associated with two fundamental loops. According to time reversal symmetry in reciprocal systems, the Lagrangian associated with the PRC depicted in Figure 4.3 has the property $\mathcal{L}_{\mathrm{r}}\left(\mathrm{q_r}, \partial_t \mathrm{q_r}\right) = \mathcal{L}_{\mathrm{r}}\left(\mathrm{q_r}, -\partial_t \mathrm{q_r}\right)$. The reciprocity principle and features of the Lagrangian of reciprocal circuits will be further examined in Subsection 4.8.1. The corresponding *Euler-Lagrange* equations of the PRC are given by

$$\frac{d}{dt}\left(\frac{\partial}{\partial \dot{q}_1}\mathcal{L}_{\mathrm{r}}\right) - \frac{\partial}{\partial q_1}\mathcal{L}_{\mathrm{r}} = 0, \tag{4.7a}$$

$$\frac{d}{dt}\left(\frac{\partial}{\partial \dot{q}_0}\mathcal{L}_{\mathrm{r}}\right) - \frac{\partial}{\partial q_0}\mathcal{L}_{\mathrm{r}} = 0, \tag{4.7b}$$

which are simplified in the form of

$$L_1\ddot{q}_1 + \left(\frac{1}{C_1} + \frac{1}{C_0}\right) q_1 - \frac{1}{C_0} q_0 = 0, \tag{4.8a}$$

$$L_0\ddot{q}_0 - \frac{1}{C_0} q_1 + \frac{1}{C_0} q_0 = 0. \tag{4.8b}$$

It is well known that the Euler-Lagrange formulations of Equations (4.8a) and (4.8b) represent the Kirchhoff voltage law for each of the two fundamental loops. The Kirchhoff voltage equations for the PRC are calculated in Subsection 4.4.1. Accordingly, each term in Equations (4.8a) and (4.8b) corresponds to the voltage drop of the relevant element, as can be seen from the current-voltage relations reviewed in Appendix D.

The circuit vector evolution equation by using the state vector of $\mathsf{q}_{\mathrm{r}} = [\mathrm{q}_{\mathrm{r}}, \partial_t \mathrm{q}_{\mathrm{r}}]^{\mathrm{T}}$ is given by

$$\partial_t \mathsf{q}_{\mathrm{r}} = \mathscr{C}_{\mathrm{r}} \mathsf{q}_{\mathrm{r}}, \quad \mathscr{C}_{\mathrm{r}} = \begin{bmatrix} 0 & 0 & 1 & 0 \\ 0 & 0 & 0 & 1 \\ -\left(\frac{1}{L_1 C_1} + \frac{1}{L_1 C_0}\right) & \frac{1}{L_1 C_0} & 0 & 0 \\ \frac{1}{L_0 C_0} & -\frac{1}{L_0 C_0} & 0 & 0 \end{bmatrix}, \tag{4.9}$$

where $\mathscr{C}_{\mathrm{r}}$ is the circuit matrix corresponding to the PRC. The characteristic polynomial related to the matrix $\mathscr{C}_{\mathrm{r}}$ defined by Equation (4.9) is expressed by

$$\chi_{\mathrm{r}}(s) = \det\{s\mathbb{I}_4 - \mathscr{C}_{\mathrm{r}}\} = s^4 + s^2(\xi_1 + \xi_0 + \delta) + \xi_1\xi_0 = 0, \tag{4.10}$$

where the loop resonance frequencies are defined as

$$\delta = \frac{1}{L_1 C_0}, \quad \xi_0 = \frac{1}{L_0 C_0}, \quad \xi_1 = \frac{1}{L_1 C_1}. \tag{4.11}$$

In the above equations, $\sqrt{\zeta_0}$ indicates the resonance frequency of the zeroth loop, $\sqrt{\zeta_1}$ indicates the resonance frequency of the first loop and $\sqrt{\delta}$ is defined as a cross loop resonance frequency or coupling term. We demonstrate the following properties in the structure of the characteristic polynomial: (i) the characteristic polynomial is a quadratic equation in s^2, so if s is the solution of the characteristic polynomial then $-s$ is its solution as well; (ii) the coefficients of the characteristic polynomial are real; hence s and s^* (* denotes the complex conjugate operation) are both solutions of the characteristic polynomial. Note that using circuit resonance frequencies defined in Equation (4.11), we recast the circuit matrix $\mathscr{C}_{\mathrm{r}}$ in Equation (4.9) as below

$$\mathscr{C}_{\mathrm{r}} = \begin{bmatrix} 0 & 0 & 1 & 0 \\ 0 & 0 & 0 & 1 \\ -\xi_1 - \delta & \delta & 0 & 0 \\ \xi_0 & -\xi_0 & 0 & 0 \end{bmatrix}, \tag{4.12}$$

which shows that matrix $\mathscr{C}_{\mathrm{r}}$ defined by Equation (4.12) is a block off-diagonal matrix.

4.4.1 Kirchoff's Equations of the Principal Reciprocal Circuit

The following is a concise review of the fundamental equations of the circuit shown in Figure 4.3 based on Kirchhoff's laws. According to Kirchhoff's voltage law in the two fundamental loops of the PRC we have

$$\ddot{q}_1 + \left(\frac{1}{L_1C_1} + \frac{1}{L_1C_0}\right) q_1 - \left(\frac{1}{L_1C_0}\right) q_0 = 0, \tag{4.13a}$$

$$\ddot{q}_0 - \left(\frac{1}{L_0C_0}\right) q_1 + \frac{1}{L_0C_0} q_0 = 0. \tag{4.13b}$$

Then, the circuit vector evolution equation and the eigenvalue problem are expressed as

$$\partial_t \mathsf{q}_\mathrm{r} = \mathscr{C}\,\mathsf{q}_\mathrm{r}, \quad \mathscr{C}_\mathrm{r} = \begin{bmatrix} 0 & 0 & 1 & 0 \\ 0 & 0 & 0 & 1 \\ -\left(\frac{1}{L_1C_1} + \frac{1}{L_1C_0}\right) & \frac{1}{L_1C_0} & 0 & 0 \\ \frac{1}{L_0C_0} & -\frac{1}{L_0C_0} & 0 & 0 \end{bmatrix}, \quad \mathsf{q}_\mathrm{r} = \begin{bmatrix} \mathrm{q}_\mathrm{r} \\ \partial_t \mathrm{q}_\mathrm{r} \end{bmatrix}, \quad \mathrm{q}_\mathrm{r} = \begin{bmatrix} q_1 \\ q_0 \end{bmatrix}, \tag{4.14}$$

which is in full agreement with circuit vector evolution equation calculated by the Euler-Lagrange formulation in Equation (4.9).

4.5 The Jordan Canonical Form of the Principal Reciprocal Circuit

We studied the PRC composed of two loops, as shown in Figure 4.3, without putting any constraints on the circuit parameters L_1, C_1, L_0, and C_0 except that they are all real and non-zero. In this section, we derive the most general conditions on the circuit parameters under which the relevant evolution matrix shows nontrivial Jordan blocks. The Lagrangian equation for the PRC is given by Equation (4.6a), and its evolution equations are the corresponding Euler-Lagrange equations:

$$s^2 q_1 + (\xi_1 + \delta)\, q_1 - \delta q_0 = 0, \tag{4.15a}$$

$$s^2 q_0 - \xi_0 q_1 + \xi_0 q_0 = 0. \tag{4.15b}$$

The Euler-Lagrange equations are readily recast in the below matrix form,

$$\mathrm{A_r}\,(s)\,\mathrm{q_r} = 0, \quad \mathrm{A_r}\,(s) = \begin{bmatrix} s^2 + \xi_1 + \delta & -\delta \\ -\xi_0 & s^2 + \xi_0 \end{bmatrix}, \tag{4.16}$$

where $\mathrm{A_r}\,(s)$ is a 2×2 monic matrix polynomial of s of degree 2, namely,

$$\mathrm{A_r}\,(s) = \sum_{j=0}^{2} s^j \mathrm{A_{r,}}_j = s^2 \mathrm{A_{r,2}} + s\mathrm{A_{r,1}} + \mathrm{A_{r,0}}, \tag{4.17a}$$

$$\mathrm{A}_{\mathrm{r},2} = \begin{bmatrix} 1 & 0 \\ \\ 0 & 1 \end{bmatrix}, \quad \mathrm{A}_{\mathrm{r},1} = \begin{bmatrix} 0 & 0 \\ \\ 0 & 0 \end{bmatrix}, \quad \mathrm{A}_{\mathrm{r},0} = \begin{bmatrix} \xi_1 + \delta & -\delta \\ \\ -\xi_0 & \xi_0 \end{bmatrix}. \tag{4.17b}$$

Then, Equation (4.16) is reduced to the standard first-order vector differential equation

$$s\mathsf{q}_{\mathrm{r,s}} = \mathscr{C}_{\mathrm{r}}\mathsf{q}_{\mathrm{r,s}}, \quad \mathsf{q}_{\mathrm{r,s}} = \begin{bmatrix} \mathrm{q}_{\mathrm{r}} \\ \\ s\mathrm{q}_{\mathrm{r}} \end{bmatrix}, \quad \mathscr{C}_{\mathrm{r}} = \begin{bmatrix} 0 & 0 & 1 & 0 \\ \\ 0 & 0 & 0 & 1 \\ \\ -\xi_1 - \delta & \delta & 0 & 0 \\ \\ \xi_0 & -\xi_0 & 0 & 0 \end{bmatrix}, \tag{4.18}$$

where $\mathscr{C}_{\mathrm{r}}$ is the 4×4 companion matrix for the matrix polynomial $\mathrm{A}_{\mathrm{r}}(s)$. The standard eigenvalue problem is expressed as

$$(s\mathbb{I}_4 - \mathscr{C}_{\mathrm{r}})\,\mathsf{q}_{\mathrm{r,s}} = 0. \tag{4.19}$$

Then, the characteristic polynomial of the matrix polynomial $\mathrm{A}_{\mathrm{r}}(s)$ is

$$\chi_{\mathrm{r}}(s) = \det\{\mathrm{A}_{\mathrm{r}}(s)\} = s^4 + s^2(\xi_1 + \xi_0 + \delta) + \xi_1\xi_0. \tag{4.20}$$

Consequently, the characteristic polynomial $\chi_{\mathrm{r}}(s) = 0$ can be used to calculate the eigenvalues associated with Equation (4.19). We aim in this chapter to find all non-zero and real values of the circuit parameters L_1, C_1, L_0 and C_0 that lead to the matrix $\mathscr{C}_{\mathrm{r}}$ defined by Equation (4.18) having a nontrivial Jordan canonical form.

4.5.1 Characteristic Polynomial and Eigenvalue Degeneracy

We present here the condition for degenerate eigenvalues in the characteristic polynomial. We rewrite the characteristic polynomial associated with the PRC matrix as

$$\chi_{\mathrm{r}}(h) = h^2 + h(\xi_1 + \xi_0 + \delta) + \xi_1\xi_0 = 0, \quad h = s^2. \tag{4.21}$$

A quadratic equation in h, $\chi_{\mathrm{r}}(h) = 0$, has exactly two solutions, viz,

$$h_{\pm} = \frac{-(\xi_1 + \xi_0 + \delta) \pm \sqrt{\Delta_{\mathrm{r},h}}}{2}, \tag{4.22}$$

where $\Delta_{\mathrm{r},h} = \delta^2 + 2\delta(\xi_1 + \xi_0) + (\xi_1 - \xi_0)^2$ is the discriminant of the quadratic in the characteristic polynomial of Equation (4.21). The four solutions of the characteristic polynomial $\chi_{\mathrm{r}}(s) = 0$, i.e., eigenvalues, are as follows:

$$s = \pm\sqrt{h_+}, \pm\sqrt{h_-}. \tag{4.23}$$

Note that the eigenvalue degeneracy condition turns into $\Delta_{\mathrm{r},h} = 0$, which is equivalently expressed as

$$\delta^2 + 2\delta(\xi_1 + \xi_0) + (\xi_1 - \xi_0)^2 = 0. \tag{4.24}$$

Equation (4.24) is a quadratic equation which has exactly two solutions. We refer to solutions of δ in Equation (4.24) as *special values of degeneracy* $\delta_{\mathrm{d},\pm}$, where these two solutions are

$$\delta_{\mathrm{d},\pm} = -\xi_1 - \xi_0 \pm 2\sqrt{\xi_1\xi_0}. \tag{4.25}$$

For the two special values of degeneracy $\delta_{\mathrm{d},\pm}$ we get from Equation (4.22) the corresponding two degenerate roots of h are given by

$$h_{\mathrm{d},\pm} = -\frac{\xi_1 + \xi_0 + \delta_{\mathrm{d},\pm}}{2} = \mp\sqrt{\xi_1 \xi_0}. \tag{4.26}$$

The expression of Equation (4.25) is real-valued if and only if $\xi_1 \xi_0 > 0$, or equivalently

$$\frac{\xi_0}{|\xi_0|} = \frac{\xi_1}{|\xi_1|} = \pm 1. \tag{4.27}$$

Equation (4.27) implies that the equality of resonance frequencies sign, $\mathrm{sign}\,(\xi_0) = \mathrm{sign}\,(\xi_1)$, is a necessary condition for the eigenvalue degeneracy condition $\Delta_{\mathrm{r},h} = 0$ provided that $\delta_{\mathrm{d},\pm}$ has to be real-valued. From Equations (4.25) and (4.27), it follows that the special values of degeneracy $\delta_{\mathrm{d},\pm}$ can be expressed as $\delta_{\mathrm{d},\pm} = -\left(\sqrt{\xi_1} \mp \sqrt{\xi_0}\right)^2$.

Theorem 1 (Nontrivial Jordan canonical form of the companion matrix)**.** *Let's assume that s_0 is an eigenvalue of the companion matrix $\mathscr{C}_{\mathrm{r}}$ given in Equation (4.18) such that its algebraic multiplicity $m\,(s_0) = 2$. Then (i) $s_0 \neq 0$; (ii) s_0 is either purely real or purely imaginary; (iii) $-s_0$ is also an eigenvalue of the companion matrix $\mathscr{C}_{\mathrm{r}}$; (iv) $m\,(s_0) = m\,(-s_0) = 2$; and (v) the nontrivial Jordan canonical form of the companion matrix $\mathscr{C}_{\mathrm{r}}$ is expressed as*

$$\mathscr{J}_{\mathrm{r}} = \begin{bmatrix} s_0 & 1 & 0 & 0 \\ 0 & s_0 & 0 & 0 \\ 0 & 0 & -s_0 & 1 \\ 0 & 0 & 0 & -s_0 \end{bmatrix}. \tag{4.28}$$

It follows that the eigenvalue degeneracy for the companion matrix $\mathscr{C}_{\mathrm{r}}$ implies that its Jordan canonical form $\mathscr{J}_{\mathrm{r}}$ has two Jordan blocks of size 2. A proof of this theorem can be found in

[86].

4.5.2 Eigenvectors and the Jordan Basis

Theorem 1 states that the degeneracy of eigenvalues in the companion matrix $\mathscr{C}_{\mathrm{r}}$ given by Equation (4.18) implies that its Jordan canonical form consists of two Jordan blocks as in Equation (4.28). The Jordan canonical form corresponding to the companion matrix $\mathscr{C}_{\mathrm{r}}$ in the non-degenerate form, $\Delta_{\mathrm{r},h} \neq 0$, is expressed as

$$\mathscr{J}_{\mathrm{r}} = \begin{bmatrix} \mathrm{i}s_1 & 0 & 0 & 0 \\ 0 & -\mathrm{i}s_1 & 0 & 0 \\ 0 & 0 & \mathrm{i}s_2 & 0 \\ 0 & 0 & 0 & -\mathrm{i}s_2 \end{bmatrix}, \quad \begin{matrix} s_1 = \sqrt{\frac{\xi_{\mathrm{r,s}} + \sqrt{\Delta_{\mathrm{r},h}}}{2}} \\ s_2 = \sqrt{\frac{\xi_{\mathrm{r,s}} - \sqrt{\Delta_{\mathrm{r},h}}}{2}} \end{matrix}, \quad \xi_{\mathrm{r,s}} = \xi_1 + \xi_0 + \delta, \tag{4.29}$$

where $\xi_{\mathrm{r,s}}$ is the sum of three resonance frequencies square defined in Equation (4.11), $\Delta_{\mathrm{r},h}$ is the discriminant of the quadratic equation and $\pm\mathrm{i}s_i$ $(i = 1, 2)$ are the corresponding eigenvalues. Following this, we write eigenvectors corresponding to the calculated non-degenerate eigenvalues as follows:

$$\mathscr{V}_{\mathrm{r}} = \left[\mathsf{e}_{\mathrm{r},+s_1} | \mathsf{e}_{\mathrm{r},-s_1} | \mathsf{e}_{\mathrm{r},+s_2} | \mathsf{e}_{\mathrm{r},-s_2}\right], \tag{4.30a}$$

$$\mathsf{e}_{\mathrm{r},\pm s_i} = \begin{bmatrix} \mp\frac{\left(-s_i^2\right)^{3/2}+(\xi_0+\delta)\sqrt{-s_i^2}}{\xi_1\xi_0} \\ \mp\frac{\left(-s_i^2\right)^{3/2}+\xi_{\mathrm{r,s}}\sqrt{-s_i^2}}{\xi_1\xi_0} \\ 1-\frac{s_i^2}{\xi_0} \\ 1 \end{bmatrix}. \tag{4.30b}$$

Next, we investigate two different cases with two special values of degeneracy $\delta_{\mathrm{d},\pm}$, which lead to degeneracy with purely imaginary or purely real degenerate eigenvalues.

Degeneracy With Purely Imaginary Eigenvalues (Purely Real Eigenfrequencies)

In the first case, if we consider $\delta = \delta_{\mathrm{d},+} = -\xi_1 - \xi_0 + 2\sqrt{\xi_1\xi_0}$, the characteristic polynomial is rewritten as

$$\chi_{\mathrm{r},+}(s) = s^4 + 2s^2\sqrt{\xi_1\xi_0} + \xi_1\xi_0 = \left(s^2 + \sqrt{\xi_1\xi_0}\right)^2 = 0. \tag{4.31}$$

Then, the degenerate companion matrix $\mathscr{C}_{\mathrm{r},+}$ for this degenerate case is given by

$$\mathscr{C}_{\mathrm{r},+} = \begin{bmatrix} 0 & 0 & 1 & 0 \\ 0 & 0 & 0 & 1 \\ -\xi_1-\delta_{\mathrm{d},+} & \delta_{\mathrm{d},+} & 0 & 0 \\ \xi_0 & -\xi_0 & 0 & 0 \end{bmatrix}, \tag{4.32}$$

and the Jordan canonical form of the degenerate companion matrix $\mathscr{C}_{\mathrm{r},+}$ with purely imaginary eigenvalues (purely real eigenfrequencies) is expressed as

$$\mathscr{J}_{\mathrm{r},+} = \begin{bmatrix} \mathrm{i}s_{\mathrm{e}} & 1 & 0 & 0 \\ 0 & \mathrm{i}s_{\mathrm{e}} & 0 & 0 \\ 0 & 0 & -\mathrm{i}s_{\mathrm{e}} & 1 \\ 0 & 0 & 0 & -\mathrm{i}s_{\mathrm{e}} \end{bmatrix}, \quad s_{\mathrm{e}} = (\xi_{\mathrm{e}})^{\frac{1}{2}} = (\xi_0\xi_1)^{\frac{1}{4}}. \tag{4.33}$$

As a result, the Jordan basis of the degenerate companion matrix $\mathscr{C}_{\mathrm{r},+}$ is obtained as follows:

$$\mathscr{Z}_{\mathrm{r},+} = \begin{bmatrix} \frac{\xi_0-\xi_{\mathrm{e}}}{4\mathrm{i}\sqrt{\xi_{\mathrm{e}}}} & \frac{1}{2} & \frac{-\xi_0+\xi_{\mathrm{e}}}{4\mathrm{i}\sqrt{\xi_{\mathrm{e}}}} & \frac{1}{2} \\ \frac{\xi_0}{4\mathrm{i}\sqrt{\xi_{\mathrm{e}}}} & 0 & -\frac{\xi_0}{4\mathrm{i}\sqrt{\xi_{\mathrm{e}}}} & 0 \\ \frac{\xi_0(\xi_{\mathrm{e}}-\xi_1)}{4\xi_{\mathrm{e}}} & \frac{\xi_0(\xi_{\mathrm{e}}-3\xi_1)}{4\mathrm{i}\xi_{\mathrm{e}}\sqrt{\xi_{\mathrm{e}}}} & \frac{\xi_0(\xi_{\mathrm{e}}-\xi_1)}{4\xi_{\mathrm{e}}} & -\frac{\xi_0(\xi_{\mathrm{e}}-3\xi_1)}{4\mathrm{i}\xi_{\mathrm{e}}\sqrt{\xi_{\mathrm{e}}}} \\ -\frac{\xi_0^2(2\xi_1-\xi_{\mathrm{e}})}{4\xi_{\mathrm{e}}(\xi_0-2\xi_{\mathrm{e}})} & -\frac{\xi_0^2(2\xi_1-\xi_{\mathrm{e}})}{4\mathrm{i}\xi_{\mathrm{e}}\sqrt{\xi_{\mathrm{e}}}(\xi_0-2\xi_{\mathrm{e}})} & -\frac{\xi_0^2(2\xi_1-\xi_{\mathrm{e}})}{4\xi_{\mathrm{e}}(\xi_0-2\xi_{\mathrm{e}})} & \frac{\xi_0^2(2\xi_1-\xi_{\mathrm{e}})}{4\mathrm{i}\xi_e\sqrt{\xi_{\mathrm{e}}}(\xi_0-2\xi_{\mathrm{e}})} \end{bmatrix}. \tag{4.34}$$

Note that the columns of matrix $\mathscr{Z}_{\mathrm{r},+}$ form the Jordan bases of the corresponding degenerate companion matrix $\mathscr{C}_{\mathrm{r},+}$, and each column of $\mathscr{Z}_{\mathrm{r},+}$ are the generalized eigenvectors of the corresponding eigenvalues.

Degeneracy With Purely Real Eigenvalues (Purely Imaginary Eigenfrequencies)

In the second case, if we consider $\delta = \delta_{\mathrm{d},-} = -\xi_1 - \xi_0 - 2\sqrt{\xi_1\xi_0}$, the characteristic polynomial is given by

$$\chi_{\mathrm{r},-}(s) = s^4 - 2s^2\sqrt{\xi_1\xi_0} + \xi_1\xi_0 = \left(s^2 - \sqrt{\xi_1\xi_0}\right)^2 = 0. \tag{4.35}$$

The corresponding degenerate companion matrix $\mathscr{C}_{\mathrm{r},-}$ is expressed by

$$\mathscr{C}_{\mathrm{r},-} = \begin{bmatrix} 0 & 0 & 1 & 0 \\ 0 & 0 & 0 & 1 \\ -\xi_1 - \delta_{\mathrm{d},-} & \delta_{\mathrm{d},-} & 0 & 0 \\ \xi_0 & -\xi_0 & 0 & 0 \end{bmatrix}. \tag{4.36}$$

Moreover, the Jordan canonical form of the corresponding degenerate companion matrix $\mathscr{C}_{\mathrm{r},-}$ in Equation (4.36) with purely real eigenvalues (purely imaginary eigenfrequencies) is written as

$$\mathscr{J}_{\mathrm{r},-} = \begin{bmatrix} s_{\mathrm{e}} & 1 & 0 & 0 \\ 0 & s_{\mathrm{e}} & 0 & 0 \\ 0 & 0 & -s_{\mathrm{e}} & 1 \\ 0 & 0 & 0 & -s_{\mathrm{e}} \end{bmatrix}. \tag{4.37}$$

Then, the Jordan basis of the degenerate companion matrix $\mathscr{C}_{\mathrm{r},-}$ is expressed as

$$\mathscr{Z}_{\mathrm{r},-} = \begin{bmatrix} \frac{\xi_0+\xi_\mathrm{e}}{4\sqrt{\xi_\mathrm{e}}} & \frac{1}{2} & -\frac{\xi_0+\xi_\mathrm{e}}{4\sqrt{\xi_\mathrm{e}}} & \frac{1}{2} \\ \frac{\xi_0}{4\sqrt{\xi_\mathrm{e}}} & 0 & -\frac{\xi_0}{4\sqrt{\xi_\mathrm{e}}} & 0 \\ \frac{\xi_0(\xi_\mathrm{e}+\xi_1)}{4\xi_\mathrm{e}} & \frac{\xi_0(\xi_\mathrm{e}+3\xi_1)}{4\xi_\mathrm{e}\sqrt{\xi_\mathrm{e}}} & \frac{\xi_0(\xi_\mathrm{e}+\xi_1)}{4\xi_\mathrm{e}} & -\frac{\xi_0(\xi_\mathrm{e}+3\xi_1)}{4\xi_\mathrm{e}\sqrt{\xi_\mathrm{e}}} \\ \frac{\xi_0^2(2\xi_1+\xi_\mathrm{e})}{4\xi_\mathrm{e}(\xi_0+2\xi_\mathrm{e})} & \frac{\xi_0^2(2\xi_1+\xi_\mathrm{e})}{4\xi_\mathrm{e}\sqrt{\xi_\mathrm{e}}(\xi_0+2\xi_\mathrm{e})} & \frac{\xi_0^2(2\xi_1+\xi_\mathrm{e})}{4\xi_\mathrm{e}(\xi_0+2\xi_\mathrm{e})} & -\frac{\xi_0^2(2\xi_1+\xi_\mathrm{e})}{4\xi_\mathrm{e}\sqrt{\xi_\mathrm{e}}(\xi_0+2\xi_\mathrm{e})} \end{bmatrix}. \tag{4.38}$$

4.6 Lagrangian and Hamiltonian Structures and Their Relation

In this section we provide a general overview of the Lagrangian and Hamiltonian structures. We explain the relationship between these two structures in detail. Then, we demonstrate the Lagrangian and Hamiltonian structures for the PRC. Ultimately, readers will gain a comprehensive understanding of these mathematical frameworks and their applicability to studying systems like the PRC.

4.6.1 Lagrangian Structure

The Lagrangian for a linear system in the general form is a quadratic function (bilinear form) of the circuit state vector $\check{\mathrm{q}}$ (column vector that contains charges) and its time derivatives $\partial_t\check{\mathrm{q}}$, that is

$$\mathcal{L} = \mathcal{L}\left(\check{\mathrm{q}}, \partial_t \check{\mathrm{q}}\right) = \frac{1}{2} \begin{bmatrix} \check{\mathrm{q}} \\ \\ \partial_t \check{\mathrm{q}} \end{bmatrix}^{\mathrm{T}} \mathrm{M_L} \begin{bmatrix} \check{\mathrm{q}} \\ \\ \partial_t \check{\mathrm{q}} \end{bmatrix}, \quad \mathrm{M_L} = \begin{bmatrix} -\eta & \theta^{\mathrm{T}} \\ \\ \theta & \alpha \end{bmatrix}, \tag{4.39}$$

where α, η and θ are 2×2 matrices (for our two-loops circuit) with real-valued entries. Moreover, we assume symmetric matrices, that is $\alpha = \alpha^{\mathrm{T}}$ and $\eta = \eta^{\mathrm{T}}$. Accordingly, we have the Lagrangian,

$$\mathcal{L} = \frac{1}{2} \partial_t \check{\mathrm{q}}^{\mathrm{T}} \alpha \partial_t \check{\mathrm{q}} + \partial_t \check{\mathrm{q}}^{\mathrm{T}} \theta \check{\mathrm{q}} - \frac{1}{2} \check{\mathrm{q}}^{\mathrm{T}} \eta \check{\mathrm{q}}. \tag{4.40}$$

As a result of Hamilton's principle, the system evolution can be explained by the Euler-Lagrange equations as

$$\frac{d}{dt} \left(\frac{\partial \mathcal{L}}{\partial \dot{\check{q}}} \right) - \frac{\partial \mathcal{L}}{\partial \check{\mathrm{q}}} = 0, \tag{4.41}$$

which, based on Equation (4.40), it can be written in the following form of a second-order vector ordinary differential equation,

$$\alpha \partial_t^2 \check{\mathrm{q}} + \left(\theta - \theta^{\mathrm{T}}\right) \partial_t \check{\mathrm{q}} + \eta \check{\mathrm{q}} = 0. \tag{4.42}$$

It is notable that matrix θ appears in Equation (4.42) through its skew-symmetric component $\left(\theta - \theta^{\mathrm{T}}\right)/2$ justifying as a possibility to impose the skew-symmetry assumption on θ, that is $\theta^{\mathrm{T}} = -\theta$. Then, under the assumption of $\theta^{\mathrm{T}} = -\theta$, Equation (4.42) is rewritten with the skew-symmetric θ as

$$\alpha \partial_t^2 \check{\mathrm{q}} + 2\theta \partial_t \check{\mathrm{q}} + \eta \check{\mathrm{q}} = 0. \tag{4.43}$$

For the PRC that we introduced and analyzed in the previous sections, Equation (4.43) and the required coefficients by considering $\check{\mathrm{q}} = \mathrm{q_r} = [q_1, q_0]^{\mathrm{T}}$ are rewritten as

$$\alpha_{\mathrm{r}} \partial_t^2 \mathrm{q_r} + 2\theta_{\mathrm{r}} \partial_t \mathrm{q_r} + \eta_{\mathrm{r}} \mathrm{q_r} = 0, \tag{4.44a}$$

$$\alpha_{\mathrm{r}} = \begin{bmatrix} L_1 & 0 \\ 0 & L_0 \end{bmatrix}, \quad \theta_{\mathrm{r}} = \begin{bmatrix} 0 & 0 \\ 0 & 0 \end{bmatrix}, \quad \eta_{\mathrm{r}} = \begin{bmatrix} \frac{1}{C_1} + \frac{1}{C_0} & -\frac{1}{C_0} \\ -\frac{1}{C_0} & \frac{1}{C_0} \end{bmatrix}. \tag{4.44b}$$

We write the Lagrangian formulation in the below form:

$$\mathcal{L}_{\mathrm{r}}\left(\mathrm{q_r}, \partial_t \mathrm{q_r}\right) = \frac{1}{2} \begin{bmatrix} \mathrm{q_r} \\ \partial_t \mathrm{q_r} \end{bmatrix}^{\mathrm{T}} \mathrm{M_{L,r}} \begin{bmatrix} \mathrm{q_r} \\ \partial_t \mathrm{q_r} \end{bmatrix}, \tag{4.45a}$$

$$\mathrm{M_{L,r}} = \begin{bmatrix} -\frac{1}{C_1} - \frac{1}{C_0} & \frac{1}{C_0} & 0 & 0 \\ \frac{1}{C_0} & -\frac{1}{C_0} & 0 & 0 \\ 0 & 0 & L_1 & 0 \\ 0 & 0 & 0 & L_0 \end{bmatrix}. \tag{4.45b}$$

It follows from Equation (4.42) that the necessary and sufficient condition for nonreciprocity is $\theta \neq \theta^{\mathrm{T}}$. Indeed, if $\theta = \theta^{\mathrm{T}}$, the circuit will not show nonreciprocity properties. Because in the case of $\theta = \theta^{\mathrm{T}}$, the second term with $\partial_t \mathrm{q}$ disappears from Equation (4.42) and all frequencies related to Equation (4.42) will be the same as in the case of zero θ which leads to time symmetry.

4.6.2 Hamiltonian

Alternatively, we can use the Hamilton equations associated with the Hamiltonian $\mathcal{H}$ instead of the second-order vector ordinary differential equations of Equation (4.42). Let us assume

that the circuit's state is described by a time-dependent column vector $\check{\mathrm{q}}$ and its dynamic is governed by a Hamiltonian $\mathcal{H} = \mathcal{H}(\check{\mathrm{p}}, \check{\mathrm{q}})$, where $\check{\mathrm{p}}$ is the column vector system momentum. We introduce the Hamiltonian representation in order to describe the circuit information in the compact matrix form,

$$\mathcal{H} = \mathcal{H}(\check{\mathrm{p}}, \check{\mathrm{q}}) = \check{\mathrm{p}}^{\mathrm{T}} \partial_t \check{\mathrm{q}} - \mathcal{L}(\check{\mathrm{q}}, \partial_t \check{\mathrm{q}}), \tag{4.46}$$

where the system momentum $\check{\mathrm{p}}$ is given by

$$\check{\mathrm{p}} = \frac{\partial \mathcal{L}}{\partial \dot{\check{q}}} = \alpha \partial_t \check{\mathrm{q}} + \theta \check{\mathrm{q}}. \tag{4.47}$$

According to Equation (4.47), current $\partial_t \check{\mathrm{q}}$ (i.e., velocity of charges) and momentum $\check{\mathrm{p}}$ vectors are related as follows:

$$\partial_t \check{\mathrm{q}} = \alpha^{-1} (\check{\mathrm{p}} - \theta \check{\mathrm{q}}). \tag{4.48}$$

Consequently, the Hamiltonian $\mathcal{H}$ expressed in Equation (4.46) is given by

$$\mathcal{H}(\check{\mathrm{p}}, \check{\mathrm{q}}) = \frac{1}{2} \left[(\check{\mathrm{p}} - \theta \check{\mathrm{q}})^{\mathrm{T}} \alpha^{-1} (\check{\mathrm{p}} - \theta \check{\mathrm{q}}) + \check{\mathrm{q}}^{\mathrm{T}} \eta \check{\mathrm{q}} \right] = \frac{1}{2} \partial_t \check{\mathrm{q}}^{\mathrm{T}} \alpha \partial_t \check{\mathrm{q}} + \frac{1}{2} \check{\mathrm{q}}^{\mathrm{T}} \eta \check{\mathrm{q}}. \tag{4.49}$$

Also, Equations (4.46), (4.47) and (4.48) imply

$$\begin{bmatrix} \check{\mathrm{q}} \\ \check{\mathrm{p}} \end{bmatrix} = \begin{bmatrix} \mathbb{I}_2 & 0_2 \\ \theta & \alpha \end{bmatrix} \begin{bmatrix} \check{\mathrm{q}} \\ \partial_t \check{\mathrm{q}} \end{bmatrix}, \quad \begin{bmatrix} \check{\mathrm{q}} \\ \partial_t \check{\mathrm{q}} \end{bmatrix} = \begin{bmatrix} \mathbb{I}_2 & 0_2 \\ -\alpha^{-1} & \theta \alpha^{-1} \end{bmatrix} \begin{bmatrix} \check{\mathrm{q}} \\ \check{\mathrm{p}} \end{bmatrix}, \tag{4.50}$$

where $\mathbb{I}_2$ is the 2×2 identity matrix and 0_2 is the 2×2 zero matrix. We also know that Hamiltonian $\mathcal{H}$ can be interpreted as the energy of the system that is a conserved quantity, so $\partial_t \mathcal{H}(\check{\mathrm{p}}, \check{\mathrm{q}}) = 0$. The function $\mathcal{H}(\check{\mathrm{p}}, \check{\mathrm{q}})$ defined by Equation (4.49) can be recast into the

following form of Hamiltonian

$$\mathcal{H}\left(\check{\mathrm{p}},\check{\mathrm{q}}\right)=\frac{1}{2}\begin{bmatrix}\check{\mathrm{q}}\\ \\ \check{\mathrm{p}}\end{bmatrix}^{\mathrm{T}}\mathrm{M_H}\begin{bmatrix}\check{\mathrm{q}}\\ \\ \check{\mathrm{p}}\end{bmatrix}, \tag{4.51}$$

where the matrix $\mathrm{M_H}$ is 4×4 with the below block form

$$\mathrm{M_H}=\begin{bmatrix}\theta^{\mathrm{T}}\alpha^{-1}\theta+\eta & -\theta^{\mathrm{T}}\alpha^{-1}\\ \\ -\alpha^{-1}\theta & \alpha^{-1}\end{bmatrix}=\begin{bmatrix}\mathbb{I}_2 & -\theta^{\mathrm{T}}\\ \\ 0_2 & \mathbb{I}_2\end{bmatrix}\begin{bmatrix}\eta & 0_2\\ \\ 0_2 & \alpha^{-1}\end{bmatrix}\begin{bmatrix}\mathbb{I}_2 & 0_2\\ \\ -\theta & \mathbb{I}_2\end{bmatrix}, \tag{4.52}$$

and the required parameters in this matrix for the PRC are given in Equation (4.44b). Then, the matrix $\mathrm{M_H}$ for the PRC is expressed as

$$\mathrm{M_{H,r}}=\begin{bmatrix}\frac{1}{C_1}+\frac{1}{C_0} & -\frac{1}{C_0} & 0 & 0\\ \\ -\frac{1}{C_0} & \frac{1}{C_0} & 0 & 0\\ \\ 0 & 0 & \frac{1}{L_1} & 0\\ \\ 0 & 0 & 0 & \frac{1}{L_0}\end{bmatrix}. \tag{4.53}$$

Also, the system momentum in Equation (4.47) by considering $\check{\mathrm{q}}=\mathrm{q_r}=[q_1,q_0]^{\mathrm{T}}$ for the PRC is expressed by

$$\mathrm{p_r}=\frac{\partial\mathcal{L}_{\mathrm{r}}}{\partial\dot{\mathrm{q}}_{\mathrm{r}}}=\alpha_{\mathrm{r}}\partial_t\mathrm{q_r}+\theta_{\mathrm{r}}\mathrm{q_r}=\partial_t\mathrm{q_r}\begin{bmatrix}L_1 & 0\\ \\ 0 & L_0\end{bmatrix}. \tag{4.54}$$

As we observe in Equation (4.54), $\theta_{\mathrm{r}}=0$ for the reciprocal case, which demonstrates the relation between the *momentum* $\mathrm{p_r}$ and the *current* $\partial_t\mathrm{q_r}$ (i.e., velocity of charges) does

not depend on $\mathrm{q_r}$ and depends only on $\partial_t \mathrm{q_r}$. The Hamiltonian form of the Euler-Lagrange formulation of Equation (4.41) is given by

$$\partial_t \begin{bmatrix} \check{\mathrm{q}} \\ \\ \check{\mathrm{p}} \end{bmatrix} = \mathbb{J}\mathrm{M_H} \begin{bmatrix} \check{\mathrm{q}} \\ \\ \check{\mathrm{p}} \end{bmatrix}, \quad \mathbb{J} = \begin{bmatrix} 0_2 & \mathbb{I}_2 \\ \\ -\mathbb{I}_2 & 0_2 \end{bmatrix}, \tag{4.55}$$

where the matrix $\mathbb{J}$ has the properties of $\mathbb{J} = -\mathbb{J}^{\mathrm{T}} = -\mathbb{J}^{-1}$. Based on Equations (4.52) and (4.55), we write

$$\mathbb{J}\mathrm{M_H} = \begin{bmatrix} -\alpha^{-1}\theta & \alpha^{-1} \\ \\ -\theta^{\mathrm{T}}\alpha^{-1}\theta - \eta & \theta^{\mathrm{T}}\alpha^{-1} \end{bmatrix}. \tag{4.56}$$

Ultimately, the Hamiltonian matrix for the PRC is expressed as

$$\mathscr{H}_{\mathrm{r}} = \mathbb{J}\mathrm{M_{H,r}} = \begin{bmatrix} 0 & 0 & \frac{1}{L_1} & 0 \\ \\ 0 & 0 & 0 & \frac{1}{L_0} \\ \\ -\frac{1}{C_1} - \frac{1}{C_0} & \frac{1}{C_0} & 0 & 0 \\ \\ \frac{1}{C_0} & -\frac{1}{C_0} & 0 & 0 \end{bmatrix}. \tag{4.57}$$

According to Equation (4.52), we know $\mathrm{M_H^T} = \mathrm{M_H}$ and

$$\mathscr{H}^{\mathrm{T}} = -\mathrm{M_H}\mathbb{J} = -\mathbb{J}\left[-\mathbb{J}\mathrm{M_H}\right]\mathbb{J} = \mathbb{J}^{-1}\left[-\mathscr{H}\right]\mathbb{J}, \tag{4.58}$$

where demonstrate that the transpose of the matrix $\mathscr{H}$ is similar to $-\mathscr{H}$.

4.6.3 Relationship Between the Lagrangian and Hamiltonian

By considering the assumption that α is invertible matrix, according to Equations (4.39), (4.51) and (4.52), we have

$$\mathrm{M_L} = \begin{bmatrix} -\eta & \theta^{\mathrm{T}} \\ \theta & \alpha \end{bmatrix}, \quad \mathrm{M_H} = \begin{bmatrix} \beta & \gamma^{\mathrm{T}} \\ \gamma & \rho \end{bmatrix} = \begin{bmatrix} \theta^{\mathrm{T}}\alpha^{-1}\theta + \eta & -\theta^{\mathrm{T}}\alpha^{-1} \\ -\alpha^{-1}\theta & \alpha^{-1} \end{bmatrix}, \tag{4.59}$$

implying that

$$\rho = \alpha^{-1}, \quad \gamma = -\alpha^{-1}\theta, \quad \beta = \theta^{\mathrm{T}}\alpha^{-1}\theta + \eta, \tag{4.60}$$

or

$$\alpha = \rho^{-1}, \quad \theta = -\rho^{-1}\gamma, \quad \eta = \beta - \gamma^{\mathrm{T}}\rho^{-1}\gamma. \tag{4.61}$$

By using the transformations between coefficients described above, the coefficients of the matrix $\mathrm{M_L}$, i.e, η, θ and α, can be converted into the coefficients of the matrix $\mathrm{M_H}$, i.e., β, γ and ρ, and vice versa. As a result, we can construct the Hamiltonian representation from the Lagrangian representation and vice versa.

4.7 Gyrator-Based Nonreciprocal Circuit

In this section, we review the implementation of a gyrator-based circuit to obtain the non-trivial Jordan canonical form that was already proposed and analyzed in our previous works [86, 87, 110, 142]. The gyrator as a basic circuit element was initially introduced by Tellegen [78]. In electric circuits without any nonreciprocal element such as a gyrator the $n \times n$ impedance matrix of n-port system Z is always symmetric, i.e., $\mathrm{Z} = \mathrm{Z}^{\mathrm{T}}$. In contrast, the presence of gyrators *may* result in an asymmetric impedance matrix, i.e, $\mathrm{Z} \neq \mathrm{Z}^{\mathrm{T}}$, which can

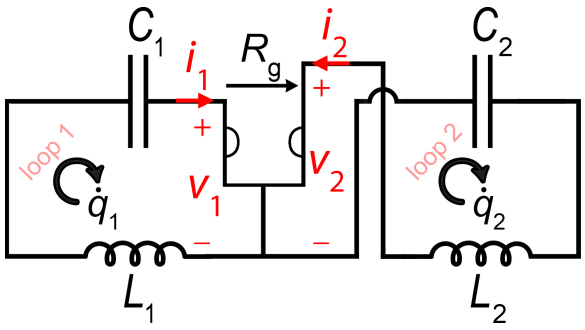

Figure 4.4: The two-loop nonreciprocal circuit coupled by an ideal gyrator. For specific combinations of values L_1, C_1, L_2, and C_2, the evolution matrix of the nonreciprocal circuit develops a degeneracy, and its nontrivial Jordan canonical form consists of exactly two Jordan blocks of size 2. A change in the sign of R_g is equivalent to reversing the gyration resistance direction (indicated by the arrow below R_g) in this circuit.

be interpreted as the nonreciprocity property. The ideal gyrator is characterized as a lossless two-port circuit element with the below relationship between the input and output voltages (v_1, v_2) and currents (i_1, i_2) (see Figure 4.4):

$$v_1 = -R_\mathrm{g} i_2 = -R_\mathrm{g} \dot{q}_2, \tag{4.62a}$$

$$v_2 = R_\mathrm{g} i_1 = R_\mathrm{g} \dot{q}_1. \tag{4.62b}$$

where q_j ($j = 1, 2$) are the charges associated with input and output currents of gyrator. The coefficient R_g is called *gyration resistance* and the corresponding antisymmetric impedance matrix of the gyrator is given by

$$\underline{\mathbf{Z}}_\mathrm{g} = \begin{bmatrix} 0 & R_\mathrm{g} \\ -R_\mathrm{g} & 0 \end{bmatrix} = \left(-\underline{\mathbf{Z}}_\mathrm{g}\right)^\mathrm{T}. \tag{4.63}$$

The Lagrangian associated with the gyrator is given by

$$\mathcal{L}_{\mathrm{g}} = \frac{R_{\mathrm{g}} \left(q_1 \partial_t q_2 - q_2 \partial_t q_1 \right)}{2}. \tag{4.64}$$

The simple form of the GNC to obtain second-order degeneracy is shown in Figure 4.4 and analyzed in the following. The circuit is composed of two LC loops coupled by a gyrator, and we study this circuit without imposing any assumptions on the circuit parameters L_1, C_1, L_2, C_2 and R_{g} except that they are all real and non-zero. The Lagrangian of the GNC is described as

$$\mathcal{L}_{\mathrm{nr}} \left(\mathrm{q_{nr}}, \partial_t \mathrm{q_{nr}} \right)|_{\Theta_{\mathrm{nr}}} = \frac{L_1 \left(\partial_t q_1 \right)^2}{2} + \frac{L_2 \left(\partial_t q_2 \right)^2}{2} - \frac{\left(q_1 \right)^2}{2C_1} - \frac{\left(q_2 \right)^2}{2C_2} + \frac{R_{\mathrm{g}} \left(q_1 \partial_t q_2 - q_2 \partial_t q_1 \right)}{2}, \tag{4.65a}$$

$$q_j \left(t \right) = \int^t i_j \left(t' \right) \, \mathrm{d}t', \quad j = 1, 2, \tag{4.65b}$$

where the last term in Equation (4.65a) is the source of nonreciprocity in the circuit and we will discuss it later in Subsection 4.8.1. Also, q_j and i_j are the charges and the currents associated with loops of the GNC depicted in Figure 4.4, $\Theta_{\mathrm{nr}} = \{L_1, L_2, C_1, C_2, R_{\mathrm{g}}\}$ is the set of circuit's parameters and we define the vector of charges for the GNC as $\mathrm{q_{nr}} = \left[q_1, q_2 \right]^{\mathrm{T}}$. In nonreciprocal systems, due to the breaking of time reversal symmetry, the Lagrangian associated with the GNC leads to $\mathcal{L}_{\mathrm{nr}} \left(\mathrm{q_{nr}}, \partial_t \mathrm{q_{nr}} \right) \neq \mathcal{L}_{\mathrm{nr}} \left(\mathrm{q_{nr}}, -\partial_t \mathrm{q_{nr}} \right)$. The corresponding evolution equations after simplification, i.e., the Euler-Lagrange equations, are expressed as

$$L_1 \ddot{q}_1 - R_{\mathrm{g}} \dot{q}_2 + \frac{1}{C_1} q_1 = 0, \tag{4.66a}$$

$$L_2 \ddot{q}_2 + R_{\mathrm{g}} \dot{q}_1 + \frac{1}{C_2} q_2 = 0. \tag{4.66b}$$

The second-order differential equations in Equations (4.66a) and (4.66b) are reduced to the standard first-order vector differential equation as

$$\partial_t \mathsf{q}_{\rm nr} = \mathscr{C}_{\rm nr}\mathsf{q}_{\rm nr}, \quad \mathscr{C}_{\rm nr} = \begin{bmatrix} 0 & 0 & 1 & 0 \\ 0 & 0 & 0 & 1 \\ -\frac{1}{L_1C_1} & 0 & 0 & \frac{R_{\rm g}}{L_1} \\ 0 & -\frac{1}{L_2C_2} & -\frac{R_{\rm g}}{L_2} & 0 \end{bmatrix}, \tag{4.67}$$

where the circuit state vector is defined as $\mathsf{q}_{\rm nr} = [\mathrm{q}_{\rm nr}, \partial_t \mathrm{q}_{\rm nr}]^{\rm T}$and $\mathscr{C}_{\rm nr}$ is the 4×4 circuit matrix for the GNC. A matrix representation of evolution equations is easily achieved by recasting them as follows:

$$\mathrm{A}_{\rm nr}(s)\,\mathrm{q}_{\rm nr} = 0, \quad \mathrm{A}_{\rm nr}(s) = \begin{bmatrix} s^2 + \frac{1}{L_1C_1} & -s\frac{R_{\rm g}}{L_1} \\ s\frac{R_{\rm g}}{L_2} & s^2 + \frac{1}{L_2C_2} \end{bmatrix}, \quad \mathrm{q}_{\rm nr} = \begin{bmatrix} q_1 \\ q_2 \end{bmatrix}, \tag{4.68}$$

where $\mathrm{A}_{\rm nr}(s)$ is a 2×2 monic matrix polynomial of s of the degree 2 and it is rewritten as

$$\mathrm{A}_{\rm nr}(s) = \sum_{j=0}^{2} s^j \mathrm{A}_{{\rm nr},j} = s^2\mathrm{A}_{\rm nr,2} + s\mathrm{A}_{\rm nr,1} + \mathrm{A}_{\rm nr,0}, \tag{4.69a}$$

$$\mathrm{A}_{\rm nr,2} = \begin{bmatrix} 1 & 0 \\ 0 & 1 \end{bmatrix}, \quad \mathrm{A}_{\rm nr,1} = \begin{bmatrix} 0 & -\frac{R_{\rm g}}{L_1} \\ \frac{R_{\rm g}}{L_2} & 0 \end{bmatrix}, \quad \mathrm{A}_{\rm nr,0} = \begin{bmatrix} \frac{1}{L_1C_1} & 0 \\ 0 & \frac{1}{L_2C_2} \end{bmatrix}. \tag{4.69b}$$

The eigenvalue problem corresponding to the Equation (4.67) is

$$(s\mathbb{I}_4 - \mathscr{C}_{\mathrm{nr}})\,\mathsf{q}_{\mathrm{nr,s}} = 0, \quad \mathsf{q}_{\mathrm{nr,s}} = \begin{bmatrix} \mathrm{q}_{\mathrm{nr}} \\ \\ s\mathrm{q}_{\mathrm{nr}} \end{bmatrix}. \tag{4.70}$$

The associated characteristic polynomial for the GNC is expressed as

$$\chi_{\mathrm{nr}}(s) = \det\{A_{\mathrm{nr}}(s)\} = \det\{s\mathbb{I}_4 - \mathscr{C}_{\mathrm{nr}}\} = s^4 + s^2\left(\frac{1}{L_1C_1} + \frac{1}{L_2C_2} + \frac{R_{\mathrm{g}}^2}{L_1L_2}\right) + \frac{1}{L_1C_1L_2C_2}, \tag{4.71}$$

and the eigenvalues of the eigenvalue problem can be calculated from the characteristic polynomial $\chi_{\mathrm{nr}}(s) = 0$. According to further analytical developments, the circuit should include the following parameters

$$\xi_1 = \frac{1}{L_1C_1}, \quad \xi_2 = \frac{1}{L_2C_2}. \tag{4.72}$$

In Equation (4.72), $\sqrt{\xi_1}$ is the resonance frequency of the first loop and $\sqrt{\xi_2}$ is the resonance frequency of the second loop. Alternatively, the circuit matrix $\mathscr{C}_{\mathrm{nr}}$ given by Equation (4.67) and its characteristic polynomial as in Equation (4.71) take the following forms

$$\mathscr{C}_{\mathrm{nr}} = \begin{bmatrix} 0 & 0 & 1 & 0 \\ \\ 0 & 0 & 0 & 1 \\ \\ -\xi_1 & 0 & 0 & \frac{R_{\mathrm{g}}}{L_1} \\ \\ 0 & -\xi_2 & -\frac{R_{\mathrm{g}}}{L_2} & 0 \end{bmatrix}, \tag{4.73a}$$

$$\chi_{\mathrm{nr}}(h) = h^2 + h\left(\xi_1 + \xi_2 + \frac{R_{\mathrm{g}}^2}{L_1L_2}\right) + \xi_1\xi_2, \quad h = s^2. \tag{4.73b}$$

Considering the degenerate eigenvalues that satisfying equation $\chi_{\mathrm{nr}}(h) = 0$, the discriminant

of the quadratic polynomial of Equation (4.73b) is given by

$$\Delta_{\mathrm{nr},h} = \frac{R_{\mathrm{g}}^4}{L_1^2 L_2^2} + \frac{2\left(\xi_1 + \xi_2\right) R_{\mathrm{g}}^2}{L_1 L_2} + \left(\xi_1 - \xi_2\right)^2, \tag{4.74}$$

where the solutions of the quadratic equation of Equation (4.73b) are

$$h_{\pm} = \frac{-\left(\xi_1 + \xi_2 + \frac{R_{\mathrm{g}}^2}{L_1 L_2}\right) \pm \sqrt{\Delta_{\mathrm{nr},h}}}{2}. \tag{4.75}$$

The corresponding four solutions s of the characteristic polynomial are given by

$$s = \pm\sqrt{h_+}, \pm\sqrt{h_-}. \tag{4.76}$$

In this case, the eigenvalue degeneracy condition becomes $\Delta_{\mathrm{nr},h} = 0$. It is possible to view degeneracy condition equation as a constraint on the coefficients of $\chi_{\mathrm{nr}}(h) = 0$ and consequently on the circuit components value, namely

$$L_1^2 L_2^2 \Delta_{\mathrm{nr},h} = g^2 + 2\left(\xi_1 + \xi_2\right) g L_1 L_2 + \left(\xi_1 - \xi_2\right)^2 L_1^2 L_2^2 = 0, \quad g = R_{\mathrm{g}}^2, \tag{4.77}$$

and we refer to g as the *gyration resistance square*. Since R_{g} is real, then $g = R_{\mathrm{g}}^2$ is positive and real as well. Equation (4.77) is a quadratic equation for g, which has exactly two solutions of

$$g_{\mathrm{d},\pm} = -L_1 L_2 \left(\sqrt{\xi_1} \mp \sqrt{\xi_2}\right)^2, \tag{4.78}$$

which lead to two degenerate cases. For the two *special value of gyration resistance square* $g_{\mathrm{d},\pm}$, we get two degenerate roots for $h_{\pm}$ as

$$h_{\mathrm{d},\pm} = -\frac{\xi_1 + \xi_2 + \frac{g_{\mathrm{d},\pm}}{L_1 L_2}}{2} = \mp\sqrt{\xi_1 \xi_2}. \tag{4.79}$$

Expression of $g_{\mathrm{d},\pm}$ shown in Equation (4.78) is real-valued if and only if $\xi_1 \xi_2 > 0$, or equivalently $\xi_1/|\xi_1| = \xi_2/|\xi_2| = \pm 1$. Also, the Jordan canonical form out of degeneracy condition, i.e., $\Delta_{\mathrm{nr},h} \neq 0$, is expressed as

$$\mathscr{J}_{\mathrm{r}} = \begin{bmatrix} \mathrm{i}s_1 & 0 & 0 & 0 \\ 0 & -\mathrm{i}s_1 & 0 & 0 \\ 0 & 0 & \mathrm{i}s_2 & 0 \\ 0 & 0 & 0 & -\mathrm{i}s_2 \end{bmatrix}, \qquad \begin{matrix} s_1 = \sqrt{\frac{\xi_{\mathrm{nr,s}} + \sqrt{L_1^2 L_2^2 \Delta_{\mathrm{nr},h}}}{2L_1 L_2}} \\ s_2 = \sqrt{\frac{\xi_{\mathrm{nr,s}} - \sqrt{L_1^2 L_2^2 \Delta_{\mathrm{nr},h}}}{2L_1 L_2}} \end{matrix}, \quad \xi_{\mathrm{nr,s}} = (\xi_1 + \xi_2) L_1 L_2 + R_{\mathrm{g}}^2, \tag{4.80}$$

where $\pm \mathrm{i}s_i$ $(i = 1, 2)$ are the non-degenerate eigenvalues of the corresponding companion matrix. We write down eigenvectors corresponding to the calculated non-degenerate eigenvalues as (when $\Delta_{\mathrm{nr},h} \neq 0$)

$$\mathscr{V}_{\mathrm{nr}} = \left[\mathsf{e}_{\mathrm{nr},+s_1} | \mathsf{e}_{\mathrm{nr},-s_1} | \mathsf{e}_{\mathrm{nr},+s_2} | \mathsf{e}_{\mathrm{nr},-s_2} \right], \tag{4.81a}$$

$$\mathsf{e}_{\mathrm{nr},\pm s_i} = \begin{bmatrix} \frac{2R_{\mathrm{g}}^2 + 2L_1 L_2 \xi_2 - \xi_{\mathrm{nr,s}} - \sqrt{L_1^2 L_2^2 \Delta_{\mathrm{nr},h}}}{2L_1 R_{\mathrm{g}} \xi_1} \\ \mp \frac{L_1 L_2 \left(-s_i^2\right)^{3/2} + \xi_{\mathrm{nr,s}} \sqrt{-s_i^2}}{L_1 L_2 \xi_1 \xi_2} \\ \pm \frac{L_1 L_2 \left(-s_i^2\right)^{3/2} + \left(R_{\mathrm{g}}^2 + L_1 L_2 \xi_2\right) \sqrt{-s_i^2}}{L_1 R_{\mathrm{g}} \xi_1} \\ 1 \end{bmatrix}. \tag{4.81b}$$

There were two values for the degenerate gyration resistance square as shown in Equation (4.78), resulting in degenerate purely imaginary or purely real eigenvalues. Firstly, if we consider $g = g_{\mathrm{d},+} = -L_1 L_2 \left(\sqrt{\xi_1} - \sqrt{\xi_2}\right)^2$, the degenerate characteristic polynomial is given by

$$\chi_{\mathrm{nr},+}(s) = s^4 + 2s^2\sqrt{\xi_1\xi_2} + \xi_1\xi_2 = \left(s^2 + \sqrt{\xi_1\xi_2}\right)^2 = 0. \tag{4.82}$$

Then, the corresponding degenerate companion matrix $\mathscr{C}_{\mathrm{nr},+}$ by substituting $g = g_{\mathrm{d},+}$ is rewritten as

$$\mathscr{C}_{\mathrm{nr},+} = \begin{bmatrix} 0 & 0 & 1 & 0 \\ 0 & 0 & 0 & 1 \\ -\xi_1 & 0 & 0 & \frac{\sqrt{g_{\mathrm{d},+}}}{L_1} \\ 0 & -\xi_2 & -\frac{\sqrt{g_{\mathrm{d},+}}}{L_2} & 0 \end{bmatrix}. \tag{4.83}$$

The Jordan canonical form of the companion matrix $\mathscr{C}_{\mathrm{nr},+}$ with purely imaginary eigenvalues (purely real eigenfrequencies) is described by

$$\mathscr{J}_{\mathrm{nr},+} = \begin{bmatrix} \mathrm{i}s_{\mathrm{e}} & 1 & 0 & 0 \\ 0 & \mathrm{i}s_{\mathrm{e}} & 0 & 0 \\ 0 & 0 & -\mathrm{i}s_{\mathrm{e}} & 1 \\ 0 & 0 & 0 & -\mathrm{i}s_{\mathrm{e}} \end{bmatrix}, \quad s_{\mathrm{e}} = (\xi_{\mathrm{e}})^{\frac{1}{2}} = (\xi_1\xi_2)^{\frac{1}{4}}. \tag{4.84}$$

Accordingly, the Jordan basis of the companion matrix $\mathscr{C}_{\mathrm{nr},+}$ is calculated as

$$\mathscr{X}_{\mathrm{nr},+} = \begin{bmatrix} \frac{\sqrt{\xi_1\xi_2}-\xi_1}{4\mathrm{i}\sqrt{\xi_\mathrm{e}}} & \frac{1}{2} & -\frac{\sqrt{\xi_1\xi_2}-\xi_1}{4\mathrm{i}\sqrt{\xi_\mathrm{e}}} & \frac{1}{2} \\ -\frac{\xi_1\sqrt{L_1L_2(2\xi_\mathrm{e}-\xi_1-\xi_2)}}{4L_2\xi_\mathrm{e}} & -\mathrm{i}\frac{\xi_1\sqrt{L_1L_2(2\xi_\mathrm{e}-\xi_1-\xi_2)}}{4L_2\xi_\mathrm{e}\sqrt{\xi_\mathrm{e}}} & -\frac{\xi_1\sqrt{L_1L_2(2\xi_\mathrm{e}-\xi_1-\xi_2)}}{4L_2\xi_\mathrm{e}} & \mathrm{i}\frac{\xi_1\sqrt{L_1L_2(2\xi_\mathrm{e}-\xi_1-\xi_2)}}{4L_2\xi_\mathrm{e}\sqrt{\xi_\mathrm{e}}} \\ \frac{\xi_1(\xi_2-\xi_\mathrm{e})}{4\xi_\mathrm{e}} & -\frac{\xi_1(\xi_2+\xi_\mathrm{e})}{4\mathrm{i}\xi_\mathrm{e}\sqrt{\xi_\mathrm{e}}} & \frac{\xi_1(\xi_2-\xi_\mathrm{e})}{4\xi_\mathrm{e}} & \frac{\xi_1(\xi_2+\xi_\mathrm{e})}{4\mathrm{i}\xi_\mathrm{e}\sqrt{\xi_\mathrm{e}}} \\ \frac{\xi_1\sqrt{L_1L_2(2\xi_\mathrm{e}-\xi_1-\xi_2)}}{4\mathrm{i}L_2\sqrt{\xi_\mathrm{e}}} & 0 & -\frac{\xi_1\sqrt{L_1L_2(2\xi_\mathrm{e}-\xi_1-\xi_2)}}{4\mathrm{i}L_2\sqrt{\xi_\mathrm{e}}} & 0 \end{bmatrix}. \tag{4.85}$$

Secondly, if we consider $g = g_{\mathrm{d},-} = -L_1L_2\left(\xi_1+\xi_2+2\sqrt{\xi_1\xi_2}\right)$, the degenerate characteristic polynomial is rewritten as

$$\chi_{\mathrm{nr},-}(s) = s^4 - 2s^2\sqrt{\xi_1\xi_2} + \xi_1\xi_2 = \left(s^2 - \sqrt{\xi_1\xi_2}\right)^2 = 0. \tag{4.86}$$

Then, the degenerate corresponding companion matrix $\mathscr{C}_{\mathrm{nr},-}$ is rewritten as

$$\mathscr{C}_{\mathrm{nr},+} = \begin{bmatrix} 0 & 0 & 1 & 0 \\ 0 & 0 & 0 & 1 \\ -\xi_1 & 0 & 0 & \frac{\sqrt{g_{\mathrm{d},-}}}{L_1} \\ 0 & -\xi_2 & -\frac{\sqrt{g_{\mathrm{d},-}}}{L_2} & 0 \end{bmatrix}. \tag{4.87}$$

The Jordan canonical form of the companion matrix $\mathscr{C}_{\mathrm{nr},-}$ with purely real eigenvalues (purely imaginary eigenfrequencies) is expressed by

$$\mathscr{J}_{\mathrm{nr},-} = \begin{bmatrix} s_{\mathrm{e}} & 1 & 0 & 0 \\ 0 & s_{\mathrm{e}} & 0 & 0 \\ 0 & 0 & -s_{\mathrm{e}} & 1 \\ 0 & 0 & 0 & -s_{\mathrm{e}} \end{bmatrix}. \tag{4.88}$$

Finally, the Jordan basis of the companion matrix $\mathscr{C}_{\mathrm{nr},-}$ is obtained as

$$\mathscr{Z}_{\mathrm{nr},-} = \begin{bmatrix} -\frac{\sqrt{\xi_1\xi_2}+\xi_1}{4\sqrt{\xi_{\mathrm{e}}}} & \frac{1}{2} & \frac{\sqrt{\xi_1\xi_2}+\xi_1}{4\sqrt{\xi_{\mathrm{e}}}} & \frac{1}{2} \\ \mathrm{i}\frac{\xi_1\sqrt{L_1L_2(2\xi_{\mathrm{e}}+\xi_1+\xi_2)}}{4L_2\xi_{\mathrm{e}}} & -\mathrm{i}\frac{\xi_1\sqrt{L_1L_2(2\xi_{\mathrm{e}}+\xi_1+\xi_2)}}{4L_2\xi_{\mathrm{e}}\sqrt{\xi_{\mathrm{e}}}} & \mathrm{i}\frac{\xi_1\sqrt{L_1L_2(2\xi_{\mathrm{e}}+\xi_1+\xi_2)}}{4L_2\xi_{\mathrm{e}}} & \mathrm{i}\frac{\xi_1\sqrt{L_1L_2(2\xi_{\mathrm{e}}+\xi_1+\xi_2)}}{4L_2\xi_{\mathrm{e}}\sqrt{\xi_{\mathrm{e}}}} \\ -\frac{\xi_1(\xi_2+\xi_{\mathrm{e}})}{4\xi_{\mathrm{e}}} & \frac{\xi_1(\xi_2-\xi_{\mathrm{e}})}{4\xi_{\mathrm{e}}\sqrt{\xi_{\mathrm{e}}}} & -\frac{\xi_1(\xi_2+\xi_{\mathrm{e}})}{4\xi_{\mathrm{e}}} & -\frac{\xi_1(\xi_2-\xi_{\mathrm{e}})}{4\xi_{\mathrm{e}}\sqrt{\xi_{\mathrm{e}}}} \\ \mathrm{i}\frac{\xi_1\sqrt{L_1L_2(2\xi_{\mathrm{e}}+\xi_1+\xi_2)}}{4L_2\sqrt{\xi_{\mathrm{e}}}} & 0 & -\mathrm{i}\frac{\xi_1\sqrt{L_1L_2(2\xi_{\mathrm{e}}+\xi_1+\xi_2)}}{4L_2\sqrt{\xi_{\mathrm{e}}}} & 0 \end{bmatrix}. \tag{4.89}$$

The fundamental of Lagrangian for a linear system is explained in Subsection 4.6.1 and the associated coefficients for the GNC are

$$\alpha_{\mathrm{nr}} = \begin{bmatrix} L_1 & 0 \\ 0 & L_2 \end{bmatrix}, \quad \theta_{\mathrm{nr}} = \begin{bmatrix} 0 & -\frac{R_{\mathrm{g}}}{2} \\ \frac{R_{\mathrm{g}}}{2} & 0 \end{bmatrix}, \quad \eta_{\mathrm{nr}} = \begin{bmatrix} \frac{1}{C_1} & 0 \\ 0 & \frac{1}{C_2} \end{bmatrix}. \tag{4.90}$$

It follows from Equation (4.42) that the necessary and sufficient condition of the nonre-

ciprocity is $\theta_{\mathrm{nr}} \neq \theta_{\mathrm{nr}}^{\mathrm{T}}$. Then, the Lagrangian equation of GNC is written as follows:

$$\mathcal{L}_{\mathrm{nr}}\left(\mathrm{q}_{\mathrm{nr}}, \partial_t \mathrm{q}_{\mathrm{nr}}\right) = \frac{1}{2} \begin{bmatrix} \mathrm{q}_{\mathrm{nr}} \\ \\ \partial_t \mathrm{q}_{\mathrm{nr}} \end{bmatrix}^{\mathrm{T}} \mathrm{M}_{\mathrm{L,nr}} \begin{bmatrix} \mathrm{q}_{\mathrm{nr}} \\ \\ \partial_t \mathrm{q}_{\mathrm{nr}} \end{bmatrix}, \tag{4.91a}$$

$$\mathrm{M}_{\mathrm{L,nr}} = \begin{bmatrix} -\frac{1}{C_1} & 0 & 0 & \frac{R_{\mathrm{g}}}{2} \\ \\ 0 & -\frac{1}{C_2} & -\frac{R_{\mathrm{g}}}{2} & 0 \\ \\ 0 & -\frac{R_{\mathrm{g}}}{2} & L_1 & 0 \\ \\ \frac{R_{\mathrm{g}}}{2} & 0 & 0 & L_2 \end{bmatrix}. \tag{4.91b}$$

Moreover, the Hamiltonian formulation can also be used to show the GNC characteristics (see Subsection 4.6.2). Then, the 4×4 matrix $\mathrm{M}_{\mathrm{H,nr}}$ required for the Hamiltonian formulation is given by

$$\mathrm{M}_{\mathrm{H,nr}} = \begin{bmatrix} \frac{R_{\mathrm{g}}^2}{4L_2} + \frac{1}{C_1} & 0 & 0 & -\frac{R_{\mathrm{g}}}{2L_2} \\ \\ 0 & \frac{R_{\mathrm{g}}^2}{4L_1} + \frac{1}{C_2} & \frac{R_{\mathrm{g}}}{2L_1} & 0 \\ \\ 0 & \frac{R_{\mathrm{g}}}{2L_1} & \frac{1}{L_1} & 0 \\ \\ -\frac{R_{\mathrm{g}}}{2L_2} & 0 & 0 & \frac{1}{L_2} \end{bmatrix}. \tag{4.92}$$

Ultimately, the Hamiltonian matrix for the GNC is given by

$$\mathscr{H}_{\mathrm{nr}} = \mathbb{J}\mathrm{M}_{\mathrm{H,nr}} = \begin{bmatrix} 0 & \frac{R_{\mathrm{g}}}{2L_1} & \frac{1}{L_1} & 0 \\ -\frac{R_{\mathrm{g}}}{2L_2} & 0 & 0 & \frac{1}{L_2} \\ -\frac{R_{\mathrm{g}}^2}{4L_2} - \frac{1}{C_1} & 0 & 0 & \frac{R_{\mathrm{g}}}{2L_2} \\ 0 & -\frac{R_{\mathrm{g}}^2}{4L_1} - \frac{1}{C_2} & -\frac{R_{\mathrm{g}}}{2L_1} & 0 \end{bmatrix}. \tag{4.93}$$

According to Equation (4.47), we can see that in the nonreciprocal circuit with $\theta_{\mathrm{nr}} \neq 0$, the relation between the *momentum* $\mathrm{p_{nr}}$ and the *current* $\partial_t \mathrm{q_{nr}}$ also depends on the charge $\mathrm{q_{nr}}$. However, it is important to point out that a circuit with gyrators does not necessarily guarantee nonreciprocity, but it *can* lead to nonreciprocity.

4.8 Analysis of Reciprocity and Nonreciprocity

In this section, we analyze reciprocity properties in both reciprocal and nonreciprocal circuits. This particular feature will be explored in the Lagrangian and eigenvectors of both PRC and GNC.

4.8.1 Lagrangian

According to investigation provided in Section 4.4, the Lagrangian associated with the PRC is depicted as

$$\mathcal{L}_{\mathrm{r}}\left(\mathrm{q_r}, \partial_t \mathrm{q_r}\right)\big|_{\Theta_{\mathrm{r}}} = \frac{L_1\left(\partial_t q_1\right)^2}{2} + \frac{L_0\left(\partial_t q_0\right)^2}{2} - \frac{\left(q_1\right)^2}{2C_1} - \frac{\left(q_1 - q_0\right)^2}{2C_0}. \tag{4.94}$$

An arrow of time is a concept that proposes the one-way direction or asymmetry of time. If we change the direction of arrow of time, the Lagrangian associated with PRC is expressed by

$$\mathcal{L}_{\mathrm{r}}\left(\mathrm{q}_{\mathrm{r}}, -\partial_t \mathrm{q}_{\mathrm{r}}\right)\big|_{\Theta_{\mathrm{r}}} = \frac{L_1\left(\partial_t q_1\right)^2}{2} + \frac{L_0\left(\partial_t q_0\right)^2}{2} - \frac{\left(q_1\right)^2}{2C_1} - \frac{\left(q_1 - q_0\right)^2}{2C_0}. \tag{4.95}$$

By comparing Equations (4.94) and (4.95) we have

$$\mathcal{L}_{\mathrm{r}}\left(\mathrm{q}_{\mathrm{r}}, \partial_t \mathrm{q}_{\mathrm{r}}\right)\big|_{\Theta_{\mathrm{r}}} = \mathcal{L}_{\mathrm{r}}\left(\mathrm{q}_{\mathrm{r}}, -\partial_t \mathrm{q}_{\mathrm{r}}\right)\big|_{\Theta_{\mathrm{r}}}. \tag{4.96}$$

In the above equation, we can see that there is symmetry in time, which refers to reciprocity within the PRC (see Definition 2).

Definition 2 (Lagrangian of reciprocal and nonreciprocal systems)**.** *For a system described by coordinates* $F = [f_i]|_{i=1}^{n}$ *and time* t*, the time reversal symmetry can be formulated as follows. For any trajectory* $F(t)$ *of the system,* $\tilde{F}(t) = F(-t)$ *is also its trajectory. In terms of the Lagrangian function* $\mathcal{L} = \mathcal{L}\left(F, \dot{F}\right)$*, it means the invariance of Lagrangian function under the transformation* $\dot{F} \to -\dot{F}$ *[118]:*

$$\mathcal{L}\left(F, \dot{F}\right) = \mathcal{L}\left(F, -\dot{F}\right). \tag{4.97}$$

Also, for a system with broken time reversal symmetry we observe $\mathcal{L}\left(F, \dot{F}\right) \neq \mathcal{L}\left(F, -\dot{F}\right)$.

On the other hand, based on the expression given in Section 4.7, the Lagrangian associated with GNC is expressed by

$$\mathcal{L}_{\mathrm{nr}}\left(\mathrm{q}_{\mathrm{nr}}, \partial_t \mathrm{q}_{\mathrm{nr}}\right)\big|_{\Theta_{\mathrm{nr}}} = \frac{L_1\left(\partial_t q_1\right)^2}{2} + \frac{L_2\left(\partial_t q_2\right)^2}{2} - \frac{\left(q_1\right)^2}{2C_1} - \frac{\left(q_2\right)^2}{2C_2} + \frac{R_{\mathrm{g}}\left(q_1 \partial_t q_2 - q_2 \partial_t q_1\right)}{2}. \tag{4.98}$$

Then, by inverting the direction of the time we have

$$\mathcal{L}_{\mathrm{nr}}\left(\mathrm{q}_{\mathrm{nr}}, -\partial_t \mathrm{q}_{\mathrm{nr}}\right)|_{\Theta_{\mathrm{nr}}} = \frac{L_1\left(\partial_t q_1\right)^2}{2} + \frac{L_2\left(\partial_t q_2\right)^2}{2} - \frac{\left(q_1\right)^2}{2C_1} - \frac{\left(q_2\right)^2}{2C_2} - \frac{R_{\mathrm{g}}\left(q_1 \partial_t q_2 - q_2 \partial_t q_1\right)}{2}, \quad (4.99)$$

where we observe the sign of nonreciprocity in the last term of the above equation. Now, by inverting the direction of gyration resistance ($R_{\mathrm{g}} \rightarrow -R_{\mathrm{g}}$) in addition to reversing the direction of time, we rewrite the Lagrangian associated with the new circuit by using a new set of parameters $\widetilde{\Theta}_{\mathrm{nr}} = \{L_1, L_2, C_1, C_2, -R_{\mathrm{g}}\}$ as

$$\mathcal{L}_{\mathrm{nr}}\left(\mathrm{q}_{\mathrm{nr}}, -\partial_t \mathrm{q}_{\mathrm{nr}}\right)|_{\widetilde{\Theta}_{\mathrm{nr}}} = \frac{L_1\left(\partial_t q_1\right)^2}{2} + \frac{L_2\left(\partial_t q_2\right)^2}{2} - \frac{\left(q_1\right)^2}{2C_1} - \frac{\left(q_2\right)^2}{2C_2} + \frac{R_{\mathrm{g}}\left(q_1 \partial_t q_2 - q_2 \partial_t q_1\right)}{2}. \quad (4.100)$$

Finally, by comparing Equations (4.98), (4.99) and (4.100), we have

$$\mathcal{L}_{\mathrm{nr}}\left(\mathrm{q}_{\mathrm{nr}}, \partial_t \mathrm{q}_{\mathrm{nr}}\right)|_{\Theta_{\mathrm{nr}}} = \mathcal{L}_{\mathrm{nr}}\left(\mathrm{q}_{\mathrm{nr}}, -\partial_t \mathrm{q}_{\mathrm{nr}}\right)|_{\widetilde{\Theta}_{\mathrm{nr}}} \neq \mathcal{L}_{\mathrm{nr}}\left(\mathrm{q}_{\mathrm{nr}}, -\partial_t \mathrm{q}_{\mathrm{nr}}\right)|_{\Theta_{\mathrm{nr}}}, \quad (4.101)$$

which demonstrate the nonreciprocity in the GNC (see Definition 2). In spite of this, the circuit with the same Lagrangian is achieved by simultaneously inverting the direction of the time and gyration resistance. Alternately, by removing the source of nonreciprocity in the circuit, i.e., the gyrator, the circuit becomes a reciprocal circuit composed of two uncoupled LC resonators. The properties of a single LC resonator are discussed in Appendix E.

4.8.2 Eigenvectors

As explained in Subsection 4.5.2, the eigenvectors associated to the PRC in the general form are expressed as

$$\mathsf{e}_{\mathrm{r},\pm s_i} = \begin{bmatrix} \mathsf{q}_{\pm s_i} \\ \\ \dot{\mathsf{q}}_{\pm s_i} \end{bmatrix} \overset{\text{def}}{=} \begin{bmatrix} \mp\frac{\left(-s_i^2\right)^{3/2}+(\xi_0+\delta)\sqrt{-s_i^2}}{\xi_0\xi_1} \\ \mp\frac{\left(-s_i^2\right)^{3/2}+\xi_{\mathrm{nr,s}}\sqrt{-s_i^2}}{\xi_0\xi_i} \\ 1-\frac{s_i^2}{\xi_0} \\ 1 \end{bmatrix}, \quad i=1,2. \tag{4.102}$$

Due to reciprocity, we observe the change in the sign of charges when we inverse the sign of s_i $(i=1,2)$, i.e., $\mathsf{q}_{+s_i} = -\mathsf{q}_{-s_i}$ $(i=1,2)$, whereas the sign of the first derivative of charges remains constant, i.e., $\dot{\mathsf{q}}_{+s_i} = \dot{\mathsf{q}}_{-s_i}$ $(i=1,2)$. The reciprocity feature of PRC is evident from these properties.

Next, we study the GNC eigenvectors to explore a reciprocity feature. Based on the presented expression in Section 4.7, the eigenvectors associated to the GNC are presented as

$$\mathsf{e}_{\mathrm{nr},\pm s_i} = \begin{bmatrix} \mathsf{q}_{\pm s_i} \\ \\ \dot{\mathsf{q}}_{\pm s_i} \end{bmatrix} \overset{\text{def}}{=} \begin{bmatrix} \frac{2R_{\mathrm{g}}^2+2L_1L_2\xi_2-\xi_{\mathrm{nr,s}}-\sqrt{L_1^2L_2^2\Delta_{\mathrm{nr},h}}}{2L_1R_{\mathrm{g}}\xi_1} \\ \mp\frac{L_1L_2\left(-s_i^2\right)^{3/2}+\xi_{\mathrm{nr,s}}\sqrt{-s_i^2}}{L_1L_2\xi_1\xi_2} \\ \pm\frac{L_1L_2\left(-s_i^2\right)^{3/2}+\left(R_{\mathrm{g}}^2+L_1L_2\xi_2\right)\sqrt{-s_i^2}}{L_1R_{\mathrm{g}}\xi_1} \\ 1 \end{bmatrix}, \quad i=1,2. \tag{4.103}$$

We cannot observe the same behavior for the sign of charges and their first derivative from the above expression for the eigenvectors of the GNC, i.e., $\mathsf{q}_{+s_i} \neq -\mathsf{q}_{-s_i}$, $\dot{\mathsf{q}}_{+s_i} \neq \dot{\mathsf{q}}_{-s_i} (i=1,2)$. In light of these eigenvector properties, it can be inferred that GNC is not reciprocal. *Our studies indicate that nonreciprocity is manifested in the breakdown of natural symmetries of the set of eigenvectors rather than eigenvalues. Indeed, the Lagrangian and eigenvectors of a circuit are capable of reflecting the reciprocity properties of the circuit. Despite this, nonre-*

ciprocity cannot be captured in the Jordan canonical form and consequently in the eigenvalues of the circuit matrix.

We demonstrated that the Jordan canonical form of the circuit does not reflect reciprocity. Consequently, despite the fact that reciprocal and nonreciprocal circuits differ from many perspectives, these two circuits with different topologies can produce the same Jordan canonical form and consequently the same eigenvalues under the certain conditions.

4.9 Reciprocal and Nonreciprocal Circuits Transformation

4.9.1 Equivalency Condition in Characteristic Polynomial

By comparing the characteristic polynomial of the PRC expressed in Equation (4.10) and the characteristic polynomial of the GNC stated in Equation (4.72) we obtain the conditions to have equivalency between the characteristic polynomials of these two circuits by equating coefficients as

$$\begin{cases} \{s^1\} : \frac{R_g^2}{L_1 L_2} + \frac{1}{L_2 C_2} + \frac{1}{L_1 C_1} = \frac{1}{L_1 C_0} + \frac{1}{L_0 C_0} + \frac{1}{L_1 C_1} \\ \{s^0\} : \frac{1}{L_1 C_1 L_2 C_2} = \frac{1}{L_0 C_0 L_1 C_1} \end{cases} \tag{4.104}$$

Then, we suppose that the first fundamental loop (that include series L_1 and C_1) in both circuits has the same resonance frequency. So, the conditions to have the same Jordan canonical form for both PRC and GNC are summarized as follows:

$$R_{\mathrm{g}}^2 = R_{\mathrm{g,eq}}^2 = \frac{L_2}{C_0} = \frac{L_0}{C_2}, \tag{4.105}$$

where $R_{\mathrm{g,eq}}$ is the *equivalency value of gyration resistance* that can be used to get the same eigenfrequencies in PRC and GNC.

4.9.2 Equivalent Circuit Representation

By using the equivalent circuit representation that can be observed from two selected points of a desired network, we can determine the equivalency condition between reciprocal and nonreciprocal circuits [151, 152]. As originally described in network theory, Thévenin's theorem asserts that "*any linear electrical network with only voltage and current sources and impedances can be substituted at input ports by using a combination of an equivalent impedance Z_{Th} in a series connection with an equivalent voltage source V_{Th}*". The equivalent impedance Z_{Th} is the impedance observed from the input port if all ideal current sources in the circuit were substituted by an open circuit and all ideal voltage sources were substituted by a short circuit. Also, the equivalent voltage V_{Th} is the voltage calculated at the input port of the circuit when the input port is open. In the case of a short circuit at the input port, the current flowing from the short circuit would be $I_{\mathrm{Th}} = V_{\mathrm{Th}}/Z_{\mathrm{Th}}$ and the equivalent impedance Z_{Th} could also be calculated as $Z_{\mathrm{Th}} = V_{\mathrm{Th}}/I_{\mathrm{Th}}$. By using Thévenin's theorem and its dual (i.e., Norton's theorem), any circuit with sources and impedances can be converted to an equivalent network; in some cases, this may be more convenient than Kirchhoff's voltage and current laws.

According to Figure 4.5(a), we cut the PRC into two segments and characterize the right segment using the Thévenin's equivalent circuit. The input impedance $Z_{\mathrm{eq,r}}$, that is identical to the equivalent Thévenin's impedance observed from port AB, for the PRC is calculated by

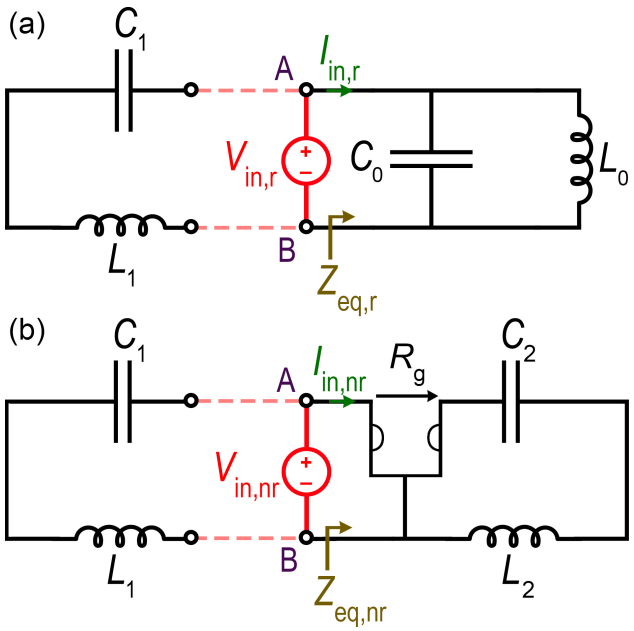

Figure 4.5: The equivalent circuit representation and the condition for obtaining (a) reciprocal and (b) nonreciprocal circuits with the same Jordan canonical forms and consequently the same eigenfrequencies by selecting the equivalency value for the gyration resistance $R_{\mathrm{g,eq}}$. The right side of both circuits can have the same equivalent impedance if $R_{\mathrm{g,eq}} = \sqrt{L_2/C_0} = \sqrt{L_0/C_2}$. The left loop in both circuits includes a series resonator with the same resonance frequency.

$$Z_{\mathrm{eq,r}} = \frac{V_{\mathrm{in,r}}}{I_{\mathrm{in,r}}} = \frac{1}{j\omega C_0 + \frac{1}{j\omega L_0}}. \tag{4.106}$$

By using the same approach for the GNC shown in Figure 4.5(b), we calculate equivalent input impedance $Z_{\mathrm{eq,nr}}$ as

$$Z_{\mathrm{eq,nr}} = \frac{V_{\mathrm{in,nr}}}{I_{\mathrm{in,nr}}} = \frac{R_{\mathrm{g}}^2}{j\omega L_2 + \frac{1}{j\omega C_2}}. \tag{4.107}$$

Then, if we consider the equality of input impedances $Z_{\mathrm{eq,r}} = Z_{\mathrm{eq,nr}}$, we write

$$R_{\mathrm{g}}^2 = R_{\mathrm{g,eq}}^2 = \frac{\omega^2 L_2 C_2 L_0 - L_0}{\omega^2 C_0 C_2 L_0 - C_2} = \frac{L_0\left(\omega^2 L_2 C_2 - 1\right)}{C_2\left(\omega^2 L_0 C_0 - 1\right)}. \tag{4.108}$$

In order to have a frequency-independent value for gyration resistance $R_{\rm g}$, we apply the following assumption:

$$L_2C_2 = L_0C_0, \text{ or equivalently } \xi_2 = \xi_0. \tag{4.109}$$

Consequently, from Equations (4.108) and (4.108), the *equivalency value of gyration resistance* is given by

$$R_{\rm g,eq}^2 = \frac{L_2}{C_0} = \frac{L_0}{C_2}. \tag{4.110}$$

The condition presented in Equation (4.105) is consistent with the condition derived in Equation (4.110) by applying a different approach.

4.10 Example With Circuit Simulator Numerical Results

We present an example here to evaluate the analysis presented in the previous sections. There are many different combinations of values that will satisfy the EPD condition for the PRC's elements, and here we assume the following set of values as an example: $L_1 = 1\,\mu$H, $L_0 = -1\,\mu$H, $C_1 = 0.25$ nF and $C_0 = -1$ nF. The proposed circuit to realize negative element values is explained in Appendix B. The negative inductance and capacitance in the right resonators are necessary to satisfy the EPD condition $\Delta_{{\rm r},h} = 0$. These values lead to $\xi_0 = 10^{15}\,(\text{rad/s})^2$, $\xi_1 = 4\times10^{15}\,(\text{rad/s})^2$ and $\delta = -10^{15}\,(\text{rad/s})^2$ which satisfy the EPD condition presented in Equation (4.24). The results in Figure 4.6(a) illustrate the two branches of the real and imaginary parts of perturbed eigenvalues calculated from the eigenvalue problem in

Equation (4.9), varying C_1 in the neighborhood of $C_{1,\mathrm{e}} = 0.25\,\mathrm{nF}$. In this plot we assume that $\Delta L_0 = \Delta L_1 = \Delta C_0 = 0$ and we only perturb $\Delta C_1 = (C_1 - C_{1,\mathrm{e}})/C_{1,\mathrm{e}}$ by varying C_1. The results in Figure 4.6(b) exhibit the two branches of the real and imaginary parts of perturbed eigenvalues calculated from the eigenvalue problem in Equation (4.9), varying L_1 in the proximity of $L_{1,\mathrm{e}} = 1\,\mu\mathrm{H}$. In this plot, we take into account that $\Delta L_0 = \Delta C_0 = \Delta C_1 = 0$ and we perturb $\Delta L_1 = (L_1 - L_{1,\mathrm{e}})/L_{1,\mathrm{e}}$ by varying L_1. We obtain $s_\mathrm{e} = \mathrm{i}\omega_\mathrm{e} = \mathrm{i}4.47 \times 10^7$ rad/s for this example and the coalesced eigenvalues at EPD are exceedingly sensitive to perturbations in circuit parameters, i.e., elements values. In the vicinity of the EPD, we observe a bifurcation, which is one of the most distinctive features of the EPD [113, 153, 154, 155]. Although the Taylor series expansion fails in the vicinity of an EPD, the Newton-Puiseux series can nevertheless be used to conduct a perturbation analysis [156, Chapter 2].

In order to validate the theoretical results presented in Figures 4.6(a) and (b), we use a time-domain circuit simulator powered by Keysight ADS, the most prestigious software for designing and analyzing circuits. We run the time-domain simulation to compute the voltages (and consequently charges) of the capacitors and take an FFT of the calculated time-domain results to compute the eigenfrequencies. The calculated values based on numerical simulations, i.e., eigenvalues of the circuit $s = \mathrm{i}\omega$, are illustrated in Figures 4.6(a) and (b) by black hollow circles. It is worth noting that the results are obtained in the stable region where the eigenvalues are purely imaginary, i.e., the real parts of the eigenvalues are zero. Further, the eigenvalues are computed only at feasible frequencies, i.e., positive frequencies. The results of circuit simulations are in excellent agreement with those obtained from theoretical calculations.

As a next step, we demonstrate that PRC and GNC can have the same eigenvalues under the conditions outlined in Section 4.9. The PRC with the required values for the elements is shown in 4.7(a) which leads to EPD. The time-domain simulation result generated us-

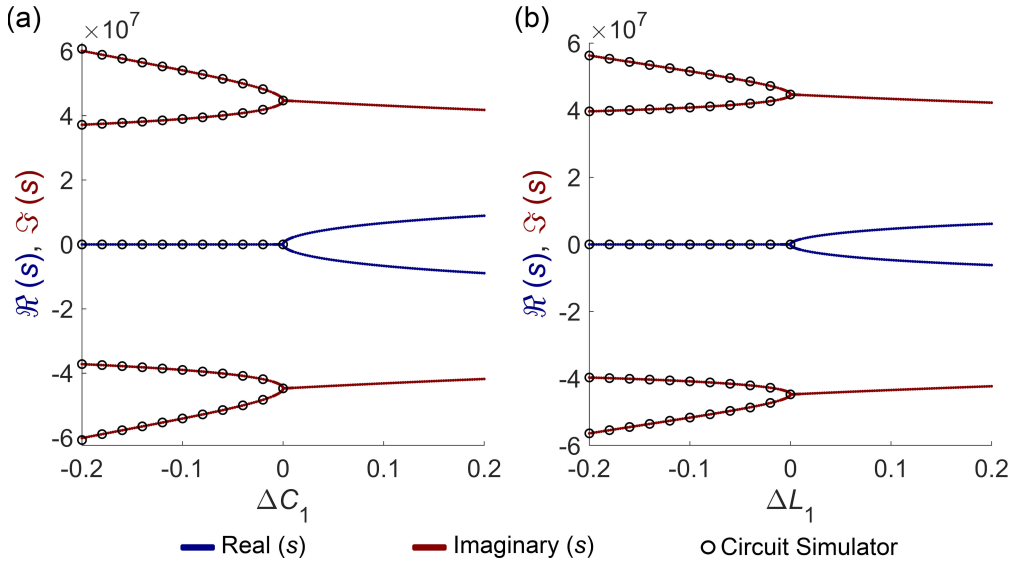

Figure 4.6: The real (dark blue solid curve) and imaginary (dark red solid curve) parts of the four eigenvalues of PRC as in Equation (4.10) assuming that (a) $\Delta L_0 = \Delta L_1 = \Delta C_0 = 0$, and ΔC_1 varies and (b) $\Delta L_0 = \Delta C_0 = \Delta C_1 = 0$, and ΔL_1 varies. In these plots, solid curves represent eigenvalues calculated theoretically, and black hollow circles represent eigenvalues obtained through numerical simulation.

ing the Keysight ADS circuit simulator is shown in Figure 4.7(b), which shows the stored charge Q_0 in the capacitor with negative capacitance C_0. To calculate the charge stored in capacitor C_0, we compute the capacitor voltage V_{C_0} using Keysight ADS and calculate the charge through an equation $Q_0 = C_0 V_{C_0}$. We put 1 mV as an initial voltage on C_1 in the time-domain simulator to establish oscillation. Figure 4.7(b) shows that the stored charge increases linearly with time. A significant aspect of the degeneracy of eigenvalues is that it is the result of coalescing circuit eigenvalues and eigenvectors that are also associated with a double pole in the circuit. It is evident from the linear growth over time that a second-order EPD exists in the circuit.

The GNC with the required values for the elements is shown in 4.7(c), in which the selected values lead to EPD. It is convenient to consider that counterpart capacitances and inductances in both circuits have the same value. So, the values of the elements in the left and right resonators of the GNC are considered equal to the values used in the previous example for the PRC. Also, the equivalency value of the gyration resistance $R_{\mathrm{g,eq}} = 31.621\,\Omega$ is

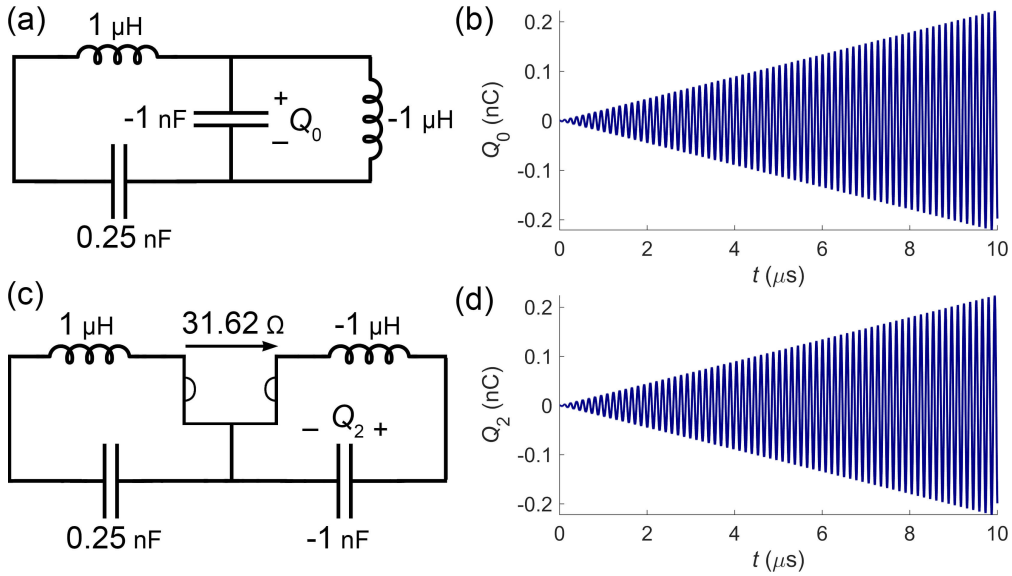

Figure 4.7: Comparison between the time-domain simulation results of (a) the PRC and (c) the GNC with the proposed equivalent element values. The stored charges in the capacitor with the negative capacitance in (b) the PRC $Q_0\,(t)$ and (d) the GNC $Q_2\,(t)$ under the EPD condition and by applying the equivalency conditions.

calculated based on the equivalency condition discussed in Section 4.9. The time-domain simulation result generated using the Keysight ADS circuit simulator is displayed in Figure 4.7(d), which represents the stored charge Q_2 in the capacitor with the negative capacitance C_2. We assigned 1 mV as the initial voltage for C_1 in the time-domain simulator. According to Figure 4.7(d), the stored charge grows linearly with increasing time. In addition, we observe the same behavior of linear growth (i.e., same growth rate) in Figure 4.7(b) and (d), demonstrating the equivalency of eigenfrequencies in the PRC and GNC.

Within the model definition, the negative inductance and capacitance on the right resonator provide energy to the system, and the positive inductance and capacitance on the left absorb energy, when linear growth occurs. The negative capacitance and inductance are realizable in practice using active components, as discussed in Appendix B and in [157].

4.11 Conclusions

We have synthesized a conservative (lossless) electric circuit capable of attaining a non-trivial Jordan canonical form for its circuit matrix and consequently exhibiting an EPD. The circuit is composed of solely conservative reciprocal elements (capacitors and inductors) and the shared capacitance and parallel inductance should be negative. Interestingly, we found that the reciprocal and nonreciprocal circuits presented in our previous chapters can produce exactly the same Jordan canonical form. We also found that the nonreciprocity is manifested in the breakdown of certain symmetries of the set of eigenvectors as well as in the Lagrangian. Further, we have thoroughly tested and confirmed all our significant findings through numerical simulations using commercial circuit simulator software.

Acknowledgments

- This material is based upon work supported by the Air Force Office of Scientific Research (AFOSR) Grant No. FA9550-19-1-0103.

- The text of Chapter 4 of this dissertation is a reprint of the material as it appears in K. Rouhi, F. Capolino, and A. Figotin, "Simple reciprocal electric circuit exhibiting exceptional point of degeneracy," Journal of Physics A: Mathematical and Theoretical, vol. 57, no. 45, Sep. 2024. The coauthors listed in this publication are Alexander Figotin, and Filippo Capolino. Alexander Figotin and Filippo Capolino directed and supervised research which forms the basis for the dissertation.

- The results of this chapter have been published in the journal paper of [21] and in the conference papers of [158, 159].

Chapter 5

Time Modulation to Manage and Increase the Power Harvested From External Vibrations

We investigate how a single resonator with a time-modulated component extracts power from an external ambient source. The collected power is largely dependent on the black precise modulation signal frequency choice. We focus on the power absorbed from external vibration using a mechanical resonator and how time modulation of the damper can make a significant difference in the amount of harvested power, leading to more than 10 times enhancement compared to an analogous system without time modulation. We also find that a narrow band pair of peak and dip in the spectrum of the absorbed power occurs because of the presence of an EPD. In this narrow frequency range, the delay between the damper modulating signal and the external vibrating signal largely affects the collected power. The high frequency-selectivity of EPD-induced power management could potentially be used in sensing and spectrometer applications.

5.1 Background, Motivation, and State of the Art

Energy harvesting has attracted considerable interest in electrical [160, 161] and mechanical [162, 163] systems. It offers a battery-less strategy by recovering energy from ambient sources such as vibrations, wind, etc., and transform it into another form, such as electrical power. Applications include MEMS vibration energy harvesters [164, 165], low-power wireless sensors [166] and fluid energy harvesting [167]. In some of these applications, only a small fraction of energy needs to be extracted to power isolated devices. Therefore, collected power from a nearby ambient source can be used to power the inside isolated circuits. A dynamic system has parametric excitation when the effect of force appears as a coefficient of a variable in the governing equations of motion [168, 169]. The parametric excitation leads to a class of time-varying equations, whose coefficients are explicit functions of time. Parametric excitation can enhance the maximum response attainable in different kind of systems [170]. Different vibration-based energy harvesting methods have been used recently [171, 172, 173, 174, 175, 176], though more work needs to be done on utilizing parametric excitation in time-varying systems. Analogous principles could be used to manage the absorption of vibration or filter out particular vibration frequencies in mechanical systems [177].

Low vibration amplitudes cannot be efficiently collected, hence various approaches are developed to increase energy harvesting efficiency [178, 179]. Vibration energy harvesters have been proposed with different nonlinear arrangements that increase their frequency range and dynamic range, most notably using nonlinear springs and dampers [180, 181]. Moreover, semi-active strategies and nonlinear damping in the form of cubic damping [174, 175] and nonlinear piezoelectric converters [182, 183] have been used to extend an energy harvester's dynamic range. In addition, some have analyzed systems where mass changes over time [184, 185, 186]. However, challenges remain about maximizing the amount of energy harvested, and the ideas should be further explored.

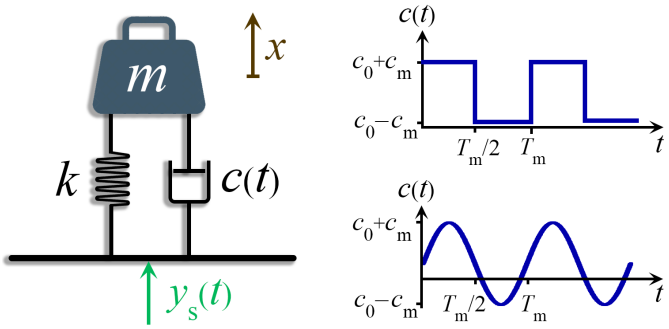

Figure 5.1: Time-modulated mechanical system for kinetic energy harvesting. The external vibrational displacement of the whole system is $y_s(t)$. Two examples of time modulation of the damper are sinusoidal and two-level piece-wise constant (used in this chapter).

In this chapter, a resonator with an LTP damper is considered for harvesting or managing energy from an outside source, focusing on a mechanical mass-spring-damper resonator subject to external vibration [162, 187], as shown in Figure 5.1. However, the physical principle here discussed is general and can be applied to other systems as shown in Sections 5.4 and 5.7. We demonstrate how parametric LTP modulation can boost motion amplitude, enabling a more efficient flow from the energy source to the harvesting system. By applying time variation to the system, power harvesting is improved (even 10 times) in a specific frequency range compared to the unmodulated system. We observe extremely narrow spectral features in the harvested energy spectrum and explain it by resorting to the concept of EPD. Such degeneracy is a point in the parameter space of a resonating system at which multiple eigenmodes coalesce in both their eigenvalues and eigenvectors [3, 62, 18, 114]. The concept of EPD has been investigated in circuits with loss and/or gain under parity-time symmetry [9, 33], and also in spatially [124, 29] and temporally [19, 92, 125] periodic structures. Moreover, the degenerate eigenvalues of the system are exceptionally sensitive to perturbations in system parameters [4] that can be used to achieve high sensitivity in various sensing scenarios [33, 37, 12, 75, 110, 188].

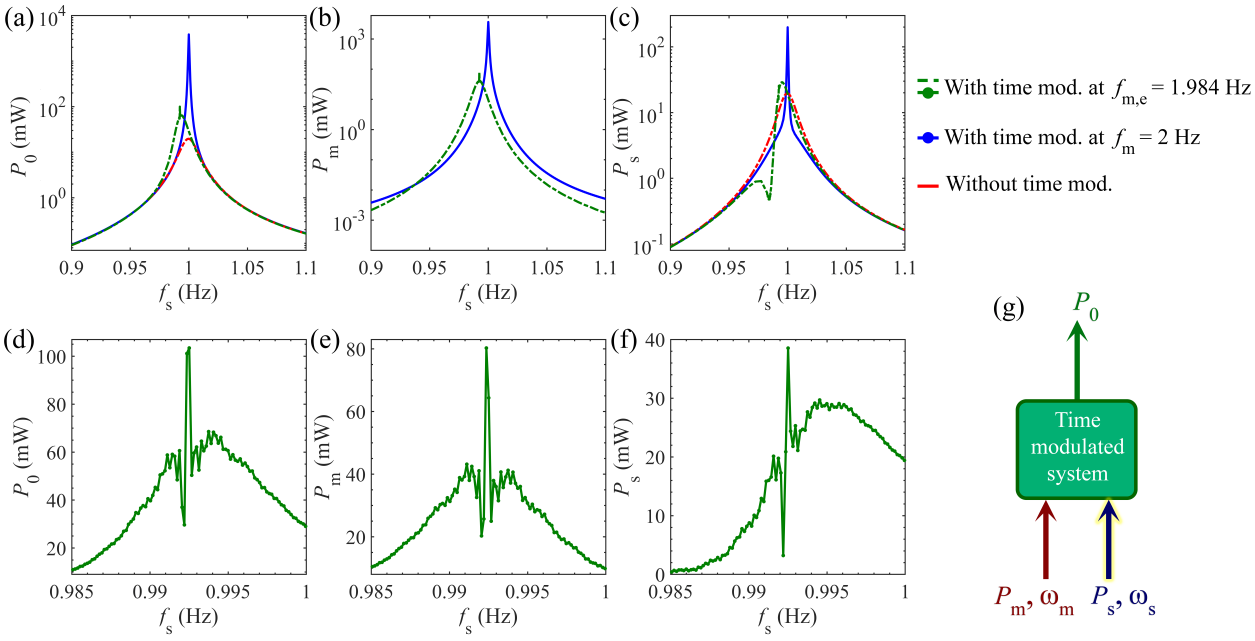

Figure 5.2: Time-averaged power levels after reaching steady state for: (a) P_0 delivered to the damper c_0; (b) P_m provided by the time-varying damper $c_\mathrm{m}(t)$; and (c) P_s extracted (harvested) from the external vibration, by varying the vibration frequency in a wide range around $f_0 = 1\,\mathrm{Hz}$. Two time-modulated cases are considered here: (i) modulation frequency $f_\mathrm{m} = 2\,\mathrm{Hz}$ at the center of the modulation gap (blue), and (ii) modulation frequency $f_\mathrm{m} = f_{\mathrm{m,e}} = 1.984\,\mathrm{Hz}$ (green). For comparison, powers are also shown for the case without time modulation (red). (d)-(f) Zoomed-in analysis for frequencies near the EPD frequency $f_\mathrm{e} = f_{\mathrm{m,e}}/2 = 0.992\,\mathrm{Hz}$ and with time modulation at $f_\mathrm{m} = f_{\mathrm{m,e}} = 1.984\,\mathrm{Hz}$. There is a remarkable highly varying power level around f_e. (g) Collected time-average power P_0 equals the sum of P_m and P_s.

5.2 Mathematical Derivation

The kinetic energy harvesting mechanical scheme discussed here is shown in Figure 5.1. The system consists of a mass connected to a spring and a damper with an additional time-varying portion. It is excited by external monochromatic vibration represented by the imposed displacement $y_\mathrm{s}(t)$, caused by an external force that drives the mechanical resonator. Here, m is the mass, k is the spring stiffness constant, $c(t) = c_0 + c_\mathrm{m}(t)$ is the damping parameter that includes a constant part c_0 and a time-periodic one $c_\mathrm{m}(t)$ of period T_m and x represents the mass displacement. The electric counterpart circuit, the possible practical methods to realize time-modulated dampers and the realistic application of a spring-mass-

damper model are discussed in Section 5.4. The governing equation of the time-varying system is

$$m\ddot{x} + c\left(t\right)\left(\dot{x} - \dot{y}_{\mathrm{s}}\right) + k\left(x - y_{\mathrm{s}}\right) = 0. \tag{5.1}$$

The constant damping coefficient $c_0 = c_{\mathrm{p}} + c_{\mathrm{t}}$ represents the energy losses within the system due to parasitic loss mechanisms c_{p} (e.g., viscous friction with air), and by the intentional mechanism of damping c_{t}, i.e., the mechanical energy extracted by the transduction mechanism [189, 190, 191]. Hence, part of the mobile mass's kinetic energy is lost in mechanical parasitic damping and some other is turned into electricity thanks to an energy converter (e.g., magnet/coil, piezoelectric material, variable capacitor, etc.) [192, 193, 194]. Here, we presume that the damping force is proportional to the velocity, which can be described as an electromechanical transducer [195, Chapter 2]. However, our study is general in nature, and this method can be applied to any system described by the differential equation shown in Equation (5.1). We define the relative mass displacement parameter $z = x - y_{\mathrm{s}}$, and the governing dynamic equation is rewritten as

$$\ddot{z} + 2\zeta\left(t\right)\omega_0\dot{z} + \omega_0^2 z = -\ddot{y}_{\mathrm{s}}, \tag{5.2}$$

where $\zeta\left(t\right) = \zeta_0 + \zeta_{\mathrm{m}}\left(t\right) = c_0/\left(2m\omega_0\right) + c_{\mathrm{m}}\left(t\right)/\left(2m\omega_0\right)$ is the time-modulated damping rate and $\omega_0 = \sqrt{k/m}$ is the natural angular frequency of the unmodulated and lossless system. Assuming a time harmonic dependence of the form $z \propto e^{j\omega t}$ for the *unmodulated* homogeneous system ($c_{\mathrm{m}} = 0$ and $y_{\mathrm{s}} = 0$), we obtain the complex eigenfrequencies $\omega = \omega_0\left(\pm\sqrt{1-\zeta_0^2} + j\zeta_0\right)$ associated to damped oscillations. We define the state vector as $\mathbf{\Psi}\left(t\right) \equiv \left[z, \dot{z}\right]^{\mathrm{T}}$, where the superscript T denotes the transpose operation, leading to

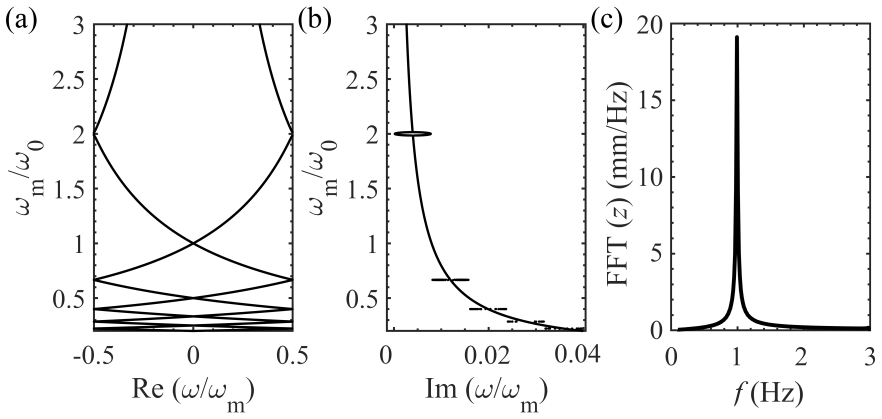

Figure 5.3: The (a) real and (b) imaginary parts of eigenfrequencies $\omega + q\omega_{\mathrm{m}}$, where q is an integer, of the system by varying ω_{m}. (c) Frequency spectrum of the relative mass displacement $z\,(t)$. The largest frequency spectral component of the displacement occurs at the fundamental harmonic $q = 0$, i.e., at the EPD frequency $f_{\mathrm{e}} = f_{\mathrm{m,e}}/2 = 0.992\,\mathrm{Hz}$.

$$\frac{\mathrm{d}\boldsymbol{\Psi}(t)}{\mathrm{d}t} = \underline{\mathbf{M}}\,(t)\,\boldsymbol{\Psi}\,(t) + \begin{pmatrix} 0 \\ \\ -\ddot{y}_{\mathrm{s}} \end{pmatrix}, \quad \underline{\mathbf{M}}\,(t) = \begin{pmatrix} 0 & 1 \\ \\ -\omega_0^2 & -2\zeta\,(t)\,\omega_0 \end{pmatrix}, \tag{5.3}$$

where $\underline{\mathbf{M}}\,(t)$ is the time-variant system matrix. We analyze the power transfer from an external vibration $y_{\mathrm{s}}\,(t) = y_0 \cos\,(2\pi f_{\mathrm{s}} t)$, where y_0 is its amplitude and f_{s} is its frequency, into the LTP spring-mass-damper system using a time-domain numerical simulator (see Section 5.4). We determine the time-averaged power P_{s} delivered by the external vibration, the time-averaged power P_{m} delivered by the time modulation, and the time-averaged power P_0 delivered to (or harvested by) the constant damper c_0. Note that f_{m} is the modulation frequency of the time-varying damper. In realistic applications, particularly those on a small scale, mechanical systems are very small, and ambient vibrations are generally low in amplitude $(0.1 - 5\,\mathrm{m/s^2})$ and frequency $(< 100\,\mathrm{Hz})$ [193]. Because of the low energy of some external sources in realistic applications, we investigate how we can maximize both the power P_{s} absorbed from the external source and the power P_0 harvested by the constant damper by using time modulation.

5.3 EPD Condition and Example of Time-modulated Mechanical System

An example is shown in Figure 5.2, where $k = 4\pi^2\,\mathrm{N/m}$ and $m = 1\,\mathrm{kg}$ leading to $f_0 = 1\,\mathrm{Hz}$, and $y_0 = 1\,\mathrm{mm}$. We only consider for simplicity a two-level piece-wise constant time-periodic damping $c\,(t)$, which is c_0+c_m in the time interval $0 \leqslant t < T_\mathrm{m}/2$ and c_0-c_m in $T_\mathrm{m}/2 \leqslant t < T_\mathrm{m}$. We assume $c_0 = 0.1\,\mathrm{Ns/m}$ and $c_\mathrm{m} = 0.15\,\mathrm{Ns/m}$. We also study the unmodulated system with constant damper $c\,(t) = c_0$, where maximum energy can be extracted when the excitation frequency f_s matches the natural frequency of the system f_0. In Figure 5.2 we compare the LTP system with the unmodulated system to show that time modulation has a strong effect on the time-averaged powers P_s and P_0. For the considered modulation frequency of $f_\mathrm{m} = 2\,\mathrm{Hz}$ that is equal to $2f_0$, P_s and P_0 are largely enhanced when f_s is in the neighbor of f_0. The plot in Figure 5.2(c) shows the maximum harvested power in the unmodulated system is $P_\mathrm{s} = 19.7\,\mathrm{mW}$, whereas the maximum power that the time modulated system absorbs from the source is $P_\mathrm{s} = 198.4\,\mathrm{mW}$ (10 times higher).

The results in Figures 5.2(a)-(c) show also another interesting feature, i.e., the very narrow frequency range around $f_\mathrm{s} = 0.992\,\mathrm{Hz}$ (which is half of $f_\mathrm{m,e}$) where the power exhibits a sharp maximum and a local minimum when $f_\mathrm{m} = f_\mathrm{m,e}$, where $f_\mathrm{m,e} = 1.984\,\mathrm{Hz}$ is a modulation frequency that leads to the EPD. This rapid power level variation is shown better in the zoomed-in frequency region in Figures 5.2(d)-(f). To understand the reasons for this very sharp variations in the time averaged power values we look at the eigenvalues of the system and their degeneracy.

We look at the eigenstates of the time-varying system without external vibration. The evolution of the state vector in the LTP system with time periodicity T_m is given by $\mathbf{\Psi}\,(t+T_\mathrm{m}) = \underline{\mathbf{\Phi}}\,(t+T_\mathrm{m},t)\,\mathbf{\Psi}\,(t)$, where $\underline{\mathbf{\Phi}}\,(t+T_\mathrm{m},t) = e^{\underline{\mathbf{M}}_2 T_\mathrm{m}/2} e^{\underline{\mathbf{M}}_1 T_\mathrm{m}/2}$ is the state transition matrix, where $\underline{\mathbf{M}}_1$ and $\underline{\mathbf{M}}_2$ are the system matrices in the first and second time intervals

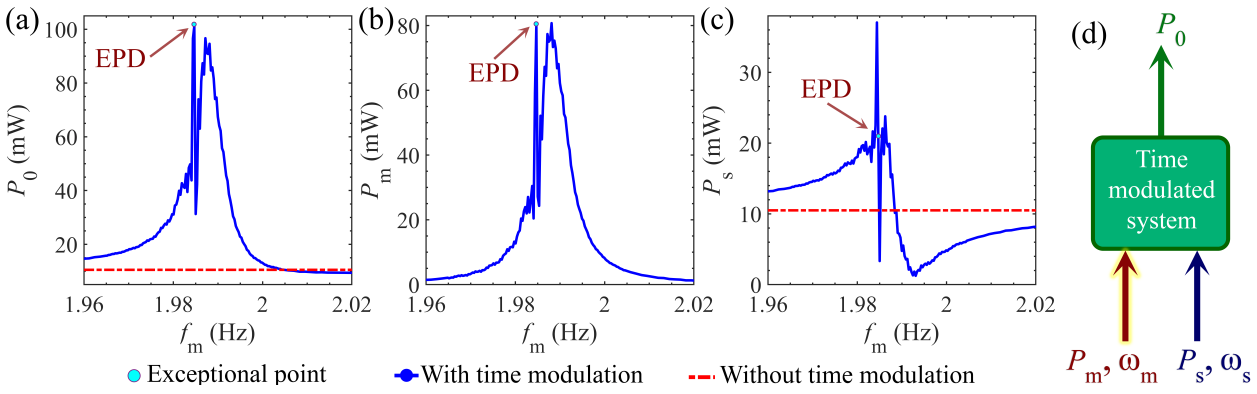

Figure 5.4: Time-averaged powers by varying the modulation frequency f_m (blue curves), for the case of $f_\mathrm{s} = f_\mathrm{m,e}/2$. (a) P_0; (b) P_m; and (c) P_s. The red dashed line is the time-averaged power level of the unmodulated system. (d) Collected time-average power P_0 equals the sum of P_m and P_s.

[196, Chapter 2]. We look for eigensolutions of the system that satisfy

$$\mathbf{\Psi}\left(t + T_\mathrm{m}\right) = e^{j\omega T_\mathrm{m}}\mathbf{\Psi}\left(t\right), \tag{5.4}$$

where ω (with all the harmonics $\omega + 2\pi q/T_\mathrm{m}$, where q is an integer) is the complex eigenfrequency. Therefore, the eigenvalue problem is

$$\underline{\mathbf{\Phi}}\mathbf{\Psi}\left(t\right) = \lambda\mathbf{\Psi}\left(t\right), \tag{5.5}$$

and the eigenvalues $\lambda_n = e^{j\omega_n T_\mathrm{m}}, n = 1, 2$, are obtained by solving the characteristic polynomial equation $\det\left(\underline{\mathbf{\Phi}} - \lambda\underline{\boldsymbol{I}}\right) = 0$. The eigensolutions $\mathbf{\Psi}\left(t\right)$ have Fourier harmonics with frequencies $\omega_n + q\omega_\mathrm{m}$, where $\omega_\mathrm{m} = 2\pi f_\mathrm{m}$ is the modulation angular frequency [19]. When a transition matrix made of real values elements describes the system, the characteristic polynomial has real coefficients, so the eigenvalues are either real or complex conjugate pairs. The transition matrix determinant is written as [196, Chapter 2]

$$\det\left(\underline{\mathbf{\Phi}}\right) = \lambda_1\lambda_2 = e^{[\mathrm{tr}(\underline{\mathbf{M}}_1 T_\mathrm{m}/2)+\mathrm{tr}(\underline{\mathbf{M}}_2 T_\mathrm{m}/2)]}, \tag{5.6}$$

where tr is the trace of the matrix. The determinant can be either $\det\left(\underline{\mathbf{\Phi}}\right) = e^{2\mathrm{Im}(\omega_1)T_\mathrm{m}}$, when eigenvalues are complex conjugate pair, or $\det\left(\underline{\mathbf{\Phi}}\right) = e^{js\pi}e^{(\mathrm{Im}(\omega_1)+\mathrm{Im}(\omega_2))T_\mathrm{m}}$, when λ_1 and λ_2 are both real and s is an integer. The two eigenvalues are

$$\lambda_{1,2} = \frac{\mathrm{tr}\left(\underline{\mathbf{\Phi}}\right)}{2} \pm \sqrt{\left(\frac{\mathrm{tr}\left(\underline{\mathbf{\Phi}}\right)}{2}\right)^2 - \det\left(\underline{\mathbf{\Phi}}\right)}, \tag{5.7}$$

and the two associated eigenvectors are

$$\mathbf{\Psi}_1 = \begin{bmatrix} \varphi_{12} \\ \\ \lambda_1 - \varphi_{11} \end{bmatrix}, \ \mathbf{\Psi}_2 = \begin{bmatrix} \varphi_{12} \\ \\ \lambda_2 - \varphi_{11} \end{bmatrix}, \tag{5.8}$$

where φ_{11} and φ_{12} are elements of the matrix $\underline{\mathbf{\Phi}}$. The two eigenvalues are degenerate ($\lambda_1 = \lambda_2 = \mathrm{tr}\left(\underline{\mathbf{\Phi}}\right)/2$) when

$$\mathrm{tr}\left(\underline{\mathbf{\Phi}}\right) = \pm 2\sqrt{\det\left(\underline{\mathbf{\Phi}}\right)}. \tag{5.9}$$

According to Equation (5.8), degenerate eigenvalues result in degenerate eigenvectors. A transition matrix at an EPD is similar to a Jordan block with two degenerate eigenvalues associated with degenerate eigenvectors. As a matter of energy analysis, in a time-periodic system energy can be transferred into or out of the system via the time-variation mechanism.

The system's eigenfrequency dispersion diagram is shown in Figures 5.3(a) and (b). EPDs happen at two modulated frequencies, $f_{\mathrm{m,e}} = 1.984$Hz and $f_{\mathrm{m,e}} = 2.015$Hz. The quality factor

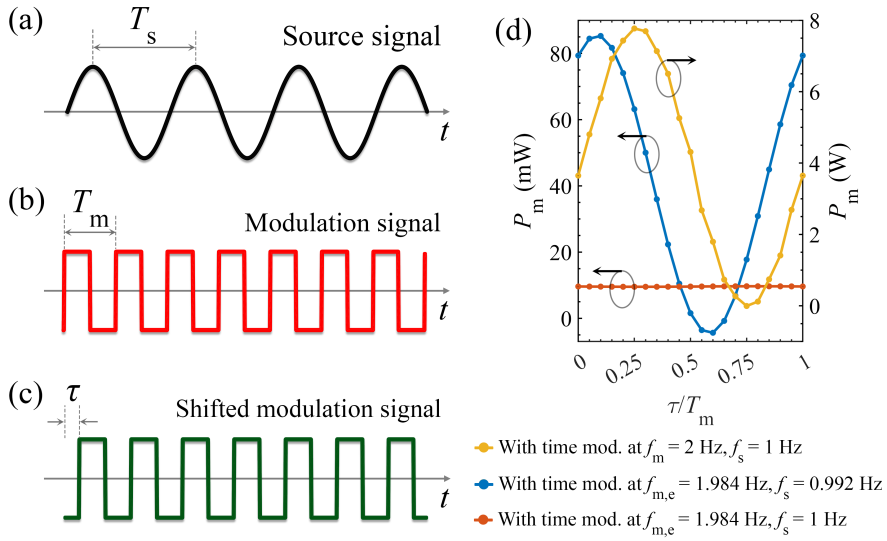

Figure 5.5: (a) Source sinusoidal signal with a period of $T_s = 2T_m$. (b) Piece-wise constant time modulated damper with a period of T_m and (c) shifted by a delay τ. (d) Time-averaged power P_m versus delay τ for three different scenarios.

of a resonating system is $Q = \mathrm{Re}(\omega) / (2\mathrm{Im}(\omega))$, that is higher for smaller $\mathrm{Im}(\omega)$. In general, a higher quality factor implies a higher power harvested by the system. A modulation gap in the dispersion diagram of eigenfrequencies happens when the two eigenfrequencies have two non-vanishing imaginary parts, i.e., between two closeby EPDs. When the modulation frequency is selected in the middle of the modulation gap, i.e., $f_m = 2\,\mathrm{Hz}$, one eigenfrequency has the smaller $\mathrm{Im}(\omega)$, corresponding to a better quality factor compared to the two neighbor EPDs at slightly higher and lower frequencies. Thus, we expect the largest improvement in harvested power in the middle of the modulation gap. Also, by selecting $f_{m,e} = 1.984\,\mathrm{Hz}$ the system experiences harsh changes around $f_s = f_{m,e}/2 = 0.992\mathrm{Hz}$ due to the degeneracy of the eigenfrequencies. The spectrum of the relative displacement $z(t)$ when the source-free system is modulated at $f_m = f_{m,e} = 1.984\,\mathrm{Hz}$ and it is excited by an initial condition (see Section 5.4) is illustrated in Figure 5.3(c). The spectrum peak is observed at $f_e = f_{m,e}/2 = 0.992\,\mathrm{Hz}$, that is same as the one obtained from solving the eigenvalue problem shown in Figures 5.3(a) and (b).

When $f_m = f_{m,e} = 1.984\,\mathrm{Hz}$, the mechanical system operates at the EPD. The frequency

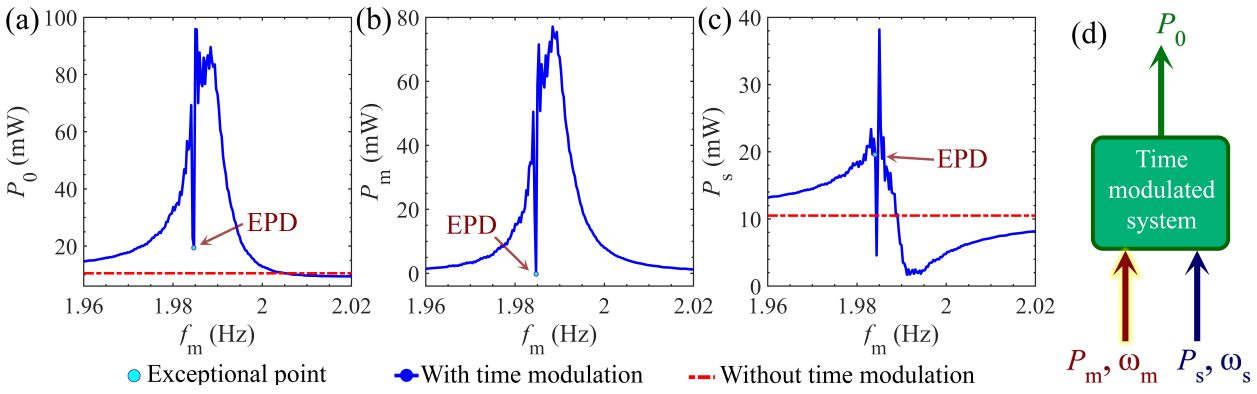

Figure 5.6: Time-averaged power levels, after reaching steady state, as in Figure 5.4, but assuming a time delay $\tau = 0.51T_{\mathrm{m}}$ in the modulation of the damper, in the case of $f_{\mathrm{s}} = f_{\mathrm{m,e}}/2$.

spectrum in Figure 5.3(c) shows that the first harmonic at $f = f_{\mathrm{e}} = f_{\mathrm{m,e}}/2 = 0.992\,\mathrm{Hz}$, carries the maximum power. After setting $f_{\mathrm{s}} = f_{\mathrm{e}} = f_{\mathrm{m,e}}/2 = 0.992\,\mathrm{Hz}$, Figure 5.4 shows the powers by varying the modulation frequency around its EPD value $f_{\mathrm{m,e}} = 1.984\,\mathrm{Hz}$. In this plot, time-modulated case is in blue curve, whereas the red dashed-line reminds the power values of the system without time-modulation. The numerical results show that the system operating close to EPD (cyan point) harvests more power from the external source ($P_{\mathrm{s}} = 20.9\,\mathrm{mW}$) compared to the system without time-modulation ($P_{\mathrm{s}} = 10.5\,\mathrm{mW}$). Thus, time modulation leads to harvest more power from external vibration, with an improvement of 99%. In addition, the time-modulated element delivers the power of $P_{\mathrm{m}} = 80.3\,\mathrm{mW}$ to the system and the constant part of the damper absorbs $P_0 = P_{\mathrm{s}} + P_{\mathrm{m}} = 101.2\,\mathrm{mW}$ from the system, at the EPD frequency.

The eigenfrequencies near the EPD are very sensitive to a system's variation, like a small change in the modulation frequency, as discussed in Section 5.6. When such a small relative perturbation $\delta_{\mathrm{m}} = (f_{\mathrm{m}} - f_{\mathrm{m,e}})/f_{\mathrm{m,e}}$ is applied, the resulting two distinct eigenfrequencies $f_{1,2}(\delta_{\mathrm{m}})$ are estimated using the Puiseux series power expansion $f_{1,2}(\delta_{\mathrm{m}}) \approx f_{\mathrm{e}} \mp j\,(f_{\mathrm{m}}/2\pi)\,\alpha_1\sqrt{\delta_{\mathrm{m}}}$ [125], where α_1 is the first-order expansion coefficient. The square root function demonstrates that the eigenfrequencies are highly sensitive to modulation frequency perturbations around the EPD, as shown in Figure 5.3. This is reflected by the power levels

that change dramatically when a small change in f_{m} is applied, as shown in Figure 5.4. To harvest power, the modulation frequency must be chosen precisely, very close to the EPD frequency. It could be chosen exactly either at the EPD or between the two EPD frequencies as explained in the following.

To control the power provided by the time modulated portion of the circuit, Figure 5.5(d) shows P_{m} delivered by $c_{\mathrm{m}}(t)$ versus delay τ. Three combinations of modulation and source frequencies are considered. For the two cases shown with blue and yellow curves in Figure 5.5(d), we assume that the frequency of the source is fixed to $f_{\mathrm{s}} = f_{\mathrm{m}}/2$, hence, the period of the modulation signal is half of the source's one when operating at the EPD ($T_{\mathrm{m,e}} = T_{\mathrm{s}}/2$). In the third case (orange line), we assume that $f_{\mathrm{m}} = f_{\mathrm{m,e}}$, and source frequency at $f_{\mathrm{s}} = 1\,\mathrm{Hz}$. It is clear that the variation of the delay τ has a strong effect on P_{m} when the modulation frequency is selected as $f_{\mathrm{m}} = 2f_{\mathrm{s}}$ (both blue and yellow curves). However, in the case shown by the orange curve, which is a slight modification from the other two cases, P_{m} is more or less constant and the delay does not have much effect on it. When $f_{\mathrm{m}} = f_{\mathrm{m,e}}$, and $f_{\mathrm{s}} = f_{\mathrm{m}}/2$ (blue curve), and at a specific delay $\tau = 0.51T_{\mathrm{m}}$, the power delivered by the time-varying damper reaches the minimum and it is as small as $P_{\mathrm{m}} = 0.04\,\mathrm{mW}$. By assuming the latter particular condition with $f_{\mathrm{s}} = f_{\mathrm{m,e}}/2$ and $\tau = 0.51T_{\mathrm{m}}$, the numerical results in Figure 5.6 show the source, modulation and constant damper powers by varying the modulation frequency (compared to the results in Figure 5.4, where $\tau = 0$). Blue curves represent the power in the system with time modulation (note that the modulated power is near zero at the EPD), while red curves illustrate the power levels for the case without time modulation, as was done in Figure 5.4. At the EPD modulation frequency $f_{\mathrm{m}} = f_{\mathrm{m,e}} = 1.984\mathrm{Hz}$ (cyan point), the power extracted from the source vibration is $P_{\mathrm{s}} = 19.38\,\mathrm{mW}$ and the power delivered to the constant part of the damper is $P_0 = 19.42\,\mathrm{mW}$. Thus, time modulation improves power harvesting by 85% compared to the case without time modulation. Note also that in this case the power delivered by the modulation is very small ($P_0 \approx P_{\mathrm{s}}$). However, the calculated powers around the EPD vary dramatically when changing the modulation frequency. That

is one of the most peculiar properties associated with an EPD, as already depicted in Figures 5.4, and 5.6. The reason is that the eigenstates at the EPD are extremely sensitive to any perturbation, as shown in Figure 5.3, which causes large variation when interacting with forced excitation. The system could possibly harvest even more power with a precise choice of modulation frequency close to EPD and proper time delay. However, even without a precise modulation frequency choice, the system harvests more power on average, over f_{s} or f_{m} variation.

5.4 Dual Circuit With Time-Modulated Conductance

We show the analogous (dual) system made of a LC resonator and an LTP conductance connected to the external source in series to the capacitor as shown in Figure 5.7. In order to calculate the power in the dual LTP system, we consider piece-wise constant time-periodic conductance $G(t)$, i.e., $G(t) = G_0 + G_{\mathrm{m}}$ during the time interval $0 \leq t < T_{\mathrm{m}}/2$, and $G(t) = G_0 - G_{\mathrm{m}}$ during the time interval $T_{\mathrm{m}}/2 \leq t < T_{\mathrm{m}}$. Analogously to the mechanical LTP system, we define the system state vector as $\mathbf{\Psi}(t) = [v(t), \dot{v}(t)]^{\mathrm{T}}$, where $v(t)$ is the voltage on the inductor and $\dot{v}(t)$ is its time derivative. In general, $G(t)$ can be either lossy or gain (positive or negative respectively). Kirchhoff's circuit laws apply to time-varying circuits as follows:

$$G(t)\,\dot{v} + \frac{v}{L} + C\left(\ddot{v} + \ddot{v}_{\mathrm{s}}\right) = 0. \tag{5.10}$$

The circuit equation is rewritten as

$$\ddot{v} + 2\alpha(t)\,\dot{v} + \omega_0^2 v = -\ddot{v}_{\mathrm{s}}. \tag{5.11}$$

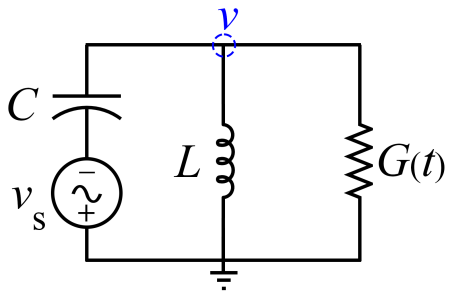

Figure 5.7: The dual time-varying circuit where an inductance is connected in parallel to a time-varying conductance, with an external source $v_{\mathrm{s}}(t)$ in series to the capacitor. The conductance is designed to have a two-level piece-wise constant time-periodic conductance, where $G(t) = G_0 + G_{\mathrm{m}}$ during the time interval $0 \leq t < T_{\mathrm{m}}/2$, and $G(t) = G_0 - G_{\mathrm{m}}$ during the time interval $T_{\mathrm{m}}/2 \leq t < T_{\mathrm{m}}$.

where $\alpha(t) = \alpha_0 + \alpha_{\mathrm{m}}(t) = G_0/(2C) + G_{\mathrm{m}}(t)/(2C)$ is the time-modulated damping factor and $\omega_0 = 1/\sqrt{LC}$ is the natural frequency of the unmodulated and lossless circuit. Assuming time harmonic dependence of the form $v \propto e^{j\omega t}$ for the unmodulated homogeneous circuit, we obtain the eigenfrequencies as $\omega = j\alpha(1 \pm \sqrt{1-\omega_0^2/\alpha^2})$. By writing the differential equation in the eigenvalue problem format, the time evolution of the state vector $\mathbf{\Psi}(t)$ is given by

$$\frac{\mathrm{d}\mathbf{\Psi}(t)}{\mathrm{d}t} = \underline{\mathbf{M}}_{\mathrm{c}}(t)\,\mathbf{\Psi}(t) + \begin{pmatrix} 0 \\ \\ -\ddot{v}_s \end{pmatrix}, \quad \underline{\mathbf{M}}_{\mathrm{c}}(t) = \begin{pmatrix} 0 & 1 \\ \\ -\omega_0^2 & -2\alpha(t) \end{pmatrix}, \tag{5.12}$$

where $\underline{\mathbf{M}}_{\mathrm{c}}(t)$ is the equivalent circuit matrix. The differential equation and the circuit matrix are dual to the time-varying mechanical system whose time-varying damper is connected to the spring and mass. The duality transformation is $k \to 1/L$, $m \to C$ and $c(t) \to G(t)$ and both systems have an external excitation $\ddot{y}(t) \to \ddot{v}_{\mathrm{s}}(t)$ as summarized in Table 5.1 [197]. Also, we show the duality of the characteristic equations in mechanical systems and their dual version in electric circuits in Table 5.2. By applying the conversion between force and current ($\mathscr{F} \longleftrightarrow i$) and velocity and voltage ($\dot{z} \longleftrightarrow v$), Newton's equations and instantaneous mechanical power relate to the electric dual equations. We analyze the dual

LTP circuit by using the Keysight ADS time-domain simulator to calculate the power. We excite the circuit with a sinusoidal source at a frequency of f_{s} and the amplitude of 10 mV. Also, the capacitor has a 10 mV as an initial condition for the case where no external source excites the system. We numerically calculate the power using a built-in power block in the simulator and then report the time-averaged power based on 1000 time periods after the time domain signal saturates (i.e., for the time window from 3500 s to 4500 s).

Table 5.1: Component values in the mechanical system and their dual values in the dual electrical circuit.

Mechanical system	Dual electrical circuit	Duality
$k = 4\pi^2\ \mathrm{N/m}$	$L = 0.025\ \mathrm{H}$	$k \to 1/L$
$m = 1\ \mathrm{kg}$	$C = 1\ \mathrm{F}$	$m \to C$
$c_0 = 0.1\ \mathrm{Ns/m}$	$G_0 = 0.1\ \mathrm{S}$	$c_0 \to G_0$
$c_{\mathrm{m}} = 0.15\ \mathrm{Ns/m}$	$G_{\mathrm{m}} = 0.15\ \mathrm{S}$	$c_{\mathrm{m}} \to G_{\mathrm{m}}$
$c(t) = \begin{cases} c_0 + c_{\mathrm{m}}, & 0 \le t < T_{\mathrm{m}}/2 \\ c_0 - c_{\mathrm{m}}, & T_{\mathrm{m}}/2 \le t < T_{\mathrm{m}} \end{cases}$	$G(t) = \begin{cases} G_0 + G_{\mathrm{m}}, & 0 \le t < T_{\mathrm{m}}/2 \\ G_0 - G_{\mathrm{m}}, & T_{\mathrm{m}}/2 \le t < T_{\mathrm{m}} \end{cases}$	$c(t) \to G(t)$

Table 5.2: Dual equations in the mechanical system and dual electrical circuit, where $\mathscr{F}$ is the force and i is the current.

Mechanical system		Dual electrical circuit	
Spring	$\mathscr{F} = kz$	$i = (1/L)\int v\, dt'$	Inductor
Mass	$\mathscr{F} = m\ddot{z}$	$i = C\dot{v}$	Capacitor
Damper	$\mathscr{F} = c\dot{z}$	$i = Gv$	Conductance
Mechanical Power	$p = \mathscr{F}\dot{z}$	$p = iv$	Electrical Power
Duality			
$\mathscr{F} \longleftrightarrow i$			
$\dot{z} \longleftrightarrow v$			

5.5 Vibration Conversion

As already mentioned, $c_0 = c_\mathrm{p} + c_\mathrm{t}$ is responsible for the energy losses within the system due to parasitic loss mechanisms c_p (e.g., viscous friction with air), and by the intentional mechanism of damping c_t, i.e., the mechanical energy extracted by the transduction mechanism. This model is based on the idea that converting energy from an oscillating mass to electricity (whatever the mechanism is) can be modeled as a linear damper in a mass-spring system. This model is quite accurate for certain types of electromechanical converters, such as those analyzed by Williams and Yates [198]. For other types of converter, such as electrostatic and piezoelectric, the model may be modified. However, the conversion will always result in a loss of mechanical kinetic energy, which can be referred to as damping [199]. Despite the fact that the current damper model does not accurately model all kinds converter types, the present analysis can be extended to electrostatic and piezoelectric systems [199]. The power extracted from the mechanical system via c_t is due to electrically induced damping and it is constitutes the whole time-averaged power P_0 if the parasitic damping vanishes. The instantaneous power in the constant part of the damper c_0, i.e., the combination of parasitic loss mechanisms c_p and transduction mechanism c_t, can be calculated as a product of induced force $c_0\dot{z}$ and velocity $\dot{z}$. Thus, the absorbed instantaneous power in the constant part of the damper is expressed by

$$p_0(t) = c_0\dot{z}^2. \tag{5.13}$$

The total time-averaged power P_0 is calculated by averaging the time domain expression. In a monochromatic regime, assuming no modulation, the total time-averaged power dissipated within the damper, i.e., the power extracted via the transduction mechanism and the power lost by parasitic damping mechanisms, is given by [190, 195, 200]

$$P_0 = \frac{m\zeta_0\omega_0\omega_{\mathrm{s}}^2\left(\frac{\omega_{\mathrm{s}}}{\omega_0}\right)^3 y_0^2}{\left(2\zeta_0\frac{\omega_{\mathrm{s}}}{\omega_0}\right)^2 + \left(1-\left(\frac{\omega_{\mathrm{s}}}{\omega_0}\right)^2\right)^2}, \tag{5.14}$$

where y_0 is the magnitude of the source vibration, $\zeta_0 = \zeta_{\mathrm{t}} + \zeta_{\mathrm{p}} = c_0/\left(2m\omega_0\right)$ is the constant damping ratio. Maximum power dissipation within the generator occurs when the device is operated at $\omega_{\mathrm{s}} = \omega_0$, and in this case the total time-averaged power dissipated in the constant part of the damper is given by

$$P_0 = \frac{m\omega_0^3 y_0^2}{4\zeta_0}. \tag{5.15}$$

5.6 Sensitivity to Perturbation

Sensitivity of a system's observable to a particular parameter is a measure of how much a perturbation to that parameter affects the observable quantity of the system. The eigenvalues of the system at EPDs are extremely sensitive to parameter changes, which is a significant feature. Applying a perturbation to a system parameter such as the modulation frequency $\delta_{\mathrm{m}} = \left(f_{\mathrm{m}} - f_{\mathrm{m,e}}\right)/f_{\mathrm{m,e}}$, leads to a perturbed transition matrix $\underline{\mathbf{\Phi}}\left(\delta_{\mathrm{m}}\right)$ and perturbed eigenvalues $\lambda_p\left(\delta_{\mathrm{m}}\right)$, with $p = 1, 2$. Therefore, the degenerate resonance frequency occurring at the EPD f_{e}, splits into two distinct resonance frequencies $f_p\left(\delta_{\mathrm{m}}\right)$, due to a small perturbation δ_{m}. We can calculate the perturbed eigenvalues near the EPD by using the convergent Puiseux fractional power series expansion, with coefficients calculated using the explicit recursive formulas in [91]. In the presented mechanical system with a second-order EPD, we utilize a first-order approximation of the perturbed eigenvalues as

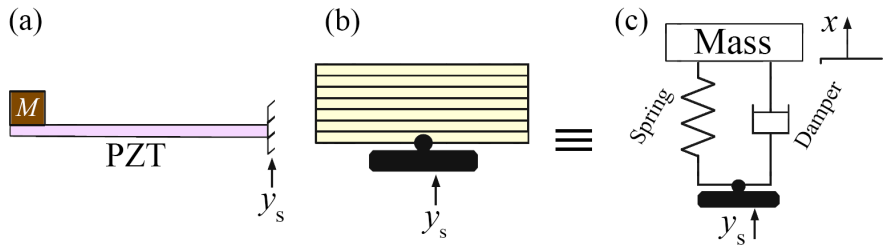

Figure 5.8: (a) The cantilever beam with tip mass, (b) multilayer PZT subjected to transverse external vibration excited at the base and (c) equivalent lumped spring-mass-damper system.

$$\lambda_p\left(\delta_{\mathrm{m}}\right) \approx \lambda_{\mathrm{e}} + (-1)^p \alpha_1 \sqrt{\delta_{\mathrm{m}}}, \tag{5.16}$$

where λ_{e} is the eigenvalue at EPD and the first order coefficient is expressed by

$$\alpha_1 = \left(-\frac{\partial H\left(\delta_{\mathrm{m}}, \lambda\right)/\partial \delta_{\mathrm{m}}}{\frac{1}{2!}\partial^2 H\left(\delta_{\mathrm{m}}, \lambda\right)/\partial \lambda^2} \right)^{\frac{1}{2}} \Bigg|_{\delta_{\mathrm{m}}=0,\, \lambda=\lambda_{\mathrm{e}}}, \tag{5.17}$$

where $H\left(\delta_{\mathrm{m}}, \lambda\right) = \det\left(\underline{\mathbf{\Phi}}\left(\delta_{\mathrm{m}}\right) - \lambda \underline{\mathbf{I}}\right)$ and $\underline{\mathbf{I}}$ is the 2×2 identity matrix. The perturbed resonance frequencies are approximately calculated as

$$f_p\left(\delta_{\mathrm{m}}\right) \approx f_{\mathrm{e}} \pm j \frac{f_{\mathrm{m}}}{2\pi} (-1)^p \alpha_1 \sqrt{\delta_{\mathrm{m}}}. \tag{5.18}$$

This formula proves that the time-modulated system supporting the EPD is very sensitive to variations in the modulation frequency f_{m}. Figures 5.2, 5.4 and 5.6 demonstrate that the harvested power is very sensitive to variations in the system's parameters when operating at or near an EPD.

5.7 Realistic Applications

In general, a mechanical model based on a spring–mass system gives a meaningful description of vibration behavior and can be used to model energy harvesting devices and inertial-based generators. For example, the cantilever can be represented by its equivalent model, which is composed of a mass, a spring and a damper. All these components are enclosed in a casing and mechanically connected to the vibration source. The most common examples of cantilever design are cantilevered balconies, walkways, and overhangs, as well as some parts of bridge designs [201, Chapter 4], [202, Chapter 11]. In addition, our method can be extended to piezomagnetoelastic cantilevers [192, 203], a basic bimorph piezoelectric cantilever [201, Chapter 4], and a piezoelectric pendulum [204] in a realistic setup.

Figure 5.8(a) shows a diagram of a cantilever beam with piezoelectric plates bonded on a substrate and a proof mass at the end; Figure 5.8(b) shows multilayer piezoelectric plates and Figure 5.8(c) provides the equivalent lumped spring-mass with external excitation. For piezoelectric energy harvesting devices, cantilever structures with tip masses are the most commonly used configurations. The vibration source is shown with an arrow at the base of the contact point. The configuration shown in Figure 5.8(c) applies to both the energy harvesting mechanisms illustrated in Figure 5.8(a) and (b).

5.8 Realization of Time-modulated Damper

The time varying mechanisms can be implemented in realistic designs using tunable/controllable devices. For example, a controllable damper can be realized via variable orifice dampers with an external actuator modifying the orifice diameter, controllable fluid dampers and adjustable tuned liquid dampers [205, 206, 207, 174]. The variable orifice dampers have shown relatively low response speeds. However, in recent years, magneto-rheological dampers where

the viscosity of the magnetic fluid is controlled via tuning of the field have received considerable attention due to their ability to rapidly alter their properties in response to the applied magnetic field [208]. In this configuration, variable damping control can be achieved by varying a small electric current to the magneto-rheological dampers [209, 210, 211].

An alternative method of achieving semi-active damping is the use of electro-rheological fluids whose viscosity can be controlled by applying an electric field. This technology has been applied to the control of semi-active suspensions and flexible structures [212, 213, 214]. More investigation into the tunability methods and review of the recent works in this area can be found in [208]. We can therefore realize the time-modulated damper needed for our proposed structure by varying the damping coefficient periodically via the described approaches.

5.9 Scale Parameter in the Mechanical System

In this chapter, we adopted practical values for system parameters. However, according to the governing equation of the time-varying system, parameters can be scaled by a factor S as shown in Table (5.3).

Table 5.3: Parameters in the mechanical system scalable by factor S.

Parameter	Scale
Mass	$m \to Sm$
Spring stiffness	$k \to Sk$
Damper damping	$c \to Sc$

As a result of applying this transformation, we obtain the same governing equation with the same eigenvalues.

5.10 Noise in the Energy Harvesting Systems

Ambient noise may strongly influence the energy harvesters performance, therefore it is important to study energy harvesting systems to improve the performance. For developing micropower generators applicable to noise environments, it has become important to harvest energy utilizing different mechanisms. Even though many configurations have been developed to harvest ambient vibration energy, crucial questions remain about how to optimize performance under different noise levels [215]. The efficiency of harvesting energy from noise has also been explored by some researchers [216, 217, 218, 219, 220, 221, 222, 223, 224]. Borowiec et al. [225] investigated the effect of noise on energy harvester performance.

In summary, noise in an energy harvesting system has been investigated from different perspectives. First, noise can affect the main resonator and the relevant circuit. Nevertheless, the resonator is isolated from the environment, which minimizes the noise effects. Secondly, noise in the ambient source can affect energy harvesting system performance. For instance, Liu et al. proposed a stochastic averaging method to study the response characteristics of an energy harvesting system in the case of colored noise [220]. Also, Su et al. analyzed the effect of Gaussian white noise intensity on the system [226]. Moreover, the influence of ambient sinusoidal excitation and additive noise on the energy harvesting performance of piecewise bistable energy harvesters were investigated in [227]. Considering the importance of this topic, many other studies have studied noise's effect on ambient sources in detail [228, 229, 230, 231, 232, 233, 234, 235]. Furthermore, noise may be a source of energy, and an energy harvester could be designed in such a way that it extracts the maximum power from the statistical external noise [236, 237, 238, 239]. Finally, noise may be affected by EPDs. Some papers have discussed the relation between noise and EPD and provided methods to analyze it [240, 241, 242, 15, 72, 243, 244, 245, 246, 17]. However, this subject is beyond the scope of this paper and requires a separate in-depth study.

5.11 Conclusions

As a conclusion, we have shown that a mechanical resonator with time modulation harvests much higher power (even ten times higher) from ambient vibration than its counterpart without time modulation. Moreover, using the concept of second-order EPDs, we also explain the existence of a very sharp spectral peak at some modulation frequencies. The power levels vary rapidly with only a very slight variation in a parameter (like modulation frequency). Indeed, using the Puiseux fractional series expansion, we have demonstrated that the degenerated system's eigenfrequency is highly sensitive to perturbations in the modulation frequency. It would be possible to use this effect for sensing applications or very precise spectrometers. The physics associated with an EPD in an LTP mechanical system is vital for getting a deeper insight into different ways to improve the narrow frequency features of the power transfer mechanism. We used a time-modulated damping factor that could be realized in a variety of ways including magneto-rheological or electro-rheological dampers where the damping factor can be tuned by changing fields. Specifically, the improvement in harvesting power is advantageous for applications with low energy requirements and low ambient source amplitude where direct access to the device is not possible and battery recharging or replacement is not feasible such as wireless sensors, bio-implantable devices, wireless body area networks, etc. Nevertheless, the capabilities of this method are not limited to low power applications and LTP energy harvesters can be beneficial for energy harvesting in building structures, roadways, railways, bridges, wind turbines, etc [247, 248].

Acknowledgments

- I would like to thank Alireza Nikzamir for collaboration on this chapter.
- There is equal contribution from Kasra Rouhi and Alireza Nikzamir to this chapter.

Kasra Rouhi was primarily responsible for developing the main idea, writing the first draft, and developing the mathematics. Alireza Nikzamir contributed primarily to the simulation results and finalized the draft.

- This material is based upon work supported by the Air Force Office of Scientific Research (AFOSR) Grant No. FA9550-19-1-0103.

- The text of Chapter 5 of this dissertation is a reprint of the material as it appears in A. Nikzamir, K. Rouhi, A. Figotin, and F. Capolino, "Time modulation to manage and increase the power harvested from external vibrations," Applied Physics Letters, vol. 123, no. 21, Nov. 2023. The coauthors listed in this publication are Alireza Nikzamir, Alexander Figotin, and Filippo Capolino. Alexander Figotin and Filippo Capolino directed and supervised research which forms the basis for the dissertation.

- The results of this chapter have been published in the journal paper of [150] and in the conference papers of [249].

Chapter 6

Exceptional Points of Degeneracy Directly Induced by Space-Time Modulation of a Single Transmission Line

We demonstrate how EPDs are induced in a single TL directly by applying periodic space-time modulation to the per-unit-length distributed capacitance. In such STM-TL, two eigenmodes coalesce into a single degenerate one, in their eigenvalues (wavenumbers) and eigenvectors (voltage-current states) when the system approaches the EPD condition. The EPD condition is achieved by tuning a parameter in the space-time modulation, such as spatial or temporal modulation frequency, or the modulation depth. We unequivocally demonstrate the occurrence of the EPD by showing that the bifurcation of the wavenumber around the EPD is described by the Puiseux fractional power series expansion. We show that the first order expansion is sufficient to approximate well the dispersion diagram, and how this "exceptional" sensitivity of the STM-TL's wavenumber to tiny changes of any TL or modulation

parameter enables a possible application as a highly sensitive TL sensor when operating at an EPD.

6.1 Background, Motivation, and State of the Art

Recent advancements in EPD concepts have attracted a surge of interests due to their potential benefits in various electromagnetic applications. An EPD is a point in parameter space of a system at which multiple eigenmodes coalesce in both their eigenvalues and eigenvectors. The concept of EPD has been studied in lossless, spatially [18, 124, 250] or temporally [251, 19] periodic structures, and in systems with loss and/or gain under parity-time symmetry [66, 114, 33, 67]. Since the characterizing feature of an exceptional point is the strong full degeneracy of at least two eigenmodes, as implied in [11], we stress the importance of referring to it as a "degeneracy", hence of including the D in EPD. In essence, an EPD is obtained when the system matrix is similar to a matrix that comprises a non-trivial Jordan block [18, 24, 252, 29], here however the formulation leads to a matrix of infinite dimensions and therefore we assess the occurrence of the EPD by invoking the Puiseux fractional power expansion series [4] to describe the bifurcation of the dispersion diagram at the EPD. There are several features associated with the development of EPDs, which lead to applications, such as active systems gain enhancement in waveguides [253, 254, 255], and enhanced sensing [71, 12, 90, 125].

Researchers have been studying how to incorporate time-variation of parameters into electromagnetic systems with the goal of adding new degrees of freedom in wave manipulation. In their pioneering work, Cassedy and Oliner studied the dispersion characteristics of wave propagation in a medium with dielectric constant modulated as a traveling-wave with sinusoidal form [256, 257]. Then, Elachi studied electromagnetic wave propagation and the wave vector diagram in general space-time periodic materials for different wave polarization [258]. In

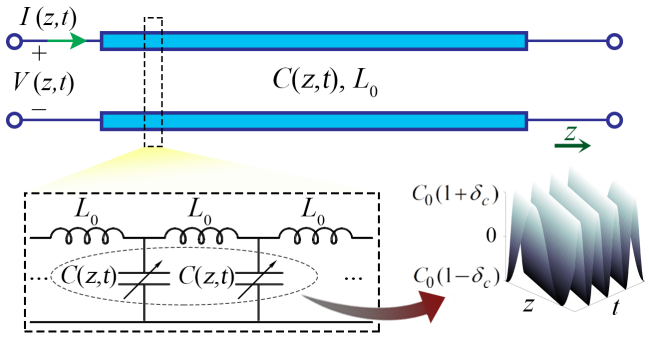

Figure 6.1: Schematic illustration of a single TL with space-time modulation of the distributed capacitance. We also show the equivalent TL circuit with the per-unit-length inductor and modulated capacitor.

[259, 260], authors analyzed the concept of temporal photonic crystals with periodic modulation of permeability and permittivity. In [261], magnetless nonreciprocity was demonstrated in spatiotemporally modulated coupled-resonator networks. Also, Taravati et al. proposed a mixer-duplexer-antenna leaky-wave system based on periodic space-time modulation [262]. Recently, in [263, 264], space-time modulation was employed to control phase and amplitude tunability in a metasurface. Several other papers have been published on time/space-time modulation to generate nonreciprocity in electromagnetic structures [265, 266, 267, 268]. In all these works, the concept of EPD in such modulated structures was not studied.

Here we leverage on the two concepts of space-time modulation and EPD and develop a general scheme to realize EPDs in space-time periodic single TL that could be used as a sensor. We investigate the occurrence of EPDs when the per-unit-length capacitance is modulated in space and time, by showing that the bifurcation of the dispersion diagram around the EPD is well approximated by the Puiseux fractional power series expansion. This EPD-related fractional expansion is also used to explain the extreme sensitivity of the wavenumber to perturbation of system parameters adding a degree of freedom to TL systems with space-only or time-only modulation.

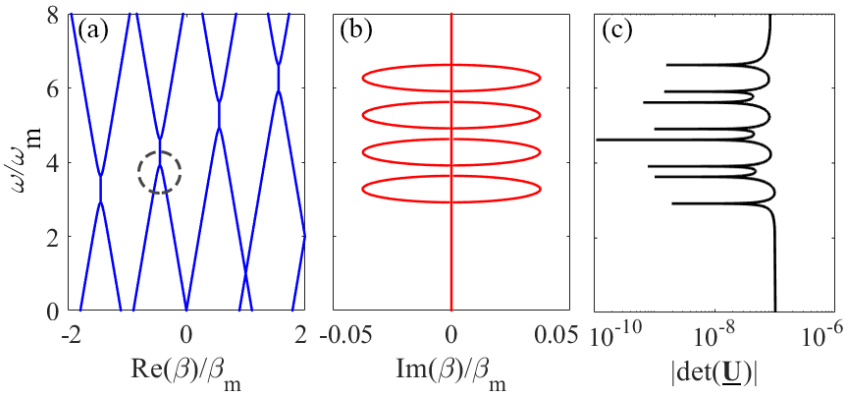

Figure 6.2: Dispersion diagram of the STM-TL with 2nd order EPDs. (a) Real part of the wavenumber of first harmonics and (b) the corresponding imaginary parts, and (c) plot of $|\det(\underline{\mathbf{U}})|$ versus frequency. The similarity transformation matrix $\underline{\mathbf{U}}$ contains eigenvectors, therefore the vanishing of $|\det(\underline{\mathbf{U}})|$ is necessary at an EPD.

6.2 Degeneracies in a Uniform Single ST-MTL

Degeneracies in wave propagation in an infinitely long TL is examined when the per-unit-length capacitance is modulated in both space and time. We employ the formalism and description of a linear TL shown in [40]. A schematic representation of an STM-TL is shown in Figure 6.1, where only the per-unit-length capacitance is space-time varying, while the per-unit-length inductance is constant throughout the TL. Without loss of generality we assume sinusoidal space-time variation; however, EPDs can be induced also by other forms of periodic space-time variation. The distributed per-unit-length space-time varying capacitance is given by

$$C(z,t) = C_0 + C_m(t) = C_0(1 + \delta_c \cos(\omega_m t - \beta_m z)), \tag{6.1}$$

where C_0 is the space-time averaged (i.e., unmodulated) per-unit-length capacitance, δ_c is the modulation depth, and ω_m and β_m are the temporal and spatial modulation frequencies, respectively. The dynamic behavior of such a TL is captured using the Telegrapher's equations, that are here represented in terms of a voltage and current state vector,

$\mathbf{\Psi}(z,t) = [V(z,t), I(z,t)]^{\mathrm{T}}$, where the superscript T denotes the transpose operation. The dynamic behavior of this state vector is described by the first order differential equations as

$$\partial_{\mathrm{z}}\mathbf{\Psi}(z,t) \;\; = \;\; -\partial_{\mathrm{t}}\left(\underline{\mathbf{M}}(z,t)\mathbf{\Psi}(z,t)\right), \tag{6.2}$$

where the STM 2×2 system matrix $\underline{\mathbf{M}}$ is given by

$$\underline{\mathbf{M}}(z,t) = \begin{bmatrix} 0 & L_0 \\ C(z,t) & 0 \end{bmatrix}. \tag{6.3}$$

We look for time-harmonic solutions, and because of the periodic nature of the modulation the state vector eigensolution is cast into an infinite space-time Floquet-Bloch series as

$$\mathbf{\Psi}(z,t) = e^{j(\omega t - \beta z)} \sum_{q=-\infty}^{\infty} \mathbf{\Psi}_q e^{jq(\omega_{\mathrm{m}} t - \beta_{\mathrm{m}} z)}, \tag{6.4}$$

where β and ω are the propagation wavenumber and the angular frequency, respectively, and $\mathbf{\Psi}_q = [V_q, I_q]^{\mathrm{T}}$ is the complex amplitude of the q-th harmonic of the state vector. We expand the space-time-varying distributed capacitance in Equation (6.1) in terms of its Fourier series

$$C(z,t) = \sum_{s=-1}^{1} C_s e^{js(\omega_{\mathrm{m}} t - \beta_{\mathrm{m}} z)}, \tag{6.5}$$

where C_s represents the amplitude of the s-th harmonic. Substituting Equations (6.4) and (6.5) in Equation (6.2) and taking the time and space derivatives, the equation for each q-th

harmonics' $\mathbf{\Psi}_q$ is obtained as

$$\sum_{q=-\infty}^{\infty} (\beta + q\beta_{\mathrm{m}})\, \mathbf{\Psi}_q e^{jq(\omega_{\mathrm{m}}t - \beta_{\mathrm{m}}z)} = \sum_{q=-\infty}^{\infty} \sum_{s=-1}^{1} \begin{bmatrix} 0 & (\omega + q\omega_{\mathrm{m}})\, L_0 \delta_{s,0} \\ (\omega + (q+s)\omega_{\mathrm{m}})\, C_s & \\ \mathbf{\Psi}_q e^{j(q+s)(\omega_{\mathrm{m}}t - \beta_{\mathrm{m}}z)} & 0 \end{bmatrix}, \tag{6.6}$$

where $\delta_{s,0}$ is the Kronecker delta. Since the exponential functions $e^{jq(\omega_{\mathrm{m}}t - \beta_{\mathrm{m}}z)}$ form a complete orthogonal set of functions, we balance the coefficient of the exponential with the same q index leading to

$$(\beta + q\beta_{\mathrm{m}})\, \mathbf{\Psi}_q = \sum_{s=-1}^{1} \begin{bmatrix} 0 & (\omega + q\omega_{\mathrm{m}})\, L_0 \delta_{s,0} \\ (\omega + q\omega_{\mathrm{m}})\, C_s & 0 \end{bmatrix} \mathbf{\Psi}_{q-s}. \tag{6.7}$$

Isolating the term with the wavenumber, the above equation is rearranged as

$$\beta \mathbf{\Psi}_q = \sum_{s=-1}^{1} \underline{\mathbf{N}}_{q,s} \mathbf{\Psi}_{q-s}, \tag{6.8}$$

where

$$\underline{\mathbf{N}}_{q,s} = \begin{bmatrix} -q\beta_{\mathrm{m}}\delta_{s,0} & (\omega + q\omega_{\mathrm{m}}) L_0 \delta_{s,0} \\ (\omega + q\omega_{\mathrm{m}}) C_s & -q\beta_{\mathrm{m}}\delta_{s,0} \end{bmatrix}. \tag{6.9}$$

The above equation can be cast in terms of a large block three-diagonal matrix $\underline{\mathbf{T}}$ as

$$\underline{\mathbf{T}}\boldsymbol{\Psi} = \beta\boldsymbol{\Psi}, \tag{6.10}$$

that can be sued to determine the system eigenvectors $\boldsymbol{\Psi} = [\boldsymbol{\Psi}_{-Q}, ..., \boldsymbol{\Psi}_0, ..., \boldsymbol{\Psi}_Q]^{\mathrm{T}}$ and eigenvalues β. A finite number $2Q+1$ of harmonics is sufficient to determine the STM-TL wave characteristics and the occurrence of EPDs, hence the dimension of the matrix $\underline{\mathbf{T}}$ is $2(2Q+1) \times 2(2Q+1)$. The real and imaginary parts of the wavenumber in the β-ω dispersion diagram are plotted in Figures 6.2(a) and (b), respectively, for the STM-TL with parameters as follows. As specified, we have considered the sinusoidal modulation given in Equation 6.1 where the modulation parameters are $\delta_{\mathrm{c}} = 0.3$, $\omega_{\mathrm{m}} = 0.05\omega_0$, and $\beta_{\mathrm{m}} = 0.8\beta_0$, where $\beta_0 = \omega_0/c$ is the free space propagation wavenumber at $\omega_0/(2\pi) = 10^9\,\mathrm{s}^{-1}$. Moreover, the TL parameters are $L_0 = 282\,\mathrm{nH/m}$ and $C_0 = 113\,\mathrm{pF/m}$. Note that the modulation frequency does not need to be comparable to the one of the radio frequency wave. We consider $2Q+1 = 21$ harmonics to calculate the dispersion diagram (we checked that a larger number provides the same result), but we show only the first two harmonics, i.e., the real part of their wavenumbers and the relevant imaginary parts. It is observed form the dispersion diagram in Figure 6.2(a) that for an STM-TL the band-gap locations form a tilted line, which indicates non symmetric dispersion ($\omega(-\beta) \neq \omega(\beta)$) in such a structure, as already pointed out in [256, 269]. Furthermore, it is clear from this figure that the eigenvalues, i.e., the propagation wavenumbers of the system, are coalescing at the band edges. To fully characterize an EPD, we have to show that the two eigenvectors corresponding to the two coalescing eigenvalues are also coalescing at the band edges. We define the similarity transformation matrix as $\underline{\mathbf{U}} = [\mathbf{U}_1 \,|\, \cdots \,|\, \mathbf{U}_{2(2Q+1)}]$, where $\underline{\mathbf{U}}_i$ is the eigenvector corresponding to the i-th eigenvalue, and such matrix diagonalizes the system matrix as $\underline{\mathbf{T}} = \underline{\mathbf{U}\boldsymbol{\Lambda}\mathbf{U}}^{-1}$. At the EPD two eigenvectors become linearly dependent, therefore we verify that $|\det(\underline{\mathbf{U}})|$ vanishes at each EPD as a necessary condition, as shown in Figure 6.2(c) [29]. Indeed, at $\omega/\omega_{\mathrm{m}} = 3.91$ we observe that two eigenvalues as well as the two associated eigenvectors are

equal to each other up to the 6 decimal digit. A sufficient condition to assess the occurrence of an EPD without looking directly at the eigenvectors is explained in the next section, by demonstrating that the dispersion diagram bifurcates at the EPD following the Puiseux fractional power expansion [4]. It is also possible to achieve EPDs in systems with space-only periodic modulation [29, 20], and such systems are reciprocal, or with time-only modulation [19]. Space-time modulation adds a new degree of freedom to control the dispersion diagram's EPD position. Both temporal and spatial modulations are needed to obtain EPD at a desired frequency-wavenumber pair. This may be important to design highly tunable traveling-wave antennas since the radiation pointing angle and beamwidth depend on the wavenumber. From the dispersion diagram in Figure 6.2(a) we observe that in an STM system, the band-gap locations form a tilted line, hence, the EPD positions in the dispersion diagram are nonreciprocal.

6.3 Puiseux Fractional Power Expansion and High Sensitivity

Extreme sensitivity to system perturbations is an intrinsic characteristic of EPDs and this is intrinsically related to the Puiseux series [4, 270, 91, 28] that singularly describe the EPD occurrence. We first demonstrate how the dispersion diagram varies by changing different system parameters, then we show the extreme sensitivity of the wavenumber to a system perturbation when operating at an EPD that follows the description of the Puiseux fractional power expansion. We analyze the STM-TL wavenumbers by varying one system parameter at the time around the value used in the example. As a first parameter, we vary the unmodulated per-unit-length capacitance of the TL, C_0, and observe its effect on the dispersion diagram. As shown in the Figure 6.3(a), by increasing C_0, the dispersion diagram shifts downwards and consequently the EPDs move in the same direction. In the next step, we

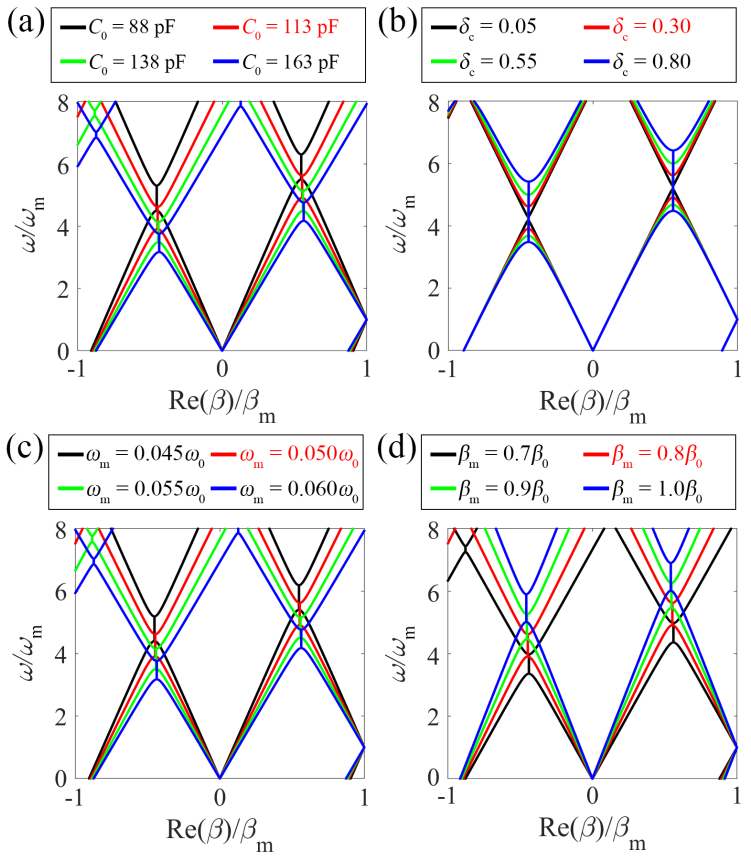

Figure 6.3: Dispersion diagrams of the real part of wavenumbers by changing one single parameter at the time. The system parameters that are changed are (a) C_0, (b) δ_c, (c) ω_m, and (d) β_m.

study the effect of the modulation depth δ_c perturbation on the dispersion diagram in Figure 6.3(b). By increasing the modulation depth, the band-gaps stretch out and become wider, meaning that EPDs at both edges of one band-gap move further apart from each other in frequency. As the third parameter, we explore the temporal modulation frequency ω_m variation on the location of the band-gaps and EPDs. Figure 6.3(c) exhibits a similar trend of changes compared to those in Figure 6.3(a). Finally, we examine the variation of spatial modulation frequency, β_m, shown in Figure 6.3(d). It is seen from this figure that a different behavior is obtained compared to varying the previous parameters. Here, by increasing the spatial modulation frequency, band-gaps become wider and move toward higher frequency in the dispersion diagram; thus, EPDs move to higher frequencies as well. As a realistic scenario, we can utilize an STM-TL in high sensitivity applications. If an external substance or object

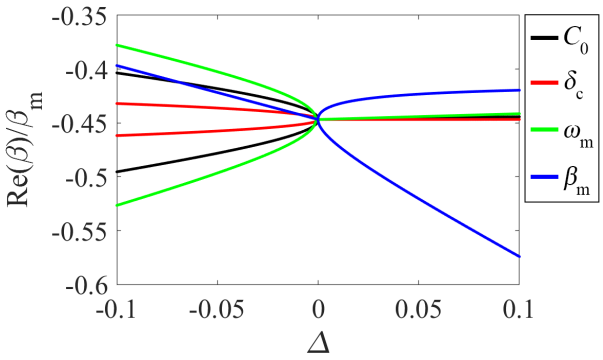

Figure 6.4: Sensitivity of the real part of the propagation wavenumber to a parameter perturbation (one at the time) around the EPD.

is placed near the TL (for instance, the microstrip line), the TL's effective parameters would be perturbed, which in turn causes a large perturbation in the wavenumber that can be, in principle, easily detected.

The eigenvalues at EPDs are exceedingly sensitive to perturbations of parameters of a time varying system [71, 19, 90, 125]. Here we show that the sensitivity of a system's observable to a specific variation of a parameter is boosted due to the degeneracy of eigenmodes. As an example, we consider the first EPD in the first band-gap with the negative real part of wavenumber (indicated by a gray circle in Figure 6.2) and we show how a modal wavenumber is perturbed by small system perturbations. We define the relative system perturbation Δ as

$$\Delta = \frac{X_{\text{pert}} - X_{\text{EPD}}}{X_{\text{EPD}}}, \tag{6.11}$$

where X_{EPD} is the unperturbed parameter value that provides the EPD condition, and X_{pert} is its perturbation. We consider variations of C_0, δ_{c}, ω_{m}, and β_{m}, one at the time. The calculated real part of the wavenumber near the first EPD at $\omega/\omega_{\text{m}} = 3.91$ is shown in Figure 6.4. We conclude from the extracted results that the individual variation of the parameters of C_0, δ_{c}, and ω_{m}, show similar sensitivity behavior, i.e., the real part of the wavenumber splits

for $\Delta < 0$. In contrast, variation of β_{m} has an opposite effect on the dispersion diagram, i.e., the real part of the wavenumber splits for $\Delta > 0$. Note that the ω_{m} perturbation shows the highest sensitivity. Higher sensitivity is obtained when the bifurcation of the dispersion diagram is wider. Furthermore, the β_{m} perturbation response shows an opposite trend to that of the other three parameters.

We explain the extreme sensitivity by resorting to the general theory of EPDs. Note that a perturbation in Δ value leads to a perturbed matrix $\underline{\mathbf{T}}(\Delta)$. Consequently, the two degenerate eigenvalues occurring at the EPD change considerably due to a small perturbation in Δ, resulting in two distinct eigenvalues $\beta_p(\Delta)$, with $p = 1, 2$, close to the first EPD. The two perturbed eigenvalues near an EPD are represented by a single convergent Puiseux series (also called fractional power expansion) where the coefficients are calculated using the explicit recursive formulas given in [91]. An approximation of $\beta_p(\Delta)$ around a second-order EPD is given by

$$\beta_p(\Delta) \approx \beta_{\mathrm{EPD}} + (-1)^p \alpha_1 \sqrt{\Delta}. \tag{6.12}$$

Following [270, 91, 28], we calculate α_1 as

$$\alpha_1 = \sqrt{\left(-\frac{\frac{\partial H}{\partial \Delta}(\Delta, \beta)}{\frac{1}{2!}\frac{\partial^2 H}{\partial \beta^2}(\Delta, \beta)} \right)}, \tag{6.13}$$

evaluated at the EPD, i.e., at $\Delta = 0$ and $\beta = \beta_{\mathrm{EPD}}$, where $H(\Delta, \beta) = \det[\underline{\mathbf{T}}(\Delta) - \beta \underline{\mathbf{I}}]$. Equation (6.12) indicates that for a small perturbation $\Delta \ll 1$ the eigenvalues change dramatically from their original degenerate value due to the square root function. As an indicative example, we consider the single STM-TL with parameters as used in Figure 6.2. In this example, we select the EPD indicated by the gray circle in Figure 6.2(a) with $\omega/\omega_{\mathrm{m}} = 3.91$,

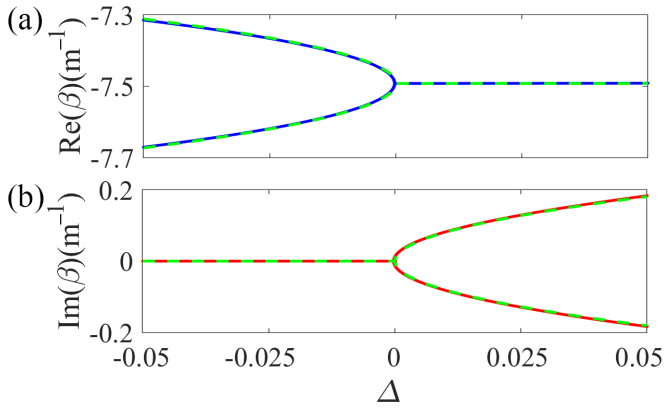

Figure 6.5: The Puiseux fractional power series expansion in Equation (6.12) (green dashed lines) describes the bifurcation of the real and imaginary parts of the two wavenumbers when a system parameter (δ_c in this case) is perturbed. The Puiseux series result is in excellent agreement with the wavenumbers evaluated using Equation (6.10) (blue and red solid lines).

and $\beta_{EPD} = -7.49\,\mathrm{m}^{-1}$ as the unperturbed EPD operation point. In this example the perturbation parameter is the modulation depth, $\Delta = (\delta_c - \delta_{c,EPD})/\delta_{c,EPD}$, and the Puiseux series coefficients is calculated as $\alpha_1 = j0.81\,\mathrm{m}^{-1}$. The result in Figure 6.5 exhibits the two branches of the exact perturbed eigenvalues β obtained from the eigenvalue problem in Equation 6.10 when the system perturbation Δ is applied. Moreover, this figure shows that such perturbed eigenvalues can be estimated with very good accuracy by employing the Puiseux series (green dashed lines) truncated at its first order. For a positive but small value of Δ, the imaginary part of the eigenvalues experience a sharp change, while its real part remains constant. Moreover, a very small negative value of Δ causes a rapid variation in the real part of the eigenvalues. This feature is actually one of the most extraordinary physical properties associated with the EPD concept, and it can be exploited for designing ultra-sensitive sensors [37, 38]. This kind of STM-TL with capacitance variation is feasible within the realm of current fabrication technologies. Varactor-loaded TL could be a proper alternative for implementing this kind of structure [271]. Recently several tunable materials have been employed to conceive devices based on the spatiotemporal variation, such as graphene [272] and liquid crystal [273].

6.4 Conclusions

A single STM-TL supports EPDs of second order directly induced by spatiotemporal modulation of the distributed (per-unit-length) capacitance. For its occurrence, an EPD does not need the presence of time-invariant gain or loss elements, as in PT symmetry, and it does not need two coupled TLs either. Here space and time modulation are not used to generate nonreciprocity or to enhance EPD properties but rather as a direct way to generate EPDs. This is in analogy to what was shown in [19] where time modulation was used to directly induce EPDs in a *single* resonator, without the need to resorting to two couple resonators with loss and gain as implied by PT-symmetry [33]. We have investigated how to perturb an EPD condition by slightly perturbing system parameters, and how this srongly modifies the degenerate eigenvector (i.e., the wavenumber). We have shown that small changes in a TL constitutive parameters lead to a very strong variation of the TL wavenumber and how this is predicted by the Puiseux fractional expansion series, suggesting a novel approach to design extremely sensitive sensors based on waveguide propagation.

Acknowledgments

- I would like to thank Hamidreza Kazemi for collaboration on this chapter.
- This material is based upon work supported by the National Science Foundation (NSF) under Grant No. ECCS-1711975.
- The text of Chapter 6 of this dissertation is a reprint of the material as it appears in A. Nikzamir, K. Rouhi, A. Figotin, and F. Capolino, "Time modulation to manage and increase the power harvested from external vibrations," Applied Physics Letters, vol. 123, no. 21, Nov. 2023. The coauthors listed in this publication are Alireza Nikzamir, Alexander Figotin, and Filippo Capolino. Alexander Figotin and Filippo

Capolino directed and supervised research which forms the basis for the dissertation.

- The results of this chapter have been published in the journal paper of [92] and in the conference paper of [249].

Chapter 7

Exceptional Degeneracies in Traveling Wave Tubes With Dispersive Slow-Wave Structure Including Space-Charge Effect

The interaction between a linear e-beam and a guided EM wave is studied in the contest of EPDs supported by such an interactive system, focusing on a linear beam TWT with a realistic helix waveguide SWS. The interaction is formulated by an analytical model that is a generalization of the Pierce model, assuming a one-dimensional electron flow along a dispersive single-mode guiding SWS and taking into account space-charge effects. The augmented model using phase velocity and characteristic impedance obtained via full-wave simulations is validated by calculating gain versus frequency and comparing it with that from more complex e-beam simulators. This comparison also shows the accuracy of our new model compared with respect to the non-dispersive Pierce model. EPDs are then investigated using the augmented model, observing the coalescence of complex-valued wavenumbers and the

system's eigenvectors. The point in the complex dispersion diagram at which the TWT-system starts/ceases to exhibit a convection instability, i.e., a mode starts/ceases to grow exponentially along the TWT, is the EPD. We also demonstrate the EPD existence by showing that the Puiseux fractional power series expansion well approximates the bifurcation of the dispersion diagram at the EPD. This latter concept also explains the "exceptional" sensitivity of the TWT-system to changes in the beam's electron velocity when operating near an EPD.

7.1 Background, Motivation, and State of the Art

High power TWT amplifiers are of high importance for telecommunications, radar applications, including atmospheric studies, precision tracking, and high-resolution imaging [274, 275, 276]. In some occasion, metamaterials have been proposed to enhance the properties of e-beam devices [277, 278, 279, 280]. A TWT uses a SWS as a key component to harvest energy from an e-beam into radio frequency waves efficiently over broad bandwidths [281, 282]. In this chapter, we focus on a realistic helix TWT with dispersive SWS's characteristic parameters. The interaction with the e-beam affects the way EM waves propagate in the so-called "hot" circuit, i.e., accounting for the beam-EM mode interaction. We refer to the eigenmodes of the system where the e-beam interacts with the EM wave of the SWS as "hot" modes, which are the modes that retain properties of both EM and space-charge waves.

An EPD in a system refers to the property of the system matrix that contains at least one nontrivial Jordan block structure, i.e., when two or more eigenvectors coalesce into a single degenerate one [283, 284, 63, 114, 24, 252]. The concept of EPD has been studied in lossless, spatially [18, 250], or temporally [19, 90] periodic structures, and in systems with loss and/or gain under PT-symmetry [66, 33]. We employ the Puiseux fractional power expansion series

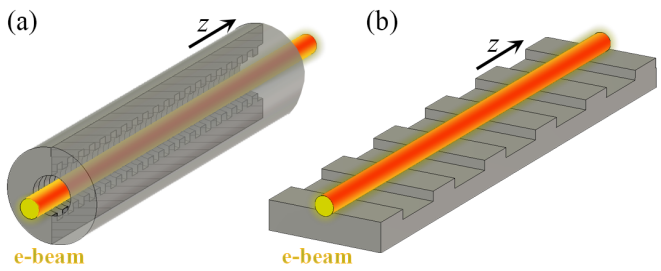

Figure 7.1: Illustrative schematics showing an e-beam in the proximity of an EM-guiding SWS. (a) Beam inside a circular waveguide with corrugations, and (b) beam near a periodic grating.

to illustrate the bifurcation of the system's dispersion diagram at the EPD [4]. The EPD has been studied for its applications in sensing devices [71, 12] and oscillators [67, 40, 255, 42].

In [26], the EPD in a system of an e-beam interacting with an EM mode guided in a non-dispersive SWS with distributed power extraction and without accounting for electrons' debunching is used to conceive an effective oscillator. The mathematical formulation in [126] does not include waveguide dispersion in the model, and above all, it cannot capture the second EPD that occurs in the real TWTs at a higher frequency (See Figure 7.4). This letter explains the fundamental physics describing the TWT operation, accounting for electrons' debunching caused by space-charge effects and SWS frequency dispersion, and describes the bifurcation points in the dispersion diagram using the coalescence of the system's eigenvectors. Also, the EPD-related fractional power expansion is used to explain the wavenumber's extreme sensitivity to perturbations to the system parameters such as operating frequency and e-beam's velocity and how EPDs are related to the TWT amplification bandwidth. We calculate the characteristic parameters of the cold guiding SWS based on what Pierce proposed in [285, 286, 287] and further developed for frequency-dependent TWT-systems in analogy (but differently) to what done in [288, 289].

7.2 How to Model TWTs

The system consists of an EM field in a guiding SWS interacting with a single e-beam flowing in the z-direction is schematically shown in Figure 7.1. The e-beam's electrons have average velocity and linear charge density u_0 and ρ_0, respectively. The e-beam has an average current $I_0 = -\rho_0 u_0$ and an equivalent kinetic non-relativistic d.c. voltage $V_0 = u_0^2/2\eta$, where $\eta = e/m = 1.758820 \times 10^{11}$ C/Kg is the charge-to-mass ratio of the electron with charge $-e$ and rest mass m. The small-signal modulation in the e-beam velocity and charge density u_b and ρ_b, respectively, describe the so-called "space-charge wave". The a.c. beam current and equivalent voltage are given by $i_\mathrm{b} = u_\mathrm{b}\rho_0 + u_0\rho_\mathrm{b}$ and $v_\mathrm{b} = u_\mathrm{b}u_0/\eta$, where we have retained only the linear terms based on the small-signal approximation [286], as explained in Section 7.5. We implicitly assume a time dependence of $\exp(j\omega t)$, so the a.c. space-charge wave modulating the e-beam is described in the phasor domain with $V_\mathrm{b}(z)$ and $I_\mathrm{b}(z)$, as

$$\partial_z V_\mathrm{b} = -j\beta_0 V_\mathrm{b} - aZI - j\frac{I_\mathrm{b}}{A\varepsilon_0\omega}, \tag{7.1}$$

$$\partial_z I_\mathrm{b} = -jgV_\mathrm{b} - j\beta_0 I_\mathrm{b}, \tag{7.2}$$

where $\beta_0 = \omega/u_0$ is the phase constant of the space-charge wave (when neglecting plasma frequency effects), $g = I_0\beta_0/(2V_0)$, Z is the equivalent TL distributed series impedance, and $I(z)$ is the equivalent TL current, as will be explained later. Furthermore, $E_z = E_\mathrm{w} + E_\mathrm{p} = aZI + jI_\mathrm{b}/(A\varepsilon_0\omega)$ is the longitudinal polarization (in the z-direction) of the electric field component that modulates the velocity and bunching of the electrons. The longitudinal field $E_z = E_\mathrm{w} + E_\mathrm{p}$ is the sum of two components. The term E_p accounts for nonuniform charge density, and in the phasor form is given by $E_\mathrm{p} = jI_\mathrm{b}/(A\varepsilon_0\omega)$ [290, Chapter 10], where A is the e-beam cross-sectional area, and ε_0 is vacuum permittivity. The term E_p is generated

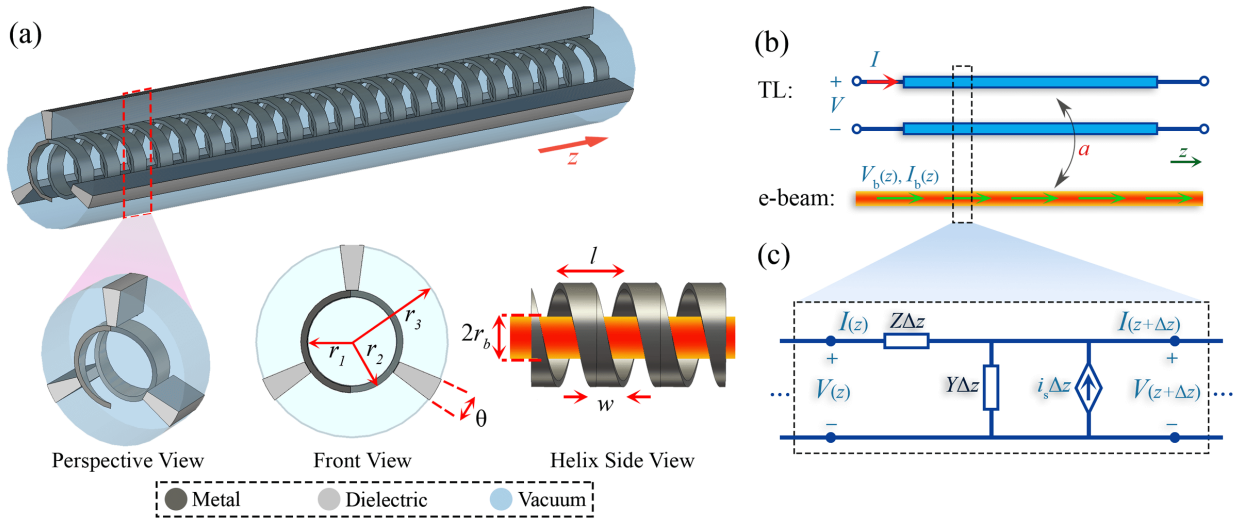

Figure 7.2: (a) Tape helix SWS in a circular metallic waveguide with radius $r_3 = 1.06$ mm. An e-beam with radius $r_\mathrm{b} = 560\ \mu$m flows along the axis of the helical conductor of inner radius $r_1 = 744\ \mu$m, and outer radius $r_2 = 846\ \mu$m supported by dielectric rods. The other geometric parameters are $l = 1.04$ mm, $w = 520\ \mu$m, and $\theta = 14.2°$. (b) Schematic of the equivalent TL coupled to the e-beam used to study the hot EM-space-charge wave modes. (c) Equivalent TL circuit showing the per-unit-length impedance, admittance and current generator i_s that represents the effect of the e-beam.

by charge distribution that also causes the so-called "debunching", and its calculation is in agreement with the Lagrangian model for TWT-systems in [291, Chapter 7], as explained in Section 7.6. In addition, the term $E_\mathrm{w} = aZI$ is the longitudinal electric field of the EM mode propagation in the SWS, affecting the bunching of the e-beam, according to the well-known Pierce model [286]. Also, the term a represents a coupling strength coefficient, that describes how the e-beam couples to the TL as already introduced in [292] and [293, 291, Chapter 3]. More details on the fundamental equations describing the interacting system are in Section 7.7. The well-known telegrapher's equations describe the EM modal propagation in the SWS, based on the equivalent TL model shown in Figures 7.2(b) and (c) where the distributed per-unit-length series impedance Z, and shunt admittance Y relate the equivalent TL voltage $V(z)$ and current $I(z)$ phasors as

$$\partial_z V = -ZI, \tag{7.3}$$

$$\partial_z I = -YV - a\partial_z I_\mathrm{b}. \tag{7.4}$$

The term $i_\mathrm{s} = -a\partial_z I_\mathrm{b}$ represents a distributed current generator [294], that accounts for the effect of the beam's charge wave flowing in the SWS [286, 292]. In order to construct an accurate model that provides precise predictions for realistic structures and overcome the simplicity of the ideal assumptions in the original Pierce model, we use frequency-dependent waveguide parameters in the equations. In practice, we first analyze wave propagation in the "cold" SWS (i.e., in the absence of the e-beam) using a full-wave method to get the values of $Z(\omega)$ and $Y(\omega)$ to be used in the formulation. To recover frequency-dependent characteristic parameters, we use the finite element method eigenmode solver in CST Studio Suite and extract the cold circuit EM phase velocity $v_\mathrm{c}(\omega) = \omega/\beta_\mathrm{c}(\omega)$, where $\beta_\mathrm{c}(\omega) = \sqrt{-Z(\omega)Y(\omega)}$ is the phase propagation constant of the cold SWS mode, and the equivalent TL characteristic impedance $Z_\mathrm{c}(\omega)$. By using the extracted values for $v_\mathrm{c}(\omega)$ and $Z_\mathrm{c}(\omega)$, the equivalent frequency-dependent distributed series impedance $Z(\omega) = j\omega Z_\mathrm{c}(\omega)/v_\mathrm{c}(\omega) = jZ_\mathrm{c}(\omega)\beta_\mathrm{c}(\omega)$ and shunt admittance $Y(\omega) = j\omega/\left(Z_\mathrm{c}(\omega)v_\mathrm{c}(\omega)\right) = j\beta_\mathrm{c}(\omega)/Z_\mathrm{c}(\omega)$ are calculated. Moreover, in Equation (7.4), when $a = 0$ the e-beam is not coupled to the TL, and when $a = 1$, the model reduces to the one developed in [286, 287]. The presence of this coupling strength coefficient generalizes what was done in [286, 287], since the beam may be subject to a strong longitudinal electric field that is not accurately accounted for by the simple circuit impedance Z_c of the originally Pierce model [286, 287]. For convenience, we define a state vector $\mathbf{\Psi}(z) = [V, I, V_\mathrm{b}, I_\mathrm{b}]^\mathrm{T}$ that describes the hot mode propagation along z, and rewrite Equations (7.1), (7.2), (7.3), and (7.4) in matrix form as

$$\partial_z \mathbf{\Psi}(z) = -j\underline{\mathbf{M}}\mathbf{\Psi}(z), \tag{7.5}$$

where $\underline{\mathbf{M}}$ is the 4×4 system matrix that after replacing $v_\mathrm{c}(\omega)$ and $\beta_\mathrm{c}(\omega)$ in the system

equations, reads as

$$\underline{\mathbf{M}} = \begin{bmatrix} 0 & \beta_{\mathrm{c}}(\omega)Z_{\mathrm{c}}(\omega) & 0 & 0 \\ \beta_{\mathrm{c}}(\omega)/(Z_{\mathrm{c}}(\omega)) & 0 & -ag & -a\beta_0 \\ 0 & a\beta_{\mathrm{c}}(\omega)Z_{\mathrm{c}}(\omega) & \beta_0 & R_{\mathrm{p}} \\ 0 & 0 & g & \beta_0 \end{bmatrix}. \tag{7.6}$$

In the above system matrix, R_{p} is a space-charge parameter related to the debunching of beam's charges, and is given by [295, 253]

$$R_{\mathrm{p}} = \frac{1}{A\varepsilon_0\omega} = \frac{2V_0\omega_{\mathrm{q}}^2}{\omega I_0 u_0}, \tag{7.7}$$

where $\omega_{\mathrm{q}} = R_{\mathrm{sc}}\omega_{\mathrm{p}}$ is the reduced plasma angular frequency, $\omega_{\mathrm{p}} = \sqrt{-\rho_0\eta/(A\varepsilon_0)}$ or $\omega_{\mathrm{p}} = \sqrt{I_0 u_0/\left(2V_0 A\varepsilon_0\right)}$ is the plasma frequency [296], and R_{sc} is the plasma frequency reduction factor [297]. The term R_{sc} accounts for reductions in the magnitude of the axial component of the space-charge electric field due to either finite beam radius or proximity of the surrounding conducting walls. Fields produced by space-charges represent repulsive forces in a dense beam of charged particles. Assuming a state vector z-dependence of the form $\mathbf{\Psi}(z) \propto \exp(-jkz)$, where k is the wavenumber of a hot mode in the EM-space-charge wave interacting system, the eigenmodes are obtained by solving the eigenvalue problem $k\mathbf{\Psi}(z) = \underline{\mathbf{M}}\mathbf{\Psi}(z)$. The resulting modal dispersion characteristic equation is given by

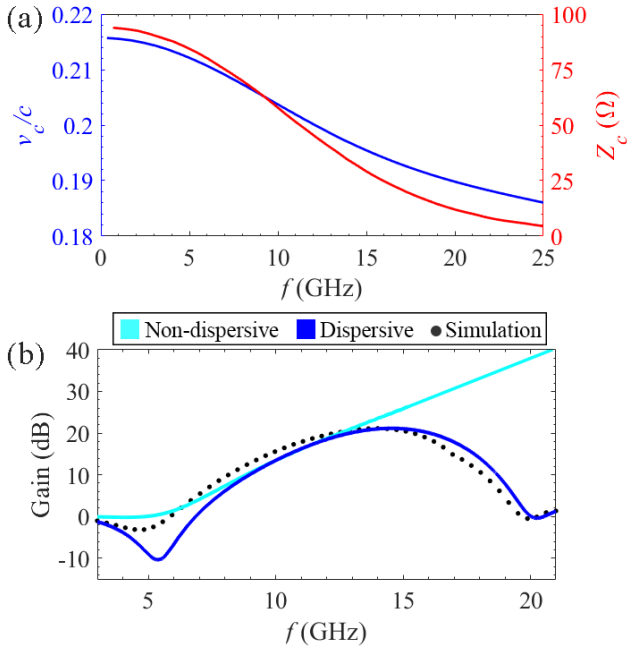

Figure 7.3: (a) Phase velocity and Pierce impedance of the EM mode in the cold SWS, obtained via full-wave eigenmode simulations. (b) Gain versus frequency from the theoretical model based on the non-dispersive (cyan curve), and dispersive (blue curve) solution of system in Equation (7.5), and simulation results using the software LATTE (black dots).

$$D(\omega,k)=\det(\underline{\mathbf{M}}-k\underline{\mathbf{I}})=k^4-k^3\left(2\beta_0\right)+k^2\left(\beta_0^2-\beta_{\mathrm{q}}^2-\beta_{\mathrm{c}}^2(\omega)+a^2g\beta_{\mathrm{c}}(\omega)Z_{\mathrm{c}}(\omega)\right) \\ +k\left(2\beta_{\mathrm{c}}^2(\omega)\beta_0\right)-\beta_{\mathrm{c}}^2(\omega)\left(\beta_0^2-\beta_{\mathrm{q}}^2\right)=0. \tag{7.8}$$

where $\beta_{\mathrm{q}}=\omega_{\mathrm{q}}/u_0=\sqrt{R_{\mathrm{p}}g}$ is the phase constant of space-charge wave traveling with a phase velocity u_0, and at an angular frequency ω_{q}. The solution of Equation (7.8) leads to four modal complex-valued wavenumbers that describe the modes in the TWT interactive system. The characteristic equation is equivalently rewritten as

$$\left(k^2-\beta_{\mathrm{c}}^2\right)\left((k-\beta_0)^2-\beta_{\mathrm{q}}^2\right)=-a^2g\beta_{\mathrm{c}}(\omega)Z_{\mathrm{c}}(\omega)k^2. \tag{7.9}$$

The first parenthesis on the left side of Equation (7.9) only contains parameters related

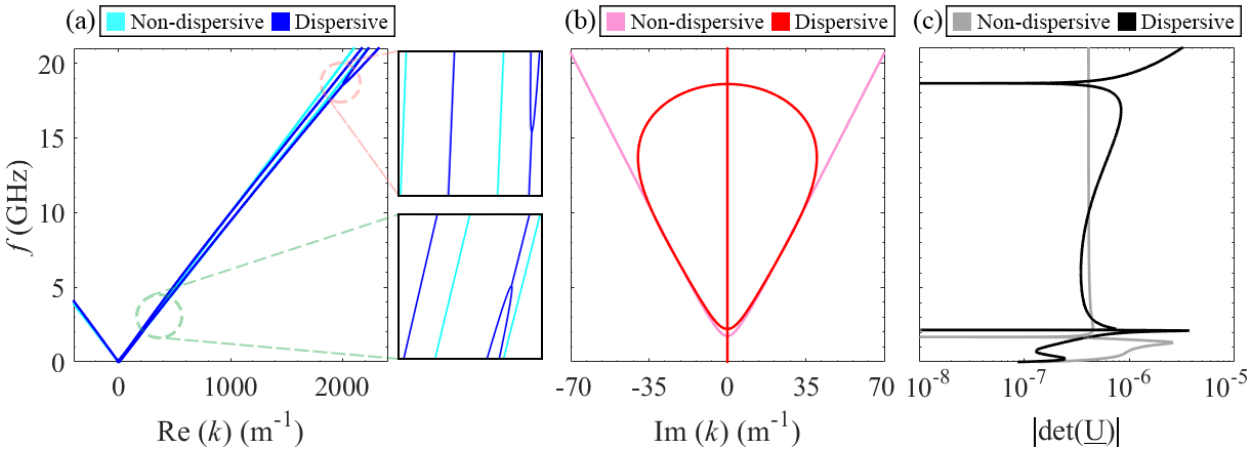

Figure 7.4: Dispersion diagram of the four complex-valued wavenumbers of the hot modes versus frequency, which shows two (one) bifurcation points correspond to the EPDs in the dispersive (non-dispersive) system, and $|\det(\underline{\mathbf{U}})|$ whose minima indicate the occurrence of EPDs.

to TL and the second parenthesis includes only the parameters of the e-beam. The term on the right side represents the interaction between the EM mode in the SWS and the e-beam, and it contains both e-beam and EM mode parameters. When the e-beam and TL are decoupled, one has $a = 0$, the two equations in parenthesis become two independent dispersion equations.

7.3 The Required Condition for an EPD

A second-order EPD occurs when two eigenmodes coalesce in their eigenvalues and eigenvectors. Thus, when such degeneracy occurs, the matrix $\underline{\mathbf{M}}$ is similar to a matrix that contains a Jordan block of order two. A necessary condition to have a second-order EPD is to have two repeated eigenvalues, which means that the characteristic equation should have two repeated roots as

$$D(\omega_e, k) \propto (k - k_e)^2, \tag{7.10}$$

where ω_{e} and k_{e} are the degenerate angular frequency and wavenumber at the EPD. This happens when $D(\omega_{\mathrm{e}}, k_{\mathrm{e}}) = 0$, and $\partial_k D(\omega_{\mathrm{e}}, k)|_{k=k_{\mathrm{e}}} = 0$. We derive the following expressions for $Z = Z_{\mathrm{e}}$ and $Y = Y_{\mathrm{e}}$, which will produce the EPD for given e-beam parameters

$$Z_{\mathrm{e}} = \frac{j\left((k_{\mathrm{e}} - \beta_0)^2 - R_{\mathrm{p}} g\right)^2}{a^2 g\left(-\beta_0^2 + k_{\mathrm{e}}\beta_0 + R_{\mathrm{p}} g\right)}, \tag{7.11}$$

$$Y_{\mathrm{e}} = \frac{j a^2 g k_{\mathrm{e}}^3 (k_{\mathrm{e}} - \beta_0)}{\left((k_{\mathrm{e}} - \beta_0)^2 - R_{\mathrm{p}} g\right)^2}, \tag{7.12}$$

where all the parameters are calculated at ω_{e} and k_{e}. Assuming that the EPD conditions for impedance and admittance in Equations (7.11) and (7.12) are satisfied, the degenerate wavenumber k_{e} is determined by the product of Equations (7.11) and (7.12)

$$Z_{\mathrm{e}} Y_{\mathrm{e}} = \frac{-k_{\mathrm{e}}^3 (k_{\mathrm{e}} - \beta_0)}{(-\beta_0^2 + k_{\mathrm{e}}\beta_0 + R_{\mathrm{p}} g)}. \tag{7.13}$$

We know that $\beta_{\mathrm{c,e}}^2 = -Z_{\mathrm{e}} Y_{\mathrm{e}}$ and $\beta_{\mathrm{q}}^2 = R_{\mathrm{p}} g$ under the EPD condition, so we calculate the wavenumber of the degenerate hot mode k_{e} by solving

$$\beta_{\mathrm{c,e}}^2 \beta_{\mathrm{q}}^2 = (k_{\mathrm{e}}^3 - \beta_{\mathrm{c,e}}^2 \beta_0)(k_{\mathrm{e}} - \beta_0). \tag{7.14}$$

In order to investigate the EPD, we analytically derive the system's eigenvector expressions related to the four wavenumbers k_n with $n = 1, 2, 3, 4$, that are written in the form of

$$\boldsymbol{\Psi}_n = \begin{bmatrix} (k_n - \beta_0)^2 - \beta_{\mathrm{q}}^2 \\ \frac{k_n}{\beta_{\mathrm{c}} Z_{\mathrm{c}}} \left((k_n - \beta_0)^2 - \beta_{\mathrm{q}}^2 \right) \\ a k_n (k_n - \beta_0) \\ a g k_n \end{bmatrix}. \tag{7.15}$$

In summary, the two conditions in Equations (7.11) and (7.12) represent constraints on the TL parameters, calculated at the EPD frequency. These two conditions need to be enforced to have a second-order EPD, where two eigenmodes of the interacting system have identical eigenvalues $k_1 = k_2 = k_{\mathrm{e}}$ and eigenvectors $\boldsymbol{\Psi}_1 = \boldsymbol{\Psi}_2 = \boldsymbol{\Psi}_e$. Suppose we find a set of parameters to satisfy the EPD condition; in that case, these values lead to the same two eigenvalues and a single corresponding eigenvector according to Equation (7.15).

7.4 Example of the Realistic Helix TWT

The helix SWS features a conventional two-body (input and output) cylindrical vacuum envelope that contains a metallic tape helix supported by three equally spaced dielectric rods, which are made of BeO with $\varepsilon_{\mathrm{r}} = 6.5$ [298]. The SWS is illustrated in Figure 7.2(a), with the helix's geometric parameters shown in the caption. Because the helix TWT dispersion is vital for pulse amplification or nonstationary problems' response of the tube, the frequency dependence of the cold circuit phase velocity and the interaction impedance must be included in the model [288, 289, 299]. We have simulated the helix SWS by using the finite element method eigenmode solver in CST Studio Suite and extracted the characteristic parameters, i.e., the cold circuit EM phase velocity $v_{\mathrm{c}}(\omega)$, and the equivalent TL characteristic impedance $Z_{\mathrm{c}}(\omega)$; then the calculated results is illustrated in Figure 7.3(a). We demonstrate

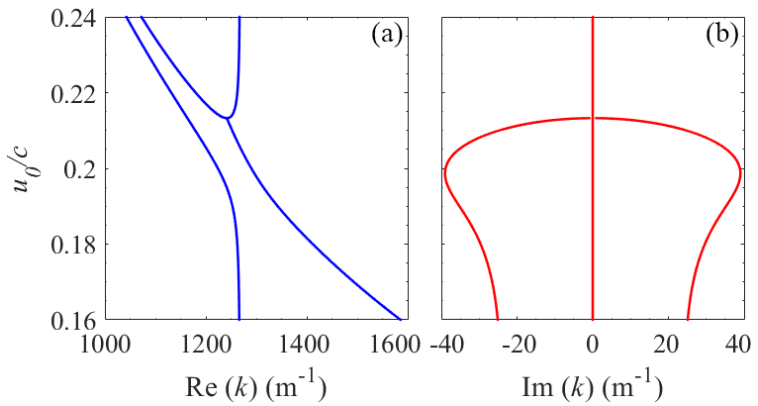

Figure 7.5: Dispersion diagram of the three wavenumbers of the hot modes versus u_0. The diagram shows a bifurcation point that corresponds to the EPD point, whereas frequency is equal to the synchronization frequency f_{sync}.

the occurrence of EPDs in the helix TWT using practical values for both the helix SWS and e-beam. For the e-beam, we assume $u_0 = 0.2c$, where c is the speed of light, $I_0 = 47\,\text{mA}$, $V_0 = 10.5\,\text{kV}$, and a e-beam radius equal to $r_\text{b} = 560\,\mu\text{m}$. The resulting plasma frequency is $f_\text{p} = \omega_\text{p}/(2\pi) = 624.6\,\text{MHz}$. We assume a plasma frequency reduction factor of $R_\text{sc} = 0.12$, which was calculated for the SWS in Figure 7.2(a) using the software LATTE [300, 288, 301]. The maximum interaction between the space-charge wave and the EM wave occurs when they are synchronized, i.e., by matching v_c to u_0, a condition that is specifically called "synchronization". We calibrate the value of the coupling strength coefficient a, which is an essential parameter of our model, to predict the gain in the TWT; this coefficient can be used to calculate the gain of longer TWT structures. In this example, we estimate $a = 0.917$, as extracted from simulations, and the required steps are explained in Section 7.12. Then, by solving the wavenumber dispersion equation for specific frequency values, we obtain the real and imaginary parts of the four hot modes wavenumbers in Figure 7.4(a) and (b). Moreover, in Figure 7.4, we illustrate the non-dispersive results by using an average value of v_c and Z_c in the predetermined frequency range (See Figure 7.3(a)). As we can observe, the non-dispersive model cannot capture the second EPD at a higher frequency, which exists in realistic structures.

The similarity transformation matrix $\underline{\mathbf{U}} = [\mathbf{U}_1, \mathbf{U}_2, \mathbf{U}_3, \mathbf{U}_4]$, where the column $\underline{\mathbf{U}}_i$ is the eigenvector corresponding to the i-th eigenvalue, diagonalizes the system matrix as $\underline{\mathbf{M}} = \underline{\mathbf{U}\mathbf{\Lambda}\mathbf{U}}^{-1}$. At an EPD, at least two eigenvectors become linearly dependent, implying that $|\det(\underline{\mathbf{U}})|$ vanishes. In this example, we consider the EPD frequency of the dispersive model at $f_{\mathrm{e}} = 18.60$ GHz in the shown frequency range, where $\beta_{0,\mathrm{e}} = 1948.16\ \mathrm{m}^{-1}$. In Figure 7.4(a) and (b), we observe the bifurcation of the wavenumbers' real and imaginary parts at the EPDs. The maximum TWT gain is at $f_{\mathrm{opt}} = 13.67$ GHz, where the maximum value of the imaginary part occurs. This frequency is close to the initial-design synchronization frequency $f_{\mathrm{sync}} = 12.10$ GHz, where $v_{\mathrm{c}} = u_0 = 0.2c$, as expected. It may be possible to shift the maximum gain frequency by changing the frequencies of EPDs through varying plasma frequency or other controllable parameters in the TWT-system. In order to validate the proposed TWT model, which accounts for waveguide mode dispersion and space-charge effect, we provide the gain versus frequency plot obtained from simulations in LATTE and compare it to the theoretically calculated gain based on applying boundary conditions for the charge wave and EM mode as explained in Section 7.12. The accuracy of the proposed method is demonstrated by the good agreement between simulated and theoretical results for the dispersive model in Figure 7.3(b). This figure shows that the non-dispersive model cannot predict the gain correctly in the illustrated frequency range.

So far, we have analyzed the dispersion diagram by varying frequency. In the next step, we investigate the wavenumber dispersion diagram varying the electron's average velocity out of synchronization and observe EPDs under these conditions. Hence, we assume the frequency to be fixed and equal to the original synchronization frequency f_{sync}. Then, we change u_0 to explore EPDs out of synchronization, leading to the results in Figure 7.5. In this figure, wavenumbers with a positive real part are displayed as mentioned in [302], and a second-order EPD exists around $u_{0,\mathrm{e}} = 0.213c$. So the bifurcation is observed in the dispersion diagram when we select u_0 larger than v_{c}. The bifurcation of the wavenumber, when u_0 is varied, is clear evidence of an EPD.

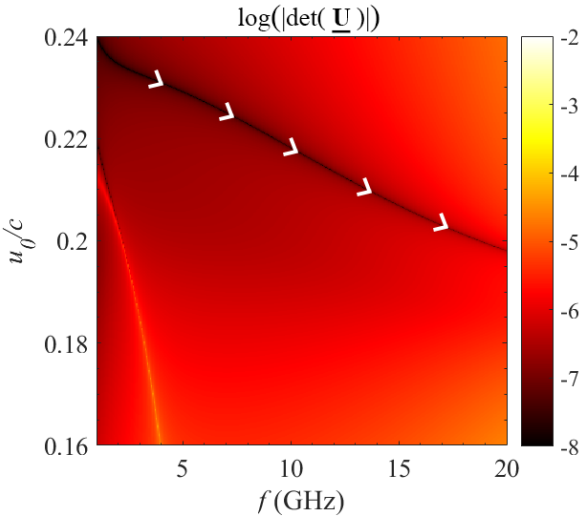

Figure 7.6: Determinant of the similarity transformation matrix $\underline{\mathbf{U}}$ varying f and u_0. The black curve under the white arrows denotes the location of the exceptional degeneracy.

Based on the results in Figures 7.4 and 7.5, we conclude that the TWT-system is very sensitive to variation in frequency and u_0 near an EPD. Figure 7.6 shows the $\log\left(|\det(\underline{\mathbf{U}})|\right)$ when frequency and u_0 are varied. The black curve shows the lowest values, which means the eigenvectors coalesce at those specific values of f and u_0. Thus, the black contour represents EPDs. EPDs can be utilized to measure e-beam parameters by changing the frequency in the TWT-system. For a practical scenario, if we have an e-beam with an unknown u_0 in the predetermined range, we can vary the operating frequency to observe EPD and find the corresponding u_0.

Here we establish that a system's sensitivity to a specific parameter variation is boosted by the eigenmodes' degeneracy [303]. For instance, let us consider the EPD in Figure 7.4 at $f_\mathrm{e} = 18.60$ GHz. To measure the sensitivity of the wavenumber to frequency variation, the system's relative perturbation parameter is defined as $\Delta = (f - f_\mathrm{e})/f_\mathrm{e}$. Consequently, the perturbed system matrix $\underline{\mathbf{M}}(\Delta)$ has two degenerate eigenvalues (i.e., the wavenumbers) occurring at the EPD shift considerably due to a small perturbation in frequency, resulting in two separate eigenvalues $k_n(\Delta)$, with $n = 1, 2$. These two perturbed eigenvalues are estimated by using a convergent Puiseux series, where the coefficients are calculated using

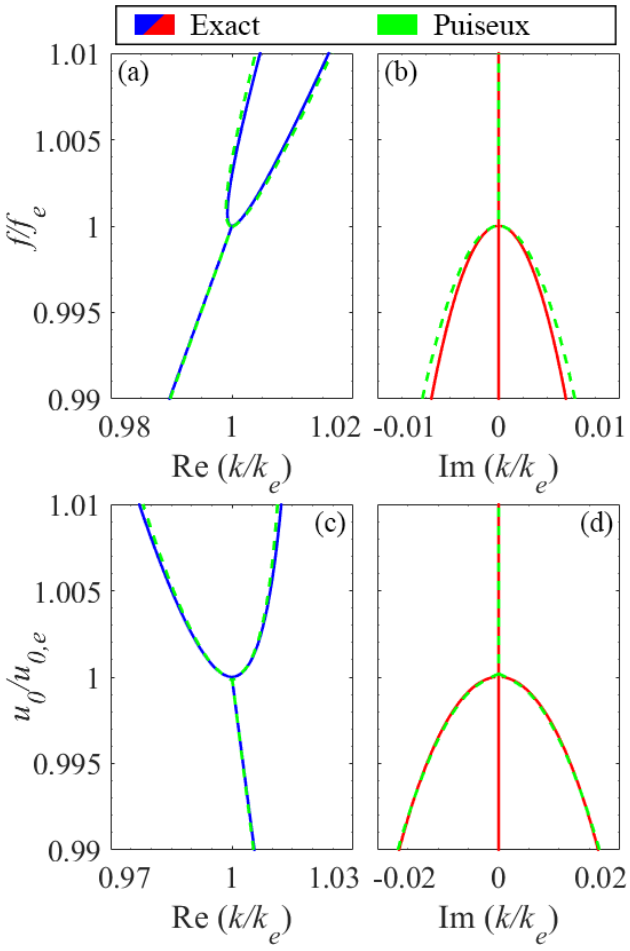

Figure 7.7: The Puiseux fractional power expansion up to the second-order approximates the dispersion diagram variation by frequency and u_0, further demonstrating that the bifurcation point is the EPD. (a) and (b) Complex-valued wavenumbers when frequency is changed, and the required coefficients are calculated as $\alpha_1 = 126.77\ \mathrm{m}^{-1}$ and $\alpha_2 = 2054.63\ \mathrm{m}^{-1}$. (c) and (d) Complex-valued wavenumbers when u_0 is changed, and the required coefficients are calculated as $\alpha_1 = 206.95\ \mathrm{m}^{-1}$ and $\alpha_2 = -667.74\ \mathrm{m}^{-1}$.

the explicit formulas given in [91]. The approximation of $k_n(\Delta)$ around a second-order EPD is given by

$$k_n(\Delta) \approx k_\mathrm{e} + (-1)^n \alpha_1 \sqrt{\Delta} + \alpha_2 \Delta. \tag{7.16}$$

Following [91], α_1 and α_2 are calculated by

$$\alpha_1 = \sqrt{\left(-\frac{\frac{\partial H}{\partial \Delta}(\Delta, k)}{\frac{1}{2!}\frac{\partial^2 H}{\partial k^2}(\Delta, k)} \right)}, \tag{7.17}$$

$$\alpha_2 = -\frac{-(\alpha_1^3 \frac{1}{3!}\frac{\partial^3 H}{\partial k^3}(\Delta, k) + \alpha_1 \frac{\partial^2 H}{\partial k \partial \Delta}(\Delta, k))}{2\alpha_1(\frac{1}{2!}\frac{\partial^2 H}{\partial k^2}(\Delta, k))}, \tag{7.18}$$

evaluated at the EPD, i.e., at $\Delta = 0$ and $k = k_{\mathrm{e}}$, where $H(\Delta, k) = \det[\underline{\mathbf{M}}(\Delta) - k\underline{\mathbf{I}}]$. Equation (7.16) indicates that for a small perturbation $|\Delta| \ll 1$ in frequency, the eigenvalues change dramatically from their original degenerate value due to the square root dependence. The results in Figures 7.7(a) and (b) produce the two branches of the exact perturbed eigenvalues k_n obtained from the eigenvalue problem when the perturbation Δ is applied. These figures explain that such perturbed eigenvalues could be estimated with high accuracy by using the Puiseux series truncated to its second order. Next, we analyze the sensitivity to variations in u_0 by defining $\Delta = (u_0 - u_{0,\mathrm{e}})/u_{0,\mathrm{e}}$ and apply the same procedure to achieve a Puiseux series coefficients. The calculated results are illustrated in Figures 7.7(c) and (d), which demonstrate the bifurcation and high-sensitivity of the wavenumbers to perturbation near the EPD.

7.5 Electron Beam Model

There are various approaches to analyzing an e-beam's interaction with a traveling EM wave on a circuit. The classical small-signal theory by J. R. Pierce is one of the approaches that still use these days for the modeling and designing of TWT. Pierce's model includes a qualitative description of traveling wave interaction that is explained in [285, 286]. Many of the parameters defined by Pierce are now part of the accepted vocabulary in traveling wave tube research and industry. For these reasons, and because the Pierce theory provides

considerable physical insight into TWT mechanics, the basic elements of the Pierce theory will be described here, together with generalizations that have been adopted.

In this section, we show the fundamental equations that describe the e-beam dynamics in both space and time. We follow the linearized equations that describe the space-charge wave as originally presented by Pierce [286]. We assume the e-beam is made of a narrow cylindrical pencil beam of electrons, which is subject to an axial (i.e., longitudinal) electric field, assumed constant over the beam's transverse cross-section; we also consider purely longitudinal electron motion due to a strong externally applied axial magnetic field which confines the beam. Because of this, the beam is described by a one-dimensional function, as will be shown. The beam's total linear charge density $\rho_b^{tot}(z,t)$, and electron velocity $u_b^{tot}(z,t)$ are represented as

$$\rho_b^{tot}(z,t) = \rho_0 + \rho_b(z,t), \tag{7.19}$$

$$u_b^{tot}(z,t) = u_0 + u_b(z,t), \tag{7.20}$$

where the subscripts "0" and "b" denote the d.c. (average value) and the a.c. (alternate current, i.e., modulation), respectively. In the above equations, ρ_0 is negative and $u_b^{tot}(z,t)$ is the electron speed in the z-direction. The basic equation that is governing the charges' longitudinal motion is

$$\frac{du_b^{tot}(z,t)}{dt} = -\eta e_z, \tag{7.21}$$

where $\eta = e/m = 1.758829 \times 10^{11} C/kg$ is the charge to mass ratio of an electron, the electron charge is equal to $-e$, and m is the rest mass of the electron. The term e_z is the total a.c.

electric field in the z-direction, provided by the superposition of two fields as $e_z = e_w + e_p$, where e_w is the z-polarization of the electric field pertaining to the EM mode guided in the waveguide, and e_p is the electric field generated by space-charge, as is discussed later in this section. Following [286], we rewrite the total derivative on the left-hand side of Equation (7.21) as

$$\frac{d(u_0 + u_b)}{dt} = \frac{\partial u_b}{\partial t} + (u_0 + u_b)\frac{\partial u_b}{\partial z} + \frac{\partial u_0}{\partial t} + (u_0 + u_b)\frac{\partial u_0}{\partial z}. \tag{7.22}$$

Some terms on this equation vanish because $\partial u_0/\partial t = 0$, and $\partial u_0/\partial z = 0$. Using a small-signal approximation, we assume that the modulating velocity u_b is small with respect to u_0; hence the term $u_b \partial u_b/\partial z$, which is a product of two a.c. small quantities, is negligible with respect to the two other terms involving u_b. Therefore, in our small-signal theory, we neglect the term $u_b \partial u_b/\partial z$, as was originally done by Pierce [286]. Thus, Equation (7.21) is rewritten as

$$\frac{\partial u_b(z,t)}{\partial t} + u_0 \frac{\partial u_b(z,t)}{\partial z} = -\eta e_z. \tag{7.23}$$

For convenience, we define the equivalent kinetic beam current as

$$i_b^{tot}(z,t) = u_b^{tot}(z,t)\rho_b^{tot}(z,t) = u_0\rho_0 + u_0\rho_b + u_b\rho_0 + u_b\rho_b \approx -I_0 + i_b(z,t), \tag{7.24}$$

Note that we assume a small-signal modulation in the beam speed and charge density, i.e., we consider a linear model by neglecting the term $u_b\rho_b$ in Equation (7.24). Here, the term $u_b\rho_b$ is a product of two small a.c. quantities and is neglected. The a.c. and d.c. portions of the e-beam current are

$$\begin{cases} i_b(z,t) = u_0\rho_b + u_b\rho_0 \\ \\ \qquad -I_0 = u_0\rho_0 \end{cases} \tag{7.25}$$

Moreover, we consider the continuity equation or conservation of charge,

$$\frac{\partial i_b^{tot}(z,t)}{\partial z} = -\frac{\partial \rho_b^{tot}(z,t)}{\partial t}, \tag{7.26}$$

which is rewritten as follows

$$\frac{\partial i_b(z,t)}{\partial z} - \frac{\partial I_0}{\partial z} = -\frac{\partial \rho_b(z,t)}{\partial t} - \frac{\partial \rho_0}{\partial t}. \tag{7.27}$$

We know that I_0 and ρ_0 are d.c. quantities, i.e., their derivatives are vanishing, so the continuity equation leads finally to

$$\frac{\partial i_b(z,t)}{\partial z} = -\frac{\partial \rho_b(z,t)}{\partial t}. \tag{7.28}$$

For a non-relativistic beam, it is convenient to define an equivalent kinetic beam voltage as

$$v_b^{tot}(z,t) = \frac{\left(u_b^{tot}(z,t)\right)^2}{2\eta} = \frac{u_0^2 + u_b^2 + 2u_0u_b}{2\eta} \approx V_0 + v_b(z,t), \tag{7.29}$$

and as explained earlier, based on the small-signal approximation, we neglect the nonlinear term u_b^2, and separate the a.c. and d.c. terms as

$$\begin{cases} v_b(z,t) = \frac{u_0 u_b}{\eta} \\ \\ V_0 = \frac{u_0^2}{2\eta} \end{cases} \tag{7.30}$$

By combining Equations (7.28), (7.25), and (7.30) we find

$$\frac{\partial i_b(z,t)}{\partial z} = \frac{\eta\rho_0}{u_0^2}\frac{\partial v_b(z,t)}{\partial t} - \frac{1}{u_0}\frac{\partial i_b(z,t)}{\partial t}. \tag{7.31}$$

Moreover, by using Equations (7.23), and (7.30) we write

$$\frac{\partial v_b(z,t)}{\partial z} + \frac{1}{u_0}\frac{\partial v_b(z,t)}{\partial t} = -e_z. \tag{7.32}$$

Equations (7.31) and (7.32) are the two equations governing the e-beam's dynamic based on the model adopted. In the next step, we elaborate more on the bunching and debunching effects of the convection beam current in a traveling-wave field. As was stated previously, the total longitudinal field e_z is represented as the sum of the electric field of the EM mode in the SWS and the a.c. space-charge field, $e_z = e_w + e_p$,where e_w is the z-component of the purely vortical field $\mathbf{e}_w = \text{curl}\mathbf{b}_w$, where $\mathbf{b}_w$ is a magnetic field of the EM mode in the passive SWS; therefore, div$\mathbf{e}_w = 0$ [290, 1]. The waveguide EM field e_w is provided by [286]

$$e_w = -a\frac{\partial v}{\partial z}, \tag{7.33}$$

where v is the voltage in the equivalent TL which describes how EM fields propagate in the waveguide, as will be explained further in the next section. In order to model the interaction strength between the e-beam and TL, we have generalized the coupling strength

using the coefficient a that represents the strength of interaction between the e-beam and the guided EM mode, as was also described in [293, 292, 291]. Physically, this coupling strength coefficient describes how strongly the electric field of a mode in the SWS affects electron motion.

The space-charge field e_p is longitudinal, i.e., polarized along the z-direction, and it is generated by electron bunching. It is determined from the Poisson equation $\nabla \cdot e_p = \rho_v/\varepsilon_0$. The volumetric charge density ρ_v is assumed to be only z-dependent, and it is related to the linear charge density by $\rho_b = \rho_v A$, where A is the transverse cross-sectional area of the beam. This leads to

$$\frac{\partial e_p}{\partial z} = \frac{\rho_b}{A\varepsilon_0}. \tag{7.34}$$

Differentiating in time on both sides of Equation (7.34) and using Equation (7.28), the above equation is reduced to

$$\frac{\partial^2 e_p}{\partial t \partial z} = -\frac{1}{A\varepsilon_0}\frac{\partial i_b}{\partial z}. \tag{7.35}$$

Now, we rewrite all the equations that will be used to find the eigenmodes in the phasor domain assuming implicitly the $\exp(j\omega t)$ time dependence for monochromatic fields. Equation (7.31) is rewritten in terms of the beam's equivalent voltage and current phasors as

$$\frac{\partial I_b}{\partial z} = -j\frac{\omega I_0}{2V_0 u_0}V_b - j\frac{\omega}{u_0}I_b, \tag{7.36}$$

which represents the first of the two main equations that govern the beam dynamics. The second equation is obtained from Equation (7.32) based on the following steps. In the phasor

domain, $E_z = E_w + E_p$, and Equation (7.33) is written as $E_w(\omega) = -a\,(dV/dz)$. Then, considering the well-known telegrapher's equation in the phasor domain $dV/dz = -ZI$, where Z is the series per-unit-length TL distributed impedance, and I is the current in the equivalent TL (see next section), the longitudinal EM-guided field is found as

$$E_w(\omega) = aZI. \tag{7.37}$$

By using the phasor form, Equation (7.35) integrated in the z-domain is rewritten as

$$E_p(z) = j\frac{1}{A\varepsilon_0\omega}I_b(z) + \text{const.} \tag{7.38}$$

Finally, using the obtained expression for total longitudinal field $E_z = E_w + E_p$, Equation (7.32) in the phasor domain yields

$$\frac{\partial V_b}{\partial z} = -aZI - j\frac{\omega}{u_0}V_b - j\frac{1}{A\varepsilon_0\omega}I_b, \tag{7.39}$$

which connects the EM mode equivalent current to the e-beam kinetic voltage and current. This is the second main equation that governs the beam's dynamics.

So far, we have achieved *two* important first-order linear differential equations that describe the dynamics of the e-beam kinetic voltage and current, Equation (7.39) and Equation (7.36), respectively. As we observe in Equation (7.36), the e-beam current is only associated with e-beam parameters, whereas Equation (7.39) indicates that TL parameters (in this case, Z and I) are also required to calculate e-beam voltage. In Equation (7.39), space-charge fields describe repulsive forces in dense beams of charged particles. These forces induce oscillations of particles at a plasma frequency, which, in a moving medium, have the form of

a propagating wave (i.e., the space-charge wave). The plasma frequency is given by

$$\omega_{\mathrm{p}} = \sqrt{-\frac{\rho_0 \eta}{A\varepsilon_0}} = \sqrt{\frac{I_0 u_0}{2V_0 A\varepsilon_0}}. \tag{7.40}$$

In reality, the beam is enclosed in a metallic structure that affects the propagation of space-charge waves. Thus, the plasma frequency of the e-beam, ω_{p}, is effectively decreased, as compared to its value in the case of an infinite transverse cross section, to a reduced plasma frequency ω_{q} [304]. Therefore, it is important to calculate the reduced plasma frequency ω_{q}. This is done by accounting for the reduction factor associated to the plasma frequency $R_{\mathrm{sc}} = \omega_{\mathrm{q}}/\omega_{\mathrm{p}}$ that accounts for the metallic tunnel. In the specific case of a thin tape helix TWT with a pencil e-beam, Branch and Mihran found that the helix can be approximated with a perfectly conducting metallic cylinder of the same internal radius [304]. In this chapter we have used a plasma frequency reduction factor equal to $R_{\mathrm{sc}} = 0.12$, which was calculated for the designed SWS using the software LATTE [300, 288, 301]. To better estimate a TWT performance, one simply replaces ω_{p} with ω_{q} in the fundamental equations. Therefore, we rewrite Equation (7.39) as

$$\frac{dV_b}{dz} = -aZI - j\frac{\omega}{u_0}V_b - j\frac{2V_0\omega_q^2}{\omega I_0 u_0}I_b. \tag{7.41}$$

The first term on the right-hand side in Equation (7.41) shows the role of the electric field of the waveguide EM mode in the e-beam equations.

7.6 Space-Charge Effect

Space-charge fields represent repulsive forces in dense beams of charged particles. These forces induce oscillations of particles at a plasma frequency, which, in a moving medium, has the form of a propagating wave (i.e., the space-charge wave). In this chapter, we have provided TWT-system equations which account for space-charge effects. This effect can be modeled based on calculations provided in Section 7.5 for the Lagrangian model of the TWT-system in [293, 291]. In the first step, we start with the extended equations represented in Equation (7.52),

$$\begin{cases} \partial_z V = -ZI \\ \partial_z I = -YV + ja\frac{\omega I_0}{2V_0 u_0}V_b + ja\frac{\omega}{u_0}I_b \\ \partial_z V_b = -aZI - j\frac{\omega}{u_0}V_b - j\frac{1}{\omega A\varepsilon_0}I_b \\ \partial_z I_b = -j\frac{\omega I_0}{2V_0 u_0}V_b - j\frac{\omega}{u_0}I_b \end{cases} \tag{7.42}$$

Then, we transform the four first-order differential equations into two second-order differential equations by removing voltages, V and V_b, leading to

$$\begin{cases} \partial_z^2 I - ZYI + a\partial_z^2 I_b = 0 \\ jag\partial_z^2 I - Y\partial_z^2 I_b - j2Y\beta_0\partial_z I_b + Y\beta_0^2 I_b - gYR_{\mathrm{p}}I_b + ja^2 g\partial_z^2 I_b = 0 \end{cases} \tag{7.43}$$

In the next step, we use the below substitutions for converting currents to charges

$$\begin{cases} I = j\omega Q \\ \\ I_b = j\omega q \end{cases} \tag{7.44}$$

After some mathematical manipulation, we obtain these equations

$$\begin{cases} L\partial_t^2 Q - \partial_z[C^{-1}(\partial_z Q + a\partial_z q)] = 0 \\ \frac{\beta_0^2}{g\omega}(\partial_t + \frac{\omega}{\beta_0}\partial_z)^2 q + \omega R_{\mathrm{p}} q - a\partial_z[C^{-1}((\partial_z Q + a\partial_z q))] = 0 \end{cases} \tag{7.45}$$

This set of equations are equivalent to Euler-Lagrange equations, which are presented in Equations (7.81), and (7.82). The term $\omega R_{\mathrm{p}} q$ is responsible for the space-charge effect. It can also be written as

$$\omega R_{\mathrm{p}} q = \frac{1}{A\varepsilon_0} q. \tag{7.46}$$

On the other hand, in the presented Euler-Lagrange equations, the term $\frac{4\pi}{\sigma_B} q$, accounts for the debunching effect (See Equation (7.82)). Since the Gaussian system of units is utilized in the Euler-Lagrange equations, we need to transform parameters to SI. After performing the mentioned transformation, we obtain the same definition as presented in Equation (7.46).

7.7 Electromagnetic Field in the Waveguide Represented by an Equivalent Transmission Line and Interaction With the Beam's Charge Wave

In the TWT-system, the flowing electrons interact with a surrounding circuit. The convection current in the beam causes current to be induced in the circuit. This induced current adds to the current already presented in the circuit, causing the circuit power to increase with distance as power is extracted from the e-beam. We model the SWS using an equivalent TL whose equations are

$$\frac{dV}{dz} = -ZI, \tag{7.47}$$

$$\frac{dI}{dz} = -YV + i_s. \tag{7.48}$$

Here, V indicates the equivalent voltage (related to the electric field), and I indicates the equivalent current (related to the magnetic field) in the phasor domain, as explained in [294, 305]. Furthermore, Z is the distributed series impedance per-unit-length, and Y is the distributed shunt admittance per-unit-length. In the above equation, the term i_s represents a distributed current generator [286, 292] that accounts for the effect of the electron stream flowing in the SWS on the EM field whose expression is given by $i_s = -a\,(dI_b/dz)$. We substitute dI_b/dz in this latter equation with Equation (7.36). Then, we obtain the set of two fundamental equations for the equivalent TL

$$\frac{dV}{dz} = -ZI, \tag{7.49}$$

$$\frac{dI}{dz} = -YV + ja\frac{\omega I_0}{2V_0 u_0}V_b + ja\frac{\omega}{u_0}I_b. \tag{7.50}$$

In the case of a lossless and non-dispersive waveguide, one has $Z = j\omega L$ and $Y = j\omega C$; however, it is important to note that these equations are here generalized for realistic lossy and dispersive waveguides by accounting for the more complex frequency dependence in $Z(\omega)$ and $Y(\omega)$. Indeed, in realistic systems like the one discussed in this chapter, the dispersive waveguide is described by parameters $Z(\omega)$ and $Y(\omega)$ with nonlinear frequency dependence. This more involved frequency dispersion can be equivalently accounted for by defining a dispersive inductance and capacitance per-unit-length as $Z = j\omega L(\omega)$ and $Y = j\omega C(\omega)$ [288, 289, 299].

As a final step, we now summarize the system of four equations comprising the differential equations in Equations (7.36), (7.41), (7.49), and (7.50). This system describes the full dynamics of the linearized (small-signal) model in terms of the equivalent TL voltage and current, $I(z)$ and $V(z)$, as well as the charge-wave current and kinetic voltage, $I_b(z)$ and $V_b(z)$, respectively. We conveniently define a space-varying state vector composed of these four EM-field and charge-wave variables as

$$\mathbf{\Psi}(z) = \begin{bmatrix} V(z) \\ I(z) \\ V_b(z) \\ I_b(z) \end{bmatrix}. \tag{7.51}$$

Without loss of generality, we assume that the TL is homogeneous (i.e., z-invariant), as was originally done by Pierce [286], and we write the four fundamental equations in matrix form as

$$\partial_z \mathbf{\Psi}(z) = -j\underline{\mathbf{M}}\mathbf{\Psi}(z), \tag{7.52}$$

where $\underline{\mathbf{M}}$ is a 4×4 system matrix [26]

$$\underline{\mathbf{M}} = \begin{bmatrix} 0 & -jZ & 0 & 0 \\ -jY & 0 & -ag & -a\beta_0 \\ 0 & -jaZ & \beta_0 & R_{\mathrm{p}} \\ 0 & 0 & g & \beta_0 \end{bmatrix}. \tag{7.53}$$

In the above matrix, we have defined the set of parameters as

$$\beta_0 = \frac{\omega}{u_0}, \tag{7.54}$$

$$g = \frac{1}{2}\frac{I_0\beta_0}{V_0}, \tag{7.55}$$

$$R_{\mathrm{p}} = \frac{1}{A\varepsilon_0\omega} = \frac{2V_0\omega_q^2}{\omega I_0 u_0}, \tag{7.56}$$

where β_0 is beam equivalent propagation constant, and g is a parameter related to the e-beam [26]. In this formulation, we have considered the effect of the bunching of the convection beam current in a traveling wave field using the R_{p} term in the above matrix, as was done in [295, 253]. This description in terms of a multidimensional first-order differential equation in Equation (7.52) is ideal for exploring the occurrence of an exceptional point of degeneracy (EPD) in the system since an EPD is a degeneracy associated with two or more coalescing eigenmodes. In other words, EPDs occur when the system matrix $\underline{\mathbf{M}}$ is similar to a matrix that contains a nontrivial Jordan block. In general, there are four independent eigenmodes and each eigenmode is described by an eigenvector $\mathbf{\Psi}$.

7.8 Dispersion Equation to Find the Hot Eigenmodes

To obtain the dispersion equation or characteristic equation, we search for solutions of the form $\mathbf{\Psi}(z) = \mathbf{\Psi}e^{-jkz}$, where k is the complex-valued wavenumber of a hot mode (With the term "hot" mode, we refer to a mode of the system where the e-beam interacts with the EM wave of the SWS, and the resulting modes carry information from the two components, the charge wave modulating the e-beam and the EM wave guided by the waveguide.). The four wavenumbers of the hot modes are obtained by solving

$$\det(\underline{\mathbf{M}} - k\underline{\mathbf{I}}) = \det \begin{bmatrix} -k & -jZ & 0 & 0 \\ -jY & -k & -ag & -a\beta_0 \\ 0 & -jaZ & -k+\beta_0 & R_{\mathrm{p}} \\ 0 & 0 & g & -k+\beta_0 \end{bmatrix} = 0. \tag{7.57}$$

After some mathematical calculations, the dispersion equation is expressed as

$$D(\omega, k) = k^4 - k^3(2\beta_0) + k^2(\beta_0^2 - gR_{\mathrm{p}} + ZY - ja^2Zg) - k(2ZY\beta_0) + ZY(\beta_0^2 - gR_{\mathrm{p}}) = 0. \tag{7.58}$$

Furthermore, the dispersion equation can be rewritten in the convenient form

$$(k^2 + ZY)\left((k-\beta_0)^2 - R_{\mathrm{p}}g\right) = ja^2gZk^2, \tag{7.59}$$

or we can rewrite it as [292]

$$(k-\beta_0)^2 - \frac{ja^2gZk^2}{k^2+ZY} = gR_{\mathrm{p}}. \tag{7.60}$$

The cold circuit phase propagation constant is $\beta_c = \sqrt{-ZY}$, and we also used the definition $\beta_{\mathrm{q}} = \omega_{\mathrm{q}}/u_0 = \sqrt{R_{\mathrm{p}}g}$ which represents the phase constant of the space charge wave traveling with a phase velocity equal to the average electron velocity and at an angular frequency equal to ω_{q}. So, the dispersion characteristic equation is equivalently rewritten as

$$(k^2 - \beta_c^2)\left((k-\beta_0)^2 - \beta_{\mathrm{q}}^2\right) = ja^2 gZk^2. \tag{7.61}$$

The right-hand side describes the coupling strength between the two guiding systems: the wavenumber dispersion in the isolated EM waveguide (i.e., without e-beam interaction) would be described by $(k^2 - \beta_c^2) = 0$, and the wavenumber dispersion in the isolated charge wave (i.e., without interacting with the guided EM wave) would be described by $\left((k-\beta_0)^2 - \beta_{\mathrm{q}}^2\right) = 0$. It is convenient to define the circuit characteristic impedance and e-beam impedance as

$$Z_{\mathrm{c}} = \frac{Z}{j\beta_c} = \sqrt{\frac{Z}{Y}}, \tag{7.62}$$

$$Z_0 = \frac{V_0}{I_0}. \tag{7.63}$$

Pierce defined the dimensionless gain parameter C_{P}, and called it "gain parameter" [287],

$$C_{\mathrm{P}}^3 = \frac{Z_{\mathrm{c}}}{4Z_0}. \tag{7.64}$$

Pierce's gain parameter, C_{P}, is a measure of the intensity of the interaction between the e-beam and SWS. The characteristic impedance of the equivalent TL Z_{c}, is also called the interaction impedance or Pierce impedance since it affects the value of Pierce's gain parameter. Consequently, the above dispersion equation is rewritten in terms of Pierce's gain parameter as

$$(k^2 - \beta_c^2)\left((k - \beta_0)^2 - \beta_{\mathrm{q}}^2\right) = -2a^2 C_{\mathrm{P}}^3 \beta_c \beta_0 k^2. \tag{7.65}$$

It may be convenient to consider a modified Pierce gain parameter to account for more realistic EM-beam coupling factors due to the extra coupling strength coefficient we explicitly consider in this chapter, as

$$C_{\mathrm{P,m}}^3 = a^2 C_{\mathrm{P}}^3. \tag{7.66}$$

By using this new modified Pierce gain parameter, the dispersion equation expressed in Equation (7.65) reduces to

$$(k^2 - \beta_c^2)\left((k - \beta_0)^2 - \beta_{\mathrm{q}}^2\right) = -2C_{\mathrm{P,m}}^3 \beta_c \beta_0 k^2. \tag{7.67}$$

Note that the term $C_{\mathrm{P,m}}^3$ on the right side determines the coupling strength between the two dispersion equations of the isolated waveguide and charge-wave guiding systems. If the wavenumber of the hot mode, k, in the above equation is solved versus angular frequency, ω, it is worth recalling that the wavenumber of the EM wave in the cold SWS, β_c, also depends on frequency if we consider the waveguide dispersion in our calculations. Furthermore, the Pierce gain parameter $C_{\mathrm{P,m}}^3$ also depends on frequency when the cold SWS dispersion makes the characteristic impedance frequency-dependent, aside from the obvious frequency-dependence of β_0. Furthermore, R_{sc} may also exhibit a slight frequency variation, though it is assumed constant in this chapter based on its numerical estimation as described in Section 7.5.

An alternative description of the hot modes is provided in terms of their phase velocities

$v = \omega/k$, rather than their wavenumbers, as was done in [291]. Accordingly, the dispersion equation takes the form of

$$\frac{(v-u_0)^2}{v^2} + \frac{ja^2 Z g u_0^2}{v^2\beta_c^2 - \omega^2} = \frac{\omega_{\mathrm{q}}^2}{\omega^2}. \tag{7.68}$$

7.9 EPD Condition

The solutions of our dispersion equations lead to four modal complex-valued wavenumbers that represent the four hot modes in the system. A second-order EPD occurs when two of these eigenmodes coalesce in their eigenvalues and eigenvectors, which means that the matrix $\underline{\mathbf{M}}$ is similar to a matrix that contains a Jordan block of order two [4, 26]. In this case, a necessary condition to have second-order EPD is to have two repeated eigenvalues, which means that the dispersion equation should have two repeated roots as

$$D(\omega_{\mathrm{e}}, k) \propto (k - k_{\mathrm{e}})^2, \tag{7.69}$$

where ω_{e} and k_{e} are the degenerate angular frequency and wavenumber in EPD condition, respectively. The relation in Equation (7.69), which guarantees to have two coalescing wavenumbers, is satisfied when

$$D(\omega_{\mathrm{e}}, k_{\mathrm{e}}) = 0, \tag{7.70}$$

$$\left.\frac{\partial D(\omega_{\mathrm{e}}, k)}{\partial k}\right|_{k=k_{\mathrm{e}}} = 0. \tag{7.71}$$

These two conditions are rewritten, respectively, in the below forms

$$k_{\mathrm{e}}^4 - k_{\mathrm{e}}^3(2\beta_0) + k_{\mathrm{e}}^2(\beta_0^2 - gR_{p,} + Z_{\mathrm{e}}Y_{\mathrm{e}} - ja^2Z_{\mathrm{e}}g) - k_{\mathrm{e}}(2Z_{\mathrm{e}}Y_{\mathrm{e}}\beta_0) + Z_{\mathrm{e}}Y_{\mathrm{e}}(\beta_0^2 - gR_{\mathrm{p}}) = 0, \tag{7.72}$$

$$4k_{\mathrm{e}}^3 - 3k_{\mathrm{e}}^2(2\beta_0) + 2k_{\mathrm{e}}(\beta_0^2 - gR_{\mathrm{p}} + Z_{\mathrm{e}}Y_{\mathrm{e}} - ja^2Z_{\mathrm{e}}g) - (2Z_{\mathrm{e}}Y_{\mathrm{e}}\beta_0) = 0. \tag{7.73}$$

In the above equations, subscript "e" in different parameters indicates the value at the EPD. The TL distributed series impedance Z_{e}, and shunt admittance Y_{e} that provide the EPD are determined after making some mathematical manipulations in the two above conditions. First, we use Equation (7.72) to get Y_{e} in terms of Z_{e} and other system parameters as

$$Y_{\mathrm{e}} = \frac{-k_{\mathrm{e}}^4 + k_{\mathrm{e}}^3(2\beta_0) - k_{\mathrm{e}}^2(\beta_0^2 - gR_{\mathrm{p}} - ja^2Z_{\mathrm{e}}g)}{Z_{\mathrm{e}}\left((k_{\mathrm{e}} - \beta_0)^2 - gR_{\mathrm{p}}\right)}, \tag{7.74}$$

then we substitute this relation into Equation (7.73) and solve it for Z_{e}, which is found to be

$$Z_{\mathrm{e}} = \frac{j\left((k_{\mathrm{e}} - \beta_0)^2 - R_{\mathrm{p}}g\right)^2}{a^2g(-\beta_0^2 + k_{\mathrm{e}}\beta_0 + R_{\mathrm{p}}g)}. \tag{7.75}$$

Finally, we substitute back the impedance value obtained from Equation (7.75) in the admittance value calculated in Equation (7.74) to find admittance

$$Y_{\mathrm{e}} = \frac{ja^2g_ek_{\mathrm{e}}^3(k_{\mathrm{e}} - \beta_0)}{\left((k_{\mathrm{e}} - \beta_0)^2 - R_{\mathrm{p}}g\right)^2}. \tag{7.76}$$

To realize an EPD, the TL series impedance $Z = Z_{\mathrm{e}}$ and shunt admittance $Y = Y_{\mathrm{e}}$ need to satisfy Equations (7.75) and (7.76). Assuming that the EPD conditions in Equations (7.75) and (7.76) are satisfied, then the degenerate wavenumber k_{e} is determined by the product of Equations (7.75) and (7.76)

$$Z_{\mathrm{e}}Y_{\mathrm{e}} = \frac{-k_{\mathrm{e}}^3(k_{\mathrm{e}} - \beta_0)}{(-\beta_0^2 + k_{\mathrm{e}}\beta_0 + R_{\mathrm{p}}g)}. \tag{7.77}$$

We know that $\beta_{\mathrm{c,e}}^2 = -Z_{\mathrm{e}}Y_{\mathrm{e}}$ and $\beta_{\mathrm{q}}^2 = R_{\mathrm{p}}g$, so we calculate k_{e} by solving the equation

$$\beta_{\mathrm{c,e}}^2\beta_{\mathrm{q}}^2 = (k_{\mathrm{e}}^3 - \beta_{\mathrm{c,e}}^2\beta_0)(k_{\mathrm{e}} - \beta_0). \tag{7.78}$$

Since we search for solution of the form $\mathbf{\Psi}(z) = \mathbf{\Psi}_n e^{-jk_n z}$, the eigenvectors $\mathbf{\Psi}_n$ of the system are determined by solving the eigenvalue problem $\underline{\mathbf{M}}\mathbf{\Psi}_n = k_n\mathbf{\Psi}_n$,or we can write it as below

$$(\underline{\mathbf{M}} - k_n\underline{\mathbf{I}})\mathbf{\Psi}_n = 0, \tag{7.79}$$

where k_n with $n = 1, 2, 3, 4$ are the wavenumbers, and they are determined from Equation (7.79). By solving Equation (7.79), the eigenvectors are written in the form of

$$\mathbf{\Psi}_n = \begin{bmatrix} (k_n - \beta_0)^2 - R_{\mathrm{p}}g \\ j\frac{k_n}{Z}\left((k_n - \beta_0)^2 - R_{\mathrm{p}}g\right) \\ ak_n(k_n - \beta_0) \\ agk_n \end{bmatrix}. \tag{7.80}$$

At the second-order EPD investigated in this chapter, two of these four eigenvectors coalesce.

7.10 Comparison to the Lagrangian Model

The Euler-Lagrange equations associated with the Lagrangian are the following system of second-order differential equations. Without loss of generality, we rewrote these equations in the case of a single stream e-beam and a single TL [293, 291]. All required parameters for this model are summarized in Tables (7.1) and (7.2), and readers can found more details about this model in [291]. The basic equations of Lagrangian model are represented as

$$L\partial_t^2 Q - \partial_z[C^{-1}(\partial_z Q + b\partial_z q)] = 0, \tag{7.81}$$

$$\frac{1}{\beta}(\partial_t + \mathring{v}\partial_z)^2 q + \frac{4\pi}{\sigma_B} q - b\partial z[C^{-1}(\partial_z Q + b\partial_z q)] = 0. \tag{7.82}$$

Table 7.1: e-beam parameters list in Lagrangian model

Name	Value
e-beam steady velocity	$\mathring{v}$
Number of electron density	$\mathring{n}$
Stream intensity	$\beta = \frac{\sigma_B}{4\pi} R_{\text{sc}}^2 \omega_{\text{p}}^2 = \frac{R_{\text{sc}}^2 e^2}{m} \mathring{N}$
Plasma frequency	$\omega_{\text{p}}^2 = \frac{4\pi \mathring{n}_s e^2}{m}$
Plasma frequency reduction factor	R_{sc}
Beam current	i
Number of electron per unit of length	$\mathring{N} = \sigma_B \mathring{n}$
Coupling between e-beam and MTL	$0 < b < 1$
Beam area	σ_B

Table 7.2: TL parameters list in Lagrangian model

Name	Value
Series inductance per-unit-length	L
Shunt capacitance per-unit-length	C
TL characteristic velocity	$w = \frac{1}{\sqrt{LC}}$
Coupling coefficient	b
TL principal coefficient	$\theta = \frac{b^2}{C}$
TWT principal parameter	$\gamma = \theta\beta = \frac{b^2}{C}\frac{\sigma_B}{4\pi}R_{\mathrm{sc}}^2\omega_{\mathrm{p}}^2$

In the above equations, $Q(z)$ represents the phasor of the total amount of a.c. charge flowing through a section at a given z in the TL, and L and C are the values of inductance and capacitance associated with the single TL. Also, $q(z)$ represents the amount of a.c. stream charges modulating the e-beam, at a given section z, in the second-order differential equations. In this section, we wish to put the equations in the matrix form to solve them. We define the state vector based on charges in the TL and charges in the e-beam as

$$\mathbf{\Psi}_{\mathrm{Q}}(z) = \begin{bmatrix} Q(z) \\ \partial_z Q(z) \\ q(z) \\ \partial_z q(z) \end{bmatrix}. \tag{7.83}$$

Next, we write the Equations (7.81) and (7.82) in the matrix form

$$\partial_z \mathbf{\Psi}_{\mathrm{Q}}(z) = -j\underline{\mathbf{M}}_{\mathrm{QL}}\mathbf{\Psi}_{\mathrm{Q}}(z), \tag{7.84}$$

where $\underline{\mathbf{M}}_{\mathrm{QL}}$ is a 4×4 is system matrix associated to the Lagrangian formulation and the

charges-based state vector $\mathbf{\Psi}_{\mathrm{Q}}$, and reads as

$$\underline{\mathbf{M}}_{\mathrm{QL}} = \begin{bmatrix} 0 & j & 0 & 0 \\ j(\frac{\beta b^2}{\mathring{v}^2 C} - 1)\omega^2 LC & 0 & -j\frac{b}{\mathring{v}^2}(\omega^2 - \frac{4\pi}{\sigma_B}\beta) & -\frac{2\omega}{\mathring{v}}b \\ 0 & 0 & 0 & j \\ -j\frac{\beta b}{\mathring{v}^2}\omega^2 L & 0 & j\frac{1}{\mathring{v}^2}(\omega^2 - \frac{4\pi}{\sigma_B}\beta) & \frac{2\omega}{\mathring{v}} \end{bmatrix}. \tag{7.85}$$

By defining $Z = j\omega L$ and $Y = j\omega C$, we rewrite Equation (7.84) as

$$\partial_z \begin{bmatrix} Q \\ \partial_z Q \\ q \\ \partial_z q \end{bmatrix} = -j \begin{bmatrix} 0 & j & 0 & 0 \\ j(1 - j\omega\frac{\beta b^2}{\mathring{v}^2 Y})ZY & 0 & -j\frac{b}{\mathring{v}^2}(\omega^2 - \frac{4\pi}{\sigma_B}\beta) & -\frac{2\omega}{\mathring{v}}b \\ 0 & 0 & 0 & j \\ -\omega\frac{\beta b}{\mathring{v}^2}Z & 0 & j\frac{1}{\mathring{v}^2}(\omega^2 - \frac{4\pi}{\sigma_B}\beta) & \frac{2\omega}{\mathring{v}} \end{bmatrix} \begin{bmatrix} Q \\ \partial_z Q \\ q \\ \partial_z q \end{bmatrix}. \tag{7.86}$$

Assuming that our solutions have a z-dependence $\mathbf{\Psi}(z) = \mathbf{\Psi}_{\mathrm{Q}} e^{-jkz}$, the eigenvalue problem reads as,

$$(\underline{\mathbf{M}}_{\mathrm{QL}} - k\underline{\mathbf{I}})\mathbf{\Psi}_{\mathrm{Q}} = 0. \tag{7.87}$$

Based on Equation (7.86), the eigenvalue problem is reduced to

$$(\underline{\mathbf{M}}_{\mathrm{QL}}-k\underline{\mathbf{I}})\mathbf{\Psi}_{\mathrm{Q}}=\begin{bmatrix} -k & j & 0 & 0 \\ j(1-j\omega\frac{\beta b^2}{\mathring{v}^2 Y})ZY & -k & -j\frac{b}{\mathring{v}^2}(\omega^2-\frac{4\pi}{\sigma_B}\beta) & -\frac{2\omega}{\mathring{v}}b \\ 0 & 0 & -k & j \\ -\omega\frac{\beta b}{\mathring{v}^2}Z & 0 & j\frac{1}{\mathring{v}^2}(\omega^2-\frac{4\pi}{\sigma_B}\beta) & -k+\frac{2\omega}{\mathring{v}} \end{bmatrix}\mathbf{\Psi}_{\mathrm{Q}}=0. \quad (7.88)$$

After some simplification, the dispersion equation is expressed as

$$\begin{aligned}\det(\underline{\mathbf{M}}_{\mathrm{QL}}-k\underline{\mathbf{I}})=k^4-k^3(\tfrac{2\omega}{\mathring{v}})+k^2(\tfrac{1}{\mathring{v}^2}(\omega^2-\tfrac{4\pi}{\sigma_B}\beta)+ZY-jb^2Z\omega\tfrac{\beta}{\mathring{v}^2})-k(ZY\tfrac{2\omega}{\mathring{v}}) \\ +ZY\tfrac{1}{\mathring{v}^2}(\omega^2-\tfrac{4\pi}{\sigma_B}\beta)=0.\end{aligned} \quad (7.89)$$

According to the Lagrangian model, the general TWT characteristic equation for the phase velocity $v=\omega/k$ of the hot modes turns into

$$v^4\frac{ZY}{\mathring{v}^2}(\omega^2-\frac{4\pi}{\sigma_B}\beta)-v^3(ZY\frac{2\omega^2}{\mathring{v}})+v^2\omega^2(\frac{1}{\mathring{v}^2}(\omega^2-\frac{4\pi}{\sigma_B}\beta)+ZY-jb^2Z\omega\frac{\beta}{\mathring{v}^2})-v(\frac{2\omega^4}{\mathring{v}})+\omega^4=0. \quad (7.90)$$

After some mathematical manipulation, the characteristic equation is expressed by [291, Chapter 25]

$$\frac{\gamma}{w^2-v^2}+\frac{(v-\mathring{v})^2}{v^2}=\frac{1}{\breve{\omega}^2}, \quad (7.91)$$

where $\breve{\omega}$ is a dimensionless (normalized) frequency [291, Chapter 25]

$$\breve{\omega} = \frac{\omega}{R_{\mathrm{sc}}\omega_{\mathrm{p}}}. \tag{7.92}$$

Finally, for convenience we provide the translation table to transform Lagrangian model parameters used in [291] to the Pierce model parameters used in this chapter. The list of transformations is summarized in Table (7.3).

Table 7.3: Translation from Lagrangian model parameters to the Pierce model parameters

Lagrangian model	Pierce model
$\mathring{v}$	$\frac{\omega}{\beta_0} = u_0$
σ_B	A
β	$\frac{g\omega}{\beta_0^2} = \frac{gu_0}{\beta_0}$
w^2	$-\frac{\omega^2}{ZY} = \frac{\omega^2}{\beta_c^2}$
γ	$\frac{a^2}{Y}\frac{jg\omega^2}{\beta_0^2} = \frac{a^2}{Y}jgu_0^2$

In the frequency-dependent SWS model that we have introduced in this chapter, we consider two frequency-dependent parameters, i.e., the cold circuit EM phase velocity v_c, and the equivalent TL characteristic impedance Z_{c}. The same procedure can be used for the demonstrated Lagrangian model in [291]. In the Lagrangian model, the TL principal coefficient, $\theta(\omega)$, and TL characteristic velocity, $w(\omega)$, are the two frequency-dependent parameters in the Lagrangian equations. Equivalently, in the displayed characteristic equation in Equation (7.91), the TWT principal parameter, $\gamma(\omega)$, and TL characteristic velocity, $w(\omega)$, are the two frequency-dependent parameters in the Lagrangian model.

7.11 An Equivalent Alternative Formulation Based on Charge

As explained in the previous section, we defined matrix equations for the TWT-system as expressed in Equation (7.53). In the next step, we start with the substitutions presented in Equation (7.44) to convert currents to charges. This leads to modified set of TWT-system equations as

$$\partial_z \begin{bmatrix} V \\ j\omega Q \\ V_b \\ j\omega q \end{bmatrix} = \begin{bmatrix} 0 & -Z & 0 & 0 \\ -Y & 0 & jag & ja\beta_0 \\ 0 & -aZ & -j\beta_0 & -jR_{\mathrm{p}} \\ 0 & 0 & -jg & -j\beta_0 \end{bmatrix} \begin{bmatrix} V \\ j\omega Q \\ V_b \\ j\omega q \end{bmatrix}. \tag{7.93}$$

The matrix is equivalent to the four equations

$$\begin{cases} \partial_z V = -jZ\omega Q \\ j\omega\partial_z Q = -YV + jagV_b - a\beta_0\omega q \\ \partial_z V_b = -jaZ\omega Q - j\beta_0 V_b + R_{\mathrm{p}}\omega q \\ j\omega\partial_z q = -jgV_b + \beta_0\omega q \end{cases} \tag{7.94}$$

By combining the equations and performing some mathematical simplification, we remove voltages (V and V_b) from equations and decrease four first-order differential equations into

two second-order differential equations based on charge:

$$
\left.\begin{cases}
\partial_z^2 Q = YZQ - ja^2 gZQ + ja\beta_0 \partial_z q - a\beta_0^2 q + agR_{\mathrm{p}} q + ja\beta_0 \partial_z q \\
\partial_z^2 q = jagZQ - j\beta_0 \partial_z q + \beta_0^2 q - gR_{\mathrm{p}} q - j\beta_0 \partial_z q
\end{cases}\right. \tag{7.95}
$$

In order to analyze the characteristics of the system like wavenumbers, we rewrite equations in the matrix form. So, we use a state vector based on charge, as was expressed before in Equation (7.83), and rewrite Equation (7.95) as

$$
\partial_z \mathbf{\Psi}_{\mathrm{Q}}(z) = -j\underline{\mathbf{M}}_Q \mathbf{\Psi}_{\mathrm{Q}}(z), \tag{7.96}
$$

$$
\underline{\mathbf{M}}_Q = \begin{bmatrix}
0 & j & 0 & 0 \\
jYZ + a^2 gZ & 0 & -ja\beta_0^2 + jagR_{\mathrm{p}} & -2a\beta_0 \\
0 & 0 & 0 & j \\
-agZ & 0 & j\beta_0^2 - jgR_{\mathrm{p}} & 2\beta_0
\end{bmatrix}. \tag{7.97}
$$

By using the same approach described before, the characteristic equation is calculated from

$$\det(\underline{\mathbf{M}}_Q - k\underline{\mathbf{I}}) = \det\begin{bmatrix} -k & j & 0 & 0 \\ jYZ + a^2gZ & -k & -ja\beta_0^2 + jagR_\mathrm{p} & -2s\beta_0 \\ 0 & 0 & -k & j \\ -agZ & 0 & j\beta_0^2 - jgR_\mathrm{p} & -k + 2\beta_0 \end{bmatrix} = 0, \quad (7.98)$$

resulting in the following dispersion equation

$$D(\omega, k) = k^4 - k^3(2\beta_0) + k^2(\beta_0^2 - gR_\mathrm{p} + ZY - a^2jZg) - k(2ZY\beta_0) + ZY(\beta_0^2 - gR_\mathrm{p}) = 0. \quad (7.99)$$

7.12 Theoretical Gain Calculation

The frequency-dependent parameters describing EM propagation in the dispersive and lossy waveguide in the proposed model have a vital role in the accuracy of the calculated results. In order to test the accuracy of the proposed model, we need to compare the theoretically calculated results with those numerically obtained from commercial software. The software LATTE is used to calculate the gain versus frequency of the helix TWT amplifier. We use our theoretical method to calculate the power gain versus input signal frequency. The utilized circuit model is illustrated in Figure 7.8. The TWT-system is modeled by the system matrix $\underline{\mathbf{M}}$, and we use the input state vector of $\mathbf{\Psi}_1 = [V_1, I_1, V_{b,1}, I_{b,1}]^T$, calculated at $z = 0$, and an output state vector $\mathbf{\Psi}_2 = [V_2, I_2, V_{b,2}, I_{b,2}]^T$ is calculated at $z = d$, i.e., at the end of the SWS. Here $d = Nl$ is the SWS length, where N indicates the number of unit-cells and l is the SWS period in the z-direction. The output state vector is calculated as

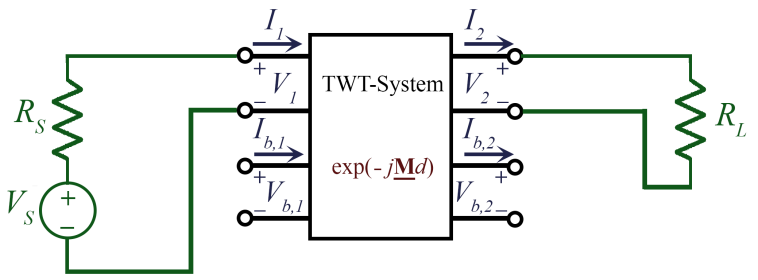

Figure 7.8: Circuit model that we use for gain calculation.

$$\mathbf{\Psi}_2 = \exp(-j\underline{\mathbf{M}}d)\mathbf{\Psi}_1. \tag{7.100}$$

We considered a helix SWS made of $N = 80$ turns, and simulated results are based on this assumption. In our model, we use the boundary condition at $z = 0$ and $z = d$ provided by the equations

$$\begin{cases} V_{b1} = 0 \\ I_{b1} = 0 \\ V_1 + I_1 R_{\mathrm{S}} = V_S \\ V_2 - I_2 R_{\mathrm{L}} = 0 \end{cases} \tag{7.101}$$

In these equations, the terminations R_{S} (generator resistance) and R_{L} (load) are assumed to be equal to the frequency-dependent characteristic impedance of SWS Z_{c} (vary with frequency, to simulate matching), and V_S is the voltage source. Then, we solve these equations at each frequency and calculate the effective current and voltage at the output of the TL (I_2, V_2). We calculate the output power $P_{\mathrm{out}} = |V_2|^2/(2R_{\mathrm{L}})$, and the available input power $P_{\mathrm{avail}} = |V_s|^2/(8R_{\mathrm{S}})$, to obtain the frequency-dependent gain $G = P_{\mathrm{out}}/P_{\mathrm{avail}}$, for the TWT-system. As explained above and in the main body of the chapter, we have introduced the coupling strength coefficient a, in our equations, which describes the strength of beam-EM

mode interaction in the system. The value of a must be optimized in order to obtain good agreement between the theoretical model and simulation results. The optimized value for the designed helix TWT is calculated as $a = 0.917$. With this coupling strength coefficient, the theoretical and simulated gain results are in agreement over the frequency range shown in the main body of the chapter. The agreement between the theoretical and simulated gain demonstrates the effectiveness of the theoretical model.

7.13 Conclusions

In conclusion, we have investigated the occurrence of EPDs in a system consisting of a linear e-beam interacting with a guided EM wave. We have focused on a practical example where the EM wave is guided by a helix-based SWS, but the same model can be applied to other guiding geometries. We have considered realistic parameters for the e-beam's space-charge effect and waveguide's dispersion of phase velocity and Pierce (interaction) impedance in the developed model. We have discovered the necessary and required conditions to establish an EPD in TWT-system. Then, we have discussed how the wavenumbers of the hot EM-space-charge wave modes participating in an EPD are extremely sensitive to system perturbations. We have shown how a bifurcation point well describes such perturbation near an EPD, demonstrated by employing the Puiseux fractional power series expansion. The very high sensitivity to variations can pave the way to new accurate measurement techniques of e-beam parameters.

Acknowledgments

- I would like to thank Robert Marosi, Tarek Mealy and Ahmed F. Abdelshafy for collaboration on this chapter.

- This material is based upon work supported by the Air Force Office of Scientific Research (AFOSR) Grant No. FA9550-18-1-0355, Grant No. FA9550-19-1-0103, and Grant No. FA9550-20-1-0409.

- The text of Chapter 7 of this dissertation is a reprint of the material as it appears in K. Rouhi, R. Marosi, T. Mealy, A. F. Abdelshafy, A. Figotin, and F. Capolino, "Exceptional degeneracies in traveling wave tubes with dispersive slow-wave structure including space-charge effect," Applied Physics Letters, vol. 118, no. 26, p. 263506, Jun. 2021. The coauthors listed in this publication are Robert Marosi, Tarek Mealy, Ahmed F. Abdelshafy, Alexander Figotin, and Filippo Capolino. Alexander Figotin and Filippo Capolino directed and supervised research which forms the basis for the dissertation.

- The results of this chapter have been published in the journal paper of [75] and in the conference papers of [306].

Chapter 8

Parametric Modeling of Serpentine Waveguide Traveling Wave Tubes

A simple and fast model for numerically calculating small-signal gain in SWTWTs is described. In the framework of the Pierce model, we consider one-dimensional electron flow along a dispersive single-mode SWS, accounting for the space-charge effect. The analytical model accounts for the frequency-dependent phase velocity and characteristic impedance obtained using various equivalent circuit models from the literature, validated by comparison with full-wave eigenmode simulation. The model includes a relation between the modal characteristic impedance and the interaction (Pierce) impedance of the SWS, including also an extra correction factor that accounts for the variation of the electric field distribution and hence of the interaction impedance over the beam cross section. By applying boundary conditions to our generalized Pierce model, we compute both the theoretical gain of a TWT and all the complex-valued wavenumbers of the hot modes versus frequency and compare our results with computationally intensive PIC simulations; the good agreement in the comparison demonstrates the accuracy and simplicity of our generalized model. For various examples where we vary the average e-beam phase velocity, average e-beam current,

number of unit cells, and input RF power, we demonstrate that our model is robust in the small-signal regime. The purpose of this chapter is not to design a TWT with performance that competes with previous ones, but to develop an accurate and simple model to predict TWT performance that can be used as a design tool.

8.1 Background, Motivation, and State of the Art

TWT is a type of common microwave vacuum electron tube that has been widely used for applications such as communication, radar, and electronic countermeasures [307, 47, 308, 49]. Among the different kinds of TWTs, the SWTWT has advantages over other kinds of millimeter wave TWTs (e.g. helix TWT, CCTWT, ring-bar TWT) due to its moderate bandwidth with power-handling capacity at higher frequencies and its compatibility with planar fabrication using lithography or micromachining [309, 310, 311, 312, 313]. SWS of the SWTWT is formed by bending rectangular waveguides in the electric field plane (E-plane). Also, a cylindrical e-beam is transported through the cylindrical beam tunnel to interact with RF propagating wave. Although the SWSWS's performance is limited by its low interaction impedance and interaction efficiency, many schemes of enhancing the on-axis interaction impedance and also enhancement of interaction efficiency have been proposed [314, 315, 316, 317, 318, 319].

In order to analyze the e-beam and EM wave dynamics of a SWTWT, it is necessary to examine the EM characteristics of the SWS. Various analytical models have been developed for its characterization. In 1987, Dohler et al. proposed a simple analytical method for determining the dispersion characteristics and the interaction impedance of the EM modes in the SW [309]. Liu suggested an analytical formulation adding the effect of bends [310]. Then, researchers developed a closed-form algebraic dispersion relation based on an equivalent circuit model that also considered the effect of mismatch between straight and bend sections as

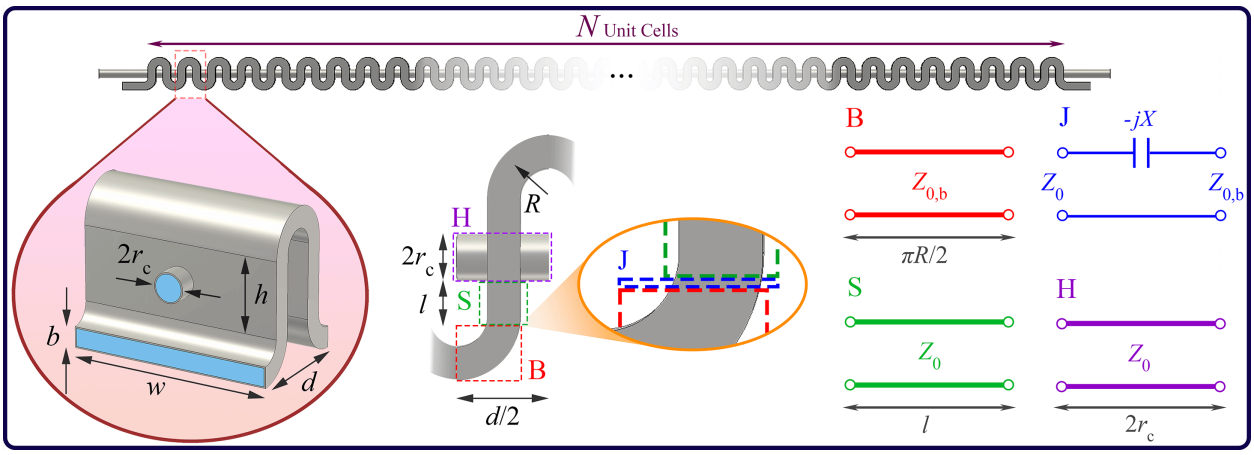

Figure 8.1: Schematic illustration of an SW unit cell, constitutive segments (colored dashed rectangles), and parametric dimensions are shown in the left and central panels. The equivalent TL model for the TE10 mode in each segment is shown in the right panel for: (B) *E*-plane circular bend, (J) circular bend to straight waveguide junction, (S) straight waveguide section, and (H) e-beam hole.

well as an approximate model for beam holes [56, 58]. A thorough equivalent circuit analysis of SWs by modeling the effect of beam tunnels as orthogonal stubs was developed by Booske et al. [320] for the calculation of dispersion characteristics, following the approach of TL cascading networks and benchmarked using 3D simulations with Ansys HFSS, MAFIA, and CST Studio Suite. Recently, Antonsen et al. [321] developed a hybrid model consisting of a combination of TL segments and lumped electrical elements, which is utilized to analyze SW dispersion characteristics and interaction impedance. The model also captures the effects of asymmetric fields and beam tunnel misalignment. Although some commercial full-wave simulation software like Ansys HFSS and CST Studio Suite are versatile and can analyze SWS characteristics, simulation times are longer than analytical methods. Therefore, analytical methods are preferred for quickly iterating through and optimizing various SWS designs.

To design and analyze SWTWTs, various beam-EM wave interaction models exist. PIC simulations are widely used to characterize the beam-EM wave interaction of TWTs because they predict amplification performance. Nevertheless, the computational burden of 3D PIC simulators is high compared to other TWT codes. The United States Naval Research Labo-

ratory applied the hybrid TL model to the large signal beam-EM wave interaction programs (CHRISTINE-CC and TESLA-CC), which are used for analyzing CC-TWTs. Then, they extended a 1D frequency-domain interaction model named CHRISTINE-FW, developed for folded waveguide TWTs [322] and a 2D frequency-domain interaction model named TESLA-FW [323, 324]. Also, a large signal beam-EM wave interaction code with computational efficiency improvements was developed by Meyne et al. [325]. A 3D steady-state beam-EM wave interaction code using a three-port network representation of the circuit and a set of discrete ray representations of the 3D e-beam was developed by Yan et al. [326]. In addition to previous models, a nonlinear model for the numerical simulation of terahertz SWTWT is described in [327], in which the propagated EM wave in the SWS is represented as an infinite set of space harmonics that interact with an e-beam. Also, an improved large-signal model was developed in [328], which predicts beam-EM wave interaction with an analytical method. Recently, Figotin [53] advanced a Lagrangian field theory of CC-TWTs that integrates into it the space-charge effects; that model can also be used for SWTWTs as explained in detail in that paper.

In this chapter, we present an analytical model for analyzing beam-EM wave interactions in SWTWTs shown in Figure 8.1. We develop a model that can be used to obtain the small-signal gain and the "hot eigenmodes" dispersion, accounting for nonuniform beam-EM wave interaction. We refer to the modes of the interactive system, where the e-beam interacts with the EM wave of the SWS, as "hot modes" or "hot eigenmodes", which are complex modes, with each hot eigenmode composed of both EM and space-charge waves. First, we show various methods from the literature that can be used to calculate SWS cold characteristics, i.e., characteristic impedance and phase velocity, based on the equivalent circuit model presented in [320]. We calculate the interaction impedance, which is one of the critical parameters for predicting TWT gain. Based on the fundamental equations of the Pierce model [285, 329, 2, 286], we further develop the model to account for frequency-dependent parameters and the space-charge effect, following the method explained in [75]

for a helix TWT. Then, we introduce the frequency-dependent coupling strength coefficient which shows the strength of the interaction between e-beam and EM wave and also connects interaction impedance and characteristic impedance. We also include the small frequency-independent factor δ_{e} that corrects for the nonuniform interaction impedance over the beam cross section. This correction factor models the nonuniform interaction between the EM wave and the e-beam in the interaction gap. Moreover, we model the e-beam effect on the equivalent TL model by using the electronic beam admittance per unit length Y_{b}, accounting for the space-charge effect. By introducing Y_{b}, it is possible to find out the conditions that lead to amplification in the TWT system. Finally, we utilize the proposed theoretical method to predict the gain versus frequency of a TWT amplifier and we compare our results to those from computationally intensive 3D PIC simulations, showing high accuracy. In order to show the flexibility and accuracy of our method, comparison with 3D PIC simulations for many examples is done by varying the e-beam parameters such as the average e-beam phase velocity, average e-beam current, number of unit cells, and input RF power.

The organization of this chapter is as follows. In Section 8.2, we highlight the main achievements of our developed model. Then, we show how to combine some analytical methods from the literature to calculate the cold parameters of the SW in Section 8.3. An example of a cold model characteristic calculation is presented in Section 8.5. We describe the conventional method to calculate interaction impedance and introduce the extra correction factor δ_{e} required for our model in Section 8.6. We develop a model for beam-EM wave interaction in Section 8.8 and evaluate it by providing an example in Section 8.11, where we apply boundary conditions to determine the TWT gain. Next, we demonstrate the accuracy and efficiency of our model in Section 8.13 by varying TWT parameters. Finally, we conclude the chapter in Section 8.14.

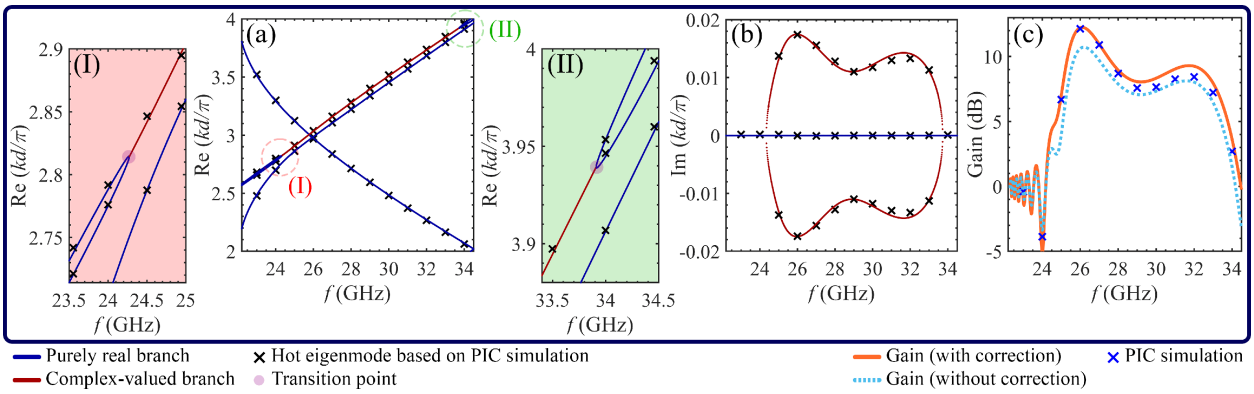

Figure 8.2: The (a) real and (b) imaginary parts of complex-valued wavenumbers of the hot modes, where dark blue curves indicate branches with purely real wavenumbers, dark red curves indicate branches with complex-valued wavenumbers, and black crosses indicate the results obtained using a hot eigenmode solver for beam-loaded SWS based on PIC simulations. (I) and (II) show the real part of the complex-valued wavenumbers of the hot modes near the two transition points (light purple circles). (c) The theoretical gain (with/without correction factor δ_e) is compared with that from PIC simulation. The parameters used for this example are provided in Sections 8.5 and 8.11.

8.2 Summary of Main Results

We present a summary of the main results calculated by our developed model and compared to PIC simulations, leaving explanations, technical details and numerical examples in the sections that follow. In our developed model, we introduce an additional correction factor δ_e that accounts for transverse variations in the axial electric field distribution that affect the average interaction impedance over the beam cross section. As a result of this correction factor, we can model the nonuniform interactions between the EM wave and the e-beam in the interaction gap. Figures 8.2(a) and (b) illustrate the real and imaginary parts of complex-valued wavenumbers of the eigenmodes supported by the SW with the e-beam, i.e., of the hot modes, for the example with the parameters provided in Sections 8.5 and 8.11. The solid lines in Figures 8.2(a) and (b) represent the calculated frequency dispersion of the hot modes resulting from the interaction between the guided EM wave in the SWS and the two space charge waves of the e-beam. The dark blue curves indicate "stable branches" whose imaginary parts of the wavenumber of the hot modes are equal to zero and hence are

not amplified. In contrast, dark red curves indicate branches whose imaginary parts of the wavenumber are nonzero, and the positive values of the imaginary part allow for amplification (unstable or amplification branch). In order to verify our theoretical calculations displayed by solid curves, we calculate the real and imaginary parts of the complex-valued wavenumbers of the hot modes at a discrete set of frequencies by using the "hot eigenmode solver" for beam-loaded SWS based on PIC simulations developed in [330] (indicated by black crosses). This eigenmode solver is based on accurate PIC simulations of finite-length hot structures, which consider the precise SWS geometry, the EM properties of the materials, the cross-sectional area of the e-beam, the confining magnetic field, and the space-charge effect. The advantage of the hot eigenmode solver is that the use of PIC simulations allows us to find the hot eigenmodes that fully account for all physical aspects of the problem without the need to rely on intermediate parameters, such as the interaction impedance or plasma frequency reduction factor used in other solvers [330]. There is excellent agreement between our theoretical model and the PIC-based eigenmode solver of [330], both in the real and imaginary parts of the complex wavenumber. In addition, we show the zoomed-in plot of the real part of the complex-valued wavenumber near the two transition points (bifurcations) in Figures 8.2(I) and (II). The light purple circles indicate the transition points that separate the stable branches with purely real wavenumbers from the unstable branches with complex-valued wavenumbers. Some features of these critical points have been previously explored in [75, 126]. Lastly, we calculate the gain versus frequency diagram for the TWT using the developed theoretical model, shown by the solid orange curve in Figure 8.2(c), and compare with results from computationally intensive 3D PIC simulations, shown by blue crosses, demonstrating very good agreement. The camel-like hump curve on the gain diagram in Figure 8.2(c) has the same shape as the unstable branch in Figure 8.2(b). The excellent agreement between our developed theoretical results and PIC simulated results in Figure 8.2 demonstrates the accuracy of our method. Furthermore, to demonstrate the importance of the extra correction factor δ_e in our model, we also calculated the gain versus frequency

curve in Figure 8.2(c) without taking into account the correction factor δ_e (dotted light blue curve). In the case without a correction factor δ_e, the calculated results are unable to predict the gain to within approximately 1.5 dB at the high amplification frequencies around 26 GHz.

8.3 Equivalent Circuit Model of Cold SWS

It is crucial to have a simple model that estimates the cold (i.e., without the e-beam) characteristics of the SWS, especially for evaluating the operational bandwidth and interaction efficiency of TWTs. Here, we present the cold equivalent circuit model and compare frequency-dependent cold results, such as phase velocity, with those of full-wave eigenmode simulations.

A schematic design of an E-plane bend SW circuit is shown in Figure 8.1. It is assumed that only the fundamental TE mode, i.e., TE10, propagates along the waveguide with a rectangular cross section. In practice, reflections at the junction with a bend cannot be completely avoided (segment J), and we also need to take into account that the characteristic impedance of the EM mode in the bend (segment B) is slightly different from that of the EM mode in the straight segment; hence, the junction between the two segments involves reactive fields [331, 332, Chapter 4]. Note that the U-shaped bends in SWs considered here produce less reflection than the right angle bends commonly found in folded waveguides [58, 57, 333]. Additionally, reactive loading from the beam hole (segment H) can affect device performance, depending on the hole's diameter. The effect of both of these kinds of reflections is the creation of a stopband that may limit the TWT's maximum operating frequency. In addition, a band edge can also be a source of instability if an e-beam synchronizes with it [58, 334]. Thus, one must carefully select a combination of beam tunnel radius and beam voltages to avoid such an absolute instability at the 3π and 4π points of the dispersion diagram, respectively.

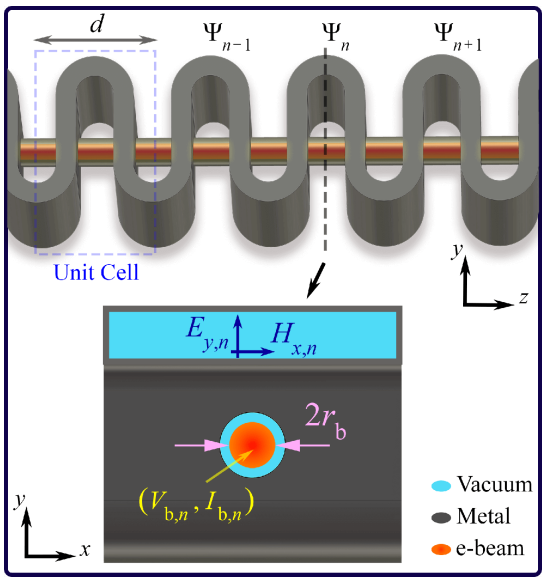

Figure 8.3: Equivalent voltage and current at the input and output of each unit cell and the corresponding TE10 electric and magnetic fields in the cross section of the SW. We also show the equivalent kinetic beam voltage and beam current pertinent to the two charge waves.

The different segments of the SW are represented in the center panel of Figure 8.1, each with its own equivalent TL circuit in the right panel. In this case, B, J, S, and H correspond to the following parts of the unit cell: E-plane circular bend, circular bend to straight waveguide junction, straight waveguide section, and e-beam hole, respectively. By multiplying (cascading) the transfer matrices of the individual segments we build the equivalent TL model corresponding to the SW's unit cell which will be further discussed in Subsection 8.4.1. We use the equivalent representation in [331, 305] that models propagation in a rectangular waveguide as a TL with equivalent voltage and current. The discrete voltages and the currents that represent the EM state in the phasor domain at different cross sections of the waveguide are defined as $V_n = \sqrt{wb/2}E_{y,n}$ and $I_n = -\sqrt{wb/2}H_{x,n}$, where $E_{y,n}$ and $H_{x,n}$ are the transverse electric and magnetic fields of the TE10 mode calculated at the center of the rectangular waveguide cross section as shown in Figure 8.3. The equivalent voltage and current in the TLs are calculated at discrete locations using the transfer matrix $\underline{\mathbf{T}}_{\mathrm{U}}$ as

$$\mathbf{\Psi}_n = \begin{bmatrix} V_n \\ \\ I_n \end{bmatrix}, \ \mathbf{\Psi}_n = \underline{\mathbf{T}}_{\mathrm{U}} \mathbf{\Psi}_{n-1}, \tag{8.1}$$

where V_{n-1} and I_{n-1} are the equivalent voltage and current [331] at the input port of the nth unit cell and V_n and I_n are the equivalent voltage and current at the output port of the nth unit cell as shown in Figure 8.3.

8.3.1 Equivalent Matrix for Each Segment

Straight Waveguide (Segment S)

The straight rectangular waveguide segment of the unit cell is modeled as a uniform TL of length l with characteristic modal impedance $Z_0 = \eta_0 / \sqrt{1 - (\omega_{\mathrm{co}}/\omega)^2}$ of the fundamental TE10 mode, where $\eta_0 = \sqrt{\mu_0/\varepsilon_0}$ is the wave impedance of free space, $\omega_{\mathrm{co}} = \pi c/w$ is the cutoff angular frequency, w is the width of the rectangular waveguide, and ω is the operating angular frequency. The phase propagation constant of the TE10 mode is $\beta_{\mathrm{g,s}} = \sqrt{k_0^2 - (\pi/w)}$, where $k_0 = 2\pi/\lambda_0$, and $\lambda_0 = 2\pi c/\omega$ is wavelength in free space. The equivalent TL circuit representation of the straight waveguide segment is shown in Figure 8.1 (segment S), and the equivalent transfer matrix is

$$\underline{\mathbf{T}}_{\mathrm{S}} = \begin{bmatrix} \cos(\beta_{\mathrm{g,s}} l) & j Z_0 \sin(\beta_{\mathrm{g,s}} l) \\ \\ j \sin(\beta_{\mathrm{g,s}} l) / Z_0 & \cos(\beta_{\mathrm{g,s}} l) \end{bmatrix}. \tag{8.2}$$

Circular Bend to Straight Waveguide Junction (Segment J)

The junction between the straight waveguide and the E-plane bend is represented by the equivalent circuit in Figure 8.1 (segment J) with equivalent lumped reactance [331, Section 5.34]

$$X = Z_0 \left(\frac{32}{\pi^7} \left(\frac{2\pi b}{\lambda_{\mathrm{g,s}}} \right)^3 \left(\frac{b}{R} \right)^2 \sum_{n=1,3,\ldots}^{\infty} \frac{1}{n^7} \sqrt{1 - \left(\frac{2b}{n\lambda_{\mathrm{g,s}}} \right)^2} \right), \tag{8.3}$$

where R is the mean radius of the bend, and $\lambda_{\mathrm{g,s}} = 2\pi/\beta_{\mathrm{g,s}} = \lambda_0/\sqrt{1 - (\omega_{\mathrm{co}}/\omega)^2}$ is the guided wavelength. The equivalent transfer matrix for the junction is

$$\underline{\mathbf{T}}_{\mathrm{J}} = \begin{bmatrix} 1 & -jX \\ 0 & 1 \end{bmatrix}. \tag{8.4}$$

E-plane Circular Bend (Segment B)

An equivalent TL circuit for the quarter E-plane bend is given in Figure 8.1 (segment B). Here, $\pi R/2$ is the mean length of the E-plane bend and the length of the equivalent TL. The modified characteristic impedance for the fundamental propagating mode in the bend is [331, Section 5.34]

$$Z_{0,\mathrm{b}} = Z_0 \left(1 + \frac{1}{12} \left(\frac{b}{R} \right)^2 \left[\frac{1}{2} - \frac{1}{5} \left(\frac{2\pi b}{\lambda_{\mathrm{g,s}}} \right)^2 \right] \right). \tag{8.5}$$

In addition, the circular bend is considered as a uniform angular waveguide with a guided wavelength of

$$\lambda_{\mathrm{g,b}} \simeq \lambda_{\mathrm{g,s}} \left(1 - \frac{1}{12}\left(\frac{b}{R}\right)^2 \left[-\frac{1}{2} + \frac{1}{5}\left(\frac{2\pi b}{\lambda_{\mathrm{g,s}}}\right)^2 - \ldots\right]\right), \tag{8.6}$$

for the fundamental mode. As a result, in the wavelength range $2b/\lambda_{\mathrm{g,s}} < 1$ [331, Section 5.34], the TL matrix for the circular bend segment is

$$\underline{\mathbf{T}}_{\mathrm{B}} = \begin{bmatrix} \cos\left(\frac{\pi^2 R}{\lambda_{\mathrm{g,b}}}\right) & jZ_{0,\mathrm{b}} \sin\left(\frac{\pi^2 R}{\lambda_{\mathrm{g,b}}}\right) \\ j\sin\left(\frac{\pi^2 R}{\lambda_{\mathrm{g,b}}}\right)/Z_{0,\mathrm{b}} & \cos\left(\frac{\pi^2 R}{\lambda_{\mathrm{g,b}}}\right) \end{bmatrix}. \tag{8.7}$$

Beam Tunnel Hole

The radius of the beam hole can slightly affect the phase velocity, dispersion and cutoff frequency of the EM mode in the SWS [335, 336]. A wide beam tunnel will add significant periodic reactive loading to the SWS and introduce a stopband at the 3π point of the modal dispersion diagram, and the larger beam tunnel radius results in a larger stopband [337]. On the other hand, a wide beam tunnel permits higher beam currents since the beam radius can be larger with the same current density, resulting in higher d.c. beam power and output RF power at saturation [338]. However, an e-beam of a very small radius (with the same d.c. beam current) will experience strong Coulomb repulsion between electrons, and it is unrealistic to apply an intense magnetic field to confine an e-beam with a small radius and high current density [337]. Also, it is desirable to have an e-beam with a lower accelerating voltage and a higher current, resulting in a higher gain. Therefore, it is necessary to trade off beam tunnel size, current density, and beam radius to optimize TWT properties, such as linear gain and efficiency.

A general and accurate circuit to model the beam tunnel hole that can be used in all cases has not been developed yet. In [56], the authors modeled the circular hole as a shunt

reactance, where the value depends on rectangular waveguide width and height and beam tunnel diameter. Also, in [320], a circuit model of the beam tunnel hole based on the modification of the model for different tunnel radii in [331] was presented. The reference structure is a circular waveguide connected orthogonally to the broad wall of a rectangular waveguide through a small aperture. The difference between the reference structure in [331] and the structure to be modeled is that the cylindrical tunnel is represented as a stub whose diameter equals the aperture diameter and is below the cutoff for propagation and there are two of these stubs present. By assuming that the hole radius is electrically small (i.e., much smaller than the guided wavelength), we can often neglect the effect of holes and model this section as a simple straight rectangular waveguide as described in Subsection 8.3.1. This approximation leads to acceptable results and more investigation for a specific example is provided in Section 8.4. In addition, several papers designed SWTWTs without considering the effect of the beam tunnel hole, and some papers used the straight waveguide model for it, including [56, 310, 339, 340].

In TWTs designed for millimeter waves and even higher frequencies, the e-beam tunnel is often enlarged to achieve higher transmission rates, thereby causing a bandgap at the 3π point. For large beam tunnel dimensions, one could obtain the S-parameters of the straight segment with non-negligible tunnel loading via full-wave simulations. The numerically obtained S-parameters can then be converted into the transmission matrix $\underline{\mathbf{T}}_{\mathrm{H}}$ and used in our model. However, if circuit models for the segment with a large beam tunnel become available, one could also include them in the present formulation.

8.4 Longitudinal Fields in the Beam Tunnel

A number of works analyzed the effect of variation in the tunnel gap between the walls of the waveguide and the effect of thin interaction gap (b in Figure 8.4) [314, 341, 342, 343, 317, 318].

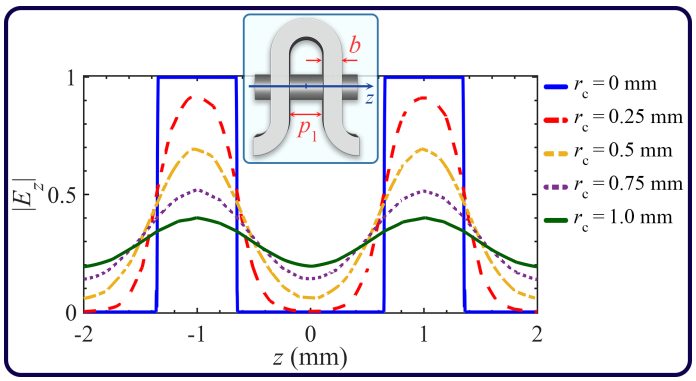

Figure 8.4: The on-axis z-component of electric field distribution as a function of longitudinal position z in a one unit cell with $d = 4\,\text{mm}$, at the center of beam tunnel (i.e., $r = 0$) for five beam tunnel radii r_c. The calculated values are normalized to the maximum value of the z-component of the electric field in the interaction area when $r_c = 0$, i.e., the case without tunnel.

In addition, the tunnel between the straight waveguide sections ($p_1 = d/2 - b$ in Figure 8.4) should be long enough to prevent the guided EM wave from directly coupling between straight sections via the beam tunnel, which operates below the cutoff [56, 58]. The analysis of the electric field distribution in the beam tunnel and interaction area of the cold single unit cell is shown in Figure 8.4. The parameters used in this example are the same as those listed in Table 8.1 and we illustrate the on-axis z-component of electric field at the center of beam tunnel by varying beam tunnel radius r_c. It should be noted that a large tunnel diameter can reduce the effective longitudinal field at the center of such a tunnel and hence decrease the gain (for instance, see the green curve in Figure 8.4). Hence, the beam tunnel radius should be selected carefully.

8.4.1 Cascaded Circuit Model

The basic SWS segments shown in Figure 8.1 are represented by equivalent TL segments, each with an equivalent transfer matrix as discussed above. The transfer matrices for the lossless circuit segments are cascaded to arrive at the transfer matrix of the unit cell represented as

$$\underline{\mathbf{T}}_{\mathrm{U}} = \begin{bmatrix} T_{11} & T_{12} \\ T_{21} & T_{22} \end{bmatrix} = \left(\underline{\mathbf{T}}_{\mathrm{U}/2}\right)^2 . \tag{8.8}$$

For convenience we use the half unit cell transfer matrix defined as

$$\underline{\mathbf{T}}_{\mathrm{U}/2} = \left(\underline{\mathbf{T}}_{\mathrm{B}}\underline{\mathbf{T}}_{\mathrm{J}}\underline{\mathbf{T}}_{\mathrm{S}}\underline{\mathbf{T}}_{\mathrm{H}}\underline{\mathbf{T}}_{\mathrm{S}}\underline{\mathbf{T}}_{\mathrm{J}}\underline{\mathbf{T}}_{\mathrm{B}}\right). \tag{8.9}$$

Using our unit cell transfer matrix $\underline{\mathbf{T}}_{\mathrm{U}}$, we find solutions for the state vector, $\mathbf{\Psi} = [V, I]^{\mathrm{T}}$, that satisfies

$$\underline{\mathbf{T}}_{\mathrm{U}}\mathbf{\Psi} = e^{-j\beta_{\mathrm{c},0}d}\mathbf{\Psi}, \tag{8.10}$$

where d is unit cell period and $\beta_{\mathrm{c},0}$ is the wavenumber of the fundamental spatial harmonic. Solving the eigenvalue problem,

$$\det\left(\underline{\mathbf{T}}_{\mathrm{U}} - \mathrm{e}^{-j\beta_{\mathrm{c},0}d}\underline{\mathbf{I}}\right) = 0, \tag{8.11}$$

for $\beta_{\mathrm{c},0}$, yields the Bloch wavenumbers of the cold EM modes allowed in the SWS, where $\underline{\mathbf{I}}$ is the 2×2 identity matrix. Then, the propagation constants for the mth spatial harmonic is

$$\beta_{\mathrm{c},m} = \beta_{\mathrm{c},0} + \frac{2m\pi}{d}, \quad m = 0, \pm 1, \pm 2, \ldots \tag{8.12}$$

The phase velocity of the spatial harmonic of the cold mode is calculated as $v_{\mathrm{c},m} = \omega/\beta_{\mathrm{c},m}$. Based on the definition of the state vector at the beginning of each unit cell, the characteristic Bloch impedance of the fundamental guided mode is calculated as

$$Z_{\mathrm{c}} = \frac{V}{I} = \frac{T_{12}}{e^{-j\beta_{\mathrm{c},0}\,d} - T_{11}} = \frac{e^{-j\beta_{\mathrm{c},0}\,d} - T_{22}}{T_{21}}. \tag{8.13}$$

Note that the characteristic Bloch impedance depends on where the section separating unit cells is defined, and if we substitute $\beta_{\mathrm{c},0}$ for $\beta_{\mathrm{c},m}$, the result does not change.

8.4.2 Equivalent Uniform TL Model

Each EM mode is comprised of a fundamental Bloch wavenumber $\beta_{\mathrm{c},0}$ and all its spatial harmonics $\beta_{\mathrm{c},m}$. However, the Pierce model [285, 2, 286] is based on the assumption that the SWS can be considered as a uniform TL supporting a single mode with wavenumber β_{c} that is velocity-synchronized with the e-beam, which is discussed here. To highlight this view, we impose that the cascaded matrix $\underline{\mathbf{T}}_{\mathrm{U}}$ in Equation (8.8) should be equal to the transfer matrix of an equivalent *uniform* single TL, as was done also in [56, 320],

$$\underline{\mathbf{T}}_{\mathrm{Uni}} = \begin{bmatrix} \cos\left(\beta_{\mathrm{c},0}d\right) & jZ_{\mathrm{c}}\sin\left(\beta_{\mathrm{c},0}d\right) \\ j\sin\left(\beta_{\mathrm{c},0}d\right)/Z_{\mathrm{c}} & \cos\left(\beta_{\mathrm{c},0}d\right) \end{bmatrix}. \tag{8.14}$$

Then, we impose $\underline{\mathbf{T}}_{\mathrm{Uni}} = \underline{\mathbf{T}}_{\mathrm{U}}$, where $\underline{\mathbf{T}}_{\mathrm{U}}$ is calculated from the cascaded circuit equivalent model of each segment as explained in the previous subsection, and we obtain the elements of $\underline{\mathbf{T}}_{\mathrm{Uni}}$ for $\beta_{\mathrm{c},0}d$, which is the effective phase shift per unit cell of the fundamental spatial harmonic. As a result, the propagation constants for all spatial harmonics are [50, Section 4.5.1]

$$\beta_{\mathrm{c},m} = \frac{\cos^{-1}\left(T_{11}\right)}{d} + \frac{2m\pi}{d}, \quad m = 0, \pm1, \pm2, \ldots, \tag{8.15}$$

where m denotes the harmonic number. In SWTWTs usually the first spatial harmonic ($m = 1$) is synchronized with the e-beam. The phase velocity corresponding to the mth spatial harmonic is $v_{c,m} = \omega/\beta_{c,m}$. The second and third elements in the equivalent transmission matrix $\underline{\mathbf{T}}_{\text{Uni}}$ are used to calculate the characteristic impedance of the equivalent uniform TL as $Z_c = \sqrt{T_{12}/T_{21}}$ [50, Section 4.5.1]. Also, by imposing $\underline{\mathbf{T}}_{\text{Uni}} = \underline{\mathbf{T}}_{\text{U}}$ to Equation (8.8) and using the reciprocity property of the transfer matrix, the latter equation for characteristic impedance will be equivalent to Equation (8.12).

8.4.3 Waveguide Projection Model (Without Considering the Junction and Bend Effect)

The guided wavenumbers $\beta_{c,m}$ can also be approximated by considering the SWS as a straightened version of the serpentine waveguide. In this simple view, the effect of the junction between straight and bend sections is ignored and we assume that the TE10 propagation constant in the curved segments is the same as in the straight segments. The on-axis phase shift per pitch for the mth spatial harmonics is $\beta_{c,m}d = \theta + 2m\pi$, where $\beta_{c,m}$ is the *effective* on-axis propagation constant, $\theta = \beta_{g,s}L$ is phase delay per pitch of EM wave, and $L = 2(\pi R + h)$ is defined as the distance traveled by the wave per pitch. The phase velocity of mth spatial harmonics is expressed by [344]

$$v_{c,m} = \frac{\omega}{\beta_{c,m}} = \frac{\omega d}{\beta_{g,s}L + 2\pi m}. \tag{8.16}$$

The derivation of Equation (8.16) assumes that the bends do not present significant mismatches to the wave. In practice, both the bends and the beam holes introduce small mismatches that may cause stopbands where the dispersion curves of spatial harmonics cross. These effects are ignored in this simplified model.

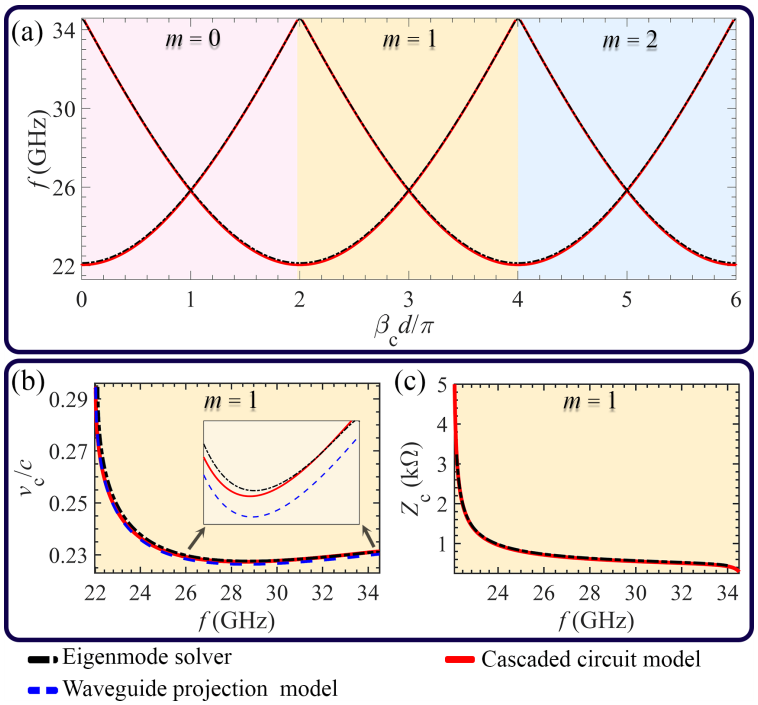

Figure 8.5: Cold simulation results for the SW using theoretical and simulation methods. (a) Modal dispersion curves for three spatial harmonics ($m = 0, 1$ and 2) by employing the full-wave eigenmode solver (dashed black curves) and cascaded circuit model (solid red curve). (b) Normalized phase velocity for the first spatial harmonic ($m = 1$) by using the eigenmode solver (dashed black curves), cascaded circuit model (solid red curve) and waveguide projection model (dashed blue curves). Also, the zoomed-in version of normalized phase velocity in the frequency range from 26 GHz to 34.5 GHz is shown to demonstrate the superior accuracy of the cascaded circuit model compared to the waveguide projection model. (c) Characteristic Bloch impedance for the first spatial harmonic ($m = 1$) calculated using the cascaded circuit model (solid red curve), compared with that from full-wave simulation (dashed black curve).

8.5 Validation of Equivalent Circuit Model

The cold SWS characteristics for a specific design are shown via the three theoretical models discussed in the previous section, compared with simulations performed using the CST Studio Suite eigenmode solver. Figure 8.1 shows the model of a typical SW with a cylindrical beam tunnel, where the geometric parameters w, b, d, h, and r_c represent the dimensions of wide side, narrow side, full period, straight waveguide wall, and radius of beam tunnel, respectively. The parameter values for a specific design are listed in Table 8.1.

Table 8.1: Designed structural parameters for the SWSWS.

Description	Parameter	Length (mm)
The width of rectangular waveguide	w	6.8
The height of rectangular waveguide	b	0.7
The full period length	d	4
The whole straight waveguide length	h	2.5
The radius of beam tunnel	r_{c}	0.5

Figure 8.5 shows the wavenumber, phase velocity and characteristic impedance of the EM modes in the cold serpentine waveguide obtained using theoretical and simulation methods. Figure 8.5(a) shows the wavenumber dispersion diagram of the modes in the SW, showing three spatial harmonics, obtained by varying the phase between periodic boundaries. The simulated results based on the CST Studio Suite eigenmode solver (dashed black curves) are in excellent agreement with the theoretical dispersion diagram calculated by the cascaded circuit model (solid red curves) discussed in Subsection 8.4.1. The cutoff frequency of the designed SW is around $f_{\mathrm{c}} = 22.15\,\mathrm{GHz}$. Then, the normalized phase velocity corresponding to the first spatial harmonic ($m = 1$) as a function of frequency ranging from 22.15 GHz to 34.5 GHz is plotted in Figure 8.5(b). There is excellent agreement between the results provided by the eigenmode solver (dashed black curve), cascaded circuit model (solid red curve) in Subsection 8.4.1, and waveguide projection model (dashed blue curve) in Subsection 8.4.3. As a general observation, the cascaded circuit model is more accurate than the waveguide projection model because it accounts for the mismatches due to circular bends and junctions. The characteristic Bloch impedance of the SWSWS using the cascaded circuit model (solid red curve) in Section 8.4.1, compared to that from full-wave simulation (dashed black curves), is shown in Figure 8.5(c). The characteristic Bloch impedance from full-wave simulation is calculated as $Z_{\mathrm{c}} = -E_y/H_x = V/I$, by using field monitors.

In order to demonstrate that the SW can be modeled by a single straight uniform TL

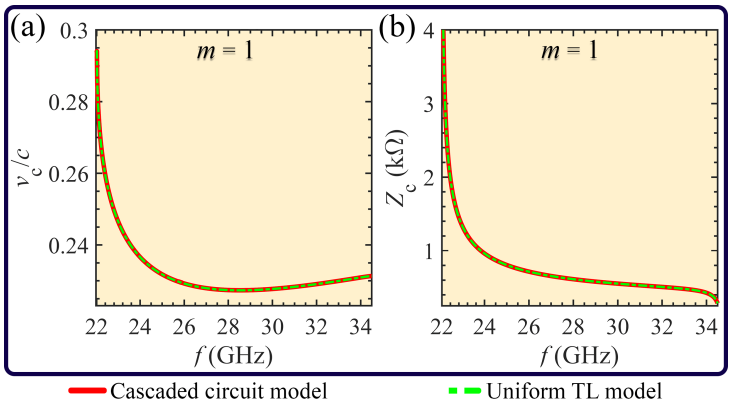

Figure 8.6: (a) Normalized phase velocity and (b) characteristic Bloch impedance of the first spatial harmonic ($m = 1$) calculated by using the cascaded circuit model (solid red curve) described in Subsection 8.4.1 and the uniform TL model (dashed green curve) described in Subsection 8.4.2.

(Section 8.4.2), we compare the results based on the uniform TL model with the cascaded circuit model (Section 8.4.1). The calculated phase velocity and characteristic impedance results for the first spatial harmonic in both cases are shown in Figure 8.6(a) and (b), and we observe excellent agreement between these two theoretical methods. Also, previous studies, such as [320], utilized the uniform TL model that is very similar to what is discussed in this chapter for the cold case. In contrast, in this chapter we also develop a model for finding the "hot eigenmodes" dispersion of the device and the TWT gain. The accurate calculation of the characteristic parameters of the cold structure, i.e., Z_c and v_c, has a vital role in our model. To reinforce this point, we note that one of the conclusions of [320] is that accurate determination of the small-signal gain in a SWTWT amplifier requires a precise evaluation of the phase velocity to within 0.5% and the interaction impedance within 10% of the actual parameters found by time-consuming full-wave eigenmode simulations. The calculated gain is very sensitive to these parameters, and requires correct phase velocity and interaction impedance specification. Sensitivity studies in [320] indicate that variations in the phase velocity of 0.5% can result in 8 dB of variation in the predicted small-signal gain, while a 10% variation in the interaction impedance can result in a 5 dB change in the predicted small-signal gain of the specific design.

8.6 Interaction Impedance

In order to predict the performance of a TWT, one needs to determine the interaction (Pierce) impedance of the SW because amplifier gain is proportional to the cubic root of this parameter [2]. The interaction impedance is a measure of how much the on-axis electric field can velocity modulate electrons for a given EM power propagating along the length of the structure [290, Chapter 10]. In the ideal case, the e-beam is assumed to be very narrow. From Pierce theory, the interaction impedance for a thin beam is defined for a specific spatial harmonic m as [290, Chapter 10]

$$Z_{\mathrm{P},m}\left(\beta_{\mathrm{c},m}\right) = \frac{\left|E_{z,m}\left(\beta_{\mathrm{c},m}\right)\right|^2}{2\beta_{\mathrm{c},m}^2 P}, \tag{8.17}$$

where $\left|E_{z,m}\left(\beta_{\mathrm{c},m}\right)\right|$ is the magnitude of the axial electric field phasor along the center of the cold SWS where the e-beam will be introduced, for a given phase constant and spatial harmonic m, and P is the time-average power flux through the SWS at the given phase propagation constant $\beta_{\mathrm{c},m}$ [290]. The quantity $|E_{z,m}|$ is the weight of the mth Floquet-Bloch spatial harmonics of the axial field decomposition $E_z\left(z,\beta_{\mathrm{c}}\right) = \sum_{m=-\infty}^{\infty} E_{z,m}\left(\beta_{\mathrm{c}}\right) e^{-j\beta_{\mathrm{c},m}z}$. It is calculated by numerically obtaining the phasor of the axial electric field $E_z\left(z,\beta_{\mathrm{c}}\right)$ of the cold SW with beam tunnel using full-wave eigenmode simulations, followed by performing the Fourier transform in space

$$E_{z,m}\left(\beta_{\mathrm{c}}\right) = \frac{1}{d}\int_0^d E_z\left(z,\beta_{\mathrm{c}}\right) e^{j\beta_{\mathrm{c},m}z} dz. \tag{8.18}$$

In addition, the time average power flux is simply calculated as $P = W_{\mathrm{t}} v_{\mathrm{g}}/d$ [345], where W_{t} is the total EM energy of the wave stored in a unit cell and $v_{\mathrm{g}} = d\omega/d\beta_{\mathrm{c}}$ is the group velocity. For an SW, the interaction impedance is typically evaluated within the first Brillouin zone (i.e., $m = 1$), where the interaction occurs. Additionally, the e-beam diameter also influences

the interaction impedance. For beam cross sections and beam tunnel diameters that are not infinitesimally thin, the longitudinal electric field and the interaction impedance within the beam tunnel can vary over the beam cross section area, becoming larger near the edges of the tunnel. As a consequence, the additional correction factor (average factor) should be considered in calculating the interaction impedance by taking into account the variation of the electric field within the interaction area (interaction gap) [346]. Additional analysis of the variation of the electric field distribution in the interaction area for the specific example can be found in Section 8.7. Therefore, a modified or "effective interaction impedance" corresponding to each spatial harmonic considering the nonuniform electric field distribution in the interaction area is given by

$$Z_{\mathrm{P,e},m} = (1 + \delta_{\mathrm{e}})^2 \, Z_{\mathrm{P},m}, \tag{8.19}$$

where, $\delta_{\mathrm{e}} > 0$ is the correction factor. The value of the correction factor δ_{e} can be found either by (i) averaging the EM axial field over the beam cross section, or (ii) by matching the maximum value of the theoretical and PIC-simulated gain at the synchronization frequency.

In this chapter, to compute the interaction impedance $Z_{\mathrm{P},m}$, we use the eigenmode solver of CST Studio Suite to calculate $E_z\left(z, \beta_{\mathrm{c}}\right)$ over z for different β_{c}. Then, we transform the electric field $E_z\left(z, \beta_{\mathrm{c}}\right)$ by Equation (8.18) and calculate the interaction impedance by Equation (8.17). The group velocity $v_{\mathrm{g}} = d\omega/d\beta_{\mathrm{c}}$ is determined directly from the dispersion diagram by using numerical differentiation. The EM energy simulated within a single unit cell between periodic boundaries in the eigenmode solver is always 1 Joule.

8.7 Longitudinal Fields in the Interaction Regions

The magnitude of the z-component of electric field distribution at the center of the longitudinal cross section (the $x = 0$ plane) of a cold SW is shown in Figure 8.7(a). For better illustration, the z-component magnitude in the beam and EM wave interaction area at various transverse cross sections of $z_0 = 0.7$ mm, $z_0 = 0.85$ mm and $z_0 = 1$ mm is shown in Figure 8.7(b). We can see that the electric field magnitude increases near the beam tunnel perimeter. Also, the magnitude of the z-component of the electric field in a straight line in the x direction, with $y = 0$, at three different z values is depicted in Figure 8.7(c). The magnitude of the z-component of the electric field is also calculated at different radii inside the beam tunnel as shown in Figure 8.7(d). These plots demonstrate that the minimum field value is obtained at the center of the beam tunnel and that the magnitude of E_z increases gradually with an increasing radius. Thus, in the interaction area, the minimum interaction impedance is calculated at the center of the beam tunnel, i.e., at $r = 0$. To account for the nonuniform distribution of the longitudinal electric field in the interaction area, the interaction impedance should be multiplied by a correction factor, i.e., $(1 + \delta_e)^2$. Since the electric field magnitude is greater near the tunnel wall, the correction factor should be greater than one ($\delta_e \geq 0$).

8.8 E-beam and EM Wave Interaction

The classical small-signal theory by J. R. Pierce is one of the most famous approaches used for TWT modeling and design [285, 329, 2, 286]. Our implementation based on the generalization of Pierce's theory is summarized here following our previous work [75]. We follow the linearized equations that describe the space-charge wave as originally presented by Pierce.

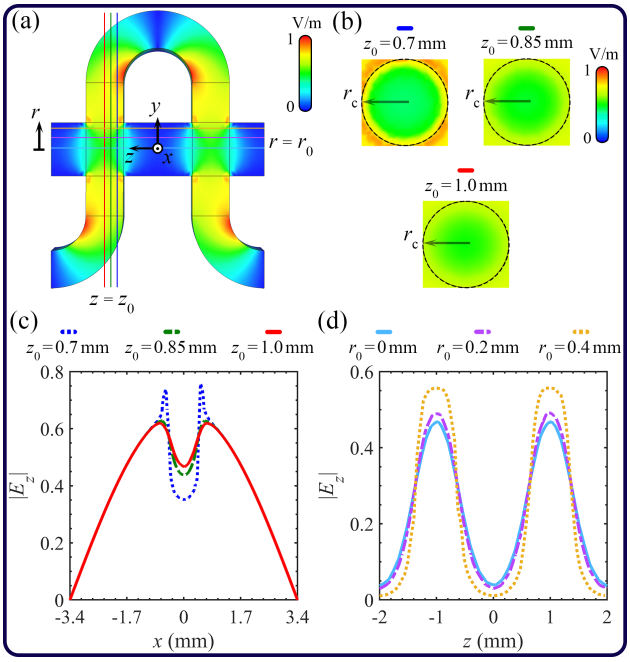

Figure 8.7: The on-axis z-component of electric field distribution in the beam tunnel area in a cold SWSWS: (a) Over the longitudinal cross section, i.e., at $x = 0$ plane; (b) in the interaction area at three different transverse cross section planes with $z_0 = 0.7$ mm, $z_0 = 0.85$ mm and $z_0 = 1$ mm; (c) in the x direction, with $y = 0$, at three different z_0 coordinate; (d) at three different radii r_0, along the beam tunnel.

The equivalent model for the TWT describes the EM wave traveling in an SW interacting with an e-beam flowing in the z direction as shown schematically in Figure 8.8. The electrons have an average velocity and linear charge density of u_0 and ρ_0, respectively. The e-beam has an average current $I_0 = -\rho_0 u_0$ in the $-z$ direction and an equivalent kinetic d.c. voltage as $V_0 \approx u_0^2/(2\eta)$ for non-relativistic beams (assuming that thermal initial velocity of the electron is neglected) or $V_0 = \left[\left(1-(u_0/c)^2\right)^{-1/2} - 1\right] c^2/\eta$ for relativistic beams, where c is the speed of light in a vacuum, $\eta = e/m = 1.758820\times10^{11}$C/Kg is the charge-to-mass ratio of the electron with charge $-e$ and rest mass m [46, Chapter 3]. The small-signal modulations in the charge velocity u_b and charge density ρ_b, describe the "space-charge wave". The a.c. equivalent beam current and kinetic voltage are given by $i_\mathrm{b} = u_\mathrm{b}\rho_0 + u_0\rho_\mathrm{b}$ and $v_\mathrm{b} = u_\mathrm{b}u_0/\eta$, where we have kept only the linear terms based on the small-signal approximation [286]. We implicitly assume a time dependence of $\exp(j\omega t)$, so the a.c. space-charge wave modulating the e-beam is described in the phasor domain with $V_\mathrm{b}(z)$ and $I_\mathrm{b}(z)$, as

$$\frac{d}{dz}V_{\mathrm{b}} = -j\beta_0 V_{\mathrm{b}} - aZI - j\frac{I_{\mathrm{b}}}{A\varepsilon_0\omega}, \tag{8.20}$$

$$\frac{d}{dz}I_{\mathrm{b}} = -jgV_{\mathrm{b}} - j\beta_0 I_{\mathrm{b}}, \tag{8.21}$$

where $\beta_0 = \omega/u_0$ is the space-charge wave equivalent phase constant (when neglecting plasma frequency effects), $g = I_0\beta_0/(2V_0)$, Z is the equivalent TL distributed series impedance, and $I(z)$ is the equivalent TL current. The term $E_{\mathrm{w}} = aZI$ is the longitudinal electric field of the EM mode propagation in the SWS, affecting the bunching of the e-beam. In addition, the coefficient a represents a coupling strength that describes how the e-beam couples to the TL, already introduced in [292, 75, 347] and [293, 291, Chapter 3] and investigated in more detail in Section 8.9. Also, the term $E_{\mathrm{p}} = jI_{\mathrm{b}}/(A\varepsilon_0\omega)$ is the longitudinal electric field term arising from the nonuniform charge density that causes the so-called "debunching" [290, Chapter 10], where A is the e-beam cross sectional area, and ε_0 is vacuum permittivity. This field is responsible of the repulsive forces in a dense beam of charged particles. Therefore, $E_z = E_{\mathrm{w}} + E_{\mathrm{p}}$ is the total longitudinal z-polarized electric field component in the hot structure (when also the e-beam is present) that modulates the velocity and bunching of the electrons. In SWTWTs, the beam-EM wave interaction occurs in the first spatial harmonic ($m = 1$), so in this section we drop the subscript harmonic index m for simplicity. The telegrapher's equations,

$$\frac{d}{dz}V = -ZI, \tag{8.22}$$

$$\frac{d}{dz}I = -YV - a\frac{d}{dz}I_{\mathrm{b}}, \tag{8.23}$$

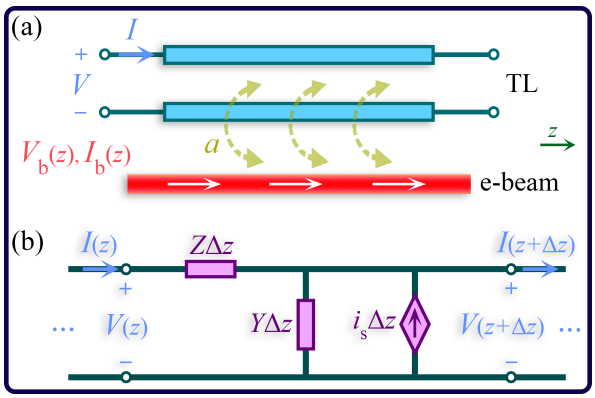

Figure 8.8: (a) Schematic of the equivalent TL coupled to the e-beam used to study the beam-EM wave interaction in the SWTWT. (b) Equivalent TL circuit showing the per-unit-length impedance, admittance and current generator $i_s = -a\partial_z I_b$ that represents the effect of the e-beam on the TL.

describe the modal propagation in the SWS of the EM mode synchronizing with the e-beam in terms of equivalent TL voltage $V(z)$ and current $I(z)$ phasors, based on the equivalent TL model shown in Figure 8.8(b). Figure 8.8(b) shows the distributed per-unit-length series impedance Z and shunt admittance Y as well as the term $i_s = -a\left(dI_b/dz\right)$ that represents an equivalent distributed current generator [294, 292, 75, 347]. This current generator accounts for the effect of the beam's charge wave flowing in the SWS. It is well known that dependent sources are used to describe gain in transistors and linear amplifiers, which justifies this approach to model the e-beams effect on the TL. The frequency dependent parameters Z and Y could be obtained using the cascaded circuit model described in Subsection 8.4.1 as follows. We evaluate the phase velocity of the cold circuit EM modes $v_c(\omega) = \omega/\beta_c(\omega)$, where $\beta_c(\omega) = \sqrt{-Z(\omega)Y(\omega)}$ is the phase propagation constant harmonic of the cold SWS mode interacting with the e-beam, and the equivalent TL characteristic impedance $Z_c(\omega)$. Then, one could obtain the equivalent frequency-dependent distributed series impedance $Z(\omega) = j\beta_c(\omega)Z_c(\omega)$ and shunt admittance $Y(\omega) = j\beta_c(\omega)/Z_c(\omega)$.

For convenience, we define a state vector $\mathbf{\Psi}(z) = [V, I, V_b, I_b]^T$ (T indicates transpose operation) that describes the hot mode propagation, and rewrite Equations (8.20), (8.21), (8.22), and (8.23) in matrix form as

$$\frac{d}{dz}\mathbf{\Psi}(z) = -j\underline{\mathbf{M}}\mathbf{\Psi}(z), \tag{8.24}$$

$$\underline{\mathbf{M}} = \begin{bmatrix} 0 & \beta_{\mathrm{c}} Z_{\mathrm{c}} & 0 & 0 \\ \beta_{\mathrm{c}}/Z_{\mathrm{c}} & 0 & -ag & -a\beta_0 \\ 0 & a\beta_{\mathrm{c}} Z_{\mathrm{c}} & \beta_0 & \zeta_{\mathrm{sc}} \\ 0 & 0 & g & \beta_0 \end{bmatrix}, \tag{8.25}$$

where $\underline{\mathbf{M}}$ is the 4×4 system matrix. Here, we have used directly the primary TL parameters $\beta_{\mathrm{c}}(\omega)$ and $Z_{\mathrm{c}}(\omega)$ instead of $Z(\omega)$ and $Y(\omega)$. In the above system matrix, ζ_{sc} is the space-charge parameter related to the debunching of beam's charges, and is given by [75]

$$\zeta_{\mathrm{sc}} = \frac{R_{\mathrm{sc}}}{A\varepsilon_0\omega} = \frac{2V_0\omega_{\mathrm{q}}^2}{\omega I_0 u_0}, \tag{8.26}$$

where $\omega_{\mathrm{q}} = R_{\mathrm{sc}}\omega_{\mathrm{p}}$ is the reduced plasma angular frequency, $\omega_{\mathrm{p}} = \sqrt{-\rho_0\eta/(A\varepsilon_0)}$ or $\omega_{\mathrm{p}} = \sqrt{I_0 u_0/(2V_0 A\varepsilon_0)}$ is the plasma frequency [296], and R_{sc} is the plasma frequency reduction factor [304, 297]. The term R_{sc} accounts for reductions in the magnitude of the axial component of the space-charge electric field due to either a finite beam radius or proximity to the surrounding conducting walls of the e-beam tunnel [300] (details in Section 8.10). As shown in Section 8.9, the coupling strength coefficient a is found by using the formula

$$a = \sqrt{\frac{Z_{\mathrm{P,e}}}{Z_{\mathrm{c}}}}, \tag{8.27}$$

and it is frequency dependent as shown later on. In summary, all the parameters of the

presented model are found using cold simulations of the EM mode in the SWSWS to estimate the performance of the hot structure. We emphasize that the calculated characteristic impedance Z_{c}, regardless of how it is defined, yields meaningful results in our theoretical model, as long as one uses the effective interaction impedance $Z_{\mathrm{P,e}}$ that is calculated from full-wave eigenmode simulations as described in Section 8.6.

8.9 Coupling Strength Coefficient

The characteristic impedance of a mode guided by a cold waveguide is Z_{c} and by using this value, matching networks can be designed to terminate the input and output ends of the TWT. In contrast, in the Pierce model, the characteristic impedance of the equivalent TL that represents EM synchronization is the interaction impedance Z_{P}. These two dispersive impedances are related by a frequency-dependent coupling strength coefficient discussed here. Other works have used this coupling strength coefficient introduced as an ad-hoc parameter, including [293, 292, 253, 295, 254, 291, 75, 348, 126, 349, 53]. Considering the modal propagation in the equivalent TL, the z-component of the a.c. electric field induced on the cold SWS was related to the phenomenological coupling strength coefficient a as [292, 75]

$$E_z = -a\frac{dV\left(z\right)}{dz}. \tag{8.28}$$

The equivalent voltage on the TL is related to the per-unit length impedance and equivalent current as $dV\left(z\right)/dz = -ZI\left(z\right)$. For a lossless TL, the per-unit-length impedance is calculated by $Z = j\beta_{\mathrm{c}}Z_{\mathrm{c}}$. Then, we relate the equivalent voltage and current of the TL via the characteristic impedance by

$$\frac{dV(z)}{dz} = -j\beta_{\mathrm{c}} Z_{\mathrm{c}} I(z). \tag{8.29}$$

Substituting Equation (8.29) in Equation (8.28), we obtain the relation between the axial electric field of the guided mode and the equivalent current of TL by

$$E_z = ja\beta_{\mathrm{c}} Z_{\mathrm{c}} I(z). \tag{8.30}$$

Then, the interaction impedance Z_{P} is calculated by Equation (8.17) for the interacting harmonic (i.e., $m = 1$). Here, we derive the coupling strength coefficient in terms of Z_{c} and Z_{P}. By substituting E_z from Equation (8.30) and time-average power along the TL $P = Z_{\mathrm{c}} |I(z)|^2 /2$ in Equation (8.17), the interaction impedance and characteristic impedance of the SWS are related through the coupling strength coefficient a, as $a = \sqrt{Z_{\mathrm{P}}/Z_{\mathrm{c}}}$. Using this relation between the characteristic impedance and the interaction impedance, one can transform the TL equivalent voltage and current of the state vector and system matrix in Equation (8.25) to be in terms of scaled state vector quantities $V'(z) = aV(z)$ and $I'(z) = I(z)/a$ that maintain the average power definition $P = \frac{1}{2}\iint_S \mathrm{Re}\left(-E_y H_{x,}^*\right) dxdy = \mathrm{Re}\left[VI^*\right]/2 = \mathrm{Re}\left[V'I'^*\right]/2$, where * is the complex conjugate operator. By making this transformation, the system equations are expressed as

$$\frac{d}{dz}\boldsymbol{\Psi}'(z) = j\underline{\mathbf{M}}'\boldsymbol{\Psi}'(z), \tag{8.31}$$

where the transformed state vector is defined as $\boldsymbol{\Psi}'(z) = \left[V', I', V_{\mathrm{b}}, I_{\mathrm{b}}\right]^{\mathrm{T}}$ and the transformed system matrix is expressed in terms of interaction impedance rather than characteristic impedance as

$$\underline{\mathbf{M}}' = \begin{bmatrix} 0 & a^2\beta_c Z_c & 0 & 0 \\ \beta_c/(a^2 Z_c) & 0 & -g & -\beta_0 \\ 0 & a^2\beta_c Z_c & \beta_0 & \zeta_{sc} \\ 0 & 0 & g & \beta_0 \end{bmatrix}, \tag{8.32}$$

or equivalently

$$\underline{\mathbf{M}}' = \begin{bmatrix} 0 & \beta_c Z_P & 0 & 0 \\ \beta_c/Z_P & 0 & -g & -\beta_0 \\ 0 & \beta_c Z_P & \beta_0 & \zeta_{sc} \\ 0 & 0 & g & \beta_0 \end{bmatrix}, \tag{8.33}$$

where the coupling strength coefficient a is not present explicitly anymore. This alternative formulation for the TWT matrix is very informative, since the interaction impedance can be readily found for a realistic SWSWS using full-wave eigenmode simulations, i.e., by performing a simulation of only one unit cell of the cold SWS. Furthermore, to improve the accuracy of our calculations, we consider the "effective interaction impedance $Z_{P,e}$" discussed in Section 8.6 by adding the correction factor δ_e that accounts for the nonuniform cross sectional distribution of the electric field in the interaction area (see Section 8.7), given by

$$Z_{P,e} = (1 + \delta_e)^2 Z_P. \tag{8.34}$$

Accordingly, the definition of the coupling strength coefficient becomes $a = \sqrt{Z_{P,e}/Z_c}$, also

reported in Equation (8.27). Consequently, the transformed system matrix of Equation (8.33) is finally rewritten as

$$\underline{\mathbf{M}}' = \begin{bmatrix} 0 & \beta_{\mathrm{c}} Z_{\mathrm{P,e}} & 0 & 0 \\ \beta_{\mathrm{c}}/Z_{\mathrm{P,e}} & 0 & -g & -\beta_0 \\ 0 & \beta_{\mathrm{c}} Z_{\mathrm{P,e}} & \beta_0 & \zeta_{\mathrm{sc}} \\ 0 & 0 & g & \beta_0 \end{bmatrix}. \tag{8.35}$$

The coupling strength coefficient a has been eliminated through the proposed transformation, and we can use the effective interaction impedance $Z_{\mathrm{P,e}}$ instead of the characteristic impedance Z_{c} in our derived equations. We can use this alternative definition when dealing with power since $P = \mathrm{Re}\left[VI^*\right]/2 = \mathrm{Re}\left[V'I'^*\right]/2$. One could also use the impedance to calculate the output power as $P_{\mathrm{out}} = \left|V^{\mathrm{o}}\right|^2/\left(2Z_{\mathrm{c}}\right) = \left|V^{\mathrm{o}\prime}\right|^2/\left(2Z_{\mathrm{P,e}}\right)$, where $Z_{\mathrm{P,e}} = a^2 Z_{\mathrm{c}}$ and $V^{\mathrm{o}\prime} = aV^{o}$, assuming the TWT is matched to the modal characteristic impedance Z_{c} (see Subsection 8.10.2).

8.10 Plasma Frequency Reduction Factor

As explained in [350, 304, 351], the finite cross section of the e-beam, along with the surrounding metallic walls of the tunnel will make the scalar electric potential of the e-beam nonuniform over the beam cross section. Consequently, the plasma frequency of the beam will be reduced by the plasma frequency reduction factor. The closed-form frequency-dependent value we use for R_{sc} is calculated as [351]

$$R_{\mathrm{sc}}^2 = 1 - 2I_1\left(\beta_0 r_{\mathrm{b}}\right)\left(K_1\left(\beta_0 r_{\mathrm{b}}\right) + \frac{K_0\left(\beta_0 r_{\mathrm{c}}\right)}{I_0\left(\beta_0 r_{\mathrm{c}}\right)} I_1\left(\beta_0 r_{\mathrm{b}}\right)\right), \tag{8.36}$$

where, we assume the beam has a cylindrical cross section with radius r_{b} and the beam tunnel is assumed to be a metallic cylinder with a radius of r_{c}. In addition, I_n and K_n are modified Bessel functions of the first and second kind, respectively. Moreover, the analytical method for calculating the reduced plasma frequency based on 3D PIC simulations is developed in [352] which can be used for cylindrical-shaped e-beam flowing inside of a cylindrical tunnel.

8.10.1 Characteristic Equation and Electronic Beam Admittance

Assuming a state vector z-dependence of the form $\mathbf{\Psi}\left(z\right) \propto \exp\left(-jkz\right)$, where k is the complex-valued wavenumber of a hot mode in the interactive system, leads to the eigenvalue problem $k\mathbf{\Psi}\left(z\right) = \underline{\mathbf{M}}\mathbf{\Psi}\left(z\right)$. The resulting modal dispersion characteristic equation is given by

$$\begin{aligned} D\left(\omega, k\right) = \det\left(\underline{\mathbf{M}} - k\underline{\mathbf{I}}\right) = k^4 - k^3\left(2\beta_0\right) + k^2\left(\beta_0^2 - \beta_{\mathrm{q}}^2 - \beta_{\mathrm{c}}^2 + a^2 g \beta_{\mathrm{c}} Z_{\mathrm{c}}\right) \\ + k\left(2\beta_{\mathrm{c}}^2\beta_0\right) - \beta_{\mathrm{c}}^2\left(\beta_0^2 - \beta_{\mathrm{q}}^2\right) = 0, \end{aligned} \tag{8.37}$$

where $\beta_{\mathrm{q}} = \omega_{\mathrm{q}}/u_0 = \sqrt{g\zeta_{\mathrm{sc}}}$ is the phase constant of space-charge wave. The solution of Equation (8.37) leads to four modal complex-valued wavenumbers of the four hot modes in the interactive system. The characteristic equation is rewritten as follows

$$\left(k^2 - \beta_{\mathrm{c}}^2\right)\left[\left(k - \beta_0\right)^2 - \beta_{\mathrm{q}}^2\right] = -a^2 g k^2 \beta_{\mathrm{c}} Z_{\mathrm{c}}, \tag{8.38}$$

to stress that the term $-a^2 g\beta_c Z_c k^2$ $(= -g\beta_c Z_{P,e} k^2)$ indicates the coupling between the two dispersion equations of the isolated EM waves in the cold SWS $(k^2 - \beta_c^2) = 0$, and isolated charge waves $\left[(k-\beta_0)^2 - \beta_q^2\right] = 0$. Here, only parameters obtained from cold SWS simulations are used to find the dispersion of the four hot modes. For a given eigenmode, the e-beam interaction with the EM wave could be completely modeled as an active TL with a voltage-dependent current source, as shown schematically in Figure 8.8, given by [292]

$$i_s = jakI_b = -Y_b V, \tag{8.39}$$

where the electronic beam admittance per unit length Y_b is

$$Y_b = -j\frac{a^2 gk^2}{\left[(k-\beta_0)^2 - \beta_q^2\right]}. \tag{8.40}$$

This admittance is a generalization of the one already provided in [292] since here we have included the space charge effect $\beta_q^2 = g\zeta_{sc}$.

8.10.2 TWT Amplifier Gain

We describe the theoretical calculation to compute the gain of a TWT amplifier using the circuit model illustrated in Figure 8.9, where a matched resistance is considered for the source generator R_S, and the output is terminated by the matched load R_L. The SWTWT is modeled by the system matrix $\underline{\mathbf{M}}$ described earlier, input state vector of $\mathbf{\Psi}_1 = \left[V^i, I^i, V_b^i, I_b^i\right]^T$ calculated at $z = 0$, and output state vector of $\mathbf{\Psi}_2 = [V^o, I^o, V_b^o, I_b^o]^T$ calculated at $z = Nd$, i.e., at the end of the TWT, where N indicates the number of unit cells. The output state vector is calculated as $\mathbf{\Psi}_2 = \underline{\mathbf{T}}\mathbf{\Psi}_1$, where $\underline{\mathbf{T}} = \exp(-j\underline{\mathbf{M}}Nd)$ is the TWT transfer matrix.

In the model, we use the following boundary conditions at $z = 0$ and $z = Nd$,

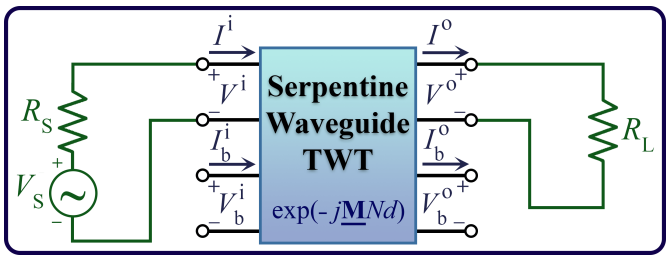

Figure 8.9: Circuit model for gain calculation considering frequency-dependent resistances for the source and load (R_{S} and R_{L}).

$$\begin{cases} V_{\mathrm{b}}^{\mathrm{i}} = 0,\ I_{\mathrm{b}}^{\mathrm{i}} = 0 \\ \\ V^{\mathrm{i}} + I^{\mathrm{i}} R_{\mathrm{S}} = V_{\mathrm{S}},\ V^{\mathrm{o}} - I^{\mathrm{o}} R_{\mathrm{L}} = 0 \end{cases} \tag{8.41}$$

In these equations, the source resistance R_{S} and load resistance R_{L} are assumed to be equal to the frequency-dependent characteristic impedance of the SW Z_{c}, and V_{S} is the generator voltage source. We solve the system of equations at each frequency and calculate the equivalent circuit current and voltage (proportional to the electric and magnetic fields) at the TWT output port. Then, we calculate the output power $P_{\mathrm{out}} = |V^{\mathrm{o}}|^2 / (2R_{\mathrm{L}})$, and the available input power $P_{\mathrm{av}} = |V_{\mathrm{S}}|^2 / (8R_{\mathrm{S}})$ (also denoted as incident power) to obtain the frequency-dependent gain as $G = P_{\mathrm{out}}/P_{\mathrm{av}}$.

In order to calculate the gain, we build the linear system $\underline{\mathbf{A}}\mathbf{X} = \mathbf{B}$, where the vector $\mathbf{X} = \left[V^{\mathrm{i}}, I^{\mathrm{i}}, V_{\mathrm{b}}^{\mathrm{i}}, I_{\mathrm{b}}^{i}, V^{\mathrm{o}}, I^{\mathrm{o}}, V_{\mathrm{b}}^{\mathrm{o}}, I_{\mathrm{b}}^{\mathrm{o}}\right]^{\mathrm{T}}$ contains the state vectors at the input and output of the TWT, and the 8×8 matrix $\underline{\mathbf{A}}$ is defined as

$$\underline{\mathbf{A}} = \begin{bmatrix} [-\exp(-j\underline{\mathbf{M}}Nd)] & & & & [\underline{\mathbf{I}}_4] & & & \\ 0 & 0 & 1 & 0 & 0 & 0 & 0 & 0 \\ 0 & 0 & 0 & 1 & 0 & 0 & 0 & 0 \\ 1 & R_{\mathrm{S}} & 0 & 0 & 0 & 0 & 0 & 0 \\ 0 & 0 & 0 & 0 & 1 & -R_{\mathrm{L}} & 0 & 0 \end{bmatrix}, \tag{8.42}$$

where $\underline{\mathbf{I}}_4$ is the 4×4 identity matrix. The input vector of the system is expressed as $\mathbf{B} = [0, 0, 0, 0, 0, 0, V_{\mathrm{S}}, 0]^{\mathrm{T}}$. Then, solving this 8×8 system of equations for the vector $\mathbf{X}$ allows us to compute the TWT gain.

8.11 Validation of Model for Hot Structure

In order to investigate the accuracy of the presented model for the interaction, we compare the theoretically calculated gain versus frequency results from our model with those numerically obtained from the commercial PIC software CST Particle Studio. As explained in Section 8.6, in our model we consider the effective interaction impedance, which describes the strength of beam-EM mode interaction in the TWT. In this chapter, the correction factor δ_{e} is calculated by matching the maximum gain value from the theoretical model with the one obtained by *only one* PIC simulation that occurs at the synchronization frequency, Z_{P} is determined from Equation (8.17) by post-processing the data extracted from CST eigenmode simulations and v_{c} is calculated by theoretical circuit models, i.e., a cascaded circuit model.

In this study, synchronization with the first spatial harmonic of the SWS is selected for

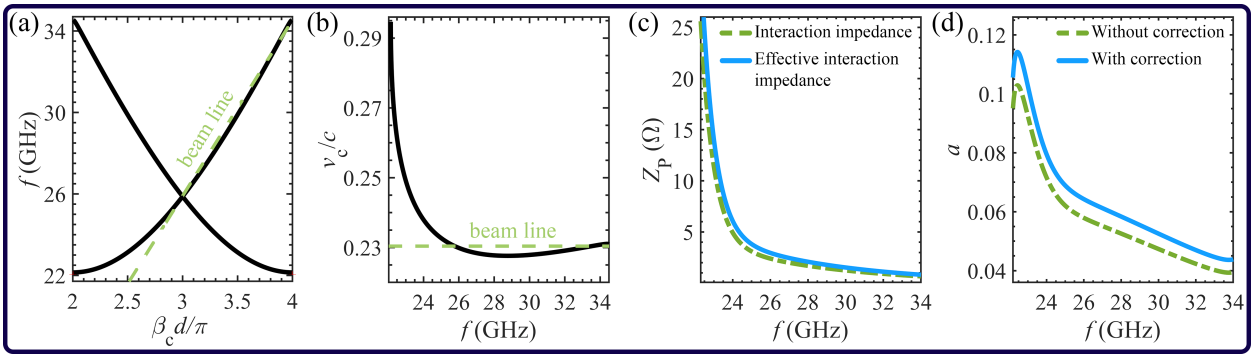

Figure 8.10: Cold results: (a) Dispersion curve and (b) normalized phase velocity of the modes in the cold SWSWS in the first spatial harmonic. (c) The on-axis interaction impedance of the serpentine waveguide SWS at the center of the beam tunnel with (solid blue) and without (dashed green) considering the correction factor δ_e. (d) The frequency-dependent value of the coupling strength coefficient a with (solid blue) and without (dashed green) correction factor δ_e.

low beam voltage operation. However, for simplicity of notation, we drop the harmonic index number and we will call the circuit modal wavenumber and phase velocity belonging to the $m = 1$ spatial harmonic simply as β_c and v_c. We consider a SWSWS with the geometry parameters listed in Table 8.1. The e-beam has $I_0 = 10$ mA and a radius $r_b = 0.35$ mm and we end up with a tunnel filling factor of $(r_b/r_c)^2 = 0.5$. For the e-beam, the normalized phase velocity u_0/c is set to be 0.230. This value corresponds to an average kinetic voltage of $V_0 = 14.077$ kV for the e-beam. Additionally, a uniform longitudinal magnetic field of 0.8 T was applied to confine the e-beam. The cold dispersion diagram and beam line are illustrated in Figure 8.10(a) where the beam line with normalized phase velocity of $u_0/c = 0.230$ is superimposed to the wavenumber of the EM mode, in the SWS on both left and right of the 3π point. Additionally, the beam line may synchronize with the EM backward mode near 3π at the intersection frequency which may result in parasitic oscillations and instability [337, 334]. So, in the design of a long SWTWT, attenuators can be used to mitigate oscillation risk. However, this issue is not discussed here, and how the presented model can be adapted to cases with attenuators will be studied in our future work. The frequency-dependent interaction impedance calculated at the beam center for the first spatial harmonic by using Equation (8.17) is shown in Figure 8.10(c). In this

example, the interaction impedance correction factor is considered to be $\delta_e = 0.11$, which is a relatively small factor. We show both the calculated interaction impedance without correction factor Z_P (see Equation (8.17)) and effective interaction impedance with correction factor $Z_{P,e}$ (see Equation (8.19)) in Figure 8.10(c) by using dashed green and solid blue curves respectively. The on-axis interaction impedance approaches very high values near the waveguide cutoff frequency at $f_c = 22.15$ GHz and gradually drops as the frequency grows further away from the cutoff frequency. The frequency-dependent value of the coupling strength coefficient without considering correction factor, $a = \sqrt{Z_P/Z_c}$, and with correction factor, $a = \sqrt{Z_{P,e}/Z_c} = (1 + \delta_e)\sqrt{Z_P/Z_c}$, are shown in Figure 8.10(d).

According to the intersection of the cold EM mode phase velocity curve v_c and the beam line in Figure 8.10(b), we observe beam-EM wave full synchronization at 25.73 GHz and 33.52 GHz, where high amplification is expected to occur. The real and imaginary parts of the complex-valued wavenumber of the hot modes (i.e., accounting for the beam-EM wave interaction) are calculated by Equation (8.38) and shown in Figures 8.11(a) and (b). The amplification regime is obtained when there is a hot mode with $\mathrm{Im}\,(k) > 0$. The numerical gain versus frequency diagram is theoretically calculated by the method described in Subsection 8.10.2 for the serpentine waveguide TWT with $N = 40$ unit cells (160 mm in length) and input power of $P_{in} = 0$ dBm. It is compared with the one obtained by computationally intensive 3D PIC simulations, resulting in excellent agreement. The comparison also validated the value of the interaction impedance correction factor $\delta_e = 0.11$. Since the analysis is in the linear regime, instead of using $N = 40$ unit cells, a quick simulation to estimate the correction factor δ_e was done based on only $N = 10$ unit cells. However, as a check we also verified that we obtained the same value when considering $N = 40$ unit cells.

The theoretical and PIC simulated gain versus frequency are illustrated in Figure 8.11(c) by solid pink and dashed blue curves, respectively. The agreement is excellent, indicating the accuracy of the model. Additionally, as predicted, maximum gains are obtained around syn-

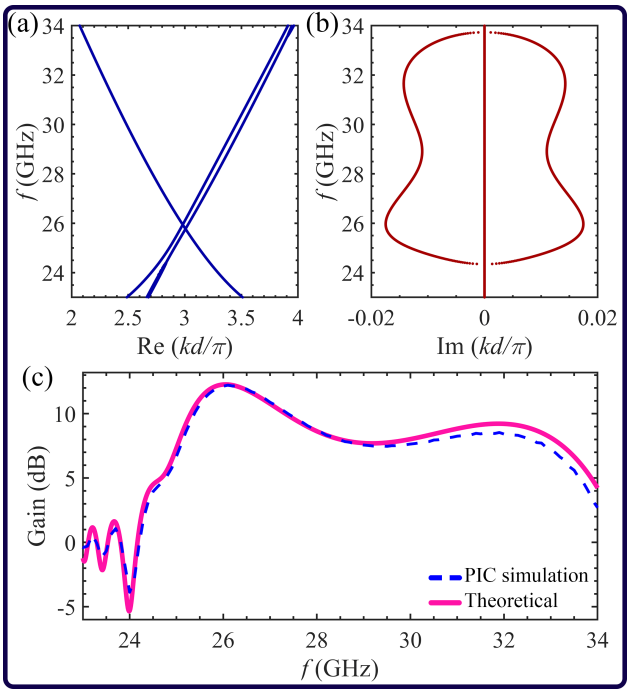

Figure 8.11: Hot results: The (a) real and (b) imaginary parts of complex-valued wavenumbers of hot modes by varying frequency. (c) TWT gain versus frequency predicted by the proposed theoretical model (solid pink), compared to 3D PIC simulations (dashed blue).

chronization frequencies. The total number of mesh cells in the simulation is approximately 2.6 million and a steady state output signal is seen after a transient time of 10 ns elapses. We use a sinusoidal signal as an excitation signal in the PIC simulation and a frequency sweep is performed to calculate output power in the selected frequency band. The required time for simulation and specification of the employed server is provided in Section 8.12. As shown in Figure 8.11(c), the 3-dB bandwidth is 9.37% covering from 25.21 GHz to 27.65 GHz. Also, the maximum amplifier gain of 12.27 dB is obtained at 26.04 GHz. We also investigated another example with a wider e-beam with tunnel filling factor of $(r_{\mathrm{b}}/r_{\mathrm{c}})^2 = 0.95$. In this case, the correction factor is $\delta_{\mathrm{e}} = 0.18$. This value is explainable since according to Figure 8.7(c) and (d) we observe bigger values of electric fields near the beam tunnel wall which leads to stronger beam-EM wave interaction. Note that the purpose of this chapter is not to design a TWT that can compete with conventional designs, but to showcase a simple and accurate model to predict TWT performance.

8.12 Computational Burden and Simulation Time

For PIC simulations, we used a Dell Server PER740XD with 2 processors of Intel(R) Xeon(R) Gold 6244 central processing unit (CPU) (24.75M Cache, 3.60 GHz) and installed 96 GB of RAM. Furthermore, the system is equipped with a powerful graphics card, the NVIDIA Tesla V100 Volta graphics processing unit (GPU) accelerator (with a RAM size of 32GB). In order to provide the PIC gain results, for the example provided in Figure 8.11(c), the total number of mesh cells in the simulation is around 2.6 million and a steady state output signal is obtained after a transient time of 10 ns elapses, and we swept the input RF frequency from 23 GHz and 34 GHz with frequency steps of 0.1 GHz. It took around 21 hours to obtain the PIC gain results over the desired frequency range using such powerful GPU acceleration in CST Studio Suite. In contrast, once the required primary data for our model (such as the interaction impedance and correction factor) is obtained with full-wave simulation of just a unit cell of the cold SWS (which are not very computationally demanding), the theoretical output gain using our model is calculated in a few seconds. This is done by using the implemented code of our developed model in Mathwork Matlab R2023a.

8.13 Parameter Study

To validate the presented model, a variety of simulation runs and comparisons have been carried out. We will apply the same correction factor $\delta_e = 0.11$ obtained in the previous section to all the following examples. In fact, the effective interaction impedance and correction factor δ_e are identical for all examples, even when changing the e-beam parameters, number of unit cells and input power in the linear regime. First, we vary u_0 to change the synchronization frequency but leave all other parameters unchanged, which are equal to the parameters used in Section 8.11. In Figure 8.12(a), we select $u_0 = 0.228c$, which is $0.002c$

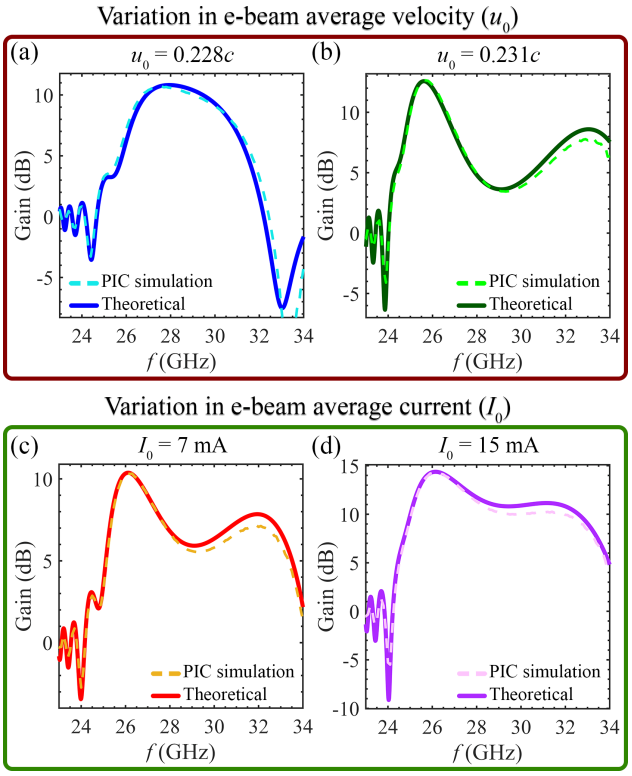

Figure 8.12: Comparison of gain versus frequency for a SWTWT calculated using our theoretical model and PIC simulations. In the first row, we show gain diagram by varying e-beam average phase velocity as (a) $u_0 = 0.228c$ and (b) $u_0 = 0.231c$. In the second row, we illustrate gain diagram by varying e-beam average current as (c) $I_0 = 7$ mA and (d) $I_0 = 15$ mA. The solid curves in these plots show the results obtained via PIC simulation whereas dashed curves are obtained based on the proposed theoretical model.

slower than the value used in the previous example. In this case, the forward branch of the modal dispersion diagram is approximately linear in the vicinity of the optimum frequency (i.e., the phase velocity remains almost constant). Here, the 3-dB bandwidth is 15.87% of the center frequency covering from 26.27 GHz to 30.70 GHz and the maximum amplifier gain of 10.82 dB is predicted at 27.93 GHz. Consequently, by establishing optimum synchronization, we can dramatically increase bandwidth. Next, in Figure 8.12(b) we increase the e-beam phase velocity to $u_0 = 0.231c$, which leads to synchronization around $f_{\text{sync}} = 25.5$ GHz and $f_{\text{sync}} = 34.26$ GHz, and calculate the gain. In these two plots, we also illustrate the theoretically calculated gain based on the proposed theoretical method, and we observe excellent agreement between theoretical (solid curves) and PIC simulation (dashed curves) results. We

stress that we did not have to recalculate the correction factor δ_e that was already calculated in the example in the previous section.

In the next step, the gain diagrams are calculated for the e-beam average currents of $I_0 = 7\,\text{mA}$ and $I_0 = 15\,\text{mA}$, shown in Figures 8.12(c) and (d). All the other parameters are as described in the previous section. The maximum gain in both cases occurs approximately at the same frequency since the e-beam phase velocity is equal in both examples. On the other hand, the maximum gain for the current value of $I_0 = 15\,\text{mA}$ is much bigger than the gain value for $I_0 = 7\,\text{mA}$. Hence, it is critical to choose the proper value for the e-beam current to avoid saturation. The solid curves obtained based on the proposed theoretical model show good agreement with the dashed curves calculated using PIC simulation. It is important to note that the correction factor $\delta_e = 0.11$ that was calculated in the previous section did not need to be adjusted or recalculated.

Our next step is to demonstrate how selecting the number of unit cells affects the gain and how this gain can be calculated accurately by the proposed model, still retaining the same correction factor $\delta_e = 0.11$ that was already calculated in the example in the previous section. The gain diagrams by varying the number of unit cells as $N = 30$ and $N = 50$ are calculated and shown in Figures 8.13(a) and (b). In both cases, the e-beam has the same phase velocity, so maximum gain occurs roughly at the same frequency. The solid curves calculated by the theoretical model show excellent agreement with the dashed curves obtained by numerically intensive PIC simulations. Increasing the number of interaction unit cells too much will eventually result in undesirable oscillations when the small-signal gain becomes too high (e.g. above the practical limit of 30 dB for a single-stage TWT). Therefore, it is critical to consider the proper number of unit cells to prevent oscillations. As a result of using the longer device for higher gain extraction, we should use sever in the design which will be investigated in detail in our future work.

Next, we show the effect of input power variation on the gain diagram, but still retaining the

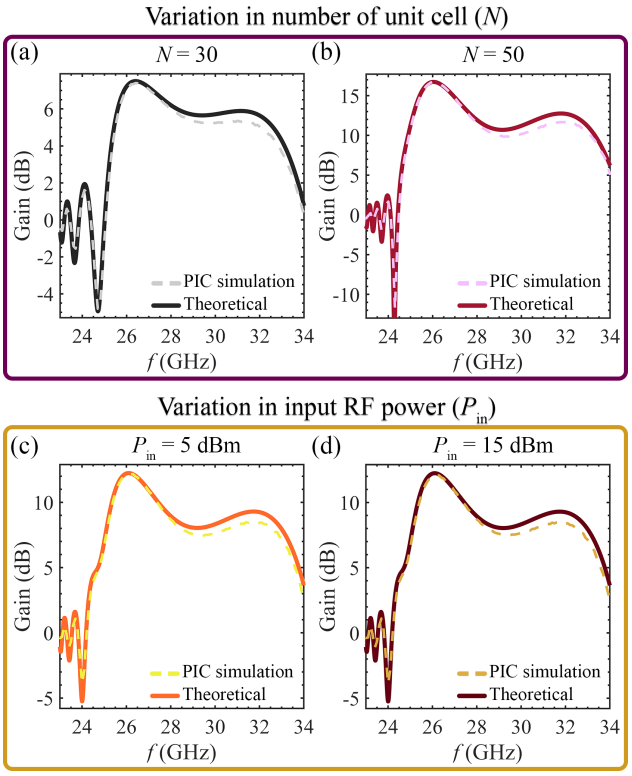

Figure 8.13: Comparison of gain versus frequency for a SWTWT calculated using our theoretical model and PIC simulations. In the first row, we show gain diagram by varying number of unit cells as (a) $N = 30$ and (b) $N = 50$. In the second row, we illustrate gain diagram by varying input power as (c) $P_{\text{in}} = 5$ dBm and (d) $P_{\text{in}} = 15$ dBm. The solid curves in these plots show the results obtained via PIC simulation whereas dashed curves are obtained based on the proposed theoretical model.

same correction factor $\delta_{\text{e}} = 0.11$ that was already calculated in the example in the previous section. Since our method is based on small-signal approximation, we neglected the effect of nonlinear terms in our model. We provide two different examples with $P_{\text{in}} = 5$ dBm and $P_{\text{in}} = 15$ dBm and the calculated results are presented in Figures 8.13(c) and (d). In comparison to the dashed curves obtained by PIC simulations, the theoretical results represented by solid curves exhibit good agreement.

As a last analysis, we calculate the gain at the synchronization frequency of $f_{\text{sync}} = 26$ GHz by assuming the parameters used in Section 8.11. The gain diagram by varying the e-beam average current is shown in Figure 8.14(a). In this plot, the theoretical gain is shown by a solid curve and the cross sign shows the corresponding simulation gain obtained from PIC

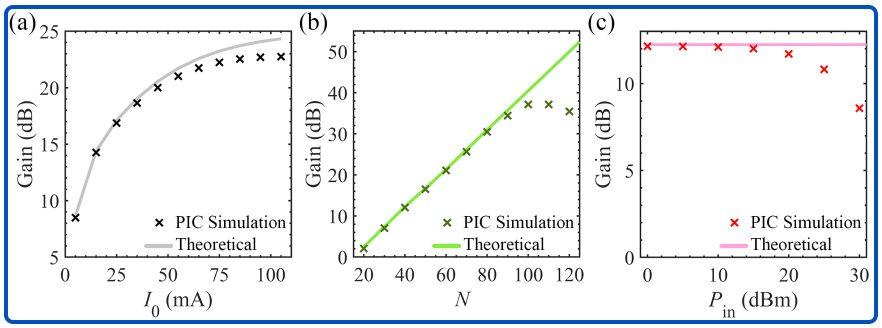

Figure 8.14: Comparison of gain versus frequency for a SWTWT calculated using our developed theoretical model (solid curves) and PIC simulations (dashed curves). In these plots, we change (a) e-beam average current, (b) number of unit cells, and (c) input power to show the accuracy of our theoretical calculation in the linear regime.

simulation at sampled currents. When the e-beam current is increased, saturation occurs, so designers should choose the proper current value carefully. The analogous analysis is provided by varying the number of unit cells and the calculated gain at the synchronization frequency by both theoretical and PIC simulation is shown in Figure 8.14(b). The simulation results confirm the calculated gain value when the number of unit cells is lower than 90 elements. It is significant to note that we did not use sever in the design of TWTs and all the simulations are provided for single-stage TWT. Finally, Figure 8.14(c) shows the linear and saturation regions of the TWT by varying the incident RF power at the TWT input port (at the cathode end). The analysis shows that by increasing the input power, we move into a nonlinear regime, where the calculated gain by using the theoretical model and PIC simulation disagree by more than 3 dB. In the large signal regime, the calculated results based on linear approximation will not reliably reproduce the TWT behavior near saturation. Our developed model is reliable for the small-signal regime and accurate results in the large-signal regime should be calculated using other specialized large-signal codes or PIC simulations. Again, it should be noted that the correction factor value in these plots has not changed from previous examples.

8.14 Conclusions

We have presented an extended analytical model for studying beam-EM wave interaction in a SWTWT that considers space-charge effects and dispersive waveguide parameters to predict gain in TWT amplifiers. Our goal is not to present a novel design method but rather to construct an accurate and robust small-signal model to predict TWT performance that could also be used for design. The method is simple because it uses an equivalent circuit model to calculate the SWS cold (i) modal wavenumber, (ii) characteristic impedance, and (iii) the interaction impedance, which are all frequency dependent. We added a frequency-independent correction factor δ_e to the interaction impedance, to model the nonuniform beam-EM wave interaction in the overlapping region of the e-beam and SWS longitudinal electric field. A theoretical method is used to predict the gain versus frequency and complex-valued wavenumber of the hot modes, and the results are compared with numerically intensive PIC simulations. The proposed method has been found always in good agreement with PIC simulations and much faster and flexible. For example, the flexibility of our method has been shown by changing the e-beam parameters, number of unit cells, and input power and by comparing the theoretical gain results with numerical gain results based on PIC simulations. The results consistently showed that our model is accurate and efficient at predicting SWTWT amplification characteristics.

Acknowledgments

- I would like to thank Robert Marosi and Tarek Mealy for collaboration on this chapter.
- This material is based upon work supported by the Air Force Office of Scientific Research (AFOSR) Multidisciplinary Research Program of the University Research Initiative (MURI) administered through the University of New Mexico under Grant

FA9550-20-1-0409.

- The text of Chapter 8 of this dissertation is a reprint of the material as it appears in K. Rouhi, R. Marosi, T. Mealy, A. Figotin, and F. Capolino, "Parametric Modeling of Serpentine Waveguide Traveling Wave Tubes," IEEE Transactions on Plasma Science, vol. 52, no. 4, pp. 1247–1263, Apr. 2024. The coauthors listed in this publication are Robert Marosi, Tarek Mealy, Alexander Figotin, and Filippo Capolino. Alexander Figotin and Filippo Capolino directed and supervised research which forms the basis for the dissertation.

- The results of this chapter have been published in the journal paper of [353] and in the conference paper of [347].

Chapter 9

Small-Signal 1D Model of Multi-Stage Serpentine Waveguide Traveling Wave Tubes With Severs

We present a model for calculating the small-signal gain of a multi-stage SWTWT with one or more severs. To mitigate the occurrence of self oscillations, the TWT stages are separated by a sever to stop RF wave propagation while the modulated e-beam is free to pass and is modeled by the electrons' motion equations. Our small-signal model is an advancement of the Pierce model, assuming 1D electron flow along a SWS, accounting for SWS dispersion, the space-charge effect, and a frequency dependent coupling strength coefficient relating the characteristic impedance to the interaction impedance. We compute the theoretical gain versus frequency for the multi-stage TWT and compare our results with PIC simulations. The good agreement demonstrates the accuracy of our analytical model for the multi-stage SWTWT with one or more severs. Here, we focus on showing the performance of our model as an effective tool for designers rather than proposing an optimal design strategy.

9.1 Background, Motivation, and State of the Art

In the design of high-gain and high-power TWT amplifiers, stability is critical. Reflections at discontinuities in the TWT often are a source of instability, and can be mitigated by optimizing the beam tunnel radius, SWS dimensions, and terminations at the input and output RF ports of the TWT. However, these considerations are not always sufficient to prevent oscillations in high-gain single-stage TWTs. A common strategy for ensuring stability when the gain is high is to design TWTs with multiple stages. Typically, these stages are electrically isolated by attenuators (the region separating the TWT stages) to eliminate regenerative oscillations caused by mismatches in the RF circuit [46, 354], as illustrated in Figure 9.1(a). The amplitude of the growing forward EM wave decays abruptly at the sever location and its power decreases to zero with minimal reflections while the velocity-modulated electrons are free to pass. The EM wave resumes growing after the sever, due to the interaction with the velocity-modulated electrons in the e-beam. The presence of the sever does not degrade TWT's performance significantly; instead, it helps to stabilize TWTs while keeping gain at a sufficiently high level.

Typically the gain of commercial TWTs is approximately 20 dB to 50 dB in most applications. However, a typical rule-of-thumb for TWT design is to have a gain of no more than 20 dB per stage to avoid oscillations and issues with nonlinear behavior [46, Chapter 12]. It is therefore necessary to divide the TWT into stages separated by severs in order to achieve a higher gain. The design of sever is often not straightforward, but a sever can still be designed inefficiently by brute-force parameter optimization in full-wave PIC simulations. To design and implement a sever in realistic TWTs, various methods have been developed. In [355], a MEMS compatible distributed loss type sever design was reported for a double vane staggered TWT amplifier. The same method was implemented in [356] for a W-band TWT using carburized porous beryllium oxide as an attenuator material, which has a high loss tangent. Alternatively, metamaterial absorbers have been proposed to absorb EM waves at the

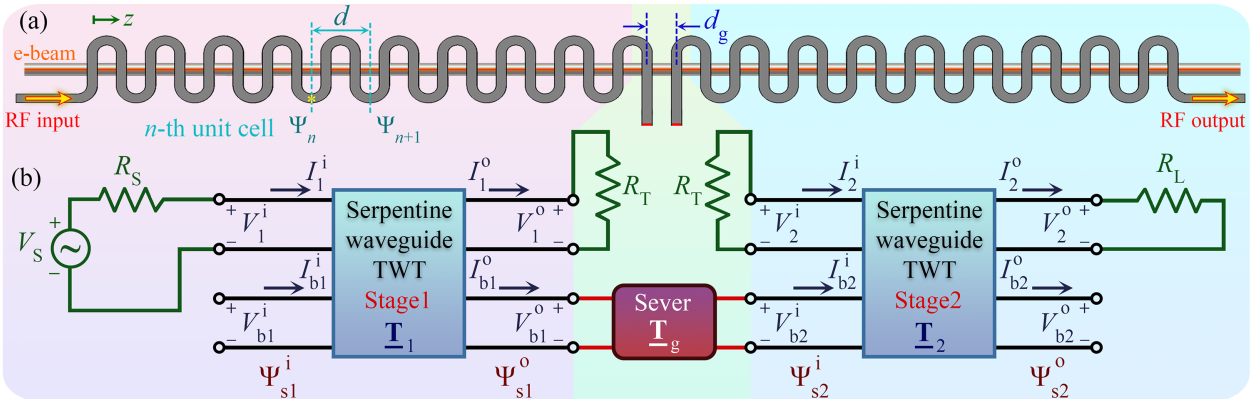

Figure 9.1: (a) Schematic of the multi-stage TWT and the interaction zone based on a SWSWS with RF input and output and an ideal sever embedded in the middle. (b) Circuit model used for gain calculation in the two-stage TWT.

sever terminations of TWTs [357, 358]. Most commonly, SWTWTs employ a wedge-shaped lossy dielectric (inside the straight rectangular waveguide or horseshoe-shaped waveguide) to absorb the wave by gradually filling the waveguide with a lossy dielectric along its length to minimize reflections [359, 360, 361, 362, 363].

In early works, Pierce analyzed TWTs with an ideal severed helix with a zero-length sever using 3-wave theory in [2, Section 9.6]. He also analyzed the actual severed helix with drift space using only two modes in the drift region in [2, Section 9.7]. In more recent studies, Chernin et al. considered a sever model in their developed 1D large-signal model of SWTWT [322], Yan et al. implemented a simple sever model in their constructed 3D large-signal model [326] and Zhang et al. developed the large-signal beam-wave interaction model using active matrix and used e-beam motion equation in the sever gap (drift region) [328].

In this chapter, we propose a simple and computationally efficient method for modeling multi-stage TWTs. The described model is an extension of the Pierce theory in [285, 2, 286] that considers the dispersive characteristics of a SWSWS and the space charge effect. The original Pierce model was developed for helix TWT with continuous beam–EM wave interaction whereas our model is developed for folded waveguide TWT with discrete interaction at interaction gaps. As a result, unlike the original model where interaction impedance is

considered as used impedance, we use a small coupling coefficient to relate the characteristic impedance of the SWS to the interaction impedance, as in [353, 364]. The model also considers variations in the nonuniform electric field distribution in the interaction gap (E_z) over the beam cross section as explained in [353]. We highlight that the proposed model is easy to use due to its transfer matrix description and due to the way the TWT gain is evaluated under the boundary conditions illustrated in Figure 9.1. We briefly explain the primary model for SWTWT according to [353]; next, we present the proposed equivalent model for the sever by considering the length of the drift region and integrate it into the primary TWT model. A detailed analysis of the different examples is presented in subsequent sections, as well as a comparison of our model with PIC simulation results. We show that the calculated results (i.e., gain versus frequency and gain versus position) based on our theoretical model are in agreement with PIC simulations and reveal that: (i) the sever model by considering the variation of electric field distribution over the beam cross section shown in this chapter is accurate; (ii) the presented model is an effective tool for designing high-gain multi-stage TWTs with severs. The use of the model allows engineers to design practical multi-stage TWTs with high gain without dealing with high computation burden of PIC simulations. However, this chapter focuses on showing the performance of our developed model rather than proposing a design strategy for severs or specific high-gain TWT designs.

9.2 E-beam and EM Wave Interaction

We summarize the foundation of the model used in this chapter that has been detailed in [353]. It is based on the linearized and non-relativistic equations for the small-signal regime that describe the four modes that result from the interaction of the e-beam, assuming 1D electron flow along an SWS, and the EM waves in a TWT system, as originally presented by Pierce [285, 2, 286]. The e-beam has an average current I_0, and an average kinetic dc voltage

V_0, which is related to the average axial velocity of electrons in the beam u_0. The relation between the electron velocity and the kinetic voltage is $V_0 \approx u_0^2/(2\eta)$ in our model (valid for non-relativistic electron velocities), where $\eta = e/m = 1.758820 \times 10^{11}$ C/Kg is the charge-to-mass ratio of the electron with charge $-e$ and rest mass m. The EM wave supported by the SWS is represented using an equivalent voltage V and current I in an equivalent TL as defined in [353]. We define a state vector in the phasor domain at $z = (n-1)\,d$, as $\mathbf{\Psi}_n = [V_n, I_n, V_{\mathrm{b},n}, I_{\mathrm{b},n}]^{\mathrm{T}}$ (T indicates transpose operation), which describes the small signal in the interactive zone of the TWT where the EM waves and e-beam interact. The elements of the state vector are defined in each unit cell at the location indicated by the yellow asterisk in Figure 9.1(a). The quantities V_n and I_n are the TL equivalent voltage and current, whereas $V_{\mathrm{b},n}$ and $I_{\mathrm{b},n}$ are the equivalent kinetic voltage and the current of the modulated e-beam, respectively. All quantities are assumed to be monochromatic and defined in [353]. The longitudinal propagation of the state vector across a unit cell is described by $\mathbf{\Psi}_{n+1} = \underline{\mathbf{T}}_{\mathrm{UC}}\mathbf{\Psi}_n$, where $\mathbf{\Psi}_n$ and $\mathbf{\Psi}_{n+1}$ are the state vectors at the input and output of the n-th unit cell ($n = 1, \ldots, N$), $\underline{\mathbf{T}}_{\mathrm{UC}} = \exp(-j\underline{\mathbf{M}}d)$ is the unit cell transfer matrix, d is the unit cell period, and $\underline{\mathbf{M}}$ is the TWT system matrix. According to the model we presented in [75] for the helix TWTs and then developed in [353] for the SWTWTs, the TWT system matrix is given by

$$\underline{\mathbf{M}} = \begin{bmatrix} 0 & \beta_{\mathrm{c}} Z_{\mathrm{c}} & 0 & 0 \\ \beta_{\mathrm{c}}/Z_{\mathrm{c}} & 0 & -ag & -a\beta_0 \\ 0 & a\beta_{\mathrm{c}} Z_{\mathrm{c}} & \beta_0 & \zeta_{\mathrm{sc}} \\ 0 & 0 & g & \beta_0 \end{bmatrix}. \tag{9.1}$$

Here, β_c is the phase propagation constant of the EM mode in the cold SWS, Z_c is the frequency-dependent characteristic impedance of the SWS, $g = I_0\beta_0/(2V_0)$, and $\beta_0 = \omega/u_0$ is the phase constant of the space-charge wave (when neglecting plasma frequency effects) [353]. Also, ζ_{sc} is a space-charge parameter accounting of the debunching of beam's charges and is given by $\zeta_{sc} = R_{sc}/(A\varepsilon_0\omega) = \left(2V_0\omega_q^2\right)/(\omega I_0 u_0)$, where A is the e-beam cross sectional area, ε_0 is vacuum permittivity, $\omega_q = R_{sc}\omega_p$ is the reduced plasma angular frequency, $\omega_p = \sqrt{I_0 u_0/(2V_0 A\varepsilon_0)}$ is the plasma frequency, and R_{sc} is the plasma frequency reduction factor [304, 297]. The term a is the frequency-dependent coupling strength coefficient which shows the strength of the interaction between the e-beam and the EM wave, and it found by the ratio of the effective interaction (Pierce) impedance and characteristic impedance, $a = \sqrt{Z_{P,e}/Z_c}$ [353]. Here, $Z_{P,e} = (1+\delta_e)^2 Z_P$ is the *effective* interaction impedance calculated by adding the constant correction factor δ_e which is considered to account for the nonuniform transverse distribution of the electric field over the cross section of the e-beam and Z_P is the interaction impedance calculated at the center of the beam tunnel, as explained in [353]. For simplicity, in this chapter we assume a constant value for the correction factor δ_e evaluated at the synchronization frequency; more information regarding this assumption is in Section 9.3.

9.3 Constant Correction Factor

In most practical applications, accurate prediction of gain near the synchronization frequency is critical. Furthermore, we assume a 1D e-beam for simplicity, which is a reasonable assumption. Figure (9.2) shows the z-component of the modal electric field at $z = 0$ mm, and $y = 0$, of the cold SWS. It demonstrates that the electric-field distribution is similar but not the same at three different frequencies. To increase our prediction accuracy at *non-synchronization* frequencies, we could consider a frequency-dependent correction factor δ_e,

that however would make our model more complicated. In this chapter we hence assumed a frequency-independent correction factor δ_{e} because it provides already a good degree of accuracy, especially at the synchronization frequency at which the correction factor was evaluated.

9.4 Multi-Stage Amplifier With Ideal Sever

Severs consist of lossy materials that gradually dissipate RF power over their length, but we will demonstrate that realistic terminations for severs in the SWTWT (with lossy dielectric wedges or other means) are often not required for accurate PIC simulations, provided that they can attenuate reflected waves to very small levels. The structure of the ideal sever in two-stage TWTs, embedded between the two stages of the SWTWT, is shown in Figure 9.1(a). The ideal sever is modeled in the following way: (i) first, the bending waveguide is removed at the sever position, and the two straight waveguides are lengthened outward, (ii) then the matched boundary condition is applied to the end of straight waveguides so that both forward and backward EM waves are perfectly absorbed with no reflections [365, 366, 317].

We propose a circuit model for calculating the gain of the SWTWT that is divided into two stages as shown in Figure 9.1(b), where $N_i d$ is the i-th stage length ($i = 1, 2$ for the bunching and amplification stages, respectively), with N_i the number of unit cells in the i-th stage, and d_{g} is the sever gap length (i.e., drift length) where only space-charge waves can propagate. We use the input and output state vectors of the two stages as below

$$\boldsymbol{\Psi}_{\mathrm{s1}}^{\mathrm{i/o}} = \begin{bmatrix} V_1^{\mathrm{i/o}} \\ I_1^{\mathrm{i/o}} \\ V_{\mathrm{b1}}^{\mathrm{i/o}} \\ I_{\mathrm{b1}}^{\mathrm{i/o}} \end{bmatrix}, \; \boldsymbol{\Psi}_{\mathrm{s2}}^{\mathrm{i/o}} = \begin{bmatrix} V_2^{\mathrm{i/o}} \\ I_2^{\mathrm{i/o}} \\ V_{\mathrm{b2}}^{\mathrm{i/o}} \\ I_{\mathrm{b2}}^{\mathrm{i/o}} \end{bmatrix}. \tag{9.2}$$

Here, $\boldsymbol{\Psi}_{\mathrm{s1}}^{\mathrm{i}}$is the state vector at the input of stage 1, calculated at $z = 0$, $\boldsymbol{\Psi}_{\mathrm{s1}}^{\mathrm{o}}$ is the output state vector of stage 1 calculated at $z = N_1 d$, $\boldsymbol{\Psi}_{\mathrm{s2}}^{\mathrm{i}}$ is the input state vector of stage 2 calculated at $z = N_1 d + d_{\mathrm{g}}$, $\boldsymbol{\Psi}_{\mathrm{s2}}^{\mathrm{o}}$ is the output state vector of stage 2 calculated at $z = N_1 d + d_{\mathrm{g}} + N_2 d$, i.e., at the end of the SWTWT. Each homogeneous TWT stage is modeled by the transfer matrix $\underline{\mathbf{T}}_i = \exp\left(-j\underline{\mathbf{M}}_i N_i d\right)$, where $\underline{\mathbf{M}}_i$ is the TWT system matrix for the corresponding stage that is shown in Equation (9.1). Therefore, in reference to Figure 9.1(b), one has

$$\boldsymbol{\Psi}_{\mathrm{s1}}^{\mathrm{o}} = \underline{\mathbf{T}}_1 \boldsymbol{\Psi}_{\mathrm{s1}}^{\mathrm{i}}, \; \boldsymbol{\Psi}_{\mathrm{s2}}^{\mathrm{o}} = \underline{\mathbf{T}}_2 \boldsymbol{\Psi}_{\mathrm{s2}}^{\mathrm{i}}. \tag{9.3}$$

The following equations describe the boundary conditions at the input (cathode end) and output (collector end) ports of the TWTs

$$V_{\mathrm{b1}}^{\mathrm{i}} = 0, \; I_{\mathrm{b1}}^{\mathrm{i}} = 0, \tag{9.4a}$$

$$V_1^{\mathrm{i}} + I_1^{\mathrm{i}} R_{\mathrm{S}} = V_{\mathrm{S}}, \; V_2^{\mathrm{o}} - I_2^{\mathrm{o}} R_{\mathrm{L}} = 0. \tag{9.4b}$$

In the boundary condition equations, the source resistance R_{S} and load resistance R_{L} are assumed to be equal to the frequency-dependent characteristic impedance of the SW for

TE10 Z_c and V_S is the generator voltage source. The sever effect is taken into account by the equations

$$V_1^o = R_T I_1^o,\ V_2^i = -R_T I_2^i, \tag{9.5a}$$

$$\begin{bmatrix} V_{b2}^i \\ I_{b2}^i \end{bmatrix} = \underline{\mathbf{T}}_g \begin{bmatrix} V_{b1}^o \\ I_{b1}^o \end{bmatrix}, \tag{9.5b}$$

where the matched termination load R_T is equal to the frequency-dependent characteristic impedance of the SW for TE10 Z_c. Furthermore, $\underline{\mathbf{T}}_g = \exp\left(-j\underline{\mathbf{M}}_g d_g\right)$ is the 2×2 transfer matrix for modeling the e-beam's equivalent ac voltage and current through the drift region in the sever gap, where $\underline{\mathbf{M}}_g$ is the gap matrix derived from the e-beam equations without coupling with the guided EM field (i.e., $a = 0$),

$$\underline{\mathbf{M}}_g = \begin{bmatrix} \beta_0 & \zeta_{sc} \\ g & \beta_0 \end{bmatrix}. \tag{9.6}$$

Finally, we solve the equations, at each frequency of interest, and calculate the output current and voltage of the second stage in the circuit model (I_2^o and V_2^o). We calculate the output RF power $P_{out} = |V_2^o|^2 / (2R_L)$, and the available input RF power $P_{av} = |V_S|^2 / (8R_S)$, to obtain the frequency-dependent transducer power gain, $G = P_{out}/P_{av}$, of the two-stage SWTWT. Note that when the input and output load impedances are not matched to the characteristic impedance of the SWS, the resulting gain ripple is cached by the generalized Pierce model, as demonstrated in [364] for a helix-based TWT. A detailed explanation of how the gain is computed is provided in Section 9.5.

9.5 Two-Stage Gain Calculation

The vector that contains the voltage and current values at the input and output of the first stage is found by solving the equation $\underline{\mathbf{A}}_1\mathbf{X}_1 = \mathbf{B}_1$, where the vectors and matrices are given by

$$\underline{\mathbf{A}}_1 = \begin{bmatrix} [-\underline{\mathbf{T}}_1] & [\underline{\mathbf{I}}_{4\times4}] \\ [\underline{\mathbf{0}}_{2\times2}] \quad [\underline{\mathbf{I}}_{2\times2}] & [\underline{\mathbf{0}}_{2\times2}] \quad [\underline{\mathbf{0}}_{2\times2}] \\ [\underline{\mathbf{C}}_{\mathrm{S}}] \quad [\underline{\mathbf{0}}_{2\times2}] & [\underline{\mathbf{C}}_{\mathrm{T1}}] \quad [\underline{\mathbf{0}}_{2\times2}] \end{bmatrix}, \tag{9.7a}$$

$$\underline{\mathbf{C}}_{\mathrm{S}} = \begin{bmatrix} 1 & R_{\mathrm{S}} \\ 0 & 0 \end{bmatrix}, \tag{9.7b}$$

$$\underline{\mathbf{C}}_{\mathrm{T1}} = \begin{bmatrix} 0 & 0 \\ 1 & -R_{\mathrm{T}} \end{bmatrix}, \tag{9.7c}$$

$$\mathbf{X}_1 = \begin{bmatrix} \boldsymbol{\Psi}^{\mathrm{i}}_{\mathrm{s1}} \\ \boldsymbol{\Psi}^{\mathrm{o}}_{\mathrm{s1}} \end{bmatrix}, \tag{9.7d}$$

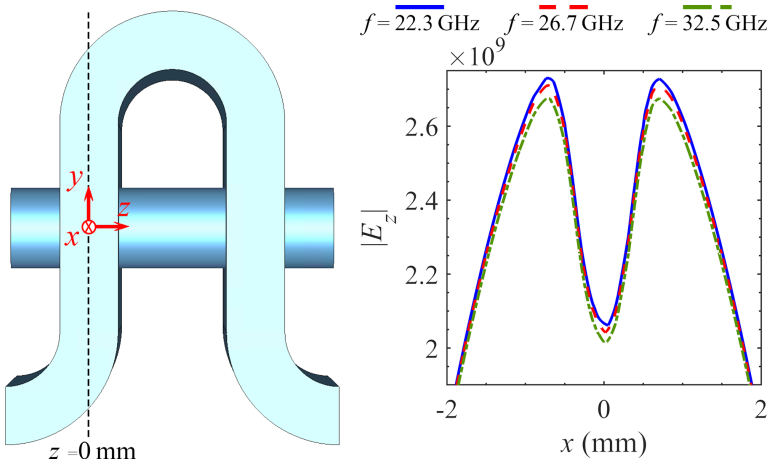

Figure 9.2: z-component of electric field at $z = 0$ mm cross-section and $y = 0$ curve of cold SWS for three different frequencies. It shows that field distribution is a function of frequency and δ_e vary by frequency.

$$\mathbf{B}_1 = [0, 0, 0, 0, 0, 0, V_S, 0]^T . \tag{9.7e}$$

Here, $\underline{\mathbf{I}}_{m\times m}$ is $m \times m$ identity matrix and $\underline{\mathbf{0}}_{m\times m}$ is $m \times m$ zero matrix. Then. the quantities V_{b2}^{i} and I_{b2}^{i} are found by multiplying the output ac beam voltage and current of the first stage (V_{b1}^{o} and I_{b1}^{o} obtained from vector $\mathbf{X}_1$) by the sever gap transfer matrix $\mathbf{\Psi}_{s2}^{i} = \underline{\mathbf{A}}_g \mathbf{\Psi}_{s1}^{o}$, where

$$\underline{\mathbf{A}}_g = \begin{bmatrix} [\underline{\mathbf{0}}_{2\times2}] & [\underline{\mathbf{0}}_{2\times2}] \\ \\ [\underline{\mathbf{0}}_{2\times2}] & [\underline{\mathbf{T}}_g] \end{bmatrix} . \tag{9.8}$$

We assume no TL voltage and current signals are transmitted from the output of the first stage to the input of the second stage (the EM waves in each stage are perfectly isolated from each other). Next, we solve another linear system to find the vector which contains the

input and output state vectors of the second stage, $\underline{\mathbf{A}}_2\mathbf{X}_2 = \mathbf{B}_2$, where

$$\underline{\mathbf{A}}_2 = \begin{bmatrix} & [-\underline{\mathbf{T}}_2] & & [\underline{\mathbf{I}}_{4\times4}] \\ [\underline{\mathbf{0}}_{2\times2}] & [\underline{\mathbf{I}}_{2\times2}] & [\underline{\mathbf{0}}_{2\times2}] & [\underline{\mathbf{0}}_{2\times2}] \\ [\underline{\mathbf{C}}_{\mathrm{T}2}] & [\underline{\mathbf{0}}_{2\times2}] & [\underline{\mathbf{C}}_{\mathrm{L}}] & [\underline{\mathbf{0}}_{2\times2}] \end{bmatrix}, \tag{9.9a}$$

$$\underline{\mathbf{C}}_{\mathrm{T}2} = \begin{bmatrix} 1 & R_{\mathrm{T}} \\ 0 & 0 \end{bmatrix}, \tag{9.9b}$$

$$\underline{\mathbf{C}}_{\mathrm{L}} = \begin{bmatrix} 0 & 0 \\ 1 & -R_{\mathrm{L}} \end{bmatrix}, \tag{9.9c}$$

$$\mathbf{X}_2 = \begin{bmatrix} \mathbf{\Psi}^{\mathrm{i}}_{\mathrm{s}2} \\ \mathbf{\Psi}^{\mathrm{o}}_{\mathrm{s}2} \end{bmatrix}, \tag{9.9d}$$

$$\mathbf{B}_2 = \left[0, 0, 0, 0, V^{\mathrm{i}}_{\mathrm{b}2}, I^{\mathrm{i}}_{\mathrm{b}2}, 0, 0\right]^{\mathrm{T}}. \tag{9.9e}$$

One can solve for $\mathbf{X}_2$ and calculate the output power by using V_2^o and I_2^{o}.

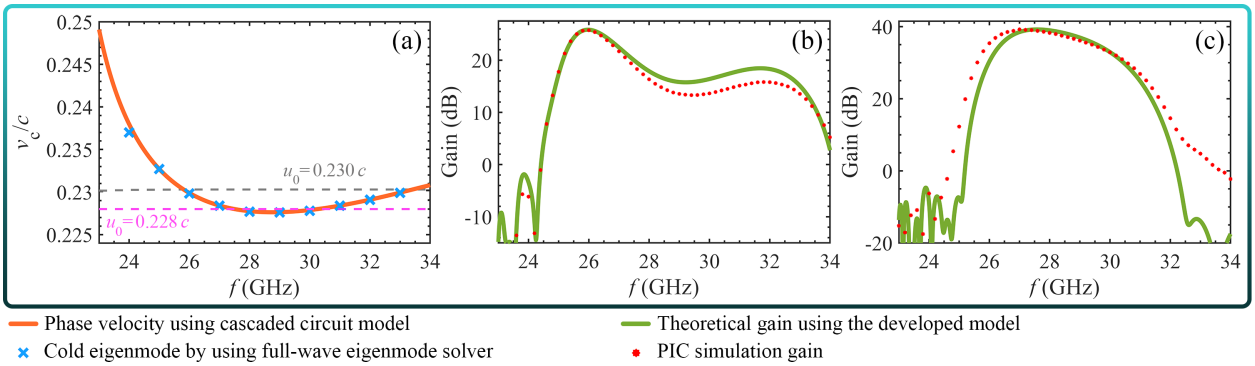

Figure 9.3: Results for the multi-stage SWTWTs. (a) Normalized phase velocity of the EM mode in the cold SWS, in the first spatial harmonic, with beam line (dashed gray for the two-stage, and dashed pink for the three-stage). The orange curve indicates the result obtained from the theoretical equivalent circuit model, while the blue crosses indicate the full-wave eigenmode solver result. Gain results: theoretical (solid green) and PIC simulation (red dots) TWT gains versus frequency for (b) two-stage and (c) three-stage TWTs, accounting for the presence of one or two ideal severs, respectively.

9.5.1 Examples of Ideal Sever for Two-Stage and Three-Stage TWTs

As a first example, we use the unit cell geometry and dimensions for the lossless SWSWS from [353]. The e-beam has a dc current of $I_0 = 10\,\text{mA}$ and radius of $r_\text{b} = 0.35\,\text{mm}$. The beam tunnel has a radius of $r_\text{c} = 0.5\,\text{mm}$ corresponds to filling factor of $(r_\text{b}/r_\text{c})^2 \simeq 0.5$. The normalized dc electron velocity is set to be $u_0/c = 0.230$, where c is the light speed. The selected phase velocity value corresponds to an average kinetic voltage of $V_0 = 13.52\,\text{kV}$ for the e-beam. Also, we use an RF input power of $P_\text{in} = 0\,\text{dBm}$ and a uniform on-axis magnetic field with an amplitude of $B = 0.4$ T to confine the e-beam. The on-axis magnetic flux density field used in PIC simulations to focus the beam is much larger than the Brillouin limit [290, Chapter 3][367, Chapter 7][354, Chapter 7][368, Chapter 1] that, for our specific example, is $B_\text{Br} = 0.022$ T (the Brillouin limit is the minimum magnetic field required to counter the space-charge expansion forces and confine the electron beam [308, Chapter 9]).

It is important that the sever be placed somewhere along the length of the TWT so that the

interaction between the e-beam and EM wave has begun to amplify a growing wave before reaching the sever; this can be verified by monitoring the growth of the state vector along the length of the TWT. However, the sever position should not be very distant from the electron emission location either as this could result in a considerable reduction in gain at the sever that cannot be compensated for in the remainder of the tube length (i.e., the wave cannot grow to a higher power with distance after the sever before being extracted at the output port). Furthermore, the amount of e-beam debunching that occurs in the drift region depends on the intensity of the beam bunching produced in the first stage and the dc current of the e-beam. As the stronger beam bunching forms before the sever, the more velocity spread occurs in the bunches, leading to reduced gain. Therefore, the bunching stage gain should be relatively small to achieve optimum performance. However, our objective is not to find the most efficient design approach for the sever or optimal TWT performance, but rather to show an effective and simple model for multi-stage TWTs. We assume the TWT has $N_{\text{total}} = N_1 + N_2 = 80$ unit cells with $N_1 = 30$ unit cells in the bunching stage (stage 1 in Figure 9.1(a)) and $N_2 = 50$ unit cells in the amplification stage (stage 2 in Figure 9.1(a)), isolated from each other by a sever with the drift length of $d_{\text{g}} = d/2$.

The phase velocity of the EM mode in the cold SWS calculated by using the theoretical equivalent circuit model (orange) from [353, Section III] and the CST eigenmode solver (blue crosses), in addition to the beam line (horizontal dashed gray), are illustrated in Figure 9.3(a). According to the intersection of the phase velocity of the EM mode in the cold SWS and beam line in Figure 9.3(a), we observe the beam-EM wave full synchronization at 25.73 GHz and 33.52 GHz, and the greatest amplification is expected to occur around these two frequencies where the beam and guided mode phase velocities intersect. The frequency-dependent interaction impedance Z_{P} and the *effective* interaction impedance $Z_{\text{P,e}} = (1 + \delta_{\text{e}})^2 Z_{\text{P}}$ for the first spatial harmonic in the SWS are calculated in [353, Section V] (see Figure 8(c) of [353]). The calculated values lead to the correction factor $\delta_{\text{e}} = 0.11$ to be used in the TWT model. Also, the frequency-dependent characteristic impedance Z_{c} is

evaluated using both the theoretical and full-wave eigenmode solver in [353, Sections III and IV] (see Figure 4(c) of [353]). Then, the frequency-dependent value of the coupling strength coefficient a to be used in Equation (9.1) is obtained as $a = \sqrt{Z_{\mathrm{P,e}}/Z_{\mathrm{c}}}$ (see Figure 8(d) of [353]).

Both the theoretical gain using our model and the PIC-simulated gain, are plotted versus frequency in Figure 9.3(b) by solid green curve and red dots, respectively. There is good agreement between the theoretical and PIC simulated gains, especially near the synchronization frequency, indicating that the sever model is accurate over the frequency range of interest. Also, we provide a comparison with the Pierce's 3-wave theory in Section 9.6. We use CST Particle Studio 2019 for the PIC simulation where for this example it uses approximately 6.5 million mesh cells and a steady state output is seen after a transient time of 9 ns elapses. The PIC simulation gain results (red dots) are obtained in the frequency range of 23 GHz to 34 GHz with a frequency step of 0.2 GHz. The maximum gains are obtained at the mentioned synchronization frequencies, as expected. As shown in Figure 9.3(b), the 3-dB bandwidth is 5.76% of the center frequency, covering the range from 25.31 GHz to 26.83 GHz. The maximum amplifier gain of 25.76 dB is obtained at 25.90 GHz. It should be noted that in this example, we were not concerned with implementing the most efficient TWT with the highest gain or bandwidth; instead, we wanted to evaluate the proposed theoretical model accounting for sever in a two-stage TWT.

Next, we analyze another example with three stages and two severs, with $N_1 = N_2 = 25$ unit cells in the first two stages and $N_3 = 65$ unit cells in the last stage to enhance the gain. In both severs, the drift length is $d_{\mathrm{g}} = d/2$. In a three-stage TWT, the placement of the severs also has a significant impact on the peak gain value and uniformity of gain over the operational frequency band. It should be noted that several other papers have used more than two stages in their structure, such as [361, 369]. We assume a dc beam current of $I_0 = 15\,\mathrm{mA}$, while the e-beam and tunnel radii are the same as in the previous example. The

normalized e-beam velocity is $u_0/c = 0.228$ (horizontal dashed pink line in Figure 9.3(a)) corresponding to an average kinetic voltage of $V_0 = 13.28\,\text{kV}$ and we assume the input RF power is $P_{\text{in}} = 0\,\text{dBm}$. Additionally, the magnetic field we use here is the same as in the two-stage example, which is much larger than the Brillouin limit B_{Br}. The PIC simulation gain results are obtained in the frequency range of 23 GHz to 34 GHz with a frequency step of 0.2 GHz. The calculated gain versus frequency for a three-stage SWTWT with more than 8.5 million mesh cells, after a transient time of 10 ns in PIC simulation, is shown in Figure 9.3(c). The maximum gain is approximately 40 dB at the synchronization frequency of 27.32 GHz. The good agreement between PIC simulation (red dots) and theoretical (solid green) gain results, particularly near the synchronization frequency, shows the reliability of the model for the three-stage TWT design. Additionally, the maximum gain value and flatness of the gain diagram can be controlled by selecting the proper e-beam current and voltage; however, this study is intended to showcase a tool for modeling multi-stage TWTs, rather than designing an amplifier with given specifications.

9.6 Comparison With Pierce 3-Wave Model

We compare our developed model with the Pierce 3-wave model for both single-stage and two-stage TWTs. The following derivation is based on the equations in [1, Section 8.5] and our original model [353]. The 4-wave dispersion equation shown in [353] is

$$\left(k^2 - \beta_{\text{c}}^2\right)\left[(k-\beta_0)^2 - \beta_{\text{q}}^2\right] = -gk^2\beta_{\text{c}}Z_{\text{P}}, \tag{9.10}$$

where $\beta_{\text{q}} = \omega_{\text{q}}/u_0 = (g\zeta_{\text{sc}})^{1/2}$ is the phase constant of the space-charge wave. It is a fourth-degree polynomial with four complex roots k_n $(n = 1, \ldots, 4)$ that are the four "hot" propagation wavenumbers as a function of frequency and other parameters of the system.

The total field in the TWT is a superposition of the four eigenwaves determined by these roots. Also, Pierce defined the dimensionless parameter C_{P} and called it the gain parameter [2, Chapter 2][1, Section 8.5.4],

$$C_{\mathrm{P}}^3 = \frac{I_0 Z_{\mathrm{P}}}{4V_0}. \tag{9.11}$$

By using Pierce gain parameter, we rewrite the dispersion equation as

$$\left(k^2 - \beta_{\mathrm{c}}^2\right)\left((k-\beta_0)^2 - \beta_{\mathrm{q}}^2\right) = -2C_{\mathrm{P}}^3 k^2 \beta_{\mathrm{c}} \beta_0. \tag{9.12}$$

Typically, one hot wave has negative $\mathrm{Re}(k)$, associated to the cold wavenumber of the backward wave $k \approx -\beta_{\mathrm{c}}$, and it does not affect the transfer of energy from the e-beam to the EM wave. Near synchronization, β_{c} is close to β_0, and the transfer of energy happens for k close β_{c}. Therefore, we approximate $k^2 - \beta_{\mathrm{c}}^2 \approx 2\beta_{\mathrm{c}}\,(k - \beta_{\mathrm{c}})$, and we obtain the 3-wave dispersion equation:

$$(k-\beta_{\mathrm{c}})\left((k-\beta_0)^2 - \beta_{\mathrm{q}}^2\right) = -C_{\mathrm{P}}^3 \beta_{\mathrm{c}}^2 \beta_0, \tag{9.13}$$

that is reduced to a third-degree equation. A reflected wave (i.e., the backward wave with negative $\mathrm{Re}(k)$) is in fact ignored in this approximation.

Further, we use the following dimensionless parameters introduced by Pierce [2][1, Section 8.5.5]. The parameter of nonsynchronism is expressed as

$$b = \frac{\beta_{\mathrm{c}} - \beta_0}{\beta_0 C_{\mathrm{P}}} = \frac{u_0 - v_{\mathrm{c}}}{v_{\mathrm{c}} C_{\mathrm{P}}}, \tag{9.14}$$

and the space-charge parameter Q is given by [2, Chapter 7][290, Chapter 10]

$$Q = \frac{\omega_{\mathrm{q}}^2}{4C_{\mathrm{P}}^3\omega^2}. \tag{9.15}$$

For simplicity in later calculations, we define parameter q as [1, Section 8.5.5]

$$q = 4QC_{\mathrm{P}} = \frac{\omega_{\mathrm{q}}^2}{\omega^2 C_{\mathrm{P}}^2} = \frac{R_{\mathrm{sc}}^2\omega_{\mathrm{p}}^2}{\omega^2 C_{\mathrm{P}}^2} = \frac{\beta_{\mathrm{q}}^2}{\beta_0^2 C_{\mathrm{P}}^2}. \tag{9.16}$$

Then, analogously to what was done in [2][290, Chapter 10][1, Section 8.5.5], we define the incremental propagation constant

$$\delta_n = -i\frac{k_n - \beta_0}{\beta_0 C_{\mathrm{P}}},\ n = 1, 2, 3. \tag{9.17}$$

Finally, by following the descriptions in [1, Section 8.5.5], a general solutions of the field, charge wave current, and charge velocity in the TWT based on the three hot eigenmodes are

$$E(z) = \sum_{k=1}^{3} A_k E_k(z),$$

$$i_{\mathrm{b}}(z) = \sum_{k=1}^{3} A_k i_{\mathrm{b},k}(z) = i\frac{I_0}{2V_0\beta_0 C_{\mathrm{P}}^2}\sum_{k=1}^{3}\frac{1}{\delta_k^2 + q}A_k E_k(z), \tag{9.18a}$$

$$u_{\mathrm{b}}(z) = \sum_{k=1}^{3} A_k u_{\mathrm{b},k}(z) = \frac{\eta}{u_0\beta_0 C_{\mathrm{P}}}\sum_{k=1}^{3}\frac{\delta_k}{\delta_k^2 + q}A_k E_k(z). \tag{9.18b}$$

Here, A_1, A_2, and A_3 are coefficients which are found from boundary conditions, and $E_k(z) = \mathscr{E}e^{-ik_k z} = \mathscr{E}e^{-i\beta_0 z}e^{\beta_0 C_{\mathrm{P}}\delta_k z}$ are the longitudinal electric field components of the three eigenmodes, all assumed to have a magnitude of $\mathscr{E} = 1\,\mathrm{V/m}$. Using the Cramer rule,

we find the following complex coefficients for the electric field [1, Section 8.5.5]

$$\begin{aligned} A_k = \tfrac{\delta_k^2+q}{(\delta_k-\delta_l)(\delta_k-\delta_m)} \{E\left(z=0\right) \\ +2\beta_0 C_{\mathrm{P}} V_0 \left[\tfrac{u_{\mathrm{b}}(z=0)}{u_0}\left(\delta_l+\delta_m\right) - iC_{\mathrm{P}}\tfrac{i_{\mathrm{b}}(z=0)}{I_0}\left(\delta_l\delta_m - q\right)\right]\Big\}, \end{aligned} \tag{9.19}$$

where $E\left(z=0\right)$ is the longitudinal component of the total electric field at the input of TWT. However, if the charge velocity and beam current modulation at the input are absent (i.e., $u_{\mathrm{b}}\left(z=0\right) = i_{\mathrm{b}}\left(z=0\right) = 0$), we have [1, Section 8.5.5]

$$A_k = \frac{\delta_k^2+q}{\left(\delta_k-\delta_l\right)\left(\delta_k-\delta_m\right)} E\left(z=0\right), \tag{9.20}$$

where l and m equal $1, 2, 3$ and $l \neq m \neq k$. The voltage gain is calculated by

$$G_{\mathrm{E}} = \frac{E\left(z=Nd\right)}{E\left(z=0\right)} = \frac{1}{E\left(z=0\right)} \sum_{k=1}^{3} A_k E_k\left(z=Nd\right) = e^{-i\beta_0 Nd} \sum_{k=1}^{3} \frac{\delta_k^2+q}{\left(\delta_k-\delta_l\right)\left(\delta_k-\delta_m\right)} e^{\delta_k \beta_0 C_{\mathrm{P}} Nd}, \tag{9.21}$$

where Nd is the stage length. Finally, the power gain is calculated by

$$G = 10\log\left|G_{\mathrm{E}}\right|^2 = 20\log\left|\sum_{k=1}^{3} \frac{\delta_k^2+q}{\left(\delta_k-\delta_l\right)\left(\delta_k-\delta_m\right)} e^{\delta_k \beta_0 C_{\mathrm{P}} Nd}\right| \mathrm{dB}. \tag{9.22}$$

Now, we consider a SWSWS with the geometry parameters already mentioned and compare two versions of the 3-wave model with our model and PIC simulations. The e-beam has $I_0 = 10$ mA and a radius $r_{\mathrm{b}} = 0.35$ mm. For the e-beam, the normalized phase velocity is set to be $u_0/c = 0.230$, which corresponds to an average kinetic voltage of $V_0 = 14.077$kV. Additionally, a uniform longitudinal magnetic field of 0.8 T was applied to confine the

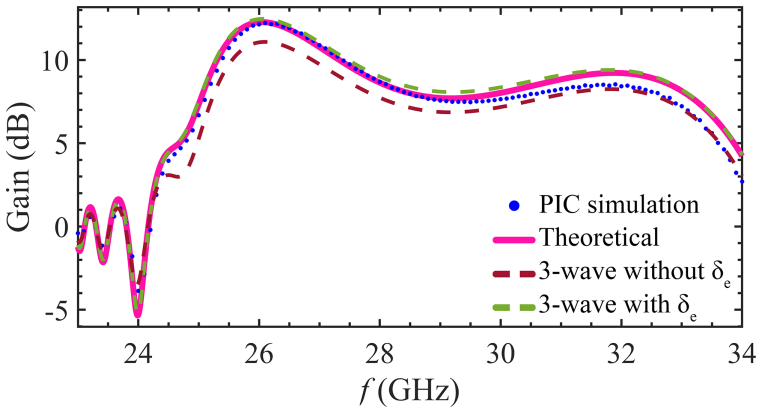

Figure 9.4: Gain versus frequency for a single-stage TWT predicted by our theoretical model (solid pink), compared with 3D PIC simulations (dotted blue). Also, this plot shows the results using the Pierce 3-wave model with (dashed green) and without (dashed dark red) correction factor δ_{e}.

e-beam. The numerical gain versus frequency diagram is theoretically calculated for the single-stage SWTWT with $N = 40$ unit cells ($Nd = 160$ mm in length) and input power of $P_{\mathrm{in}} = 0$dBm. The gain using the theoretical (our model) and PIC simulations is illustrated in Figure 9.4 by solid pink and dashed blue curves, respectively. Also, the gain results using the described Pierce 3-wave model with (dashed green) and without (dashed dark red) correction factor δ_{e} (described in this chapter and in [353]) are shown in the same plot. We use the coefficients given in Equation (9.20) to calculate the solutions. The calculated results show good agreement between our developed model and the 3-wave model *when* considering the correction factor δ_{e}. This plot clearly shows the importance of our proposed correction factor which is considered to account for the nonuniform transverse distribution of the electric field over the e-beam cross section.

In the next step, we provide a comparison for the *two-stage TWT* shown in Section 9.4. To calculate the output results, we must obtain the required e-beam parameters before the server gap (i.e., $u_{\mathrm{b}}(z = N_1 d)$ and $i_{\mathrm{b}}(z = N_1 d)$), as we did for the single stage examples. Then, using Equation (9.19), we substitute such e-beam parameters (obtained at the end of the first stage) as initial values for the modulated e-beam at the beginning of the second stage. Also, at the beginning of the second stage, in the 3-wave model the longitudinal

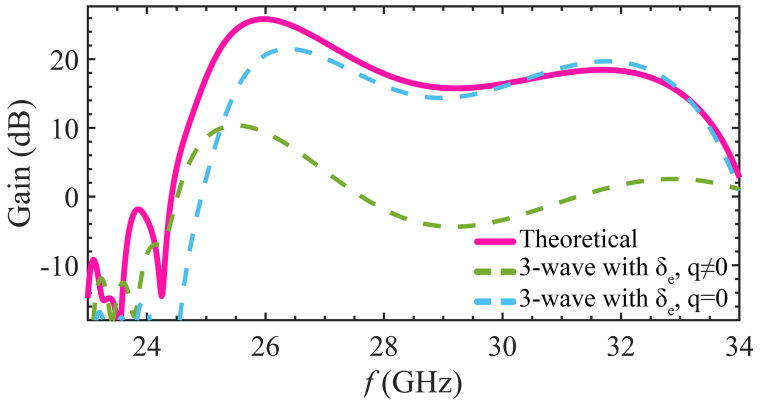

Figure 9.5: Gain versus frequency for the two-stage TWT with ideal sever predicted by our theoretical model (solid pink), compared to the results using Pierce 3-wave model with correction factor δ_e, with space-charge effect [1, Chapter 8] (dashed green) and without space-charge effect [2, Chapter 9] (dashed blue).

component of the electric field is set to zero in Equation (9.19), due to the termination caused by the sever [2, Chapter 9]. The theoretical gain versus frequency using our model is illustrated in Figure 9.5 in solid pink. Then, we calculate the gain versus frequency by using the described Pierce 3-wave model with correction factor δ_e. The results are shown in dashed green when we consider the space-charge effect as in the earlier formulas, following [1, Chapter 8]. The result is not in good agreement with our model (which is in agreement with PIC simulations, see Figure 9.3(b)). We also calculated the gain results using the 3-wave theory *without* considering the space-charge effect, i.e. $q = 0$, as was done in the original Pierce model [2, Chapter 9]. The calculated result is shown in dashed blue in Figure 9.5. Interestingly, in the case of the two-stage TWT, the results of Pierce's three-wave theory agree better with our model when the space charge parameter is neglected.

9.7 Two-Stage TWT With Realistic Sever Using Wedge-Shaped Absorbers

In order to demonstrate the effectiveness of the proposed model, a third example is provided here with a two-stage TWT. The differences with respect to the previous case are that the second stage is longer and the beam current is higher than in the previous case, and the sever is made of a long waveguide with a wedge-shaped absorber. In previous research such as [370], a design strategy for a wedge-shaped absorber in multi-stage SWTWTs with a three-dimensional structure was shown. Here, we implement a realistic design based on a wedge-shaped lossy dielectric embedded in a rectangular waveguide, integrated into SWTWT stages as depicted in Figure 9.6(a), to achieve small-signal gain exceeding 35 dB. After the last unit cell of the SWS in the first stage, a smooth E-plane bend in the opposite direction guides the signal into the wedge-shaped lossy material of the sever. The same bend configuration is used in the first unit cell of the second stage. The number of periods in the first and second stages are $N_1 = 30$ and $N_2 = 70$, respectively, and the drift length is $d_\mathrm{g} = d/2$.

The values of the geometrical parameters of the sever shown in Figure 9.6(a) are optimized to obtain an input reflection coefficient below -10 dB over the desired operating band, leading to $L_1 = 4.25$ mm, $L_2 = 5d = 20$ mm and $b_2 = 0.875$ mm. The attenuator length (L_2) should be long enough to attenuate incident and reflected RF waves to sufficiently low levels. Conversely, the drift length of sever (d_g) should also be as short as possible to minimize velocity spread in the electron bunches. For the attenuator, we use a material with relative permittivity of $\varepsilon_\mathrm{r} = 10.5$ and loss tangent of $\tan\delta = 0.2$ in PIC simulations [360]. The reflection coefficient of the wedge-shaped sever is shown in Figure 9.6(b), indicating good matching performance and high enough attenuation, below -10 dB, in the operating frequency range.

In this example, we assume a dc beam current of $I_0 = 15$ mA, while the e-beam and tunnel

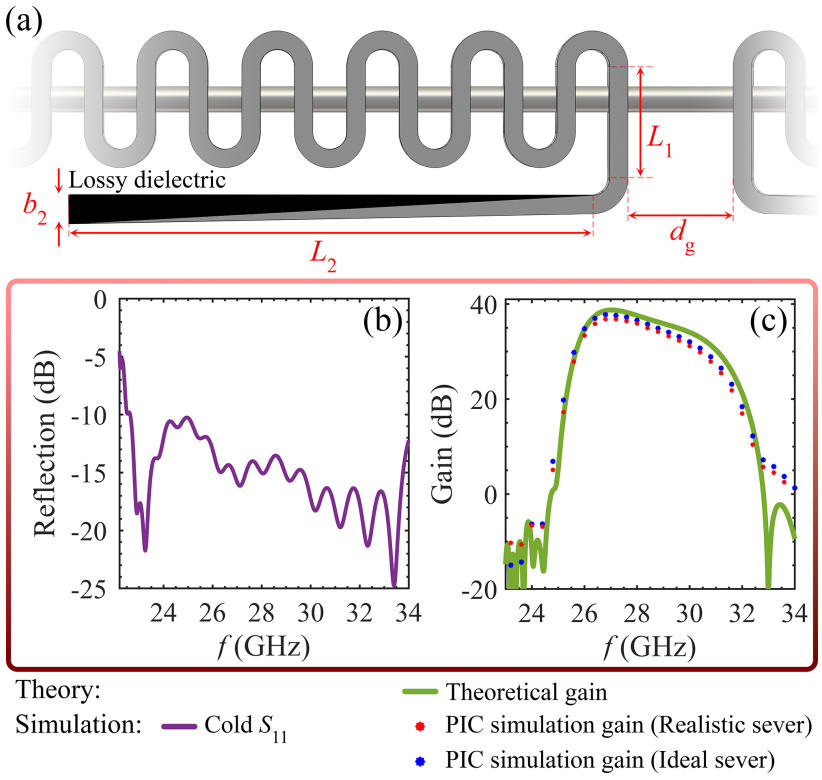

Figure 9.6: (a) Wedge-shaped sever with lossy dielectric and corresponding geometrical parameters. (b) Simulated reflection at the input of the first stage, for the wedge-shaped sever, over the frequency range from 22.5 GHz to 34 GHz. (c) Gain versus frequency for the two-stage TWT amplifier: theoretical calculation (solid green), PIC simulation using the ideal sever (blue dots), and PIC simulation using the realistic wedge-shaped sever (red dots).

radii are as in the previous examples. The normalized dc electron velocity is $u_0/c = 0.229$, which corresponds to an average kinetic voltage of $V_0 = 13.40$ kV. We assume the input RF power is $P_{\text{in}} = 0$ dBm and the magnetic flux density is $B = 0.4$ T. The calculated gain for a two-stage SWTWT with wedge-shaped sever, using more than 27 million mesh cells in PIC simulations, is displayed in Figure 9.6(c) by the red dots and achieves a maximum gain of more than 37 dB at 27 GHz. We employ CST Particle Studio for PIC simulations, and the gain is calculated in the frequency range of 23.2 GHz to 34 GHz with a frequency step of 0.4 GHz. In addition, the blue dots represent the gain based on PIC simulations, but assuming an ideal sever. The theoretically calculated TWT gain based on the proposed method is illustrated by the solid green curve, in good agreement with the PIC simulation

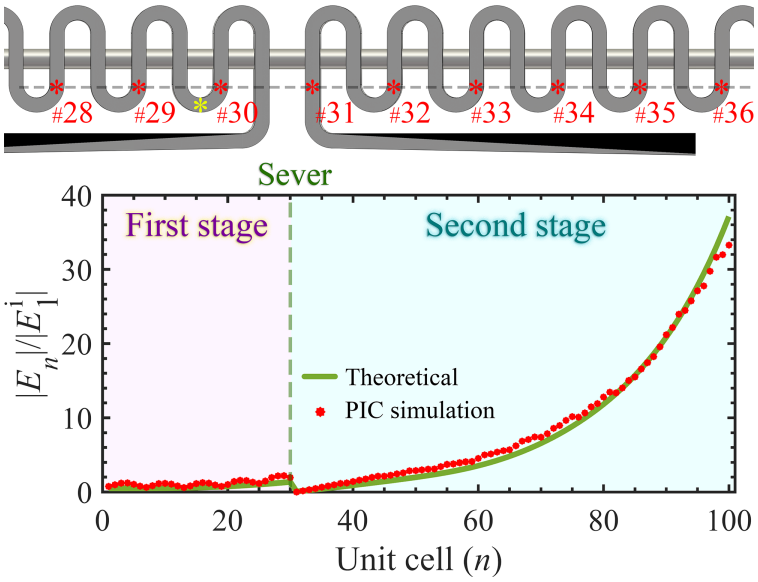

Figure 9.7: Amplification of RF wave during propagation in the SWTWT at $f = 28$ GHz along the two TWT stages. The plot shows the normalized electric field at each unit cell by using the theoretical model (solid green) and PIC simulation (red dots), in good agreement.

results. Therefore, the theoretical model is accurate for this multi-stage design with bigger length and higher gain than in the two-stage example provided in the previous section, also when compared against the case with a realistic sever with a wedge-shaped absorber.

Next, we compute the RF wave's growth as it propagates through the length of the TWT and interacts with the e-beam. The electric field at $f = 28$ GHz is monitored along the gray dashed line in the schematic of the SWTWT depicted in Figure 9.7. We added the electric field monitor to the CST PIC simulation at $f = 28$ GHz . Then we normalized the calculated z-component of the electric field to the one obtained at the input of the first unit cell. In Figure 9.7, red dots represent the normalized electric field magnitude $|E_n| / \left|E_1^{\mathrm{i}}\right|$ from the full-wave PIC simulation. As an alternative, in a much faster way, we also calculate the equivalent TL voltage along the TWT by using our theoretical model to track the evolution of the state vector as it propagates through each unit cell. We normalize the calculated voltage at the beginning of each unit cell by the amplitude of the voltage at the input of the first unit cell, $|V_n| / \left|V_1^{\mathrm{i}}\right|$. The calculated theoretical result is represented by a solid green curve in Figure 9.7. As explained in [353, Section III], the normalized values of the electric

field in the SWS and voltage in the equivalent TL can be compared due to the direct relation between the electric field and equivalent TL voltage ($|E_n| / \left|E_1^{\mathrm{i}}\right| = |V_n| / \left|V_1^{\mathrm{i}}\right|$). However, the calculated voltages are obtained at the center of the bottom bends, related to the beginning of the unit cell, while the PIC-simulated electric field is calculated at the end of the same quarter bends (for instance, see yellow and red asterisk points in the 30-th unit cell), without compromising the observed trends. According to Figure 9.7, the RF wave amplifies in the first stage, but drops abruptly at the sever. Then, we observe strong exponential growth in the second stage due to synchronization with the modulated e-beam. The results shown in Figure 9.7, which compare the theoretical model with the PIC simulation, demonstrate the high accuracy of our developed theoretical model. We stress that a result like this is obtained in a very fast way using our proposed model in contrast to PIC simulations with a high computational burden.

9.8 Conclusions

We have developed a model for analyzing the small-signal gain of multi-stage SWTWTs with the incorporation of one or more severs as attenuating elements. A sever is used to cut off the RF path between the input and output RF ports of the SWS to effectively attenuate the EM waves in both directions to mitigate the possibility of unwanted oscillations. We have demonstrated that the proposed sever model is accurate and simple to use for predicting the performance of multi-stage TWTs, thereby eliminating the computational burden associated with PIC simulations. The results obtained from our theoretical model align closely with PIC simulation results, confirming its accuracy. It provides engineers with a valuable tool for developing high-gain multi-stage TWTs efficiently.

Acknowledgments

- I would like to thank Robert Marosi and Tarek Mealy for collaboration on this chapter.
- This material is based upon work supported by the Air Force Office of Scientific Research (AFOSR) Multidisciplinary Research Program of the University Research Initiative (MURI) administered through The University of New Mexico under Grant FA9550-20-1-0409.
- The results of this chapter have been published in the conference paper of [371].

Chapter 10

Super-Exponential Amplification of Wavepacket Propagation in Traveling Wave Tubes

We analyze wavepacket propagation in TWTs analytically and numerically. TWT design in a nutshell comprises a pencil-like electron beam in vacuum interacting with an electromagnetic wave guided by a SWS. In our study, the electron beam is represented by one-dimensional electron flow and the SWS is represented by a transmission line. The analytical considerations are based on the Lagrangian field theory for TWTs. Mathematical analysis of wavepacket propagation in one-dimensional space is based on the relevant Euler-Lagrange equations which are second-order differential equations in time and space. Wavepacket propagation analysis is not simple and we develop a numerically efficient algorithm to do that. In particular, if the initial pulse has a Gaussian shape at the input port, it acquires non-Gaussian features as it propagates through the TWT. These features include: (i) super-exponential (faster than exponential) amplification, (ii) shift of the pulse frequency spectrum toward higher frequencies and (iii) change in the shape of the pulse that becomes

particularly pronounced when the pulse frequency band contains a transitional point from stability to instability.

10.1 Background, Motivation, and State of the Art

TWTs are devices widely used for telecommunications, radar, and high-resolution imaging [372, 373, 60, 47]. These devices utilize the kinetic energy of a flow of electrons in vacuum to amplify RF signals [1, 51]. J. R. Pierce introduced a simple and effective model that accounts for (i) transfer of energy from an electron beam to an electromagnetic wave, and (ii) signal amplification as it propagates through a TWT [285, 374, 375, 286]. The Pierce model was extensively studied and extended by many authors [376, 377, 378, 292]. Also, in [293, 291], the analytical Lagrangian field theory for TWT was constructed to generalize the original Pierce model. In this model, a multi-transmission line can be coupled to the multi-stream electron beam. Moreover, the original Pierce theory without considering the space charge effect [285] can be viewed as a high-frequency approximation of the Lagrangian field theory [291, Chapter 29]; however, when considering the space charge effect as in [375], Pierce theory leads to the same results of the Lagrangian field theory, as demonstrated in the Appendix of [75].

The subject of pulse amplification is an important topic in numerous applications such as wideband RF communications, impulse radar, remote sensing, imaging, spectroscopy, and time domain characterization of devices. In particular, TWTs were used for generating nanosecond carrier pulses in [379, 380, 381] which can be used for radar applications. Also, in [382], the authors show that pulse radars have greater spectral efficiency than conventional narrow-band radars. In [383], a technique for the simulation of wideband pulses excited in a regular dispersive delay line by an electron beam is proposed. Chernin et al. developed a three-dimensional multi-frequency large signal model of the beam-electromagnetic wave in-

teraction in a helix TWT, in which both forward and backward synchronous space harmonics are included [384]. Also, Converse et al., proposed a new one-dimensional time domain model to be used in the analysis of the pulse response of the helix TWT [385, 386]. That model incorporates waveguide dispersion, and a nonlinear time-domain method was employed to examine the response of a wideband helix TWT to an input Gaussian pulse. Subsequently, Setayesh and Abrishamian developed a variation of the Converse et al. model [299, 387], extending their pseudo-spectral method to an arbitrary order of accuracy in time and space derivatives. Recently, Aliane et al. analyzed short-pulse amplification in TWTs using the Hamiltonian discrete model [388]. Aside from technological uses, short pulses can be used for probing the TWT dispersion relation and gain.

In this chapter, we study pulse propagation and amplification in TWTs and develop a numerically efficient algorithm to analyze pulse propagation and detect its nontrivial features. In a nutshell, we apply the Lagrangian field theory for TWTs developed in [293, 291] to analyze pulse propagation. We conduct our studies initially in the frequency domain and demonstrate the efficiency of our method through numerical simulations. According to the results, the propagating wave is amplified, and the frequency content of the wavepacket is shifted to higher frequencies when the wavepacket bandwidth is in the frequency range where the complex-valued wavenumber of the amplifying hot mode is more or less dispersionless. In addition to that, the number of local peaks in the wavepacket spectrum increases when the wavepacket moves away from the input port. An example of these two phenomena is illustrated in Figures 10.1(b)-(d). It will be demonstrated that as long as the operation frequency is in the dispersionless region, the computed results using our developed "exact method" and "approximate method" show good agreement (see Section 10.4). In the approximate method, we consider constant complex velocity for the "hot modes" , using it as a benchmark ("hot modes" or "TWT modes" are those modes that account for the interaction of the electromagnetic wave and the charge waves, and complex velocity refers to the complex-valued analytic continuation of the phase velocity of the hot mode $u = \omega/k$).

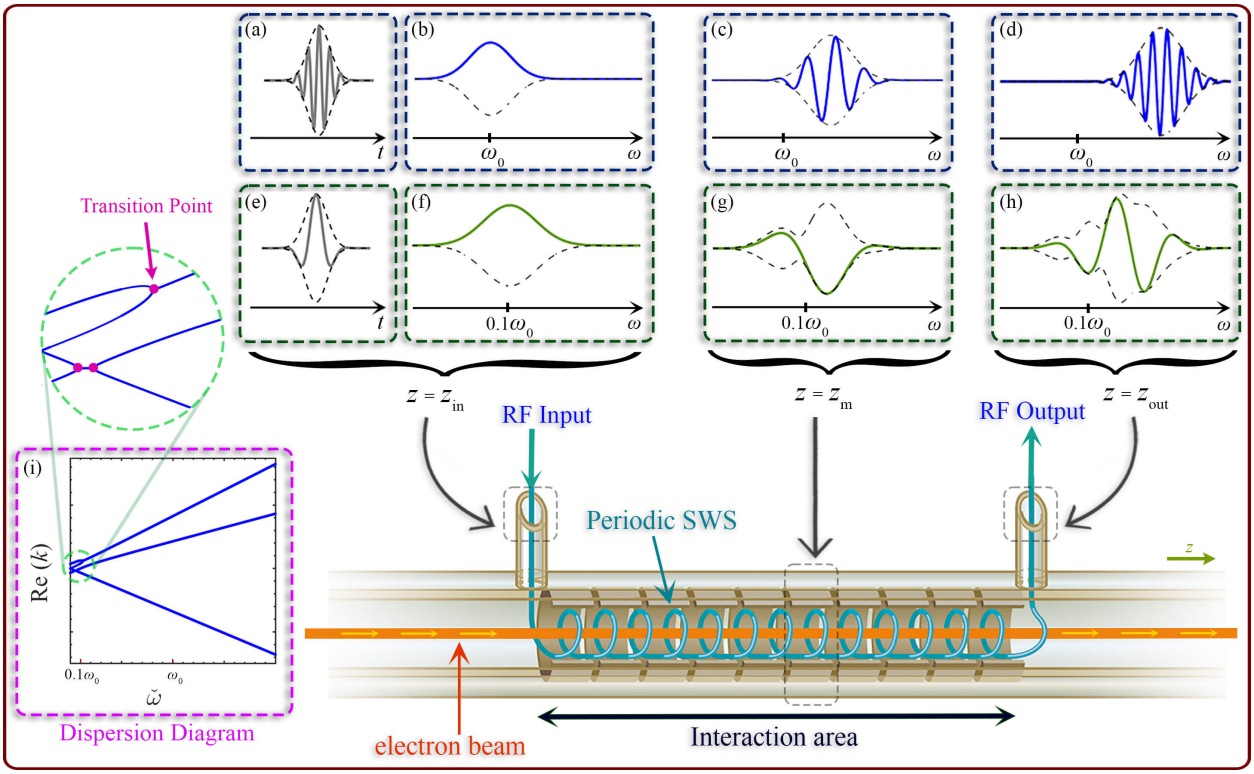

Figure 10.1: The plot illustrates wavepacket propagation in a TWT. The initial Gaussian pulse enters the RF input port on the left ($z = z_{\text{in}}$), and the amplified output pulse is extracted from the RF output port on the right ($z = z_{\text{out}}$). (a)-(d) show wavepacket propagation when its frequency band is in the constant hot mode complex velocity region (far from the point of transition between stability and instability). Instead, (e)-(h) show wavepacket propagation when its frequency band is close to or covers the transition point. (i) The real part of the complex-valued wavenumbers of the hot modes which pink dots in the magnified plot show the transition points. When the operating frequency is in the region where the complex velocity of the hot modes is more or less constant (i.e., the dispersionless region), we notice interesting phenomena during propagation in space such as (i) super-exponential amplification, (ii) shifts in the center frequency and (iii) an increase in the number of local peaks in the wavepacket spectrum within the wavepacket bandwidth. However, if the wavepacket frequency bandwidth contains a transition point, the wavepacket shape is significantly altered as it propagates.

The approximate method fails to provide credible results when the wavepacket frequency spectrum composition includes transition points. It happens due to an abrupt change in the complex velocity of the hot modes at transition points and the wavepacket shape and frequency content are altered during propagation as shown in Figures 10.1(f)-(h). Therefore, when the hot mode complex velocity is not constant with respect to frequency changes, like when the pulse bandwidth contains a transition point, the exact method we propose is the only alternative. Our developed method and numerical implementation provide insights into pulse propagation and amplification in TWTs that can be used to design TWTs that operate with pulses as an RF input signal.

This chapter is organized as follows. Section 10.2 highlights concisely the significant results and nontrivial phenomena during wavepacket propagation in TWTs. In Section 10.3, we briefly review the Lagrangian field theory used to analyze TWTs. Section 10.4 discusses the analytical method and relevant approximations of wavepacket propagation in TWTs. Then, in Section 10.5, we show the effectiveness of the developed analytical method and its approximation using several examples including a realistic TWT design. Finally, we conclude the chapter in Section 10.6.

10.2 Statement of the Main Results

We use an analytical model to study different aspects of wavepacket propagation in TWTs. We find that if the pulse frequency composition involves exponentially growing modes, the pulse shape and frequency content change significantly as it propagates through the TWT. Here, we briefly highlight our main results and achievements, leaving explanations, technical details and numerical examples for the following sections.

Our main statements regarding pulse propagation in a typical TWT can be summarized as

follows:

1. Detectable super-exponential amplification (see Remark 10.4.1) of the wavepacket as it propagates through the TWT (see Figures 10.1(b)-(d));

2. Noticeable shift of the pulse frequency band toward higher frequencies (see Figures 10.1(c) and (d));

3. Noticeable increase in the number of local peaks in the wavepacket spectrum in the pulse bandwidth as it propagates through the TWT (see Figures 10.1(c) and (d));

4. Significant distortion in the pulse shape occurs when the pulse frequency bandwidth contains the frequency of a transition point separating stability from instability (see Figures 10.1(f)-(h)).

The above-mentioned results are illustrated in Figure 10.1. In the first row, the center frequency of the input pulse is located far away from the transition frequency of the TWT dispersion diagram (see Figures 10.1(a) and (b)). The hot mode phase velocity is constant in this region, and the propagated wavepacket can also be calculated via the approximate method presented in [291, Chapter 16]. In this case, the wavepacket center frequency is shifted as the pulse propagates through the TWT (see Figures 10.1(c) and (d)). In addition, the number of local peaks in the wavepacket spectrum in the pulse bandwidth is gradually increased while the wavepacket travels toward the output port. Also, the wavepacket amplitude is amplified rapidly, representing the most significant feature of TWTs in the amplification regime. In the second row of Figure 10.1, the Gaussian pulse with the low center frequency enters the input port of the TWT (see Figures 10.1(e) and (f)). The center frequency of the input pulse is located near the transition point, i.e., the bifurcation point in the dispersion diagram. The complex-valued analytic continuation of the hot mode phase velocity near transition points is strongly dependent on frequency. So, every spectral

component of the pulse is amplified with a different amplitude and phase, leading to distortion in the propagated wavepacket. As a result, the extracted wavepacket shapes at the middle of TWT and at the output port do not resemble the original Gaussian pulse shape (see Figures 10.1(g) and (h)). Consequently, when the wavepacket frequency bandwidth contains the transition point frequency, we observe significant alterations in the wavepacket envelope. Detailed analysis of these nontrivial effects and phenomena requires more accurate investigation, which is available in Section 10.4 with different examples in Section 10.5.

10.3 Review of the Lagrangian Field Theory for TWT

We briefly review the analytical model used in this chapter for studying TWTs. As a pioneer in TWT modeling, Pierce developed a mathematical model [375]. This model can be considered the simplest one that accounts for electromagnetic wave amplification in the TWT [1, 51]. The Pierce model, also known as the 4-wave theory of a TWT, is a one-dimensional linear theory in which the slow wave structure (SWS) is represented by a transmission line assumed to be homogeneous [285, 375]. Also, the 3-wave small-signal theory, which laid the foundation for TWT design, can be viewed as an approximation of the 4-wave theory [375].

In this chapter, we use an analytical model based on the Lagrangian field framework developed in [293, 291]. The Lagrangian field theory also allows for modeling more complex SWSs than Pierce's simple one by involving more than one guided electromagnetic wave and the multi-stream beam [293, 291]. As shown in [75], the equivalent transmission line equations that one would get directly from generalizing the Pierce model agree with the analytical Lagrangian field theory.

10.3.1 Fundamental Equations

We assume the electron stream to be confined by an external static magnetic field to an infinitely long cylinder along the z direction [389]. The area of the cross-section σ_{B} of the electron stream is supposed to be small enough to ignore transverse variations in relevant physical quantities. The plasma frequency of the corresponding electron stream is given by [390, 391]

$$\omega_{\mathrm{p}}^2 = \frac{4\pi \mathring{n} \mathrm{e}^2}{m}, \tag{10.1}$$

where $\mathring{n}$ denotes electron density, $-\mathrm{e}$ is the electron charge, and m is the electron rest mass. The electron stream steady velocity is denoted by $\mathring{v}$, and another key parameter related to the electron stream is the stream intensity, which is defined as

$$\beta = \frac{\sigma_{\mathrm{B}}}{4\pi} R_{\mathrm{sc}}^2 \omega_{\mathrm{p}}^2, \tag{10.2}$$

where R_{sc} is the so-called plasma frequency reduction factor that accounts phenomenologically for the finite dimensions of the electron stream cylinder and geometric features of the SWS [304]. The physical dimension of the electron stream intensity is the square of velocity. A larger stream intensity value is associated with a larger value of electron density or a larger electron stream cross-sectional area. The electron stream steady velocity $\mathring{v}$, and electron stream intensity β, play a significant role in defining TWT properties, so we combine them into a set of electron stream significant parameters as in [291]. We use the stream charge to build up the electron stream interaction with the electromagnetic wave, defined as the time integral of the corresponding electron stream current $i\left(t, z\right)$, as $q\left(t, z\right) = \int_{t_0}^{t} i\left(t', z\right) \, \mathrm{d}t'$. The variable $q\left(t, z\right)$ represents the amount of charge that has traversed the electron stream cross-section, at point z, from the initial time of t_0 to time t. Electromagnetic propaga-

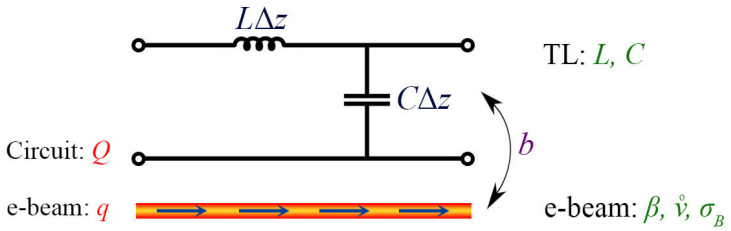

Figure 10.2: Equivalent transmission line representation of the SWS where the equivalent transmission line is represented conceptually as a circuit, with C and L being the per-unit-length capacitance and inductance, respectively, and b represents the coupling strength with the charge waves.

tion in the SWS is modeled as a single equivalent transmission line, which describes the electromagnetic modal propagation in the SWS, based on the equivalent transmission line model shown in Figure 10.2. Here, the distributed per-unit-length series inductance L and shunt capacitance C are used to describe the electromagnetic properties of the equivalent transmission line [392, 393, 394, 395]. In the well-known definition of equivalent transmission line characteristics, we use voltage $V(t,z)$ and current $I(t,z)$, alongside the charge definition $Q(t,z) = \int_{t_0}^{t} I(t',z)\ \mathrm{d}t'$. This value is a primary parameter for describing the equivalent transmission line, which indicates the amount of charge that has crossed the cross-section of the equivalent transmission line from the initial time of t_0 to time t. Note that $q(t,z)$ and $Q(t,z)$ are purely real in the Lagrangian equations. Also, cutoff conditions could be modeled by resonant series and shunt reactive elements in the transmission line equivalent circuit model [396, 397, 398]. However, for simplicity, in this chapter we assume we work not close to a waveguide cutoff frequency and hence we ignore this feature. Accordingly, using the transmission line formalism, the phase velocity of the electromagnetic wave is calculated as $w = 1/\sqrt{LC}$. The coupling strength between the electron stream and the electromagnetic guided wave in the SWS is represented by the parameter b (denoted by a in [292, 75, 353]). The term b describes how the electron stream couples to the electromagnetic wave where the representation of the coupling between an electron stream and electromagnetic wave guided by SWS goes back to Ramo [399]. The value of $b = 0$ indicates that the electron stream is not coupled to the guided electromagnetic wave.

Then, following [293, 291], we introduce the TWT system Lagrangian $\mathcal{L}_{\mathrm{TB}}$ as

$$\mathcal{L}_{\mathrm{TB}} = \mathcal{L}_{\mathrm{Tb}} + \mathcal{L}_{\mathrm{B}}, \tag{10.3}$$

where the Lagrangian components $\mathcal{L}_{\mathrm{Tb}}$ and $\mathcal{L}_{\mathrm{B}}$ are associated with the electromagnetic wave and the electron stream respectively and are defined as follows [293, 291]

$$\mathcal{L}_{\mathrm{Tb}} = \frac{L}{2}\left(\partial_t Q\right)^2 - \frac{1}{2C}\left(\partial_z Q + b\partial_z q\right)^2, \tag{10.4}$$

$$\mathcal{L}_{\mathrm{B}} = \frac{1}{2\beta}\left(\partial_t q + \mathring{v}\partial_z q\right)^2 - \frac{2\pi}{\sigma_{\mathrm{B}}} q^2. \tag{10.5}$$

The symbols ∂_t and ∂_z represent the partial derivative with respect to time t and space z, respectively. Also, the space-charge debunching effects are considered by the term $2\pi q^2/\sigma_{\mathrm{B}}$ in the above equation. For the TWT system, we find the following Euler-Lagrange equations associated with the Lagrangian [293, 291]

$$L\partial_t^2 Q - \partial_z\left[C^{-1}\left(\partial_z Q + b\partial_z q\right)\right] = 0, \tag{10.6}$$

$$\frac{1}{\beta}\left(\partial_t + \mathring{v}\partial_z\right)^2 q + \frac{4\pi}{\sigma_{\mathrm{B}}} q - b\partial_z\left[C^{-1}\left(\partial_z Q + b\partial_z q\right)\right] = 0. \tag{10.7}$$

In the following, we look at the spectrum content of Q and q, and we use the standard complex-signal notation by assuming that all the quantities are proportional to $\exp\left(\mathrm{i}\omega t\right)$; therefore; the time derivative leads to multiplying by $\mathrm{i}\omega$ for every spectrum component. We

introduce the TWT principal parameter γ, which is assumed to be frequency-independent

$$\gamma = \frac{b^2}{C}\beta. \tag{10.8}$$

According to this definition, we have a larger value for the TWT principal parameter γ when a higher coupling strength coefficient b or a stream intensity β (i.e., larger electron density) are considered. In addition, if we select the smaller shunt capacitance per-unit-length C, we obtain a larger value of the TWT principal parameter γ. To obtain additional physical insights, we use the convenient dimensionless version of the TWT principal parameter $\check{\gamma}$, defined as

$$\check{\gamma} = \frac{\gamma}{\mathring{v}^2}. \tag{10.9}$$

Then, we define the system's state vector as $\mathbf{\Psi}(z) \equiv [Q, \partial_z Q, q, \partial_z q]^{\mathrm{T}}$, where T indicates transpose operator. The state vector consists of a combination of charge in the electron stream, charge in the equivalent transmission line and their first-order spatial derivatives. Finally, the system evolution along the z direction is described by the differential equation,

$$\partial_z \mathbf{\Psi}(z) = -\mathrm{i}\underline{\mathbf{M}}\mathbf{\Psi}(z), \tag{10.10}$$

where $\underline{\mathbf{M}}$ is a 4×4 TWT matrix and is given by

$$\underline{\mathbf{M}} = \begin{bmatrix} 0 & \mathrm{i} & 0 & 0 \\ \mathrm{i}\left(\check{\gamma}-1\right)\frac{\omega^2}{w^2} & 0 & \mathrm{i}\frac{b}{\mathring{v}^2}\left(R_{\mathrm{sc}}^2\omega_{\mathrm{p}}^2-\omega^2\right) & -\frac{2\omega}{\mathring{v}}b \\ 0 & 0 & 0 & \mathrm{i} \\ -\mathrm{i}\check{\gamma}\frac{1}{b}\frac{\omega^2}{w^2} & 0 & -\mathrm{i}\frac{1}{\mathring{v}^2}\left(R_{\mathrm{sc}}^2\omega_{\mathrm{p}}^2-\omega^2\right) & \frac{2\omega}{\mathring{v}} \end{bmatrix}. \tag{10.11}$$

Note that here, we assume the equivalent transmission line to be uniform, i.e., z invariant; therefore, $\underline{\mathbf{M}}$ is invariant in the z direction, but a further generalization to treat nonuniform SWSs is also possible.

10.3.2 Modal Dispersion Relation

We assume a state vector z-dependence of the form $\mathbf{\Psi}\left(z\right) \propto \exp\left(\mathrm{i}\omega t - \mathrm{i}kz\right)$, where k is the complex-valued wavenumber of a hot mode that accounts for the interaction of the electromagnetic wave in the SWS with the beam's charge waves. Then, the four hot eigenmodes are obtained by solving the eigenvalue problem $k\mathbf{\Psi}\left(z\right) = \underline{\mathbf{M}}\mathbf{\Psi}\left(z\right)$. The modal dispersion relation or characteristic equation is given by

$$D\left(\omega, k\right) = \det\left(\underline{\mathbf{M}} - k\underline{\mathbf{I}}\right) = 0. \tag{10.12}$$

After some mathematical calculation and by using the system matrix in Equation (10.11), the dispersion relation is expressed by

$$D\left(\omega, k\right) \equiv k^4 - 2k^3\frac{\omega}{\mathring{v}} + k^2\left(\frac{\omega^2}{\mathring{v}^2} - \frac{\omega^2}{w^2} + \frac{\check{\gamma}\omega^2}{w^2} - \frac{R_{\mathrm{sc}}^2\omega_{\mathrm{p}}^2}{\mathring{v}^2}\right) + 2k\frac{\omega^3}{w^2\mathring{v}} + \omega^2\frac{R_{\mathrm{sc}}^2\omega_{\mathrm{p}}^2 - \omega^2}{w^2\mathring{v}^2} = 0. \tag{10.13}$$

The solution of the dispersion relation leads to four complex modal wavenumbers that describe the four hot modes in the electromagnetic and electron stream interactive system. Since all coefficients in the characteristic equation are purely real, modal wavenumber solutions are either purely real or complex conjugates. If we simplify the dispersion relation by using the complex-valued analytic continuation of the phase velocity of the hot mode $u = \omega/k$ (in the following simply referred to as complex velocity), we obtain a simplified form of the TWT characteristic equation [291]

$$\frac{\gamma}{w^2 - u^2} + \frac{(u - \mathring{v})^2}{u^2} = \frac{1}{\breve{\omega}^2}, \qquad \breve{\omega} = \frac{\omega}{R_{\mathrm{sc}}\omega_{\mathrm{p}}}, \tag{10.14}$$

where $\breve{\omega}$ is the normalized (dimensionless) frequency which is real-valued in our analysis. We have concisely written the dispersion equation as a function of the three main physical parameters: (i) the electron stream steady velocity $\mathring{v}$; (ii) the cold electromagnetic wave modal phase velocity w; and (iii) the TWT principal parameter γ. A convenient dimensionless form of the same dispersion relation is expressed by

$$\frac{\check{\gamma}}{\breve{w}^2 - \breve{u}^2} + \frac{(\breve{u} - 1)^2}{\breve{u}^2} = \frac{1}{\breve{\omega}^2}, \qquad \breve{u} = \frac{u}{\mathring{v}}, \qquad \breve{w} = \frac{w}{\mathring{v}}, \tag{10.15}$$

where $\breve{u}$ and $\breve{w}$ are dimensionless parameters. The Euler-Lagrange relations in Equations (10.6) and (10.7) and the system of first-order differential equation in Equation (10.10) are written in the centimeter-gram-second system (CGS-Gaussian system). However, the dispersion relation is written using dimensionless parameters and therefore SI units could also be used. The table for CGS to SI transformation is provided in Appendix F. The formalism translation between the Lagrangian model parameters used in this framework and the parameters used in the Pierce model is listed in Appendix G, and more details are in [75].

10.4 Wavepacket Propagation in TWT

An analytical approach to studying wavepacket propagation in TWTs is presented in this section. We focus on Gaussian pulse propagation in TWTs but the analysis can be extended to other forms of wavepackets. We use analytical formulas based on the Lagrangian field theory explained in Section 10.3 to describe wavepacket propagation. Then, we calculate the approximate propagated wavepacket under specific assumptions. The results are compared to those using the transfer matrix approach that takes into account all the four hot modes in the TWT.

10.4.1 Wavepacket Propagation and Amplification Under the Assumption That u Is Constant (Approximate Method)

Any wavepacket propagating in a dispersive medium can be represented as a linear composition of its spectral constituents of different frequencies. Ideally, a wavepacket propagates through a medium without distortions if the relevant modal dispersion relation is linear, i.e., the complex velocity of each hot mode $u = \omega/k$ is constant and does not depend on frequency. In this subsection, we consider only the growing hot mode that amplifies the wavepacket and neglect the frequency variation of its phase velocity in the frequency domain of interest. We assume that for this single dispersionless growing hot mode $u(\omega) = \overline{u}$, where $\overline{u}$ is constant with imaginary part $\Im\{\overline{u}\} < 0$ that leads to amplification (see Figure 10.3(e) and (f)). The dispersionless assumption for this mode is valid only when the operating frequency is far enough from a transition point in the wavenumber dispersion diagram (see wavenumber dispersion diagram in Figures 10.1(i) and 10.3(e)).

A Gaussian wavepacket that represents the forward electromagnetic wave in the TWT is described by the complex charge representation,

$$Q\left(t,z\right)=\frac{A}{2\pi}\exp\left(\mathrm{i}\omega_0\left(t-\frac{z}{\overline{u}}\right)-\frac{1}{\tau_{\mathrm{w}}^2}\left(t-\frac{z}{\overline{u}}\right)^2\right), \tag{10.16}$$

where A is the pulse amplitude (in unit of charge), ω_0 indicates the pulse center angular frequency, τ_{w} show the pulse time constant. The wavepacket frequency information is obtained by applying the Fourier transform as defined in [400, Chapter 4], leading to

$$\widetilde{Q}\left(\omega,z\right)=\frac{A\tau_{\mathrm{w}}}{2\sqrt{\pi}}\exp\left(-\frac{\tau_{\mathrm{w}}^2\left(\omega-\omega_0\right)^2}{4}-\mathrm{i}\omega\frac{z}{\overline{u}}\right). \tag{10.17}$$

The complex velocity of the growing hot mode is calculated in terms of the power gain factor $\alpha_0<0$ that is defined as [291, Chapter 6.1]

$$\alpha_0=-\frac{\Im\left\{k\right\}}{\Re\left\{k\right\}}=\frac{\Im\left\{\overline{u}\right\}}{\Re\left\{\overline{u}\right\}}. \tag{10.18}$$

In the above equation, $\Im\left\{\overline{u}\right\}$ shows the imaginary part and $\Re\left\{\overline{u}\right\}$ shows the real part of the growing hot mode complex velocity. Therefore, we conveniently rewrite the single dispersionless growing hot mode complex velocity as [291, Chapter 16.2]

$$\overline{u}=\Re\left\{\overline{u}\right\}\left(1+\mathrm{i}\alpha_0\right). \tag{10.19}$$

It is convenient to define another parameter, related to wave energy velocity [291, Chapter 16.2],

$$u_{\mathrm{en}}=\Re\left\{\overline{u}\right\}\left(1+\alpha_0^2\right), \tag{10.20}$$

which is called the pseudo-real part of $\overline{u}$, defined as $1/u_{\mathrm{en}}=\Re\left\{1/\overline{u}\right\}$. Notice that the wave energy velocity u_{en} is larger than the real part of the hot mode complex velocity $\Re\left\{\overline{u}\right\}$ when

$\Im\{\overline{u}\} \neq 0$. The wave energy velocity u_{en} can be significantly larger than $\Re\{\overline{u}\}$ if $\Im\{\overline{u}\}$, and consequently the power gain factor α_0, is sufficiently large [291, Chapter 16.2]. Then, the exponent of $\widetilde{Q}(\omega, z)$ is given by

$$\ln\left(\widetilde{Q}(\omega, z)\right) = \ln\left(\frac{A\tau_{\text{w}}}{2\sqrt{\pi}}\right) - \frac{\tau_{\text{w}}^2(\omega - \omega_0)^2}{4} - \mathrm{i}\omega\frac{z}{\overline{u}}. \tag{10.21}$$

We obtain the following expressions for the real and imaginary parts [291, Chapter 16.2],

$$\Re\left\{\ln\left(\widetilde{Q}(\omega, z)\right)\right\} = \ln\left(\frac{A\tau_{\text{w}}}{2\sqrt{\pi}}\right) - \frac{\tau_{\text{w}}^2(\omega - \omega_0)^2}{4} - \frac{\omega\alpha_0}{u_{\text{en}}}z, \tag{10.22}$$

$$\Im\left\{\ln\left(\widetilde{Q}(\omega, z)\right)\right\} = -\frac{\omega}{u_{\text{en}}}z. \tag{10.23}$$

Next, the real part is rewritten as

$$\begin{aligned}\Re\left\{\ln\left(\widetilde{Q}(\omega, z)\right)\right\} &= \ln\left(\frac{A\tau_{\text{w}}}{2\sqrt{\pi}}\right) - \frac{\tau_{\text{w}}^2(\omega - \omega_{\text{w}}(z))^2}{4} + \frac{\tau_{\text{w}}^2(\omega_{\text{w}}^2(z) - \omega_0^2)}{4} \\ &= \ln\left(\frac{A\tau_{\text{w}}}{2\sqrt{\pi}}\right) - \frac{\tau_{\text{w}}^2(\omega - \omega_{\text{w}}(z))^2}{4} + \frac{\tau_{\text{w}}^2\omega_0^2\delta_{\text{w}}(z)(2 + \delta_{\text{w}}(z))}{4},\end{aligned} \tag{10.24}$$

where

$$\omega_{\text{w}}(z) = \omega_0(1 + \delta_{\text{w}}(z)), \tag{10.25}$$

$$\delta_{\text{w}}(z) = \frac{\omega_{\text{w}}(z) - \omega_0}{\omega_0} = -\frac{2\alpha_0}{u_{\text{en}}\omega_0\tau_{\text{w}}^2}z. \tag{10.26}$$

These two equations define $\omega_{\mathrm{w}}(z)$ as the wavepacket shifted angular frequency, and $\delta_{\mathrm{w}}(z)$ as the wavepacket relative frequency shift. These new quantities demonstrate that the complex velocity of the hot mode $\overline{u}$ causes the shift of the wavepacket center angular frequency from ω_0 to $\omega_{\mathrm{w}}(z)$ and the angular frequency shift is calculated by $\omega_0\delta_{\mathrm{w}}(z)$. Note that the frequency shift is directly associated to the presence of the imaginary part of $\overline{u}$. As we observe in Equations (10.25) and (10.26), $\omega_{\mathrm{w}}(z)$ and $\delta_{\mathrm{w}}(z)$ are position-dependent. Equation (10.26) implies that the relative frequency deviation from the center frequency increases linearly when the exponentially growing wavepacket travels inside the TWT (increasing z). The field amplification exponent or amplification factor appears in $\Re\left\{\ln\left(\widetilde{Q}(\omega,z)\right)\right\}$, and it accounts for the wavepacket amplification [291, Chapter 16.2]. Therefore, the signal amplification is defined as

$$S_{\mathrm{amp}}(z)=\ln\left(\frac{\widetilde{Q}\left(\omega_{\mathrm{w}}(z),z\right)}{\widetilde{Q}(\omega_0,0)}\right)=\ln\left(\frac{\widetilde{Q}\left(\omega_{\mathrm{w}}(z),z\right)}{A\tau_{\mathrm{w}}/\left(2\sqrt{\pi}\right)}\right). \tag{10.27}$$

and, according to Equation (10.24), it is equal to

$$S_{\mathrm{amp}}(z)=\frac{\tau_{\mathrm{w}}^2\left(\omega_{\mathrm{w}}^2(z)-\omega_0^2\right)}{4}=\frac{\tau_{\mathrm{w}}^2\omega_0^2\delta_{\mathrm{w}}(z)\left(2+\delta_{\mathrm{w}}(z)\right)}{4}, \tag{10.28}$$

This parameter shows the ratio between the maximum value of the amplified wavepacket at the shifted center frequency and the maximum value of the input Gaussian pulse by assuming the excitation of single dispersionless growing hot mode. It is clear that the maximum value of the propagated wavepacket occurs when the second term in Equation (10.24) vanishes since it has a negative value. Thus, the maximum value is obtained at $\omega=\omega_{\mathrm{w}}(z)$, which is the center frequency of the traveled wavepacket. According to Equation (10.28), an amplification factor is position-dependent because it is related to the relative frequency shift along z. As already mentioned, in this subsection, we used the charge $\widetilde{Q}(\omega,z)$ to describe the propagated wavepacket; however, this method can be applied to other quantities of the wavepacket such

as current, electric fields, etc.

Remark (Super-exponential amplification). Generally speaking, super-exponential means more than exponential, so a function is super-exponential if it grows faster than any exponential function. According to Equation (10.28), the amplification factor can be written as

$$S_{\text{amp}}(z) = C_1 \delta_{\text{w}}(z) + C_2 \delta_{\text{w}}^2(z), \tag{10.29}$$

where C_1 and C_2 are constant, system dependent, coefficients. On the other hand, the wavepacket shifted relative frequency is a linear function of z, i.e., $\delta_{\text{w}}(z) \propto z$ (see Equation (10.26)). As a result, the amplification occurs super-exponentially or faster than exponential by propagating through the TWT (increasing z) due to the presence of a quadratic term at the exponent, which results in super-exponential growth.

10.4.2 Gaussian Wavepacket as an Excitation Pulse (Exact Method)

In the frequency domain, the initial boundary condition state vector at $z = 0^+$ is

$$\mathbf{\Psi}(z_0) = \begin{bmatrix} \widetilde{Q}(\omega, z)\Big|_{z=0^+} \\ \partial \widetilde{Q}(\omega, z)/\partial z\Big|_{z=0^+} \\ 0 \\ 0 \end{bmatrix}. \tag{10.30}$$

If we assume the field is excited by a Gaussian pulse at the beginning of the TWT, the field initial conditions are

$$\begin{cases} \widetilde{Q}\left(\omega,z\right)\Big|_{z=0^{+}} = \frac{A\tau_{\mathrm{w}}}{2\sqrt{\pi}}\exp\left(-\frac{\tau_{\mathrm{w}}^{2}(\omega-\omega_{0})^{2}}{4}\right) \\ \partial\widetilde{Q}\left(\omega,z\right)/\partial z\Big|_{z=0^{+}} = -\frac{\mathrm{i}\omega}{\overline{u}}\,\widetilde{Q}\left(\omega,z\right)\Big|_{z=0^{+}} \end{cases} \tag{10.31}$$

In the second of the latter equations, we have assumed that the initial velocity is the one of the hot mode $\overline{u}$. In the frequency domain, the propagated wavepacket is represented by the state vector at any arbitrary coordinate $z = z_1$ via

$$\mathbf{\Psi}\left(z_1\right) = \underline{\mathbf{T}}\left(z_1, z_0\right)\mathbf{\Psi}\left(z_0\right), \tag{10.32}$$

where $\underline{\mathbf{T}}\left(z_1, z_0\right) = \exp\left(-\mathrm{i}\underline{\mathbf{M}}\left(z_1 - z_0\right)\right)$ is the TWT transfer matrix, which transfers the state vector $\mathbf{\Psi}\left(z\right)$ between the two points of z_0 and z_1 in the TWT. It is assumed in this calculation that the TWT is fully matched in the output and there is no reflection from that port.

10.5 Results and Discussion

According to the discussion in Section 10.3, we need two sets of parameters to analyze wavepacket propagation. Firstly, we need the fundamental TWT parameters, and secondly, we should express the initial pulse at an arbitrary position in the TWT, i.e., at the RF input port. In Subsections 10.5.1-10.5.3, we provide examples that are designed in a special way to highlight some nontrivial features of pulse propagation in TWTs. Then, in Subsection 10.5.4, we use some realistic parameters for a design in the microwave regime.

In Examples (1)-(3) provided in Subsections 10.5.1-10.5.3, we examine our developed method where the electron stream parameters are $\breve{\sigma}_{\mathrm{B}} = 5.524 \times 10^{-21}$, $R_{\mathrm{sc}} = 1$, $\breve{\omega}_{\mathrm{p}} = 1$, and $\breve{v} = 1$. We use dimensionless variables (with inverted hat sign) and the normalization factor for each physical quantity is described in Appendix H. We consider the equivalent transmission

line parameters as $C = 16.667$ ($= 1.854\,\mathrm{nF/m}$) and $L = 1.5 \times 10^{-2}\,\mathrm{s^2/cm^2}$ ($= 1.348\,\mathrm{TH/m}$) and we assume that the electron stream and electromagnetic wave are in strong coupling by considering $b = 1$. Then, the normalized TWT principal parameter is calculated as $\check{\gamma} = 0.234$. In general, the interaction between the electromagnetic wave and the charge wave occurs when they are synchronized, i.e., when the cold electromagnetic wave phase velocity $w = 1/\sqrt{LC}$ and the average velocity of the electrons $\mathring{v}$ are matched. In the specified frequency range, the cold electromagnetic wave phase velocity w is assumed to be dispersionless due to the dispersionless per-unit-length series inductance L and shunt capacitance C. The modal dispersion diagram of the hot modes in the presented TWT is shown in Figures 10.3(a)-(d) by using the previously mentioned parameters for TWT and substituting them in Equation (10.15).

Due to the centrosymmetry of the set of modes in the TWT system (with respect to $\omega = 0$), we only show positive frequencies. This is because the modes of negative frequencies can be easily recovered from the centrosymmetry transformation. Centrosymmetry is a property where for every point in the plot, there exists another point directly opposite to it through zero-frequency. In other words, if a point is on the plot, the same point reflected through the center will also be on the plot. The conventional dispersion relation of the hot modes is defined as the relation between real-valued angular frequency ω and complex-valued wavenumber k. The dispersion plots integrate the dispersion relations of TWT system modal branches and provide partial information on TWT system instabilities. The complete information on the TWT system dispersion relation is encoded in the characteristic equations for the complex-valued phase velocity of the hot modes (see Equation (10.13)). The characteristic equation has exactly four complex-valued k solutions for every ω, taking into account their algebraic multiplicity. Moreover, every hot mode in the TWT system is determined by its frequency and wavenumber, that is, by the pair $(\omega, k\,(\omega))$ with complex-valued $k\,(\omega)$.

In order to represent the convective (i.e., in space) unstable and stable (oscillatory) modes of

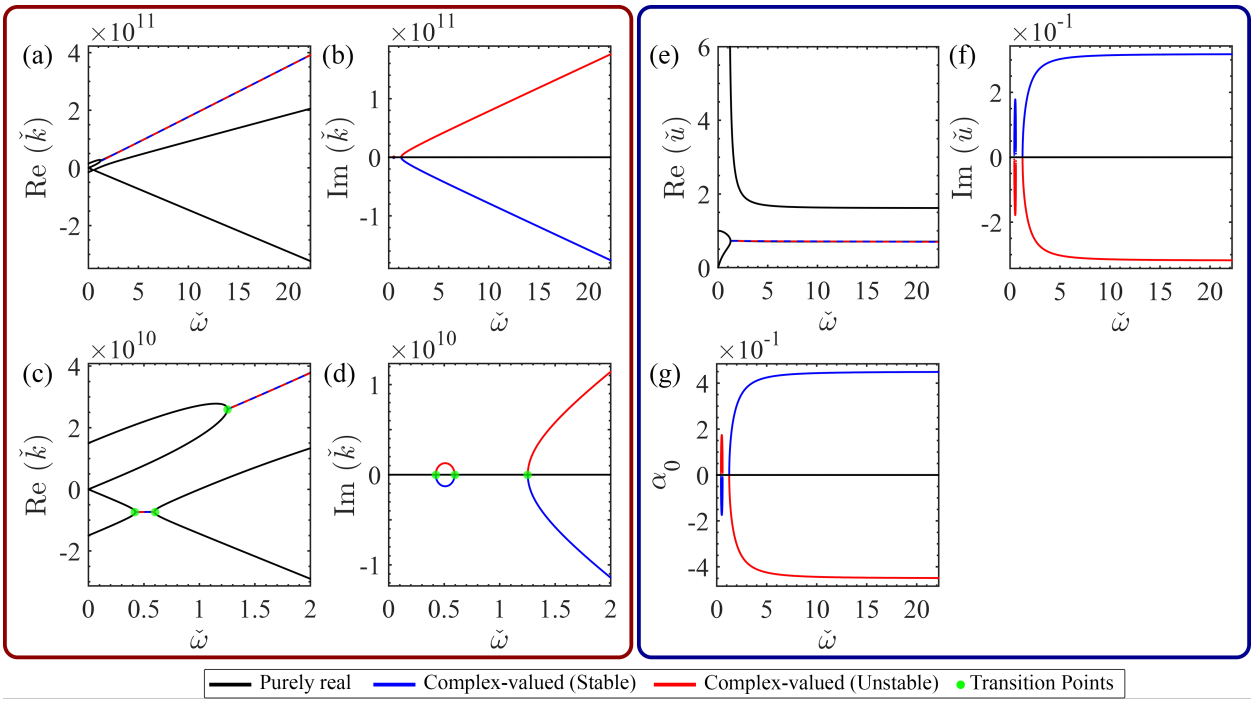

Figure 10.3: Normalized wavenumber k of the hot modes as a function of normalized angular frequency for the data in Examples (1)-(3) that are provided in Subsections 10.5.1-10.5.3: (a) and (c), real part; (b) and (d), imaginary part. The bottom plots (c) and (d) are magnified fragments of the dispersion relation in (a) and (b) showing more details around the transition points. The green dots show the transition points separating stability from instability. (e) and (f) show the real and imaginary parts of the complex velocity of the hot mode $u = \omega/k$ which are approximately frequency-independent at the high frequency. (g) Power gain factor α_0 which is negative for the growing mode. In these plots, the modes with purely real wavenumber are shown in black, the growing modes with $\Im(k) > 0$ are shown in red and the decaying modes with $\Im(k) < 0$ are shown in blue.

the TWT system, we proceed as follows. Our first step is to parameterize every mode in the TWT system uniquely using the pair $(\omega, k(\omega))$. If $k(\omega)$ is degenerate, it is counted a relevant number of times according to its multiplicity. Because of the importance of mode instability, that is when $\Im\{k(\omega)\} \neq 0$, we divide all the TWT system modes represented by pairs $(\omega, k(\omega))$ into two distinct classes of unstable and stable (oscillatory) modes, based on the complex velocity of hot modes $u(\omega)$. When the wavenumber of the hot mode $k(\omega) = \omega/u(\omega)$ is purely real or complex-valued with negative imaginary part, we can consider the associated mode as a stable (oscillatory) mode. Oppositely, we refer to the TWT system mode as a convective unstable mode if the wavenumber of hot mode $k(\omega)$ is complex-valued with a positive imaginary part. Notice that every point $(\omega, \Re\{k(\omega)\})$ in the convective unstable mode is associated with two complex conjugate TWT system modes with $\pm\Im\{k(\omega)\}$, which only one of them with positive value leads to amplification and the another mode with negative value will decay. There are two regions of operation in an interactive system based on four hot eigenmodes: (i) Amplification region: in this region the four modes are divided into two sets of modes: the first set consists of two exponentially growing and decaying oscillatory modes (amplifying/decaying, $\Im(k) \neq 0$) such that two modes wavenumbers are complex conjugate to each other (i.e., $k_1 = k_2^*$); the second set consists of two convectively stable (oscillatory) modes (unamplifying/undecaying, $\Im(k) = 0$) that vary harmonically in time and are bounded in the entire space by a constant; (ii) Non-amplified region: in this region the four modes are convectively stable (oscillatory) with real-valued wavenumbers (i.e., $\Im(k) = 0$).

We define a critical transition point separating stability from instability in the modal dispersion diagram. A transition point is a point (ω_c, k_c) in the $\omega - k$ plane that marks a transitional point from stability (oscillation) to instability (exponential growth) region. Transition points are the points at which dispersion relations develop second-order degeneracy. We refer to ω_c as nodal frequencies (transition frequencies) and k_c as nodal wavenumbers (transition wavenumbers), which are indicated by green dots in Figure 10.3(a)-(d). The amplification

regime starts or stops at this frequencies, and a deeper investigation into the features of these critical points (they are exceptional points of degeneracy) is provided in [75, 126]. The complex velocity changes dramatically at this critical point, which is one of the distinctive features of the transition point (or exceptional point). The real and imaginary parts of the complex velocity of the hot mode $u = \omega/k$ with approximately frequency-independent value at the high frequency are shown in Figure 10.3(e)-(f). Also, the power gain factor α_0 is illustrated in Figure 10.3(g). In these plots, the black curves show the modes with purely real wavenumber, the red curves show the growing modes with $\Im(k) > 0$ and the blue curves show the decaying modes with $\Im(k) < 0$.

In particular, in Subsection 10.4.2, we investigated pulse propagation along the TWT by using the "exact method" and we will employ this method in Examples (1)-(4) below. In addition, in Subsection 10.4.1, we studied pulse propagation along the TWT by using the "approximate method" (under constant u assumption) and we will apply this method in Examples (1) and (2) as a benchmark. We also compare the results obtained by the exact and approximate method in Examples (1) and (2) and discuss when the approximate method provides reasonable accuracy.

10.5.1 Example (1) - Wavepacket Frequency Band Is Far From the Transition Points

In this example, we study wavepacket propagation when the operating frequency and the pulse bandwidth are far from the transition points. We show how under this condition the approximate method can calculate the propagated wavepacket with acceptable accuracy. The input pulse parameters are set as $A = 1\,\mathrm{StatC}$, $\breve{\tau}_{\mathrm{w}} = 0.279$ and $\breve{\omega}_0 = 17.143$ for this example. We use dimensionless variables, and the normalization factor for each quantity is described in Appendix H; for this example the length, time and frequency normalization

factors are $\lambda_{\mathrm{p}} = 2.691 \times 10^{10}$ cm, $T_{\mathrm{p}} = 0.898$ s and $\omega_{\mathrm{p}} = 7$ rad/s, respectively. Based on the selected data, we calculate the propagated wavepacket in the SWS at certain positions using the method described in Subsection 10.3.1. Then we compare the exact calculated wavepacket with the results obtained under the constant u assumption. We start from the input port and show the results for the propagated wavepacket at different positions in Figure 10.4. The solid blue curves show the real part, the solid red curves depict the imaginary part, and the black dashed curves show the absolute value or envelope of the propagating wavepacket at different positions. Then, we move along the TWT and increase $\breve{z} = 0$ to $\breve{z} = \breve{z}_0$, where $\breve{z}_0 = 3 \times 10^{-11}$. Calculated results in Figures 10.4(e) and (f) show that the center angular frequency is increased by $\breve{\omega}_0 \times \delta_{\mathrm{w}}^{\mathrm{ex}}(\breve{z}_0) = 0.98$, and according to Equation (10.26) the angular frequency shift is obtained as $\breve{\omega}_0 \times \delta_{\mathrm{w}}^{\mathrm{app}}(\breve{z}_0) = 0.974$. At this point, we obtain the amplification factor $S_{\mathrm{amp}}^{\mathrm{ex}}(z)$ as a natural logarithm of the maximum amplitude of the propagated wavepacket that is obtained at the shifted center frequency. Figure 10.4(e) shows that the amplification factor is $S_{\mathrm{amp}}^{\mathrm{ex}}(\breve{z}_0) = 25.482$, and theoretical approximation based on Equation (10.28) demonstrates that $S_{\mathrm{amp}}^{\mathrm{app}}(\breve{z}_0) = 26.3$. In order to compare the results extracted from exact method and the approximate method under the constant u assumption, the real and imaginary parts of the propagated wavepacket at $\breve{z} = \breve{z}_0$ under the constant u assumption are calculated and shown in Figures 10.4(g) and (h).

Next, we increase $\breve{z}$ to $2\breve{z}_0$ to analyze the propagated pulse at the farther point. The propagated wavepacket obtained by using the exact method are represented in Figures 10.4(i) and (j). We find that the center frequency has been increased and the amplitude of the wavepacket has been significantly boosted. The calculated result demonstrates that the center angular frequency is increased by $\breve{\omega}_0 \delta_{\mathrm{w}}^{\mathrm{ex}}(2\breve{z}_0) = 1.96$ and theoretical approximation under constant u assumption predicts $\breve{\omega}_0 \delta_{\mathrm{w}}^{\mathrm{app}}(2\breve{z}_0) = 1.948$. Also, we found that the amplification factor at this point is $S_{\mathrm{amp}}^{\mathrm{ex}}(2\breve{z}_0) = 53.237$, and approximate calculations result in $S_{\mathrm{amp}}^{\mathrm{app}}(2\breve{z}_0) = 54.053$. The number of local peaks in the frequency domain increases at further distances from the input, compared to the results obtained for the points near the input.

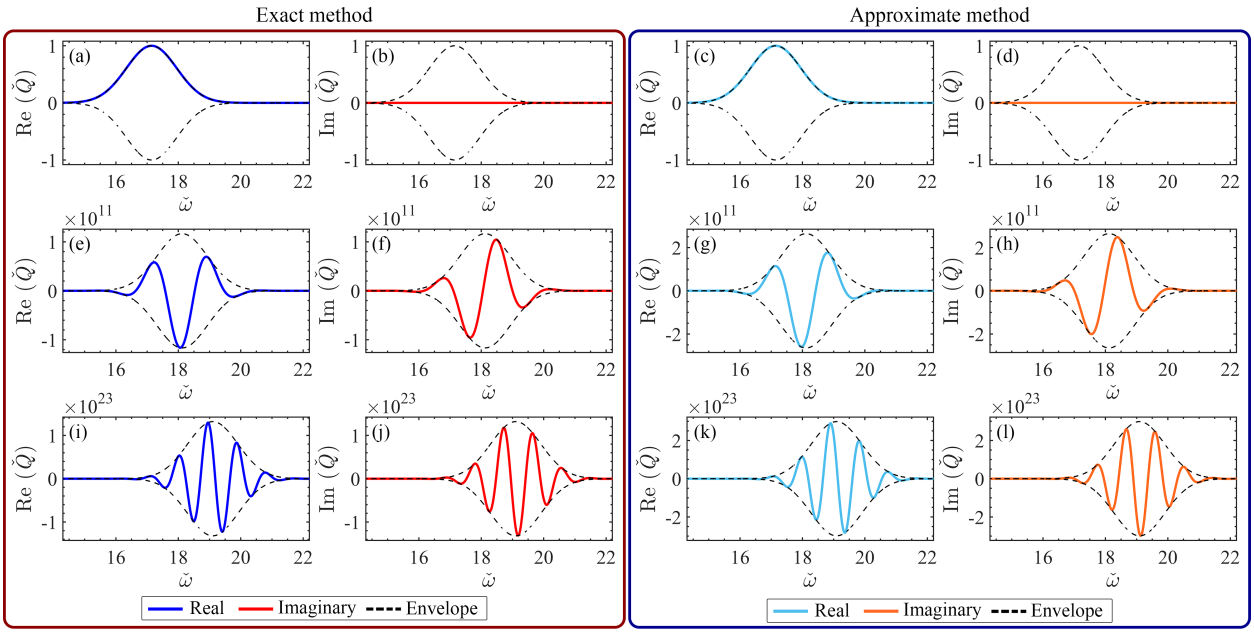

Figure 10.4: Pulse propagation when the operating frequency is *far* from the transition points frequency. Plots (a)-(l) display the propagating wavepackets of Example (1) in Subsection 10.5.1 at different $z-$positions inside the TWT. These plots show the real (blue/cyan) and imaginary (red/orange) parts at: (1) $\breve{z} = 0$ - first row from the top; (2) $\breve{z} = \breve{z}_0$ - second row from the top; (3) $\breve{z} = 2\breve{z}_0$ - third row from the top. The first and second columns show the real and imaginary parts of the propagated wavepacket calculated using the exact method. The third and fourth columns display the real and imaginary parts of the propagated wavepacket calculated under the constant u assumption. We observe amplification, shift in center frequency, and increase in the number of local peaks in the wavepacket spectrum within the pulse bandwidth as the pulse propagates through TWT.

Table 10.1: Comparison between calculated results for Gaussian pulse propagation under the constant u assumption (indicated by app) versus the exact results obtained by using Equation (10.10) (indicated by ex) in the Example (1) in Subsection 10.5.1.

	$\breve{\omega}_{\mathrm{w}}^{\mathrm{ex}}(z)$	$\breve{\omega}_{\mathrm{w}}^{\mathrm{app}}(z)$	$S_{\mathrm{amp}}^{\mathrm{ex}}(z)$	$S_{\mathrm{amp}}^{\mathrm{app}}(z)$	$\mathcal{E}r(\omega_{\mathrm{w}}(z))$	$\mathcal{E}r(S_{\mathrm{amp}}(z))$
$\breve{z}=0$	17.143	17.143	0	0	0%	0%
$\breve{z}=3\times10^{-11}$	18.123	18.117	25.482	26.3	0.034%	3.211%
$\breve{z}=6\times10^{-11}$	19.103	19.091	53.237	54.053	0.06%	1.533%

In order to evaluate the error in comparison of exact and approximate methods, the error function is defined as

$$\mathcal{E}r(X)=\left|\frac{X^{\mathrm{app}}-X^{\mathrm{ex}}}{X^{\mathrm{ex}}}\right|, \tag{10.33}$$

where X can be $\omega_{\mathrm{w}}(z)$ or $S_{\mathrm{amp}}(z)$, and superscript "app" shows the approximate value under constant u assumption and superscript "ex" indicates the exact value based on analytical exact method. Finally, the calculated results are summarized in Table 10.1. It demonstrates that the exact calculation and the prediction under the assumption of a constant u are in very close agreement. This is because the center frequency of the input pulse is chosen in the dispersionless region with approximately constant hot mode complex velocity $\overline{u}$.

10.5.2 Example (2) - Wavepacket Frequency Band Is Near the Transition Points

In Example (1) in Subsection 10.5.1, we assumed that the wavepacket center frequency was far enough from the transition points. Consequently, the constant value assumption for hot mode complex velocity was valid in our computations. *But the question is, does this assumption work in other cases as well?* In order to answer the question, we study another example where the pulse bandwidth *contains* the transition frequency. Let us assume $\breve{\omega}_0=\breve{\omega}_{\mathrm{c},3}=1.25$

Table 10.2: Comparison between calculated results for Gaussian pulse propagation under the constant u assumption (indicated by app) versus the exact results obtained by using Equation (10.10) (indicated by ex) in the Example (2) in Subsection 10.5.2.

	$\breve{\omega}_{\mathrm{w}}^{\mathrm{ex}}(z)$	$\breve{\omega}_{\mathrm{w}}^{\mathrm{app}}(z)$	$S_{\mathrm{amp}}^{\mathrm{ex}}(z)$	$S_{\mathrm{amp}}^{\mathrm{app}}(z)$	$\mathcal{E}r(\omega_{\mathrm{w}}(z))$	$\mathcal{E}r(S_{\mathrm{amp}}(z))$
$\breve{z}=0$	1.25	1.25	0	0	0%	0%
$\breve{z}=3\times10^{-11}$	2.327	2.224	1.357	2.591	4.436%	90.922%
$\breve{z}=6\times10^{-11}$	3.346	3.198	4.957	6.636	4.416%	33.876%

where $\breve{\omega}_{\mathrm{c},3}$ is the frequency of the third transition point, as shown in Figure 10.3. The calculated propagated wavepacket by using the mentioned pulse center frequency are illustrated in Figure 10.5, and significant outcomes are summarized in Table 10.2. The calculated results in Figure 10.5 show that both center frequency and field amplitude exponent are increased by moving throughout the TWT in a forward direction. In addition, the number of local peaks in the wavepacket spectrum within the pulse bandwidth is increased gradually. The real and imaginary parts of the propagated wavepacket using an approximate method are shown in the third and fourth columns of Figure 10.5. According to the calculated error in Table 10.2, we observe a significant deviation in the approximate results compared to the exact calculation. The presented example demonstrates that the approximate method under constant u assumption cannot deliver precise results if the center frequency is near transition points or if the pulse bandwidth contains a transition point. Thus, we must be sure that $\breve{\omega}_0 >> \breve{\omega}_{\mathrm{c}}$ to use the advantages of approximate method for calculating the propagated wavepacket. However, the approximate method was only used as a benchmark and the developed exact method is efficient and fast enough to use in practical applications.

There is distortion in the envelope of the propagated wavepacket in the second row of Figure 10.5 due to nontrivial phenomena of non-Gaussian pulses in the system. The exact result is distorted at lower frequencies, but the approximate result is not. This is due to the proximity of the wavepacket bandwidth to the transition point. This phenomenon can be better understood by looking at the following example.

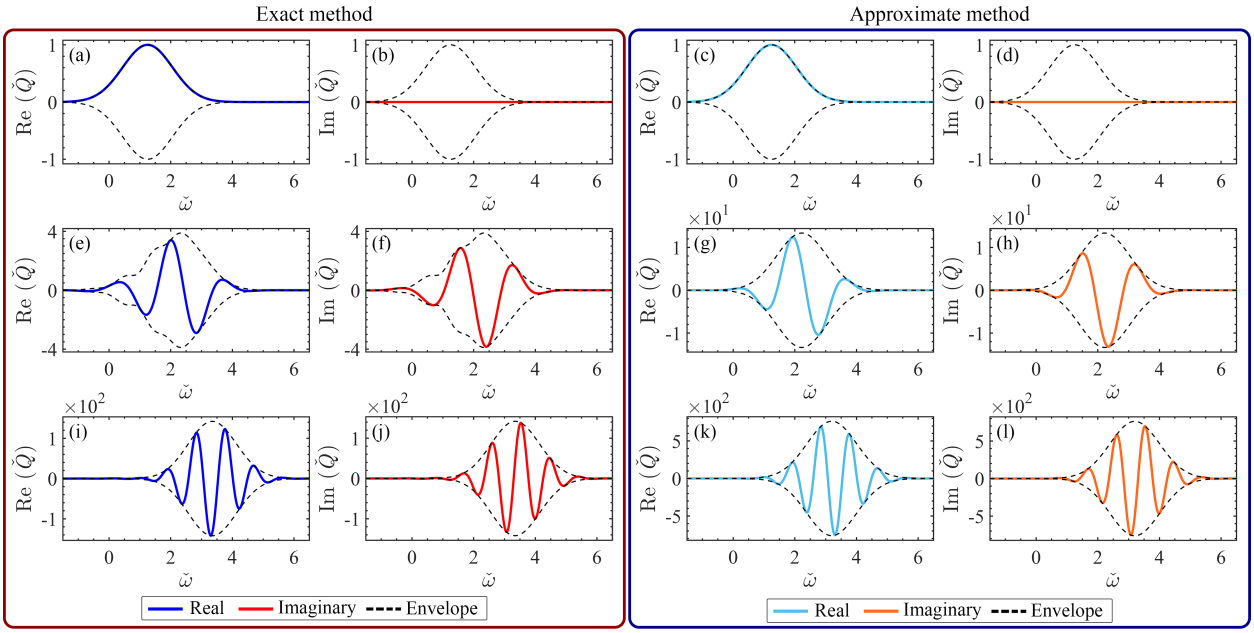

Figure 10.5: As in Figure 10.4, but for the case when the pulse bandwidth *contains* the transition point. Pulses in the second row are significantly distorted compared to those in the first row due to the pulse spectrum proximity to the third transition point (plots (e) and (f)). The approximate results under the constant u assumption (plots (g) and (h)) cannot predict the propagated pulse shape and amplitude correctly.

10.5.3 Example (3) - Variation In the Center Frequency of the Wavepacket

The purpose of this example is to examine the effect of changing the center frequency of the input pulse on the shape of the pulse envelope after it travels along the TWT. As we discussed in Examples (1) and (2) in Subsections 10.5.1 and 10.5.2, we should select the proper operating frequency to avoid distortion in the wavepacket. Let us consider a TWT with the parameters used in previous examples and the same parameters for the Gaussian input pulse. Then, we vary the center frequency of the wavepacket and calculate the propagated wavepacket at $\breve{z} = 4 \times 10^{-11}$. We select five different center frequencies for the input wavepacket, indicated by different colors in the dispersion diagram in Figure 10.6(a). The first input frequency is chosen at the first transition point, where the center angular frequency is $\breve{\omega}_0 = \breve{\omega}_{c,1} = 0.423$. Then the second input frequency is chosen at

the second transition point, which is $\breve{\omega}_0 = \breve{\omega}_{c,2} = 0.594$. The results for these two center frequencies at $\breve{z} = 4\times10^{-11}$ are shown in Figures 10.6(b) and (c). The propagated wavepacket exhibits significant distortion since the pulse bandwidth contains the transition point. Next, we increase the center angular frequency to $\breve{\omega}_0 = 1$ and $\breve{\omega}_0 = \breve{\omega}_{c,3} = 1.253$. The calculated results for these two cases are shown in Figures 10.6(d) and (e), where a small distortion in the shape of the propagated wavepacket can be recognized. In the case shown in Figure 10.6(e), the lower frequencies of the pulse bandwidth are distorted since it contains a transition point. In contrast, the higher frequencies of the pulse bandwidth are amplified without any distortion since they are located in the dispersionless region with a constant value of hot mode complex velocity. Finally, we select the center frequency of the input pulse in the dispersionless region, which is far from the transition points. In this case, $\breve{\omega}_0 = 2.9$ and the input pulse is amplified without distortion as illustrated in Figure 10.6(f).

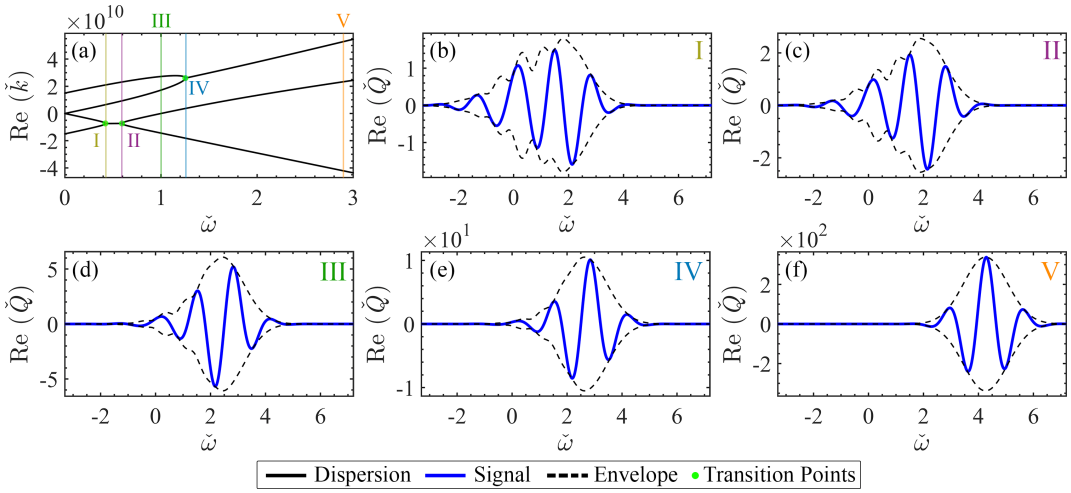

Figure 10.6: Pulse propagation in different frequency regimes. Plot (a) shows the real part of the hot mode eigenvalues in the Example (3) in Subsection 10.5.3, and it also indicates the selected center frequencies of the input pulse for five cases. Plots (b)-(f) display the calculated results for distinct center frequencies of the input Gaussian pulse, namely the real parts of pulse for an observer located at $\breve{z} = 4 \times 10^{-11}$ in the various center frequency of (b) $\breve{\omega}_0 = 0.423$, (c) $\breve{\omega}_0 = 0.594$, (d) $\breve{\omega}_0 = 1$, (e) $\breve{\omega}_0 = 1.253$, and (f) $\breve{\omega}_0 = 2.9$. The propagated wavepacket is distorted when the center frequency of the input pulse is near a transition point (Cases I, II, III and IV). The propagated pulse completely maintains its Gaussian shape when the center frequency of the input pulse is far enough away from the transition point (dispersionless region) since the hot mode complex velocity is constant (Case V).

10.5.4 Example (4) - Realistic Helix TWT

In order to evaluate the presented analysis for a specific design in the microwave regime, we use the characteristic parameters of a helix TWT with realistic settings in this example. The helix TWT is illustrated in Figure 10.7(a), which was already designed and utilized in [75] and [401]. In a helix-based SWS, a metallic tape-helix is surrounded by a metallic waveguide [402]. The helix SWS utilizes a conventional two-body cylindrical vacuum envelope that contains a metallic tape helix supported by three dielectric BeO rods [298]. An electron stream flows along the axis of the helical conductor with inner radius $r_1 = 7.44 \times 10^{-2}$ cm, and outer radius $r_2 = 8.46 \times 10^{-2}$ cm. The metallic circular waveguide has a radius of $r_3 = 1.06 \times 10^{-1}$ cm and the three equally spaced dielectric rods support that physically hold the helix are made of BeO with a relative dielectric constant of $\varepsilon_\mathrm{r} = 6.5$. Moreover, the other geometric parameters are $l = 1.04 \times 10^{-1}$ cm, $d = 5.2 \times 10^{-2}$ cm, and $\varphi = 14.2°$. The input and output RF pulses of the structure are defined as RF input port and RF output port as shown in Figure 10.1. A finite-element eigenmode solver in CST Studio Suite by DS SIMULIA is used to simulate the helix SWS. The eigenmode solver enforces a phase shift across the structure period in the longitudinal direction of propagation and solves for the real-valued eigenfrequencies in the absence of electron stream. The simulation is repeated for each phase shift to extract the characteristic parameters, i.e., the cold electromagnetic wave phase velocity and the equivalent transmission line characteristic impedance. Then, the calculated parameters for the mentioned geometry are illustrated in Figure 10.7(b). For the sake of simplicity, we assume constant values for the cold electromagnetic wave phase velocity and characteristic impedance. In this example, we use values around the synchronization point, which is $f_\mathrm{sync} = 12$ GHz. The maximum interaction between the electromagnetic and the space-charge wave occurs when they are synchronized, i.e., by matching w and $\mathring{v}$. The selected values for this example are chosen as $w/c = 0.2c$ and $Z_\mathrm{c} = 43\,\Omega$. By using the extracted values for w and Z_c at the synchronization point, the equivalent distributed series inductance

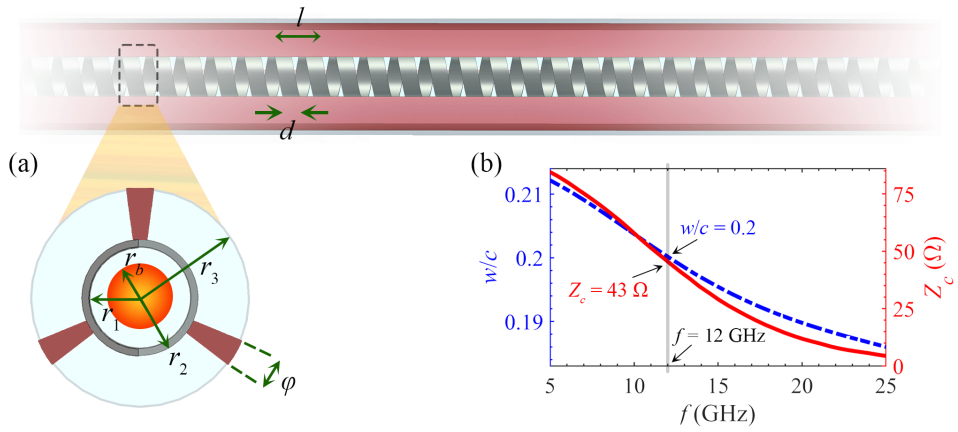

Figure 10.7: (a) Schematic of the tape helix SWS in a circular metallic waveguide. (b) Cold electromagnetic wave phase velocity and characteristic impedance of the first forward mode of the helix SWS obtained from cold full-wave simulations in the absence of the electron stream, using the finite-element method eigenmode solver.

$L = Z_c/w$ and shunt capacitance $C = 1/(Z_c w)$ are calculated. For this case, we obtain $L = 717.162\,\mathrm{nH/m}$ $(= 7.980 \times 10^{-21}\,\mathrm{s^2/cm^2})$ and $C = 387.865\,\mathrm{pF/m}$ $(= 3.486)$. Such TWT amplifier uses a solid linear electron stream with a radius of $r_b = 5.6 \times 10^{-2}\,\mathrm{cm}$. The electron stream phase velocity is 0.2 times the speed of light ($\mathring{v} = 0.2c$) to have synchronization around $f_{\mathrm{sync}} = 12\,\mathrm{GHz}$. The value of the emitted current was set to $I_0 = 47\,\mathrm{mA}$ $(= 1.41 \times 10^8\,\mathrm{StatA})$ and the corresponding plasma angular frequency is $\omega_p = 2\pi \times 624.6 \times 10^6\,\mathrm{rad/s}$. We use a plasma frequency reduction factor of $R_{\mathrm{sc}} = 0.12$, which was calculated and used in [75] and [401]. According to the calibration used in [75], the value of the coupling strength factor b, which is an essential parameter in the Lagrangian model, is estimated as $b = 0.92$. By using the introduced parameters, we calculate the required parameters of the Lagrangian model as $\beta = 1.739 \times 10^{14}\,\mathrm{cm^2/s^2}$ and $\gamma = 4.194 \times 10^{13}\,\mathrm{cm^2/s^2}$. Additionally, the dimensionless version of parameters required for the dimensionless form of the dispersion equation in Equation (10.15) are expressed as $\check{w} = 1$ and $\check{\gamma} = 1.167 \times 10^{-6}$.

Next, we study the nontrivial phenomena during the Gaussian pulse propagation for this specific design. The real and imaginary parts of the complex-valued wavenumber of hot modes are shown in Figures 10.8(a) and (b). In the proposed example, parameters of the

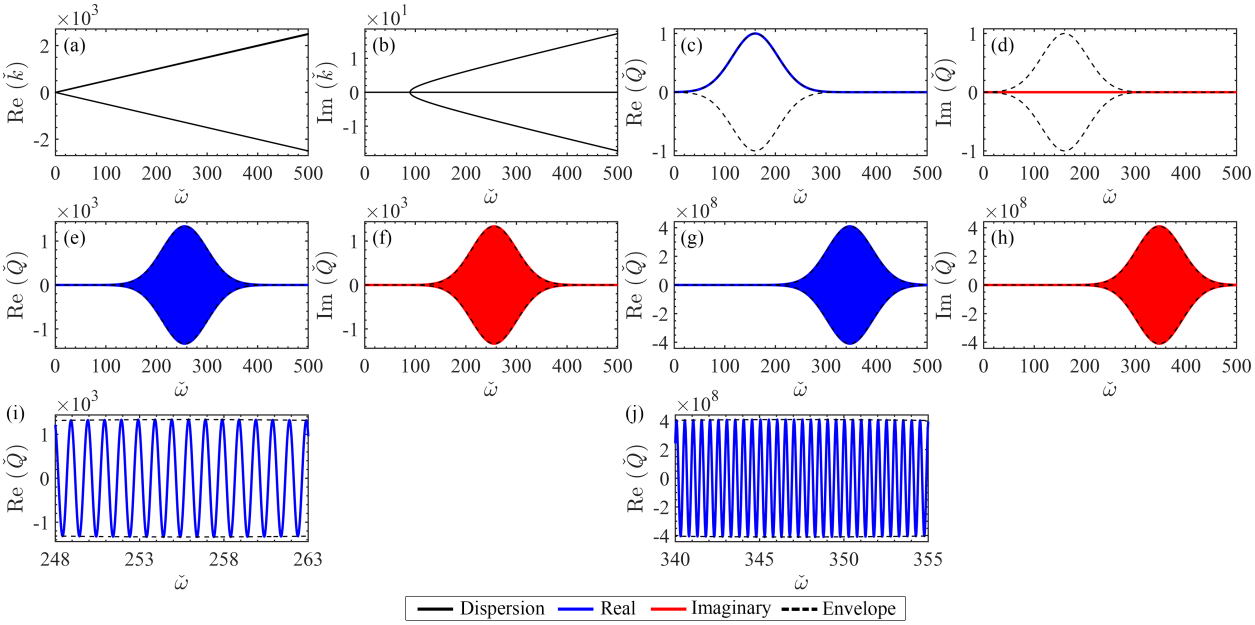

Figure 10.8: (a) Real and (b) imaginary parts of the complex-valued wavenumber for the Example (4) in Subsection 10.8. Plots (c)-(h) display the real and imaginary part of the spectrum of the propagated wavepacket at different positions along the TWT at: (c) and (d) $\breve{z} = 0$; (e) and (f) $\breve{z} = 0.2$; (g) and (h) $\breve{z} = 0.4$. The calculated results are obtained by using Equation (10.10). Plots (i) and (j) show the enlarged version of the real parts of the spectrum of the propagated wavepacket at $\breve{z} = 0.2$ and $\breve{z} = 0.4$ in the frequency range of $\breve{\omega} = 248$ to $\breve{\omega} = 263$ ($\Delta\breve{\omega} = 15$) and $\breve{\omega} = 340$ to $\breve{\omega} = 355$ ($\Delta\breve{\omega} = 15$). These two plots demonstrate that the number of local peaks in the wavepacket spectrum is increased in the same bandwidth by moving along the TWT.

RF input pulse are set as $A = 10^4$ C ($= 2.998 \times 10^{13}$ Fr), $\breve{\tau}_{\mathrm{w}} = 5 \times 10^{-3}$ and $\breve{\omega}_0 = 160.103$. Since the center frequency of the RF input signal is sufficiently far from transition points, we can consider the constant value for the hot mode complex velocity u. The normalization factors used for length, time and frequency in this example are $\lambda_{\mathrm{p}} = 4.000\,\mathrm{m}$, $T_{\mathrm{p}} = 13.342\,\mathrm{ns}$ and $\omega_{\mathrm{p}} = 2\pi \times 624.6 \times 10^6\,\mathrm{rad/s}$ respectively. Then, we calculate the propagated wavepacket in the SWS at certain positions using the analytical method described in Section 10.3.1. We start from the initial point, i.e., input port at $\breve{z} = 0$, and show the extracted calculated results in Figures 10.8 (c) and (d). The solid blue curves depict the real part, solid red curves depict the imaginary part, and black dashed curves indicate the absolute value or envelope of the RF input wavepacket. Then, we move further in the TWT and increase $\breve{z} = 0$ to $\breve{z} = 0.2$. Calculated results in Figures 10.8(e) and (f) show that the center frequency is increased and

the wavepacket is amplified dramatically. The huge amplification in the wavepacket occurred due to imaginary parts of the dispersion diagram in the operating frequencies. Next, we move further in the SWS and calculate the propagated wavepacket at $\breve{z} = 0.4$. The real and imaginary part of propagated wavepacket are presented in Figures 10.8(g) and (h). By comparing the calculated results at two selected points we observe that the center frequency of the pulse is increased by traveling in the SWS. Moreover, the magnified version of the real part of the wavepacket in the same frequency range in Figures 10.8(i) and (j) shows that the number of local peaks in the wavepacket spectrum is increasing. This example explains nontrivial phenomena that can happen during pulse propagation in a structure with realistic parameters.

10.6 Conclusions

We have introduced an efficient method for wavepacket propagation analysis in TWTs based on the Lagrangian field theory. The corresponding Euler-Lagrange equations are second order differential equations in time and space. For simplicity, we assume the RF input pulse has a Gaussian waveform but the algorithm works for any arbitrary input pulse. In the case of wave packets with spectral contents located in a linear region of the dispersion diagram, the analytical method can provide accurate results.

The proposed method provides useful insights into wavepacket propagation in TWTs. In particular, we observe a number of phenomena such as super amplification, shift in center frequency and increase in the number of local peaks in the wavepacket spectrum as the pulse propagates along the TWT. We apply our model to an example with realistic parameters and most of the claimed phenomena are observable in TWTs with realistic data.

Acknowledgments

- This material is based upon work supported by the Air Force Office of Scientific Research (AFOSR) Multidisciplinary Research Program of the University Research Initiative (MURI) administered through The University of New Mexico under Grant FA9550-20-1-0409.

Bibliography

[1] Shulim E Tsimring. *Electron beams and microwave vacuum electronics*. John Wiley & Sons, 2006.

[2] J. R. Pierce. *Traveling-wave tubes*. D.Van Nostrand Company Inc., 1950.

[3] Marko Iosifovich Vishik and Lazar Aronovich Lyusternik. The solution of some perturbation problems for matrices and selfadjoint or non-selfadjoint differential equations I. *Russian Mathematical Surveys*, 15(3):1, 1960.

[4] Tosio Kato. *Perturbation theory for linear operators*. Springer Science & Business Media, 1966.

[5] C Dembowski, B Dietz, H-D Gräf, HL Harney, A Heine, WD Heiss, and A Richter. Encircling an exceptional point. *Physical Review E—Statistical, Nonlinear, and Soft Matter Physics*, 69(5):056216, 2004.

[6] Aqiang Guo, Greg J Salamo, David Duchesne, Roberto Morandotti, Maite Volatier-Ravat, Vincent Aimez, Georgios A Siviloglou, and Demetrios N Christodoulides. Observation of PT-symmetry breaking in complex optical potentials. *Physical review letters*, 103(9):093902, 2009.

[7] Konstantinos G Makris, Ramy El-Ganainy, Demetrios N Christodoulides, and Ziad H Musslimani. PT-symmetric optical lattices. *Physical Review A*, 81(6):063807, 2010.

[8] Konghao Sun and Wei Yi. Encircling the liouvillian exceptional points: a brief review. *AAPPS Bulletin*, 34(1):22, 2024.

[9] T Stehmann, WD Heiss, and FG Scholtz. Observation of exceptional points in electronic circuits. *Journal of Physics A: Mathematical and General*, 37(31):7813, 2004.

[10] Bo Zhen, Chia Wei Hsu, Yuichi Igarashi, Ling Lu, Ido Kaminer, Adi Pick, Song-Liang Chua, John D Joannopoulos, and Marin Soljačić. Spawning rings of exceptional points out of dirac cones. *Nature*, 525(7569):354–358, 2015.

[11] Michael V Berry. Physics of nonhermitian degeneracies. *Czechoslovak journal of physics*, 54(10):1039–1047, 2004.

[12] Pai-Yen Chen, Maryam Sakhdari, Mehdi Hajizadegan, Qingsong Cui, Mark Ming-Cheng Cheng, Ramy El-Ganainy, and Andrea Alù. Generalized parity–time symmetry condition for enhanced sensor telemetry. *Nature Electronics*, 1(5):297–304, 2018.

[13] Mohammad-Ali Miri and Andrea Alu. Exceptional points in optics and photonics. *Science*, 363(6422):eaar7709, 2019.

[14] Şahin Kaya Özdemir, Stefan Rotter, Franco Nori, and L Yang. Parity–time symmetry and exceptional points in photonics. *Nature materials*, 18(8):783–798, 2019.

[15] Jan Wiersig. Review of exceptional point-based sensors. *Photonics Research*, 8(9):1457–1467, 2020.

[16] Midya Parto, Yuzhou GN Liu, Babak Bahari, Mercedeh Khajavikhan, and Demetrios N Christodoulides. Non-hermitian and topological photonics: optics at an exceptional point. *Nanophotonics*, 10(1):403–423, 2020.

[17] Aodong Li, Heng Wei, Michele Cotrufo, Weijin Chen, Sander Mann, Xiang Ni, Bingcong Xu, Jianfeng Chen, Jian Wang, Shanhui Fan, et al. Exceptional points and non-hermitian photonics at the nanoscale. *Nature Nanotechnology*, 18(7):706–720, 2023.

[18] Alexander Figotin and Ilya Vitebskiy. Oblique frozen modes in periodic layered media. *Physical Review E*, 68(3):036609, 2003.

[19] Hamidreza Kazemi, Mohamed Y Nada, Tarek Mealy, Ahmed F Abdelshafy, and Filippo Capolino. Exceptional points of degeneracy induced by linear time-periodic variation. *Physical Review Applied*, 11(1):014007, 2019.

[20] Alex Figotin and Ilya Vitebskiy. Slow-wave resonance in periodic stacks of anisotropic layers. *Physical Review A—Atomic, Molecular, and Optical Physics*, 76(5):053839, 2007.

[21] Kasra Rouhi, Filippo Capolino, and Alexander Figotin. Simple reciprocal electric circuit exhibiting exceptional point of degeneracy. *Journal of Physics A: Mathematical and Theoretical*, 2024.

[22] Alex Figotin and Ilya Vitebskiy. Frozen light in photonic crystals with degenerate band edge. *Physical Review E—Statistical, Nonlinear, and Soft Matter Physics*, 74(6):066613, 2006.

[23] Farshad Yazdi, Mohamed AK Othman, Mehdi Veysi, Alexander Figotin, and Filippo Capolino. A new amplification regime for traveling wave tubes with third-order modal degeneracy. *IEEE Transactions on Plasma Science*, 46(1):43–56, 2017.

[24] Alex Figotin and Ilya Vitebskiy. Gigantic transmission band-edge resonance in periodic stacks of anisotropic layers. *Physical review E*, 72(3):036619, 2005.

[25] Mohamed AK Othman, Vincenzo Galdi, and Filippo Capolino. Exceptional points of degeneracy and pt symmetry in photonic coupled chains of scatterers. *Physical Review B*, 95(10):104305, 2017.

[26] Tarek Mealy, Ahmed F Abdelshafy, and Filippo Capolino. Exceptional point of degeneracy in a backward-wave oscillator with distributed power extraction. *Physical Review Applied*, 14(1):014078, 2020.

[27] Tarek Mealy, Ahmed F Abdelshafy, and Filippo Capolino. High-power backward-wave oscillator using folded waveguide with distributed power extraction operating at an exceptional point. *IEEE Transactions on Electron Devices*, 68(7):3588–3595, 2021.

[28] George W Hanson, Alexander B Yakovlev, Mohamed AK Othman, and Filippo Capolino. Exceptional points of degeneracy and branch points for coupled transmission lines—linear-algebra and bifurcation theory perspectives. *IEEE Transactions on Antennas and Propagation*, 67(2):1025–1034, 2018.

[29] Ahmed F Abdelshafy, Mohamed AK Othman, Dmitry Oshmarin, Ahmad T Almutawa, and Filippo Capolino. Exceptional points of degeneracy in periodic coupled waveguides and the interplay of gain and radiation loss: Theoretical and experimental demonstration. *IEEE Transactions on Antennas and Propagation*, 67(11):6909–6923, 2019.

[30] Carl M Bender. Making sense of non-hermitian hamiltonians. *Reports on Progress in Physics*, 70(6):947, 2007.

[31] R. El-Ganainy, K. G. Makris, D. N. Christodoulides, and Ziad H. Musslimani. Theory of coupled optical PT-symmetric structures. *Optics Letters*, 32(17):2632, aug 2007.

[32] Ziad H Musslimani, Konstantinos G Makris, Ramy El-Ganainy, and Demetrios N Christodoulides. Optical solitons in pt periodic potentials. *Physical Review Letters*, 100(3):030402, 2008.

[33] Joseph Schindler, Ang Li, Mei C Zheng, Fred M Ellis, and Tsampikos Kottos. Experimental study of active LRC circuits with PT symmetries. *Physical Review A*, 84(4):040101, 2011.

[34] Stefano Longhi. Pt-symmetric laser absorber. *Physical Review A—Atomic, Molecular, and Optical Physics*, 82(3):031801, 2010.

[35] IV Barashenkov, L Baker, and NV Alexeeva. PT-symmetry breaking in a necklace of coupled optical waveguides. *Physical Review A—Atomic, Molecular, and Optical Physics*, 87(3):033819, 2013.

[36] Alexander B Yakovlev and George W Hanson. On the nature of critical points in leakage regimes of a conductor-backed coplanar strip line. *IEEE transactions on microwave theory and techniques*, 45(1):87–94, 1997.

[37] Hossein Hodaei, Absar U Hassan, Steffen Wittek, Hipolito Garcia-Gracia, Ramy El-Ganainy, Demetrios N Christodoulides, and Mercedeh Khajavikhan. Enhanced sensitivity at higher-order exceptional points. *Nature*, 548(7666):187–191, 2017.

[38] Weijian Chen, Şahin Kaya Özdemir, Guangming Zhao, Jan Wiersig, and Lan Yang. Exceptional points enhance sensing in an optical microcavity. *Nature*, 548(7666):192–196, 2017.

[39] Mohamed AK Othman and Filippo Capolino. Demonstration of a degenerate band edge in periodically-loaded circular waveguides. *IEEE Microwave and Wireless Components Letters*, 25(11):700–702, 2015.

[40] Mohamed AK Othman, Mehdi Veysi, Alexander Figotin, and Filippo Capolino. Low starting electron beam current in degenerate band edge oscillators. *IEEE Transactions on Plasma Science*, 44(6):918–929, 2016.

[41] Mohamed AK Othman, Xuyuan Pan, Georgios Atmatzakis, Christos G Christodoulou, and Filippo Capolino. Experimental demonstration of degenerate band edge in metallic periodically loaded circular waveguide. *IEEE Transactions on Microwave Theory and Techniques*, 65(11):4037–4045, 2017.

[42] Ahmed F Abdelshafy, Dmitry Oshmarin, Mohamed AK Othman, Michael M Green, and Filippo Capolino. Distributed degenerate band edge oscillator. *IEEE Transactions on Antennas and Propagation*, 69(3):1821–1824, 2020.

[43] Dmitry Oshmarin, Ahmed F Abdelshafy, Alireza Nikzamir, Michael M Green, and Filippo Capolino. Experimental demonstration of a new oscillator concept based on degenerate band edge in microstrip circuit. *arXiv preprint arXiv:2109.07002*, 2021.

[44] Ahmed F Abdelshafy, Tarek Mealy, Ehsan Hafezi, Alireza Nikzamir, and Filippo Capolino. Exceptional degeneracy in a waveguide periodically loaded with discrete gain and radiation loss elements. *Applied Physics Letters*, 118(22), 2021.

[45] Alireza Nikzamir and Filippo Capolino. Exceptional-point degeneracy as a desirable operation point for an oscillator array with discrete nonlinear gain and radiative elements. *Physical Review Applied*, 21(2):024037, 2024.

[46] AS Gilmour. *Principles of traveling wave tubes*. Artech House Radar Library, 1994.

[47] Patrick Wong, Peng Zhang, and John Luginsland. Recent theory of traveling-wave tubes: A tutorial-review. *Plasma research express*, 2(2):023001, 2020.

[48] Steven H Gold and Gregory S Nusinovich. Review of high-power microwave source research. *Review of Scientific instruments*, 68(11):3945–3974, 1997.

[49] Claudio Paoloni, Diana Gamzina, Rosa Letizia, Yuan Zheng, and Neville C Luhmann Jr. Millimeter wave traveling wave tubes for the 21st century. *Journal of electromagnetic waves and applications*, 35(5):567–603, 2021.

[50] Richard G Carter. *Microwave and RF vacuum electronic power sources*. Cambridge University Press, 2018.

[51] AS Gilmour. *Klystrons, traveling wave tubes, magnetrons, crossed-field amplifiers, and gyrotrons*. Artech House, 2011.

[52] John T Mendel. Helix and coupled-cavity traveling-wave tubes. *Proceedings of the IEEE*, 61(3):280–298, 1973.

[53] Alexander Figotin. Analytic theory of coupled-cavity traveling wave tubes. *Journal of mathematical physics*, 64(4):042705, 2023.

[54] Jeffrey D Wilson and Carol L Kory. Simulation of cold-test parameters and rf output power for a coupled-cavity traveling-wave tube. *IEEE Transactions on Electron Devices*, 42(11):2015–2020, 1995.

[55] Jeffrey D Wilson. Design of high-efficiency wide-bandwidth coupled-cavity traveling-wave tube phase velocity tapers with simulated annealing algorithms. *IEEE Transactions on Electron Devices*, 48(1):95–100, 2001.

[56] JJ Choi, CM Armstrong, AK Ganguly, and F Calise. Folded waveguide gyrotron traveling-wave-tube amplifier. *Physics of Plasmas*, 2(3):915–922, 1995.

[57] Sudeep Bhattacharjee, John H Booske, Carol L Kory, Dan W Van Der Weide, Steve Limbach, Sean Gallagher, John D Welter, Mike R Lopez, Ronald M Gilgenbach, R Lawrence Ives, et al. Folded waveguide traveling-wave tube sources for terahertz radiation. *IEEE transactions on plasma science*, 32(3):1002–1014, 2004.

[58] Hyun-Jun Ha, Soon-Shin Jung, and Gun-Sik Park. Theoretical study for folded waveguide traveling wave tube. *International journal of infrared and millimeter waves*, 19(9):1229–1245, 1998.

[59] Dan M Goebel, Yuval Carmel, and Gregory S Nusinovich. Advances in plasma-filled microwave sources. *Physics of plasmas*, 6(5):2225–2232, 1999.

[60] James Benford, John A Swegle, and Edl Schamiloglu. *High power microwaves*. CRC press, 2007.

[61] Peter Lancaster. On eigenvalues of matrices dependent on a parameter. *Numerische Mathematik*, 6(1):377–387, 1964.

[62] Alexander P Seyranian. Sensitivity analysis of multiple eigenvalues. *Mechanics of Structures and Machines*, 21(2):261–284, 1993.

[63] WD Heiss. Repulsion of resonance states and exceptional points. *Physical Review E*, 61(1):929, 2000.

[64] WD Heiss. Exceptional points–their universal occurrence and their physical significance. *Czechoslovak Journal of physics*, 54:1091–1099, 2004.

[65] Hamidreza Ramezani, Tsampikos Kottos, Vassilios Kovanis, and Demetrios N Christodoulides. Exceptional-point dynamics in photonic honeycomb lattices with PT symmetry. *Physical Review A—Atomic, Molecular, and Optical Physics*, 85(1):013818, 2012.

[66] Carl M Bender and Stefan Boettcher. Real spectra in non-hermitian hamiltonians having pt symmetry. *Physical review letters*, 80(24):5243, 1998.

[67] Hossein Hodaei, Mohammad-Ali Miri, Matthias Heinrich, Demetrios N Christodoulides, and Mercedeh Khajavikhan. Parity-time–symmetric microring lasers. *Science*, 346(6212):975–978, 2014.

[68] Maryam Sakhdari, Mehdi Hajizadegan, Yue Li, Mark Ming-Cheng Cheng, Jonathan CH Hung, and Pai-Yen Chen. Ultrasensitive, parity–time-symmetric wireless reactive and resistive sensors. *IEEE Sensors Journal*, 18(23):9548–9555, 2018.

[69] Yun Jing Zhang, Hoyeong Kwon, Mohammad-Ali Miri, Efthymios Kallos, Helena Cano-Garcia, Mei Song Tong, and Andrea Alu. Noninvasive glucose sensor based on parity-time symmetry. *Physical Review Applied*, 11(4):044049, 2019.

[70] Jan Wiersig. Enhancing the sensitivity of frequency and energy splitting detection by using exceptional points: application to microcavity sensors for single-particle detection. *Physical review letters*, 112(20):203901, 2014.

[71] Jan Wiersig. Sensors operating at exceptional points: General theory. *Physical review A*, 93(3):033809, 2016.

[72] Jan Wiersig. Robustness of exceptional-point-based sensors against parametric noise: the role of Hamiltonian and Liouvillian degeneracies. *Physical Review A*, 101(5):053846, 2020.

[73] Jan Wiersig. Prospects and fundamental limits in exceptional point-based sensing. *Nature communications*, 11(1):2454, 2020.

[74] Sunjae Gwak, Hyundong Kim, Hyeon-Hye Yu, Jinhyeok Ryu, Chil-Min Kim, and Chang-Hwan Yi. Rayleigh scatterer-induced steady exceptional points of stable-island modes in a deformed optical microdisk. *Optics Letters*, 46(12):2980–2983, 2021.

[75] Kasra Rouhi, Robert Marosi, Tarek Mealy, Ahmed F Abdelshafy, Alexander Figotin, and Filippo Capolino. Exceptional degeneracies in traveling wave tubes with dispersive slow-wave structure including space-charge effect. *Applied physics letters*, 118(26), 2021.

[76] P Djorwe, Yan Pennec, and Bahram Djafari-Rouhani. Exceptional point enhances sensitivity of optomechanical mass sensors. *Physical Review Applied*, 12(2):024002, 2019.

[77] Qi Wang and Yu Liu. Review of optical fiber bending/curvature sensor. *Measurement*, 130:161–176, 2018.

[78] Bernard DH Tellegen. The gyrator, a new electric network element. *Philips Res. Rep*, 3(2):81–101, 1948.

[79] David C Hamill. Lumped equivalent circuits of magnetic components: the gyrator-capacitor approach. *IEEE transactions on power electronics*, 8(2):97–103, 1993.

[80] DF Sheahan and HJ Orchard. Integratable gyrator using mos and bipolar transistors. *Electronics letters*, 2(10):390–391, 1966.

[81] TN Rao and RW Newcomb. Direct-coupled gyrator suitable for integrated circuits and time variation. *Electronics Letters*, 2(7):250–251, 1966.

[82] A Morse and L Huelsman. A gyrator realization using operational amplifiers. *IEEE Transactions on Circuit Theory*, 11(2):277–278, 1964.

[83] RHS Riordan. Simulated inductors using differential amplifiers. *Electronics Letters*, 2(3):50–51, 1967.

[84] Athanasios Antoniou. Gyrators using operational amplifiers. *Electronics Letters*, 3(8):350–352, 1967.

[85] Alireza Nikzamir, Kasra Rouhi, Alexander Figotin, and Filippo Capolino. Demonstration of exceptional points of degeneracy in gyrator-based circuit for high-sensitivity applications. *arXiv preprint arXiv:2107.00639*, 2021.

[86] Alexander Figotin. Synthesis of lossless electric circuits based on prescribed Jordan forms. *Journal of Mathematical Physics*, 61(12), 2020.

[87] Alexander Figotin. Perturbations of circuit evolution matrices with Jordan blocks. *Journal of Mathematical Physics*, 62(4):042703, 2021.

[88] Mehrdad Ehsani, Iqbal Husain, and Mehmet Oruç Bilgiç. Power converters as natural gyrators. *IEEE Transactions on Circuits and Systems I: Fundamental Theory and Applications*, 40(12):946–949, 1993.

[89] B Shenoi. Practical realization of a gyrator circuit and RC-gyrator filters. *IEEE Transactions on Circuit Theory*, 12(3):374–380, 1965.

[90] Hamidreza Kazemi, Amirhossein Hajiaghajani, Mohamed Y Nada, Manik Dautta, Muhannad Alshetaiwi, Peter Tseng, and Filippo Capolino. Ultra-sensitive radio frequency biosensor at an exceptional point of degeneracy induced by time modulation. *IEEE Sensors Journal*, 21(6):7250–7259, 2020.

[91] Aaron Welters. On explicit recursive formulas in the spectral perturbation analysis of a Jordan block. *SIAM Journal on Matrix Analysis and Applications*, 32(1):1–22, 2011.

[92] Kasra Rouhi, Hamidreza Kazemi, Alexander Figotin, and Filippo Capolino. Exceptional points of degeneracy directly induced by space–time modulation of a single transmission line. *IEEE Antennas and Wireless Propagation Letters*, 19(11):1906–1910, 2020.

[93] T Li, W Wang, and Xuexi Yi. Enhancing the sensitivity of optomechanical mass sensors with a laser in a squeezed state. *Physical Review A*, 104(1):013521, 2021.

[94] RMA Azzam. Light-reflection liquid-level sensor. *IEEE Transactions on Instrumentation and Measurement*, 29(2):113–115, 1980.

[95] Binfeng Yun, Na Chen, and Yiping Cui. Highly sensitive liquid-level sensor based on etched fiber Bragg grating. *IEEE photonics technology letters*, 19(21):1747–1749, 2007.

[96] E Vorathin, ZM Hafizi, AM Aizzuddin, Muhammad Khairol Annuar Zaini, and Kok Sing Lim. A novel temperature-insensitive hydrostatic liquid-level sensor using chirped FBG. *IEEE Sensors Journal*, 19(1):157–162, 2018.

[97] Sarfraz Khaliq, Stephen W James, and Ralph P Tatam. Fiber-optic liquid-level sensor using a long-period grating. *Optics letters*, 26(16):1224–1226, 2001.

[98] Hossein Golnabi. Design and operation of a fiber optic sensor for liquid level detection. *Optics and Lasers in Engineering*, 41(5):801–812, 2004.

[99] Xiao Lin, Liyong Ren, Yiping Xu, Nana Chen, Haijuan Ju, Jian Liang, Zhengquan He, Enshi Qu, Baowen Hu, and Yulin Li. Low-cost multipoint liquid-level sensor with plastic optical fiber. *IEEE Photonics Technology Letters*, 26(16):1613–1616, 2014.

[100] VE Sakharov, SA Kuznetsov, BD Zaitsev, IE Kuznetsova, and SG Joshi. Liquid level sensor using ultrasonic Lamb waves. *Ultrasonics*, 41(4):319–322, 2003.

[101] Ferry N Toth, Gerard CM Meijer, and Matthijs van der Lee. A planar capacitive precision gauge for liquid-level and leakage detection. *IEEE transactions on Instrumentation and Measurement*, 46(2):644–646, 1997.

[102] Hüseyin Canbolat. A novel level measurement technique using three capacitive sensors for liquids. *IEEE transactions on Instrumentation and Measurement*, 58(10):3762–3768, 2009.

[103] Kanadit Chetpattananondh, T Tapoanoi, P Phukpattaranont, and Nattha Jindapetch. A self-calibration water level measurement using an interdigital capacitive sensor. *Sensors and Actuators A: Physical*, 209:175–182, 2014.

[104] Jayalaxmi Rajesh Hanni and Santhosh Krishnan Venkata. A novel helical electrode type capacitance level sensor for liquid level measurement. *Sensors and Actuators A: Physical*, 315:112283, 2020.

[105] Brajesh Kumar, G Rajita, and Nirupama Mandal. A review on capacitive-type sensor for measurement of height of liquid level. *Measurement and control*, 47(7):219–224, 2014.

[106] Konstantinos Loizou and Eftichios Koutroulis. Water level sensing: State of the art review and performance evaluation of a low-cost measurement system. *Measurement*, 89:204–214, 2016.

[107] Satish Chandra Bera, Jayanta Kumar Ray, and Subrata Chattopadhyay. A low-cost noncontact capacitance-type level transducer for a conducting liquid. *IEEE Transactions on Instrumentation and Measurement*, 55(3):778–786, 2006.

[108] Edin Terzic, Jenny Terzic, Romesh Nagarajah, and Muhammad Alamgir. *A neural network approach to fluid quantity measurement in dynamic environments*. Springer Science & Business Media, 2012.

[109] Nur Shahida Midi, Kaito Sasaki, Ryu-ichiro Ohyama, and Naoki Shinyashiki. Broadband complex dielectric constants of water and sodium chloride aqueous solutions with different DC conductivities. *IEEJ Transactions on Electrical and Electronic Engineering*, 9(1):8–12, 2014.

[110] Kasra Rouhi, Alireza Nikzamir, Alexander Figotin, and Filippo Capolino. Exceptional point in a degenerate system made of a gyrator and two unstable resonators. *Physical Review A*, 105(3):032214, 2022.

[111] Kasra Rouhi, Alireza Nikzamir, Alexander Figotin, and Filippo Capolino. Enhanced sensitivity of degenerate system made of two unstable resonators coupled by gyrator operating at an exceptional point. *arXiv preprint arXiv:2110.01860*, 2021.

[112] Kasra Rouhi, Alireza Nikzamir, Alexander Figotin, and Filippo Capolino. Enhanced sensitivity of gyrator-based circuit at exceptional point composed of unstable resonators. In *2022 United States National Committee of URSI National Radio Science Meeting (USNC-URSI NRSM)*, pages 66–67. IEEE, 2022.

[113] AP Seyranian, ON Kirillov, and AA Mailybaev. Coupling of eigenvalues of complex matrices at diabolic and exceptional points. *Journal of Physics A: Mathematical and General*, 38(8):1723, 2005.

[114] WD Heiss. Exceptional points of non-Hermitian operators. *Journal of Physics A: Mathematical and General*, 37(6):2455, 2004.

[115] Walter D Heiss. The physics of exceptional points. *Journal of Physics A: Mathematical and Theoretical*, 45(44):444016, 2012.

[116] WD Heiss. Green's functions at exceptional points. *International Journal of Theoretical Physics*, 54:3954–3959, 2015.

[117] Jan Schnabel, Holger Cartarius, Jörg Main, Günter Wunner, and Walter Dieter Heiss. PT-symmetric waveguide system with evidence of a third-order exceptional point. *Physical Review A*, 95(5):053868, 2017.

[118] Alex Figotin and Ilya Vitebsky. Spectra of periodic nonreciprocal electric circuits. *SIAM Journal on Applied Mathematics*, 61(6):2008–2035, 2001.

[119] Yu-Hung Lai, Yu-Kun Lu, Myoung-Gyun Suh, Zhiquan Yuan, and Kerry Vahala. Observation of the exceptional-point-enhanced sagnac effect. *Nature*, 576(7785):65–69, 2019.

[120] Hoi-Kwan Lau and Aashish A Clerk. Fundamental limits and non-reciprocal approaches in non-hermitian quantum sensing. *Nature communications*, 9(1):4320, 2018.

[121] Wolfgang Langbein. No exceptional precision of exceptional-point sensors. *Physical Review A*, 98(2):023805, 2018.

[122] Mengzhen Zhang, William Sweeney, Chia Wei Hsu, Lan Yang, AD Stone, and Liang Jiang. Quantum noise theory of exceptional point amplifying sensors. *Physical review letters*, 123(18):180501, 2019.

[123] Chong Chen, Liang Jin, and Ren-Bao Liu. Sensitivity of parameter estimation near the exceptional point of a non-hermitian system. *New Journal of Physics*, 21(8):083002, 2019.

[124] Mohamed Y Nada, Mohamed AK Othman, and Filippo Capolino. Theory of coupled resonator optical waveguides exhibiting high-order exceptional points of degeneracy. *Physical Review B*, 96(18):184304, 2017.

[125] Hamidreza Kazemi, Mohamed Y Nada, Alireza Nikzamir, Franco Maddaleno, and Filippo Capolino. Experimental demonstration of exceptional points of degeneracy in linear time periodic systems and exceptional sensitivity. *Journal of Applied Physics*, 131(14):144502, 2022.

[126] Alexander Figotin. Exceptional points of degeneracy in traveling wave tubes. *Journal of mathematical physics*, 62(8):082701, 2021.

[127] Jinhan Ren, Hossein Hodaei, Gal Harari, Absar U Hassan, Weng Chow, Mohammad Soltani, D Christodoulides, and Mercedeh Khajavikhan. Ultrasensitive micro-scale parity-time-symmetric ring laser gyroscope. *Optics letters*, 42(8):1556–1559, 2017.

[128] DF Sheahan and HJ Orchard. High-quality transistorised gyrator. *Electronics Letters*, 7(2):274–275, 1966.

[129] T Yanagisawa and Y Kawashima. Active gyrator. *Electronics Letters*, 3(3):105–107, 1967.

[130] HT Chua and RW Newcomb. Integrated direct-coupled gyrator. *Electronics Letters*, 5(3):182–184, 1967.

[131] WH Holmes, S Gruetzmann, and WE Heinlein. High-performance direct-coupled gyrators. *Electronics Letters*, 2(3):45–46, 1967.

[132] H Th Van Looij and KM Adams. Wideband electronic gyrator circuit. *Electronics Letters*, 20(4):431–432, 1968.

[133] A Antoniou. New gyrator circuits obtained by using nullors. *Electronics Letters*, 5(4):87–88, 1968.

[134] A Antoniou. 3-terminal gyrator circuits using operational amplifiers. *Electronics letters*, 4(26):591–592, 1968.

[135] Andreas Antoniou. Realisation of gyrators using operational amplifiers, and their use in RC-active-network synthesis. In *Proceedings of the Institution of Electrical Engineers*, volume 116, pages 1838–1850. IET, 1969.

[136] ANDREAS Antoniou and K Naidu. Modeling of a gyrator circuit. *IEEE Transactions on circuit theory*, 20(5):533–540, 1973.

[137] HJ Orchard and AN Willson. New active-gyrator circuit. *Electronics letters*, 13(10):261–262, 1974.

[138] A Antoniou and K Naidu. A compensation technique for a gyrator and its use in the design of a channel-bank filter. *IEEE Transactions on Circuits and Systems*, 22(4):316–323, 1975.

[139] Ronald Y Barazarte, Guadalupe G Gonzalez, and Mehrdad Ehsani. Generalized gyrator theory. *IEEE Transactions on Power Electronics*, 25(7):1832–1837, 2010.

[140] Ali Toker, Oguzhan Cicekoglu, and Hakan Kuntman. New active gyrator circuit suitable for frequency-dependent negative resistor implementation. *Microelectronics Journal*, 30(1):59–62, 1999.

[141] IM Filanovsky. Current conveyor, voltage conveyor, gyrator. In *Proceedings of the 44th IEEE 2001 Midwest Symposium on Circuits and Systems. MWSCAS 2001 (Cat. No. 01CH37257)*, volume 1, pages 314–317. IEEE, 2001.

[142] Kasra Rouhi, Alireza Nikzamir, Alexander Figotin, and Filippo Capolino. High-sensitivity in various gyrator-based circuits with exceptional points of degeneracy. *EPJ Applied Metamaterials*, 9:8, 2022.

[143] Alireza Nikzamir, Kasra Rouhi, Alexander Figotin, and Filippo Capolino. How to achieve exceptional points in coupled resonators using a gyrator or PT-symmetry, and in a time-modulated single resonator: high sensitivity to perturbations. *EPJ Applied Metamaterials*, 9:14, 2022.

[144] A Nikzamir, K Rouhi, A Figotin, and F Capolino. Exceptional points of degeneracy in gyrator-based coupled resonator circuit. In *2021 Fifteenth International Congress on Artificial Materials for Novel Wave Phenomena (Metamaterials)*, pages 302–304. IEEE, 2021.

[145] WD Heiss and AL Sannino. Avoided level crossing and exceptional points. *Journal of Physics A: Mathematical and General*, 23(7):1167, 1990.

[146] Hamidreza Ramezani, Tsampikos Kottos, Ramy El-Ganainy, and Demetrios N Christodoulides. Unidirectional nonlinear PT-symmetric optical structures. *Physical Review A*, 82(4):043803, 2010.

[147] IV Barashenkov, DE Pelinovsky, and P Dubard. Dimer with gain and loss: Integrability and-symmetry restoration. *Journal of Physics A: Mathematical and Theoretical*, 48(32):325201, 2015.

[148] Albert Herrero-Parareda, Ilya Vitebskiy, Jacob Scheuer, and Filippo Capolino. Frozen mode in an asymmetric serpentine optical waveguide. *Advanced Photonics Research*, 3(9):2100377, 2022.

[149] J Schindler, Z Lin, J M Lee, H Ramezani, F M Ellis, and T Kottos. PT-symmetric electronics. *Journal of Physics A: Mathematical and Theoretical*, 45(44):444029, 2012.

[150] Alireza Nikzamir, Kasra Rouhi, Alexander Figotin, and Filippo Capolino. Time modulation to manage and increase the power harvested from external vibrations. *Applied Physics Letters*, 123(21):211701, 2023.

[151] Fa-Yueh Wu. Theory of resistor networks: the two-point resistance. *Journal of Physics A: Mathematical and General*, 37(26):6653, 2004.

[152] N Sh Izmailian, Ralph Kenna, and FY Wu. The two-point resistance of a resistor network: a new formulation and application to the cobweb network. *Journal of Physics A: Mathematical and Theoretical*, 47(3):035003, 2013.

[153] Holger Cartarius, Daniel Haag, Dennis Dast, and Günter Wunner. Nonlinear Schrödinger equation for a PT-symmetric delta-function double well. *Journal of Physics A: Mathematical and Theoretical*, 45(44):444008, 2012.

[154] Robin Gutöhrlein, Jörg Main, Holger Cartarius, and Günter Wunner. Bifurcations and exceptional points in dipolar Bose–Einstein condensates. *Journal of Physics A: Mathematical and Theoretical*, 46(30):305001, 2013.

[155] Robin Gutöhrlein, Holger Cartarius, Jörg Main, and Günter Wunner. Bifurcations and exceptional points in a PT-symmetric dipolar Bose–Einstein condensate. *Journal of Physics A: Mathematical and Theoretical*, 49(48):485301, 2016.

[156] Alexander P Seyranian and Alexei A Mailybaev. *Multiparameter stability theory with mechanical applications*, volume 13. World Scientific, 2003.

[157] Sergei A Tretyakov and Stanislav I Maslovski. Veselago materials: What is possible and impossible about the dispersion of the constitutive parameters. *IEEE Antennas and Propagation Magazine*, 49(1):37–43, 2007.

[158] K Rouhi, A Nikzamir, A Figotin, and F Capolino. Two resonators with negative and positive reactive components to achieve an exceptional point of degeneracy. In *2022 Sixteenth International Congress on Artificial Materials for Novel Wave Phenomena (Metamaterials)*, pages 374–376. IEEE, 2022.

[159] K Rouhi, A Nikzamir, A Figotin, and F Capolino. Second-order exceptional point of degeneracy in two directly coupled resonator. In *2024 United States National Committee of URSI National Radio Science Meeting (USNC-URSI NRSM)*, pages 263–263. IEEE, 2024.

[160] Shashank Priya. Modeling of electric energy harvesting using piezoelectric windmill. *Applied Physics Letters*, 87(18):184101, 2005.

[161] Adam M Wickenheiser and Ephrahim Garcia. Power optimization of vibration energy harvesters utilizing passive and active circuits. *Journal of Intelligent Material Systems and Structures*, 21(13):1343–1361, 2010.

[162] Neil G Stephen. On energy harvesting from ambient vibration. *Journal of Sound and Vibration*, 293(1-2):409–425, 2006.

[163] In-Ho Kim, Hyung-Jo Jung, Bo Mi Lee, and Seon-Jun Jang. Broadband energy-harvesting using a two degree-of-freedom vibrating body. *Applied Physics Letters*, 98(21):214102, 2011.

[164] Yasuyuki Naito and Keisuke Uenishi. Electrostatic mems vibration energy harvesters inside of tire treads. *Sensors*, 19(4):890, 2019.

[165] Hiroshi Toshiyoshi, Suna Ju, Hiroaki Honma, Chang-Hyeon Ji, and Hiroyuki Fujita. Mems vibrational energy harvesters. *Science and Technology of Advanced Materials*, 20(1):124–143, 2019.

[166] Joseph A Paradiso and Thad Starner. Energy scavenging for mobile and wireless electronics. *IEEE Pervasive computing*, 4(1):18–27, 2005.

[167] Soon-Duck Kwon. A t-shaped piezoelectric cantilever for fluid energy harvesting. *Applied Physics Letters*, 97(16):164102, 2010.

[168] SC Sinha and A David. Parametric excitation. In S. Braun, editor, *Encyclopedia of Vibration*, pages 1001–1009. Elsevier, 2001.

[169] Jerzy Warminski. Nonlinear dynamics of self-, parametric, and externally excited oscillator with time delay: van der pol versus rayleigh models. *Nonlinear Dynamics*, 99(1):35–56, 2020.

[170] Mehrdad Aghamohammadi, Vladislav Sorokin, and Brian Mace. Dynamic analysis of the response of duffing-type oscillators subject to interacting parametric and external excitations. *Nonlinear Dynamics*, 107(1):99–120, 2022.

[171] AF Arrieta, P Hagedorn, Alper Erturk, and Daniel J Inman. A piezoelectric bistable plate for nonlinear broadband energy harvesting. *Applied Physics Letters*, 97(10):104102, 2010.

[172] Seok-Min Jung and Kwang-Seok Yun. Energy-harvesting device with mechanical frequency-up conversion mechanism for increased power efficiency and wideband operation. *Applied Physics Letters*, 96(11):111906, 2010.

[173] Michele Zilletti, Stephen J Elliott, and Emiliano Rustighi. Optimisation of dynamic vibration absorbers to minimise kinetic energy and maximise internal power dissipation. *Journal of Sound and Vibration*, 331(18):4093–4100, 2012.

[174] Francesco Di Monaco, Maryam Ghandchi Tehrani, Stephen J Elliott, Elvio Bonisoli, and Stefano Tornincasa. Energy harvesting using semi-active control. *Journal of Sound and Vibration*, 332(23):6033–6043, 2013.

[175] Maryam Ghandchi Tehrani and Stephen J Elliott. Extending the dynamic range of an energy harvester using nonlinear damping. *Journal of Sound and Vibration*, 333(3):623–629, 2014.

[176] Matteo Scapolan, Maryam Ghandchi Tehrani, and Elvio Bonisoli. Energy harvesting using parametric resonant system due to time-varying damping. *Mechanical Systems and Signal Processing*, 79:149–165, 2016.

[177] Weijian Jiao and Stefano Gonella. Intermodal and subwavelength energy trapping in nonlinear metamaterial waveguides. *Physical Review Applied*, 10(2):024006, 2018.

[178] Dibin Zhu, Michael J Tudor, and Stephen P Beeby. Strategies for increasing the operating frequency range of vibration energy harvesters: a review. *Measurement Science and Technology*, 21(2):022001, 2009.

[179] Xiudong Tang and Lei Zuo. Enhanced vibration energy harvesting using dual-mass systems. *Journal of Sound and Vibration*, 330(21):5199–5209, 2011.

[180] Roszaidi Ramlan, MJ Brennan, BR Mace, and I Kovacic. Potential benefits of a non-linear stiffness in an energy harvesting device. *Nonlinear Dynamics*, 59(4):545–558, 2010.

[181] H Laalej, Zi Qiang Lang, Stephen Daley, I Zazas, SA Billings, and GR Tomlinson. Application of non-linear damping to vibration isolation: an experimental study. *Nonlinear Dynamics*, 69:409–421, 2012.

[182] Marco Ferrari, Vittorio Ferrari, Michele Guizzetti, Bruno Ando, Salvatore Baglio, and Carlo Trigona. Improved energy harvesting from wideband vibrations by nonlinear piezoelectric converters. *Sensors and Actuators A: Physical*, 162(2):425–431, 2010.

[183] Junyi Cao, Wei Wang, Shengxi Zhou, Daniel J Inman, and Jing Lin. Nonlinear time-varying potential bistable energy harvesting from human motion. *Applied Physics Letters*, 107(14):143904, 2015.

[184] WT Van Horssen, AK Abramian, et al. On the free vibrations of an oscillator with a periodically time-varying mass. *Journal of Sound and Vibration*, 298(4-5):1166–1172, 2006.

[185] WT Van Horssen, OV Pischanskyy, and JLA Dubbeldam. On the forced vibrations of an oscillator with a periodically time-varying mass. *Journal of Sound and Vibration*, 329(6):721–732, 2010.

[186] Miodrag Zukovic and Ivana Kovacic. An insight into the behaviour of oscillators with a periodically piecewise-defined time-varying mass. *Communications in Nonlinear Science and Numerical Simulation*, 42:187–203, 2017.

[187] Giuseppe Giorgi and Nicolás Faedo. Performance enhancement of a vibration energy harvester via harmonic time-varying damping: A pseudospectral-based approach. *Mechanical Systems and Signal Processing*, 165:108331, 2022.

[188] Alireza Nikzamir and Filippo Capolino. Highly sensitive coupled oscillator based on an exceptional point of degeneracy and nonlinearity. *Physical Review Applied*, 18(5):054059, 2022.

[189] SP Beeby, MJ Tudor, and NM White. Energy harvesting vibration sources for microsystems applications. *Measurement Science and Technology*, 17(12):R175–R195, 2006.

[190] Steve P Beeby, Russel N Torah, M John Tudor, Peter Glynne-Jones, Terence O'Donnell, Chitta R Saha, and Saibal Roy. A micro electromagnetic generator for vibration energy harvesting. *Journal of Micromechanics and Microengineering*, 17(7):1257–1265, 2007.

[191] Sushanta Kundu and Harshal B Nemade. Modeling and simulation of a piezoelectric vibration energy harvester. *Procedia Engineering*, 144:568–575, 2016.

[192] Alper Erturk, J Hoffmann, and Daniel J Inman. A piezomagnetoelastic structure for broadband vibration energy harvesting. *Applied Physics Letters*, 94(25):254102, 2009.

[193] Sebastien Boisseau, Ghislain Despesse, and Bouhadjar Ahmed Seddik. Nonlinear h-shaped springs to improve efficiency of vibration energy harvesters. *Journal of Applied Mechanics*, 80(6):061013, 2013.

[194] Philippe Basset, Elena Blokhina, and Dimitri Galayko. *Electrostatic kinetic energy harvesting*. John Wiley & Sons, 2016.

[195] Peter Spies, Markus Pollak, and Loreto Mateu. *Handbook of energy harvesting power supplies and applications*. CRC Press, 2015.

[196] John A Richards. *Analysis of periodically time-varying systems*. Springer Science & Business Media, 1983.

[197] Philippe Le Corbeiller and Ying-Wa Yeung. Duality in mechanics. *The Journal of the Acoustical Society of America*, 24(6):643–648, 1952.

[198] CB Williams and Rob B Yates. Analysis of a micro-electric generator for microsystems. *sensors and actuators A: Physical*, 52(1-3):8–11, 1996.

[199] Shad Roundy, Paul K Wright, and Jan Rabaey. A study of low level vibrations as a power source for wireless sensor nodes. *Computer communications*, 26(11):1131–1144, 2003.

[200] Chongfeng Wei and Xingjian Jing. A comprehensive review on vibration energy harvesting: Modelling and realization. *Renewable and Sustainable Energy Reviews*, 74:1–18, 2017.

[201] Neil White. *Energy harvesting for autonomous systems*. Artech House, 2010.

[202] Niell Elvin and Alper Erturk. *Advances in energy harvesting methods*. Springer Science & Business Media, 2013.

[203] Samuel C Stanton, Clark C McGehee, and Brian P Mann. Reversible hysteresis for broadband magnetopiezoelastic energy harvesting. *Applied Physics Letters*, 95(17), 2009.

[204] Yunus Uzun and Erol Kurt. The effect of periodic magnetic force on a piezoelectric energy harvester. *Sensors and Actuators A: Physical*, 192:58–68, 2013.

[205] D. Karnopp, M. J. Crosby, and R. A. Harwood. Vibration control using semi-active force generators. *Journal of Engineering for Industry*, 96(2):619–626, 1974.

[206] S. Rakheja and S. Sankar. Vibration and shock isolation performance of a semi-active on-off damper. *Journal of Vibration, Acoustics, Stress, and Reliability in Design*, 107(4):398–403, 1985.

[207] Yanqing Liu, Hiroshi Matsuhisa, and Hideo Utsuno. Semi-active vibration isolation system with variable stiffness and damping control. *Journal of sound and vibration*, 313(1-2):16–28, 2008.

[208] Stefan Hurlebaus and Lothar Gaul. Smart structure dynamics. *Mechanical systems and signal processing*, 20(2):255–281, 2006.

[209] Yanqing Liu, Hiroshi Matsuhisa, Hideo Utsuno, and Jeong Gyu Park. Vibration isolation by a variable stiffness and damping system. *JSME International Journal Series C Mechanical Systems, Machine Elements and Manufacturing*, 48(2):305–310, 2005.

[210] Yanqing Liu, Hiroshi Matsuhisa, Hideo Utsuno, and Jeong Gyu Park. Variable damping and stiffness vibration control with magnetorheological fluid dampers for two degree-of-freedom system. *JSME International Journal Series C Mechanical Systems, Machine Elements and Manufacturing*, 49(1):156–162, 2006.

[211] Yanqing Liu, Hiroshi Matsuhisa, Hideo Utsuno, and Jeong Gyu Park. Vibration control by a variable damping and stiffness system with magnetorheological dampers. *JSME International Journal Series C Mechanical Systems, Machine Elements and Manufacturing*, 49(2):411–417, 2006.

[212] N Harris McClamroch, DS Oritz, Henri P Gavin, and Robert D Hanson. Electrorheological dampers and semi-active structural control. In *Proceedings of 1994 33rd IEEE Conference on Decision and Control*, volume 1, pages 97–102. IEEE, 1994.

[213] N Harris McClamroch and Henri P Gavin. Electrorheological dampers and semi-active structural control. In *Proceedings of 1995 34th IEEE Conference on Decision and Control*, volume 4, pages 3528–3533. IEEE, 1995.

[214] KW Wang, YS Kim, and DB Shea. Structural vibration control via electrorheological-fluid-based actuators with adaptive viscous and frictional damping. *Journal of Sound and Vibration*, 177(2):227–237, 1994.

[215] Sha Zhou and Tianjun Yu. Performance comparisons of piezoelectric energy harvesters under different stochastic noises. *AIP Advances*, 10(3), 2020.

[216] Son Duy Nguyen, Einar Halvorsen, and Geir U Jensen. Wideband mems energy harvester driven by colored noise. *Journal of microelectromechanical systems*, 22(4):892–900, 2013.

[217] RL Harne and KW Wang. Prospects for nonlinear energy harvesting systems designed near the elastic stability limit when driven by colored noise. *Journal of Vibration and Acoustics*, 136(2):021009, 2014.

[218] Qifan He and Mohammed F Daqaq. New insights into utilizing bistability for energy harvesting under white noise. *Journal of Vibration and Acoustics*, 137(2):021009, 2015.

[219] Li Haitao, Qin Weiyang, Lan Chunbo, Deng Wangzheng, and Zhou Zhiyong. Dynamics and coherence resonance of tri-stable energy harvesting system. *Smart Materials and Structures*, 25(1):015001, 2015.

[220] Di Liu, Yong Xu, and Junlin Li. Probabilistic response analysis of nonlinear vibration energy harvesting system driven by gaussian colored noise. *Chaos, Solitons & Fractals*, 104:806–812, 2017.

[221] IS Mokem Fokou, C Nono Dueyou Buckjohn, M Siewe Siewe, and Clément Tchawoua. Probabilistic distribution and stochastic p-bifurcation of a hybrid energy harvester under colored noise. *Communications in Nonlinear Science and Numerical Simulation*, 56:177–197, 2018.

[222] Sovan Sundar Dasgupta, Vasudevan Rajamohan, and Abhishek Kumar Jha. Dynamic characterization of a bistable energy harvester under gaussian white noise for larger time constant. *Arabian Journal for Science and Engineering*, 44:721–730, 2019.

[223] Subramanian Ramakrishnan and Connor Edlund. Stochastic stability of a piezoelectric vibration energy harvester under a parametric excitation and noise-induced stabilization. *Mechanical Systems and Signal Processing*, 140:106566, 2020.

[224] Hang Deng, Jimin Ye, and Dongmei Huang. Design and analysis of a galloping energy harvester with v-shape spring structure under gaussian white noise. *Chaos, Solitons & Fractals*, 175:113962, 2023.

[225] Marek Borowiec, Grzegorz Litak, and Stefano Lenci. Noise effected energy harvesting in a beam with stopper. *International Journal of Structural Stability and Dynamics*, 14(08):1440020, 2014.

[226] Meng Su, Wei Xu, Ying Zhang, and Guidong Yang. Response of a vibro-impact energy harvesting system with bilateral rigid stoppers under gaussian white noise. *Applied Mathematical Modelling*, 89:991–1003, 2021.

[227] Xingbao Huang. Stochastic resonance in a piecewise bistable energy harvesting model driven by harmonic excitation and additive gaussian white noise. *Applied Mathematical Modelling*, 90:505–526, 2021.

[228] Wen-An Jiang and Li-Qun Chen. Energy harvesting of monostable duffing oscillator under gaussian white noise excitation. *Mechanics Research Communications*, 53:85–91, 2013.

[229] Wen-An Jiang and Li-Qun Chen. An equivalent linearization technique for nonlinear piezoelectric energy harvesters under gaussian white noise. *Communications in Nonlinear Science and Numerical Simulation*, 19(8):2897–2904, 2014.

[230] Yong-Ge Yang and Wei Xu. Stochastic analysis of monostable vibration energy harvesters with fractional derivative damping under gaussian white noise excitation. *Nonlinear Dynamics*, 94:639–648, 2018.

[231] O Foupouapouognigni, C Nono Dueyou Buckjohn, M Siewe Siewe, and C Tchawoua. Hybrid electromagnetic and piezoelectric vibration energy harvester with gaussian white noise excitation. *Physica A: Statistical Mechanics and Its Applications*, 509:346–360, 2018.

[232] Yanxia Zhang, Yanfei Jin, and Pengfei Xu. Dynamics of a coupled nonlinear energy harvester under colored noise and periodic excitations. *International Journal of Mechanical Sciences*, 172:105418, 2020.

[233] GJ Fezeu, IS Mokem Fokou, C Nono Dueyou Buckjohn, M Siewe Siewe, and C Tchawoua. Resistance induced p-bifurcation and ghost-stochastic resonance of a hybrid energy harvester under colored noise. *Physica A: Statistical Mechanics and its Applications*, 557:124857, 2020.

[234] Shu-Ling Guo, Yong-Ge Yang, and Ya-Hui Sun. Stochastic response of an energy harvesting system with viscoelastic element under gaussian white noise excitation. *Chaos, Solitons & Fractals*, 151:111231, 2021.

[235] Qinyuan Liu, Zidong Wang, Hongli Dong, and Changjun Jiang. Remote estimation for energy harvesting systems under multiplicative noises: A binary encoding scheme with probabilistic bit flips. *IEEE Transactions on Automatic Control*, 68(1):343–354, 2022.

[236] Vicenç Méndez, Daniel Campos, and Werner Horsthemke. Efficiency of harvesting energy from colored noise by linear oscillators. *Physical Review E*, 88(2):022124, 2013.

[237] Miquel Lopez-Suarez, Gabriel Abadal, Luca Gammaitoni, and Riccardo Rurali. Noise energy harvesting in buckled bn nanoribbons from molecular dynamics. *Nano Energy*, 15:329–334, 2015.

[238] Nuanyang Cui, Long Gu, Jinmei Liu, Suo Bai, Jiawen Qiu, Jiecai Fu, Xinli Kou, Hong Liu, Yong Qin, and Zhong Lin Wang. High performance sound driven triboelectric nanogenerator for harvesting noise energy. *Nano Energy*, 15:321–328, 2015.

[239] Ali Ghodsi, Hamid Jafari, Saber Azizi, and Mohammad Reza Ghazavi. On the dynamics of a novel energy harvester to convert the energy of the magnetic noise into electrical power. *Energy*, 207:118268, 2020.

[240] Christian Wolff, Christos Tserkezis, and N Asger Mortensen. On the time evolution at a fluctuating exceptional point. *Nanophotonics*, 8(8):1319–1326, 2019.

[241] Zhicheng Xiao, Huanan Li, Tsampikos Kottos, and Andrea Alù. Enhanced sensing and nondegraded thermal noise performance based on p t-symmetric electronic circuits with a sixth-order exceptional point. *Physical Review Letters*, 123(21):213901, 2019.

[242] Changdong Chen and Lina Zhao. The effect of thermal-induced noise on doubly-coupled-ring optical gyroscope sensor around exceptional point. *Optics Communications*, 474:126108, 2020.

[243] Robert Duggan, Sander A Mann, and Andrea Alu. Limitations of sensing at an exceptional point. *ACS Photonics*, 9(5):1554–1566, 2022.

[244] Rodion Kononchuk, Jizhe Cai, Fred Ellis, Ramathasan Thevamaran, and Tsampikos Kottos. Exceptional-point-based accelerometers with enhanced signal-to-noise ratio. *Nature*, 607(7920):697–702, 2022.

[245] William Tuxbury, Rodion Kononchuk, and Tsampikos Kottos. Non-resonant exceptional points as enablers of noise-resilient sensors. *Communications Physics*, 5(1):210, 2022.

[246] Zhipeng Li, Chenhui Li, Ze Xiong, Guoqiang Xu, Yongtai Raymond Wang, Xi Tian, Xin Yang, Zhu Liu, Qihang Zeng, Rongzhou Lin, et al. Stochastic exceptional points for noise-assisted sensing. *Physical Review Letters*, 130(22):227201, 2023.

[247] Joseph W Matiko, Neil J Grabham, Steve P Beeby, and Michael J Tudor. Review of the application of energy harvesting in buildings. *Measurement Science and Technology*, 25(1):012002, 2013.

[248] Hao Wang, Abbas Jasim, and Xiaodan Chen. Energy harvesting technologies in roadway and bridge for different applications–a comprehensive review. *Applied energy*, 212:1083–1094, 2018.

[249] K Rouhi, A Nikzamir, A Figotin, and F Capolino. Exceptional points of degeneracy induced by time-periodic modulation. In *2023 Seventeenth International Congress on Artificial Materials for Novel Wave Phenomena (Metamaterials)*, pages 312–314. IEEE, 2023.

[250] Mohamed AK Othman, Farshad Yazdi, Alex Figotin, and Filippo Capolino. Giant gain enhancement in photonic crystals with a degenerate band edge. *Physical Review B*, 93(2):024301, 2016.

[251] Stefano Longhi. Floquet exceptional points and chirality in non-hermitian hamiltonians. *Journal of Physics A: Mathematical and Theoretical*, 50(50):505201, 2017.

[252] Mohamed AK Othman and Filippo Capolino. Theory of exceptional points of degeneracy in uniform coupled waveguides and balance of gain and loss. *IEEE Transactions on Antennas and Propagation*, 65(10):5289–5302, 2017.

[253] Mohamed AK Othman, Venkata Ananth Tamma, and Filippo Capolino. Theory and new amplification regime in periodic multimodal slow wave structures with degeneracy interacting with an electron beam. *IEEE Transactions on Plasma Science*, 44(4):594–611, 2016.

[254] Ahmed F Abdelshafy, Mohamed AK Othman, Farshad Yazdi, Mehdi Veysi, Alexander Figotin, and Filippo Capolino. Electron-beam-driven devices with synchronous multiple degenerate eigenmodes. *IEEE Transactions on Plasma Science*, 46(8):3126–3138, 2018.

[255] Mehdi Veysi, Mohamed AK Othman, Alexander Figotin, and Filippo Capolino. Degenerate band edge laser. *Physical Review B*, 97(19):195107, 2018.

[256] Edwards S Cassedy and Arthur A Oliner. Dispersion relations in time-space periodic media: Part I—stable interactions. *Proceedings of the IEEE*, 51(10):1342–1359, 1963.

[257] Edwards S Cassedy. Dispersion relations in time-space periodic media part II—unstable interactions. *Proceedings of the IEEE*, 55(7):1154–1168, 1967.

[258] Charles Elachi. Electromagnetic wave propagation and wave-vector diagram in space-time periodic media. *IEEE Transactions on Antennas and Propagation*, 20(4):534–536, 1972.

[259] Jorge R Zurita-Sánchez, P Halevi, and Juan C Cervantes-Gonzalez. Reflection and transmission of a wave incident on a slab with a time-periodic dielectric function $\epsilon(t)$. *Physical Review A—Atomic, Molecular, and Optical Physics*, 79(5):053821, 2009.

[260] Juan Sabino Martínez-Romero, OM Becerra-Fuentes, and P Halevi. Temporal photonic crystals with modulations of both permittivity and permeability. *Physical Review A*, 93(6):063813, 2016.

[261] Nicholas Aaron Estep, Dimitrios L Sounas, and Andrea Alù. Magnetless microwave circulators based on spatiotemporally modulated rings of coupled resonators. *IEEE Transactions on Microwave Theory and Techniques*, 64(2):502–518, 2016.

[262] Sajjad Taravati and Christophe Caloz. Mixer-duplexer-antenna leaky-wave system based on periodic space-time modulation. *IEEE transactions on antennas and propagation*, 65(2):442–452, 2016.

[263] Hamid Rajabalipanah, Ali Abdolali, and Kasra Rouhi. Reprogrammable spatiotemporally modulated graphene-based functional metasurfaces. *IEEE Journal on Emerging and Selected Topics in Circuits and Systems*, 10(1):75–87, 2020.

[264] Seyed Ehsan Hosseininejad, Kasra Rouhi, Fan Wang, Mohsen Khalily, and Rahim Tafazolli. High-speed terahertz communication with graphene-based time-modulated low-bit phase coding metasurfaces: A novel architecture for enhanced performance. *Materials Today Communications*, 40:109726, 2024.

[265] Shihan Qin, Qiang Xu, and Yuanxun Ethan Wang. Nonreciprocal components with distributedly modulated capacitors. *IEEE Transactions on Microwave Theory and Techniques*, 62(10):2260–2272, 2014.

[266] Konstantin A Lurie and Vadim V Yakovlev. Energy accumulation in waves propagating in space-and time-varying transmission lines. *IEEE Antennas and Wireless Propagation Letters*, 15:1681–1684, 2016.

[267] Fengchuan Wu, Yuejun Zheng, Fang Yuan, and Yunqi Fu. Magnetic-free isolators based on time-varying transmission lines. *Electronics*, 8(6):684, 2019.

[268] Xiaohu Wu, Xiaoguang Liu, Mark D Hickle, Dimitrios Peroulis, Juan Sebastián Gómez-Díaz, and Alejandro Álvarez Melcón. Isolating bandpass filters using time-modulated resonators. *IEEE Transactions on Microwave Theory and Techniques*, 67(6):2331–2345, 2019.

[269] Zongfu Yu and Shanhui Fan. Complete optical isolation created by indirect interband photonic transitions. *Nature photonics*, 3(2):91–94, 2009.

[270] Julio Moro, James V Burke, and Michael L Overton. On the Lidskii–Vishik–Lyusternik perturbation theory for eigenvalues of matrices with arbitrary Jordan structure. *SIAM Journal on Matrix Analysis and Applications*, 18(4):793–817, 1997.

[271] Frank Ellinger, Heinz Jackel, and Werner Bachtold. Varactor-loaded transmission-line phase shifter at C-band using lumped elements. *IEEE Transactions on Microwave Theory and Techniques*, 51(4):1135–1140, 2003.

[272] Kasra Rouhi, Hamid Rajabalipanah, and Ali Abdolali. Multi-bit graphene-based bias-encoded metasurfaces for real-time terahertz wavefront shaping: From controllable orbital angular momentum generation toward arbitrary beam tailoring. *Carbon*, 149:125–138, 2019.

[273] Andrei Komar, Ramón Paniagua-Domínguez, Andrey Miroshnichenko, Ye Feng Yu, Yuri S Kivshar, Arseniy I Kuznetsov, and Dragomir Neshev. Dynamic beam switching by liquid crystal tunable dielectric metasurfaces. *Acs Photonics*, 5(5):1742–1748, 2018.

[274] D Shiffler, John A Nation, and CB Wharton. High-power traveling-wave tube amplifier. *Applied physics letters*, 54(7):674–676, 1989.

[275] Chien-Lun Hung. High-power, stable ka/v dual-band gyrotron traveling-wave tube amplifier. *Applied Physics Letters*, 100(20):203502, 2012.

[276] Carter M Armstrong, Richard Kowalczyk, Andrew Zubyk, Kevin Berg, Clark Meadows, Danny Chan, Thomas Schoemehl, Ramon Duggal, Nora Hinch, Richard B True, et al. A compact extremely high frequency mpm power amplifier. *IEEE Transactions on Electron Devices*, 65(6):2183–2188, 2018.

[277] David M French, Don Shiffler, and Keith Cartwright. Electron beam coupling to a metamaterial structure. *Physics of Plasmas*, 20(8):083116, 2013.

[278] Chien-Hao Liu, Paul Carrigan, Brian J Kupczyk, Xun Xiang, Nader Behdad, John E Scharer, and John H Booske. Metamaterials for rapidly forming large-area distributed plasma discharges for high-power microwave applications. *IEEE Transactions on Plasma Science*, 43(12):4099–4109, 2015.

[279] Tyler Rowe, John H Booske, and Nader Behdad. Metamaterial-enhanced resistive wall amplifiers: Theory and particle-in-cell simulations. *IEEE Transactions on Plasma Science*, 43(7):2123–2131, 2015.

[280] Zhaoyun Duan, Michael A Shapiro, Edl Schamiloglu, Nader Behdad, Yubin Gong, John H Booske, BN Basu, and Richard J Temkin. Metamaterial-inspired vacuum electron devices and accelerators. *IEEE Transactions on Electron Devices*, 66(1):207–218, 2018.

[281] SA Naqvi, GS Kerslick, JA Nation, and L Schächter. Axial extraction of high-power microwaves from relativistic traveling wave amplifiers. *Applied physics letters*, 69(11):1550–1552, 1996.

[282] Joe X Qiu, Baruch Levush, John Pasour, Allen Katz, Carter M Armstrong, David R Whaley, Jack Tucek, Kenneth Kreischer, and David Gallagher. Vacuum tube amplifiers. *IEEE Microwave Magazine*, 10(7):38–51, 2009.

[283] W. D. Heiss. Exceptional points of a hamiltonian and phase transitions in finite systems. *Zeitschrift für Physik A Atomic Nuclei*, 329(2):133–138, 1988.

[284] W. D. Heiss and JCH Chiang. Random perturbation of systematic degeneracies and quantum chaos. *Physical Review A*, 47(4):2533, 1993.

[285] J. R. Pierce. Theory of the beam-type traveling-wave tube. *Proceedings of the IRE*, 35(2):111–123, 1947.

[286] J. R. Pierce. Waves in electron streams and circuits. *Bell System Technical Journal*, 30(3):626–651, 1951.

[287] J. R. Pierce. *Traveling-wave tubes*. D.Van Nostrand Company Inc., 1954.

[288] John G Wohlbier, John H Booske, and Ian Dobson. The multifrequency spectral eulerian (muse) model of a traveling wave tube. *IEEE Transactions on Plasma Science*, 30(3):1063–1075, 2002.

[289] Mark C Converse, John H Booske, and Susan C Hagness. Impulse amplification in a traveling-wave tube-i: Simulation and experimental validation. *IEEE transactions on plasma science*, 32(3):1040–1048, 2004.

[290] James W Gewartowski and Hugh A Watson. *Principles of electron tubes: including grid-controlled tubes, microwave tubes, and gas tubes*. Van Nostrand, 1965.

[291] Alexander Figotin. *An Analytic Theory of Multi-stream Electron Beams in Traveling Wave Tubes*. World Scientific, 2020.

[292] Venkata Ananth Tamma and Filippo Capolino. Extension of the pierce model to multiple transmission lines interacting with an electron beam. *IEEE Transactions on Plasma Science*, 42(4):899–910, 2014.

[293] Alexander Figotin and Guillermo Reyes. Multi-transmission-line-beam interactive system. *Journal of Mathematical Physics*, 54(11):111901, 2013.

[294] N Marcuvitz and J Schwinger. On the representation of the electric and magnetic fields produced by currents and discontinuities in wave guides. I. *Journal of Applied Physics*, 22(6):806–819, 1951.

[295] Mohamed AK Othman, Mehdi Veysi, Alexander Figotin, and Filippo Capolino. Giant amplification in degenerate band edge slow-wave structures interacting with an electron beam. *Physics of plasmas*, 23(3), 2016.

[296] JM Hammer. Coupling between slow waves and convective instabilities in solids. *Applied Physics Letters*, 10(12):358–360, 1967.

[297] John H Booske and Mark C Converse. Insights from one-dimensional linearized pierce theory about wideband traveling-wave tubes with high space charge. *IEEE transactions on plasma science*, 32(3):1066–1072, 2004.

[298] Yong Han, Yan-Wen Liu, Yao-Gen Ding, Pu-Kun Liu, and Chun-Hua Lu. Thermal analysis of a helix twt slow-wave structure. *IEEE transactions on electron devices*, 55(5):1269–1272, 2008.

[299] Amir Setayesh and Mohammad Sadegh Abrishamian. Pawaic-psaofdtd: Particle-wave interaction code with pseudospectral arbitrary-order accurate temporal and spatial derivatives fdtd technique for helix twt. *IEEE Transactions on Electron Devices*, 64(11):4706–4714, 2017.

[300] TM Antonsen and Baruch Levush. Traveling-wave tube devices with nonlinear dielectric elements. *IEEE transactions on plasma science*, 26(3):774–786, 1998.

[301] JG Wohlbier, MC Converse, J Plouin, A Rawal, A Singh, and JH Booske. Latte/muse numerical suite: An open source teaching and research code for traveling wave tube amplifiers. In *4th IEEE International Conference on Vacuum Electronics, 2003*, pages 16–17. IEEE, 2003.

[302] Patrick Y Wong, David Chernin, and YY Lau. Modification of pierce's classical theory of traveling-wave tubes. *IEEE Electron Device Letters*, 39(8):1238–1241, 2018.

[303] Xingping Zhou, Samit Kumar Gupta, Zhong Huang, Zhendong Yan, Peng Zhan, Zhuo Chen, Minghui Lu, and Zhenlin Wang. Optical lattices with higher-order exceptional points by non-hermitian coupling. *Applied Physics Letters*, 113(10):101108, 2018.

[304] GM Branch and TG Mihran. Plasma frequency reduction factors in electron beams. *IRE Transactions on Electron Devices*, 2(2):3–11, 1955.

[305] Leopold B Felsen and Nathan Marcuvitz. *Radiation and scattering of waves*, volume 31. John Wiley & Sons, 1994.

[306] Kasra Rouhi, Robert Marosi, Tarek Mealy, Ahmed F Abdelshafy, Alexander Figotin, and Filippo Capolino. Model of helix traveling wave tube including the slow-wave structure dispersion characteristics and space-charge effect. In *2022 23rd International Vacuum Electronics Conference (IVEC)*, pages 478–479. IEEE, 2022.

[307] Seong-Tae Han, Jin-Kyu So, Kyu-Ha Jang, Young-Min Shin, Jong-Hyun Kim, Suk-Sang Chang, Nikita M Ryskin, and Gun-Sik Park. Investigations on a microfabricated FWTWT oscillator. *IEEE transactions on electron devices*, 52(5):702–708, 2005.

[308] James Benford, John A Swegle, and Edl Schamiloglu. *High power microwaves*. CRC press, 2015.

[309] G Dohler, D Gagne, D Gallagher, and R Moats. Serpentine waveguide TWT. In *1987 International electron devices meeting*, pages 485–488. IEEE, 1987.

[310] Shunkang Liu. Folded waveguide circuit for broadband MM wave TWTs. *International journal of infrared and millimeter waves*, 16:809–815, 1995.

[311] CE Collins, RE Miles, RD Pollard, DP Steenson, JW Digby, GM Parkhurst, JM Chamberlain, NJ Cronin, SR Davies, and John Wesley Bowen. Technique for micro-machining millimetre-wave rectangular waveguide. *Electronics Letters*, 34(10):996–997, 1998.

[312] CE Collins, RE Miles, JW Digby, GM Parkhurst, RD Pollard, JM Chamberlain, DP Steenson, NJ Cronin, SR Davies, and John Wesley Bowen. A new micro-machined millimeter-wave and terahertz snap-together rectangular waveguide technology. *IEEE microwave and guided wave letters*, 9(2):63–65, 1999.

[313] Huarong Gong, Yubin Gong, Tao Tang, Jin Xu, and Weng-Xiang Wang. Experimental investigation of a high-power ka-band folded waveguide traveling-wave tube. *IEEE transactions on electron devices*, 58(7):2159–2163, 2011.

[314] Jun He, Yanyu Wei, Zhigang Lu, Yubin Gong, and Wenxiang Wang. Investigation of a ridge-loaded folded-waveguide slow-wave system for the millimeter-wave traveling-wave tube. *IEEE transactions on plasma science*, 38(7):1556–1562, 2010.

[315] Mingliang Liao, Yanyu Wei, Yubin Gong, Jun He, Wenxiang Wang, and Gun-Sik Park. A rectangular groove-loaded folded waveguide for millimeter-wave traveling-wave tubes. *IEEE transactions on plasma sience*, 38(7):1574–1578, 2010.

[316] Yanyan Tian, Lingna Yue, Jin Xu, Wenxiang Wang, Yanyu Wei, Yubin Gong, and Jinjun Feng. A novel slow-wave structure-folded rectangular groove waveguide for millimeter-wave TWT. *IEEE transactions on electron devices*, 59(2):510–515, 2011.

[317] Yan Hou, Yubin Gong, Jin Xu, Shaomeng Wang, Yanyu Wei, Lingna Yue, and Jinjun Feng. A novel ridge-vane-loaded folded-waveguide slow-wave structure for 0.22-THz traveling-wave tube. *IEEE transactions on electron devices*, 60(3):1228–1235, 2013.

[318] Yanyu Wei, Guo Guo, Yubin Gong, Lingna Yue, Guoqing Zhao, Luqi Zhang, Chong Ding, Tao Tang, Minzhi Huang, Wenxiang Wang, et al. Novel W-band ridge-loaded folded waveguide traveling wave tube. *IEEE electron device letters*, 35(10):1058–1060, 2014.

[319] Robert Marosi, Tarek Mealy, Alexander Figotin, and Filippo Capolino. Three-way serpentine slow wave structures with stationary inflection point and enhanced interaction impedance. *IEEE Transactions on Plasma Science*, 50(12):4820–4833, 2022.

[320] John H Booske, Mark C Converse, Carol L Kory, Christine T Chevalier, David A Gallagher, Kenneth E Kreischer, Vernon O Heinen, and Sudeep Bhattacharjee. Accurate parametric modeling of folded waveguide circuits for millimeter-wave traveling wave tubes. *IEEE transactions on electron devices*, 52(5):685–694, 2005.

[321] Thomas M Antonsen, Alexander N Vlasov, David P Chernin, Igor A Chernyavskiy, and Baruch Levush. Transmission line model for folded waveguide circuits. *IEEE transactions on electron devices*, 60(9):2906–2911, 2013.

[322] David Chernin, Thomas M Antonsen, Alexander N Vlasov, Igor A Chernyavskiy, Khanh T Nguyen, and Baruch Levush. 1-D large signal model of folded-waveguide traveling wave tubes. *IEEE Transactions on Electron Devices*, 61(6):1699–1706, 2014.

[323] Igor A Chernyavskiy, Alexander N Vlasov, Baruch Levush, Thomas M Antonsen, and Khanh T Nguyen. Parallel 2D large-signal modeling of cascaded TWT amplifiers. In *2013 IEEE 14th international vacuum electronics conference (IVEC)*, pages 1–2. IEEE, 2013.

[324] Igor A Chernyavskiy, Thomas M Antonsen, Alexander N Vlasov, David Chernin, Khanh T Nguyen, and Baruch Levush. Large-signal 2-D modeling of folded-waveguide traveling wave tubes. *IEEE transactions on electron devices*, 63(6):2531–2537, 2016.

[325] Sascha Meyne, Pierre Bernadi, Philip Birtel, Jean-François David, and Arne F Jacob. Large-signal 2.5-D steady-state beam-wave interaction simulation of folded-waveguide traveling-wave tubes. *IEEE transactions on electron devices*, 63(12):4961–4967, 2016.

[326] Wei-Zhong Yan, Yu-Lu Hu, Yun-Xian Tian, Jian-Qing Li, and Bin Li. A 3-D large-signal model of folded-waveguide TWTs. *IEEE Transactions on Electron Devices*, 63(2):819–826, 2016.

[327] Ke Li, Wenxin Liu, Yong Wang, and Miaomiao Cao. A nonlinear analysis of the terahertz serpentine waveguide traveling-wave amplifier. *Physics of plasmas*, 22(4):043115, 2015.

[328] Ruifeng Zhang, Xiaoyi Lin, Tieyang Wang, Xiaoyi Xiao, Zhanliang Wang, Zhaoyun Duan, Yubin Gong, Jinjun Feng, Gil Travish, and Huarong Gong. An active transmission matrix-based nonlinear analysis for folded waveguide TWT. *IEEE transactions on electron devices*, 67(3):1205–1210, 2020.

[329] John R Pierce and William B Hebenstreit. A new type of high-frequency amplifier. *The Bell system technical journal*, 28(1):33–51, 1949.

[330] Tarek Mealy and Filippo Capolino. Traveling wave tube eigenmode solution for beam-loaded slow wave structure based on particle-in-cell simulations. *IEEE transactions on plasma science*, 50(3):635–648, 2022.

[331] Nathan Marcuvitz. *Waveguide handbook*. IET, 1951.

[332] Robert E Collin. *Foundations for Microwave Engineering*. John Wiley & Sons, 2001.

[333] Murugan Sumathy, Deepu Augustin, Subrata Kumar Datta, Latha Christie, and Lalit Kumar. Design and RF characterization of W-band meander-line and folded-waveguide slow-wave structures for TWTs. *IEEE transactions on electron devices*, 60(5):1769–1775, 2013.

[334] DMH Hung, IM Rittersdorf, P Zhang, D Chernin, YY Lau, TM Antonsen Jr, JW Luginsland, DH Simon, and RM Gilgenbach. Absolute instability near the band edge of traveling-wave amplifiers. *Physical review letters*, 115(12):124801, 2015.

[335] Shunkang Liu. Study of propagating characteristics for folded waveguide TWT in millimeter wave. *International journal of infrared and millimeter waves*, 21(4):655–660, 2000.

[336] Ke Li, Wenxin Liu, Yong Wang, and Miaomiao Cao. Dispersion characteristics of two-beam folded waveguide for terahertz radiation. *IEEE transactions on electron devices*, 60(12):4252–4257, 2013.

[337] Khanh T Nguyen, Alexander N Vlasov, Lars Ludeking, Colin D Joye, Alan M Cook, Jeffrey P Calame, John A Pasour, Dean E Pershing, Edward L Wright, Simon J Cooke, et al. Design methodology and experimental verification of serpentine/folded-waveguide TWTs. *IEEE transactions on electron devices*, 61(6):1679–1686, 2014.

[338] Sascha Meyne. *Simulation and design of traveling-wave tubes with folded-waveguide delay lines*. Technische Universität Hamburg-Harburg, 2017.

[339] Young Ho Na, Sang Wook Chung, and Jin Joo Choi. Analysis of a broadband q band folded waveguide traveling-wave tube. *IEEE transactions on plasma science*, 30(3):1017–1023, 2002.

[340] Seong-Tae Han, Jung-II Kim, and Gun-Sik Park. Design of a folded waveguide traveling-wave tube. *Microwave and Optical Technology Letters*, 38(2):161–165, 2003.

[341] Jun He, Yanyu Wei, Yubin Gong, Wenxiang Wang, and Gun-Sik Park. Investigation on a W band ridge-loaded folded waveguide TWT. *IEEE transactions on plasma science*, 39(8):1660–1664, 2011.

[342] Yan Hou, Jin Xu, Hai-Rong Yin, Yan-Yu Wei, Ling-Na Yue, Guoqing Zhao, and Yu-Bin Gong. Equivalent circuit analysis of ridge-loaded folded-waveguide slow-wave structures for millimeter-wave traveling-wave tubes. *Progress in electromagnetics research*, 129:215–229, 2012.

[343] Guo Guo, Yanyu Wei, Lingna Yue, Yubin Gong, Xiong Xu, Jun He, Guoqing Zhao, Wenxiang Wang, and Gun-Sik Park. A tapered ridge-loaded folded waveguide slow-wave structure for millimeter-wave traveling-wave tube. *Journal of infrared, millimeter, and terahertz waves*, 33:131–140, 2012.

[344] Ruilin Zheng and Xuyuan Chen. Parametric simulation and optimization of cold-test properties for a 220 ghz broadband folded waveguide traveling-wave tube. *Journal of infrared, millimeter, and terahertz waves*, 30(9):945–958, 2009.

[345] Rajendra Kumar Sharma, Andre Grede, Shailendra Chaudhary, Vishnu Srivastava, and Heino Henke. Design of folded waveguide slow-wave structure for W-band TWT. *IEEE transactions on plasma science*, 42(10):3430–3436, 2014.

[346] HS Sudhamani, Jyothi Balakrishnan, and SUM Reddy. Investigation of instabilities in a folded-waveguide sheet-beam TWT. *IEEE transactions on electron devices*, 64(10):4266–4271, 2017.

[347] Kasra Rouhi, Robert Marosi, Tarek Mealy, Alexander Figotin, and Filippo Capolino. Modeling of serpentine waveguide traveling wave tube to calculate gain diagram. In *2023 24th International vacuum electronics conference (IVEC)*, pages 1–2. IEEE, 2023.

[348] Ahmed F Abdelshafy, Mohamed AK Othman, Alexander Figotin, and Filippo Capolino. *Multitransmission line model for slow wave structures interacting with electron beams and multimode synchronization*, pages 17–56. John Wiley & Sons, Ltd, 2021.

[349] Alexander Figotin. Analytic theory of multicavity klystrons. *Journal of mathematical physics*, 63(6):062703, 2022.

[350] Simon Ramo. The electronic-wave theory of velocity-modulation tubes. *Proceedings of the IRE*, 27(12):757–763, 1939.

[351] Subrata Kumar Datta and Lalit Kumar. A simple closed-form formula for plasma-frequency reduction factor for a solid cylindrical electron beam. *IEEE transactions on electron devices*, 56(6):1344–1346, 2009.

[352] Tarek Mealy, Robert Marosi, and Filippo Capolino. Reduced plasma frequency calculation based on particle-in-cell simulations. *IEEE Transactions on Plasma Science*, 50(10):3570–3577, 2022.

[353] Kasra Rouhi, Robert Marosi, Tarek Mealy, Alexander Figotin, and Filippo Capolino. Parametric modeling of serpentine waveguide traveling wave tubes. *IEEE Transactions on Plasma Science*, pages 1–17, 2024.

[354] Robert J Barker, Neville C Luhmann, John H Booske, and Gregory S Nusinovich. *Modern microwave and millimeter-wave power electronics*. John Wiley & Sons, 2005.

[355] Anisullah Baig, Larry R Barnett, Diana Gamzina, Neville C Luhmann Jr, et al. MEMS compatible sever for 220 GHz ultra wide band TWTA: Design and particle-in-cell analysis. *Progress In Electromagnetics Research Letters*, 41:135–148, 2013.

[356] Cunjun Ruan, Muwu Zhang, Jun Dai, Changqing Zhang, Shuzhong Wang, Xiudong Yang, and Jinjun Feng. W-band multiple beam staggered double-vane traveling wave tube with broad band and high output power. *IEEE Transactions on Plasma Science*, 43(7):2132–2139, 2015.

[357] Ningfeng Bai, Wenchen Xiang, Jingxuan Shen, Changsheng Shen, and Xiaohan Sun. A Ka-band folded waveguide traveling wave tube with lumped resistance metamaterial absorber. *IEEE Transactions on Electron Devices*, 67(3):1248–1253, 2020.

[358] Yang Xie, Ningfeng Bai, Changsheng Shen, Hehong Fan, Zhaofu Chen, and Xiaohan Sun. Backward-wave oscillation suppression in folded waveguide traveling-wave tube with metamaterial absorber. *IEEE Access*, 11:4830–4837, 2023.

[359] Huarong Gong, Jin Xu, Tao Tang, Yanyu Wei, Yubin Gong, Changqing Zhang, Xiaogang Su, Shaolun Cai, Gang Wu, and Jinjun Feng. A 1-kW 32–34-GHz folded waveguide traveling wave tube. *IEEE Transactions on Plasma Science*, 42(1):8–12, 2014.

[360] Yinfu Hu, Jinjun Feng, Jun Cai, Xianping Wu, Yinghua Du, Jingkai Liu, Ji Chen, and Xiaoqing Zhang. Design and experimental study of a widebandwidth W-band folded waveguide continuous-wave TWT. *IEEE Transactions on Plasma Science*, 42(10):3380–3386, 2014.

[361] Anurag Srivastava. Numerical design of a 100 W, 38 dB gain, W-band multi-section serpentine waveguide vacuum electronic TWT. *AEU-International Journal of Electronics and Communications*, 82:145–151, 2017.

[362] Li Fei, Xiao Liu, Jiandong Zhao, Ma Tianjun, Sun Yuhui, Wang Jian, Gao Cha, Linlin Cao, and Mingguang Huang. Development of W-band folded waveguide TWT with lowered operating voltage and improved gain flatness. *IEEE Transactions on Plasma Science*, 48(8):2939–2947, 2020.

[363] Fei Li, Liu Xiao, Tianjun Ma, Yuhui Sun, Jiandong Zhao, Jian Wang, Cha Gao, Linlin Cao, and Mingguang Huang. Demonstration of W-band 30-W continuous-wave folded waveguide traveling wave tube with lowered operation voltage and improved gain flatness. *Journal of Infrared, Millimeter, and Terahertz Waves*, 41:1252–1266, 2020.

[364] Robert Marosi, Kasra Rouhi, Tarek Mealy, Alexander Figotin, and Filippo Capolino. Small-signal model for inhomogeneous helix traveling-wave tubes using transfer matrices. *arXiv preprint arXiv:2405.07956*, 2024.

[365] Ruilin Zheng, Per Ohlckers, and Xuyuan Chen. Particle-in-cell simulation and optimization for a 220-ghz folded-waveguide traveling-wave tube. *IEEE transactions on electron devices*, 58(7):2164–2171, 2011.

[366] Guo Guo, Yanyu Wei, Lingna Yue, Yubin Gong, Guoqing Zhao, Minzhi Huang, Tao Tang, and Wenxiang Wang. A research of W-band folded waveguide traveling wave tube with elliptical sheet electron beam. *Physics of Plasmas*, 19(9):093117, 2012.

[367] BN Basu. *Electromagnetic theory and applications in beam-wave electronics*. World scientific, 1996.

[368] Joseph A Eichmeier and Manfred Thumm. *Vacuum electronics: components and devices*. Springer Science & Business Media, 2008.

[369] Ruifeng Zhang, Mengzhen Li, Zugen Guo, Feng Lan, Yubin Gong, Zhaoyun Duan, Fei Xiao, and Huarong Gong. Improved gain equalization technique for Q-band folded-waveguide TWT for potential application in high-data-rate communication. *IEEE Transactions on Electron Devices*, 69(5):2631–2636, 2022.

[370] Sascha Meyne, Djamschid Safi, and Arne F Jacob. Design procedure for hot-matched severs in folded-waveguide traveling-wave tubes. In *2016 German Microwave Conference (GeMiC)*, pages 361–364. IEEE, 2016.

[371] Kasra Rouhi, Robert Marosi, Tarek Mealy, Alexander Figotin, and Filippo Capolino. Modeling of sever in two-stage serpentine waveguide traveling wave tubes. In *2024 Joint International Vacuum Electronics Conference and International Vacuum Electron Sources Conference (IVEC+ IVESC)*, pages 1–2. IEEE, 2024.

[372] D Shiffler, JA Nation, L Schachter, JD Ivers, and GS Kerslick. A high-power two stage traveling-wave tube amplifier. *Journal of applied physics*, 70(1):106–113, 1991.

[373] GG Denisov, VL Bratman, AW Cross, W He, ADR Phelps, K Ronald, SV Samsonov, and CG Whyte. Gyrotron traveling wave amplifier with a helical interaction waveguide. *Physical review letters*, 81(25):5680, 1998.

[374] JR Pierce. Dotlble-stream amplifiers. *Proceedings of the IRE*, 37(9):980–985, 1949.

[375] JR Pierce. *Traveling-Wave Tubes*. D. van Nostrand, 1950.

[376] Bernard Friedman. Amplification of the traveling wave tube. *Journal of Applied Physics*, 22(4):443–447, 1951.

[377] Peter Andrew Sturrock. Kinematics of growing waves. *Physical Review*, 112(5):1488, 1958.

[378] GS Kino. Parametric amplifier theory for plasmas and electron beams. *Journal of Applied Physics*, 31(8):1449–1458, 1960.

[379] WA Klute. Pulse generation and shaping at microwave frequencies. *Bell Lab. Rec*, 29(5):216–220, 1951.

[380] AC Beck. Microwave traveling-wave tube millimicrosecond pulse generators. *IEEE Transactions on Microwave Theory and Techniques*, 3(6):48–51, 1955.

[381] K Miyauchi. Traveling-wave tube nanosecond pulse generator in 24-gc region. *IEEE Transactions on Microwave Theory and Techniques*, 11(1):3–17, 1963.

[382] Merrill I Skolnik. An introduction to impulse radar. Technical report, NAVAL RESEARCH LAB WASHINGTON DC, 1990.

[383] AV Gritsunov and NV Skachkova. Propagation of short radio pulses through delay line of a cold twt. In *2006 IEEE International Vacuum Electronics Conference held Jointly with 2006 IEEE International Vacuum Electron Sources*, pages 121–122. IEEE, 2006.

[384] David Chernin, TM Antonsen, Baruch Levush, and David R Whaley. A three-dimensional multifrequency large signal model for helix traveling wave tubes. *IEEE Transactions on Electron Devices*, 48(1):3–11, 2001.

[385] Mark C Converse, John H Booske, and Susan C Hagness. Impulse amplification in a traveling-wave tube-i: Simulation and experimental validation. *IEEE transactions on plasma science*, 32(3):1040–1048, 2004.

[386] Mark C Converse and John H Booske. Impulse amplification in a traveling-wave tube-ii: Large signal physics. *IEEE transactions on plasma science*, 32(3):1049–1056, 2004.

[387] Amir Setayesh and Mohammad Sadegh Abrishamian. New version of pawaic helix-twt particle-wave interaction code based on pseudospectral analytical time-domain technique with collocated space and time-marching scheme: Pawaic-psatd-csat. *IEEE Transactions on Electron Devices*, 65(2):716–723, 2018.

[388] Khalil Aliane, Yves Elskens, Frederic Andre, and Damien FG Minenna. Many-particle models and short-pulse amplification in traveling wave tubes. *IEEE Transactions on Electron Devices*, 68(12):6476–6481, 2021.

[389] H Nishihara and M Terada. Measurement on misalignment of the axis of a magnetic field for electron-beam focusing. *Journal of Applied Physics*, 41(8):3322–3324, 1970.

[390] David Bohm and Eugene P Gross. Theory of plasma oscillations. a. origin of medium-like behavior. *Physical Review*, 75(12):1851, 1949.

[391] Murray A Lampert. Plasma oscillations at extremely high frequencies. *Journal of Applied Physics*, 27(1):5–11, 1956.

[392] L Brillouin. The traveling-wave tube (discussion of waves for large amplitudes). *Journal of Applied Physics*, 20(12):1196–1206, 1949.

[393] Hermann A Haus. Noise in one-dimensional electron beams. *Journal of Applied Physics*, 26(5):560–571, 1955.

[394] Kimball Milton and Julian Schwinger. *Electromagnetic radiation: variational methods, waveguides and accelerators*. Springer Science & Business Media, 2006.

[395] Clayton R Paul. *Analysis of multiconductor transmission lines*. John Wiley & Sons, 2007.

[396] GS Kino and SF Paik. Circuit theory of coupled transmission systems. *Journal of Applied Physics*, 33(10):3002–3008, 1962.

[397] VN Singh, BN Basu, BB Pal, and NC Vaidya. Equivalent circuit analysis of a system of coupled helical transmission lines in a complex environment. *Journal of Applied Physics*, 54(7):4141–4146, 1983.

[398] Giovanni Miano and Antonio Maffucci. *Transmission lines and lumped circuits: fundamentals and applications*. Elsevier, 2001.

[399] Simon Ramo. Currents induced by electron motion. *Proceedings of the IRE*, 27(9):584–585, 1939.

[400] Alan V Oppenheim, Alan S Willsky, and Syed Hamid Nawab. *Signals & systems*. Pearson Educacion, 1996.

[401] Ahmed F Abdelshafy, Filippo Capolino, and Alexander Figotin. An accurate analytic model for traveling wave tube dispersion relation. *arXiv preprint arXiv:2201.01712*, 2022.

[402] DA Watkins and EA Ash. The helix as a backward-wave circuit structure. *Journal of Applied Physics*, 25(6):782–790, 1954.

[403] A Willson and H Orchard. Realization of ideal gyrators. *IEEE Transactions on Circuits and Systems*, 21(6):729–732, 1974.

[404] C Lester Hogan. The ferromagnetic faraday effect at microwave frequencies and its applications. *Reviews of Modern Physics*, 25(1):253, 1953.

[405] Toshiro Kodera, Dimitrios L Sounas, and Christophe Caloz. Magnetless nonreciprocal metamaterial (mnm) technology: Application to microwave components. *IEEE transactions on microwave theory and techniques*, 61(3):1030–1042, 2013.

[406] Qingfeng Zhang, Tongfeng Guo, Bakhtiar Ali Khan, Toshiro Kodera, and Christophe Caloz. Coupling matrix synthesis of nonreciprocal lossless two-port networks using gyrators and inverters. *IEEE Transactions on Microwave Theory and Techniques*, 63(9):2782–2792, 2015.

[407] Richard C Dorf. *The engineering handbook*. CRC press, 2018.

[408] Afshin Izadian. *Fundamentals of modern electric circuit analysis and filter synthesis*. Springer, 2023.

[409] WJ Tzeng and FY Wu. Theory of impedance networks: the two-point impedance and LC resonances. *Journal of Physics A: Mathematical and General*, 39(27):8579, 2006.

[410] Wilhelm Cauer. *Synthesis of linear communication networks*, volume 1. McGraw-Hill, 1958.

[411] Norman Balabanian and Theodore A Bickart. *Electrical network theory*. John Wiley & Sons, 1969.

[412] William Hart Hayt and Gerold W Neudeck. *Electronic circuit analysis and design*. Houghton Mifflin Company, 1984.

[413] J David Irwin and R Mark Nelms. *Basic engineering circuit analysis*. John Wiley & Sons, 2020.

[414] Paul I Richards. *Manual of mathematical physics*. Macmillan, 1959.

[415] John David Jackson. Classical electrodynamics, 1999.

Appendix A

Gyrator Implementation

A gyrator is a nonreciprocal component, so any gyrator network should include at least one nonreciprocal component [403]. The gyrator network can be realized using a medium consisting of particles carrying permanent electric and permanent magnetic dipoles or through a gyromagnetic effect of a ferromagnetic medium [78]. There is an apparent need to develop a gyrator circuit that is antireciprocal with extremely low input and output impedances [78]. Various methods of realization are suggested for the gyrator, such as the Hall-effect gyrator, but the most practical are those based on transistors or other electronic active devices designed to operate as amplifiers.

Nowadays, the well-known nonreciprocal component is a transistor or a combination of transistors as integrated opamps. These components are found in almost all suitable gyrator circuits [403]. Also, it is not possible to implement an efficient gyrator with only one amplifier [403]. Many published transistor-based gyrator circuits can be integrated [89, 80, 81, 128, 129, 130, 131, 132], but because a special-purpose integrated circuit must be manufactured, the cost per device is expected to be significant. However, integrated-circuit opamps are commonly available as off-the-shelf components, and they are inexpensive, so they can be

used to design practical gyrators [82, 84, 133, 134, 135, 136, 137, 138]. As a result, they may be used to make low-cost hybrid gyrator circuits.

The ideal gyrator's admittance matrix may be divided up to realize a gyrator as [128, 131]

$$\begin{bmatrix} 0 & G_{\mathrm{g}} \\ -G_{\mathrm{g}} & 0 \end{bmatrix} = \begin{bmatrix} 0 & G_{\mathrm{g}} \\ 0 & 0 \end{bmatrix} + \begin{bmatrix} 0 & 0 \\ -G_{\mathrm{g}} & 0 \end{bmatrix}. \tag{A.1}$$

Voltage-controlled current sources can be used to make the two independent off-diagonal transconductances. This can be achieved by connecting two amplifiers to make a closed loop. In this circuit, the first amplifier has a phase change from input to the output of zero, while the second has π. Moreover, the input and output impedances of each amplifier are both high. The main diagonal terms on the gyrator matrix are kept to small magnitudes by high impedances [128]. In [128], a gyrator in an integration ready form has been built. The proposed gyrator could make inductances with Q-factors of 500 produced by capacitors, and the circuit is highly stable. By providing an active feedback path, Shenoi has developed a gyrator circuit with only three transistors [89]. The circuit operates as a two-way feedback system with transfer admittance parameters equal in magnitude and opposite in phase [89]. Sheahan et al. also created a high-quality gyrator that can operate at frequencies up to 100 kHz [80]. This circuit allows temperature-independent and high Q-factor inductance generation from a low-loss, integratable capacitor [80]. In [131], the design of a new integratable high-performance direct-coupled gyrator circuit is explained, as well as other design features. Simulated inductances of up to 200 H are reached in the proposed design, with stable Q-factors of several thousand. Yanagisawa et al. propose a straightforward way for constructing an active gyrator based on two controlled current sources [129]. A simplified experiment features inherent negative input and output resistances in this work, leading to

optimal impedance-inverting properties. Moreover, in [130], an integrated gyrator circuit uses one diode, 12 resistors, and nine transistors (two of them are lateral PNP). The gyration resistance, input impedance, and resonant-circuit Q-factor obtained from experimental data show outstanding agreement with theory [130].

Because of the current state of technology, opamp-based gyrators are the most feasible design method for gyrators. For instance, Antoniou designed an ideal negative-impedance invertor using a voltage-controlled voltage source [84]. A practical circuit based on an opamp is used to demonstrate the suggested technique. To develop new gyrator circuits, it is used with negative-impedance convenors [84]. In [135], negative-impedance convertors and negative-impedance invertors are used to make equivalent circuits for gyrators. This paper presents a stability analysis of gyrator circuits, as well as a proof of a relevant passivity theorem [135].

Finally, one of the most practical and straightforward circuits to realize an ideal gyrator using opamp is proposed in [136]. A capacitively terminated opamp-based gyrator circuit model is derived using a typical range of amplifier specifications. Also, amplifier imperfections such as finite input and output resistances, as well as finite frequency-dependent amplification, are also taken into account in this model [136]. Experimentation and an exact computer-based analysis are used to confirm the model's validity. The model demonstrates how each amplifier imperfection affects the gyrator circuit's performance. By using ideal amplifiers, the Y-parameters of the gyrator circuit are obtained as [136]

$$\underline{\mathbf{Y}} = \begin{bmatrix} 0 & \frac{R_4}{R_1 R_2} \\ -\frac{1}{R_3} & 0 \end{bmatrix}, \tag{A.2}$$

which $R_n (n = 1, \ldots, 4)$ are the resistors used in the proposed circuit [136]. All that is required to fabricate the circuit is a thin-film or thick-film substrate with four resistors and

a chip dual. The amplifier and substrate are affordable, resulting in a low-cost gyrator circuit. Furthermore, the presented results in [136] show that only one of the four resistors can be trimmed to change the gyration resistance.

The gyrator can also be realized at higher frequencies. The nonreciprocal property of the Faraday effect is indeed used to realize a microwave circuit element analogous to Tellegen's gyrator [404], using a combination of ferrite material and twisted waveguide. Gyrators could be realized by also using magnetless nonreciprocal metamaterial [405, 406].

Appendix B

Negative Impedance Converter

Our circuits require negative capacitances and inductances, which can be provided by a number of physical devices. [407, Chapter 29]. Figure B.1 shows suggested circuits that use opamps in order to obtain negative impedance, capacitance and inductance [408, Chapter 10]. The voltage and current relation and input impedance for the opamp-based circuits shown in Figure B.1 are respectively as follows:

(i) for the negative impedance converter (Figure B.1(a)):

$$I_1 = I_2 = \frac{V_{\text{in}}}{R}, \quad V_{\text{o}} = 2V_{\text{in}} \;\Rightarrow\; Z_{\text{in}} = \frac{V_{\text{in}}}{I_{\text{in}}} = -Z; \tag{B.1}$$

(ii) for the negative capacitance converter(Figure B.1(b)):

$$I_1 = I_2 = \frac{V_{\text{in}}}{R}, \quad V_{\text{o}} = 2V_{\text{in}} \;\Rightarrow\; Z_{\text{in}} = \frac{V_{\text{in}}}{I_{\text{in}}} = -\frac{1}{\mathrm{i}\omega C}; \tag{B.2}$$

(iii) for the negative inductance converter (Figure B.1(c)):

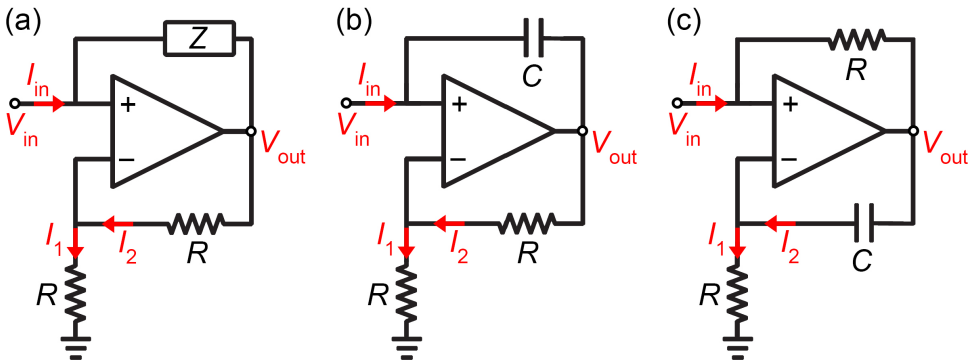

Figure B.1: Opamp-based (a) negative impedance converter, (b) negative capacitance converter and (c) negative inductance converter.

$$I_1 = I_2 = \frac{V_{\rm in}}{R}, \quad V_{\rm o} = V_{\rm in}\left(1 + \frac{1}{{\rm i}\omega RC}\right) \;\Rightarrow\; Z_{\rm in} = \frac{V_{\rm in}}{I_{\rm in}} = -{\rm i}\omega\left(R^2 C\right). \tag{B.3}$$

There are limitations associated with any physical realization of an opamp due to deviations from ideal assumptions. Most opamps deviate from ideal conditions as a result of their limited frequency band and frequency dependence. By tuning the circuit elements properly, the EPD property can be restored at a single frequency. It is important to note that the opamp-based circuits of impedance converters shown in Figure B.1 are only examples; there are many other implementations with different features available.

At a single frequency, negative inductance and positive capacitance can be made to have the same negative imaginary impedance and be equivalent, but they would differ when varying frequency. For example, when frequency increases, the reactance of a negative inductance decreases as ωL, whereas the reactance of a capacitance decreases as $-1/(\omega C)$.

Appendix C

Asymmetric Gyrator

Although the gyrator is described by its gyration resistance value with the unit of ohm, it is a lossless component. The instantaneous power of the gyrator is calculated as

$$p(t) = v_1 i_1 + v_2 i_2 = (-R_{\mathrm{g}} i_2)\, i_1 + (R_{\mathrm{g}} i_1)\, i_2 = 0. \tag{C.1}$$

The gyrator can be generalized to an asymmetric form, in which the forward and backward gyration resistances are different. The asymmetric gyrator impedance matrix is defined as

$$\underline{\mathbf{Z}} = \begin{bmatrix} 0 & -R_{\mathrm{gf}} \\ R_{\mathrm{gb}} & 0 \end{bmatrix}, \tag{C.2}$$

where R_{gf} is forward gyration resistance and R_{gb} is backward gyration resistance. Devices for the condition that R_{gf} does not equal R_{gb} are referred to as active gyrators. Indeed, this is no longer a passive circuit component since the net instantaneous power is different from

zero,

$$p(t) = v_1 i_1 + v_2 i_2 = \left(-R_{\mathrm{gf}} i_2\right) i_1 + \left(R_{\mathrm{gb}} i_1\right) i_2 = i_1 i_2 \left(R_{\mathrm{gb}} - R_{\mathrm{gf}}\right) \neq 0. \tag{C.3}$$

This asymmetric network can be realized by the circuit proposed in [136]. In order to realize asymmetric gyrator, we should consider proper value for resistors, so we have [136]

$$\begin{cases} R_{\mathrm{gf}} = R_3 \\ \\ R_{\mathrm{gb}} = \frac{R_1 R_2}{R_4} \end{cases} \tag{C.4}$$

where $R_n (n = 1, \ldots, 4)$ are the resistors used in the proposed circuit for the gyrator [136].

Appendix D

Basics of Electric Networks

As a matter of self-consistency, we summarize here an overview of the basic concepts and notations of electrical network theory. Graph theory concepts of branches (edges), nodes (vertices) and their incidences are used in the construction of electrical network theory. The Kirchhoff current and voltage laws can be used in this approach, which is effective in loop analysis and selecting independent variables. Specifically, we are interested in conservative electrical networks, which are composed of three types of electric elements: capacitors, inductors, and gyrators [409]. Inductors and capacitors are two-terminal electric elements, while gyrators are four-terminal electric elements.

In this case, a capacitor, an inductor, a resistor, and a gyrator are the elements of the basic electric circuit. These elements are characterized by current-voltage relationships as follows [410, 411, 412, 413]:

$$i_{\mathrm{c}} = C\partial_t v_{\mathrm{c}}, \quad v_{\mathrm{i}} = L\partial_t i_{\mathrm{l}}, \quad v_{\mathrm{r}} = Ri_{\mathrm{r}}, \tag{D.1}$$

where i_{c}, i_{l} and i_{r} are currents and v_{c}, v_{i} and v_{r} are voltages, and real C, L and R are called respectively the capacitance, the inductance and the resistance as shown in Figure D.1.

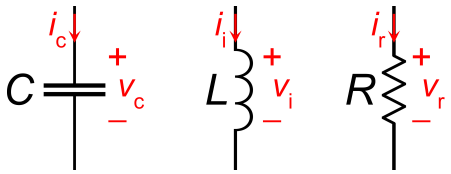

Figure D.1: Capacitance, inductance and resistance symbols and the relevant parameters in the electric circuits.

In addition to the current and voltage we introduce the charge q and the momentum p as

$$q\left(t\right)=\int i\left(t\right)\,dt,\quad i\left(t\right)=\partial_t q, \tag{D.2a}$$

$$p\left(t\right)=\int v\left(t\right)\,dt,\quad v\left(t\right)=\partial_t p. \tag{D.2b}$$

Also, we describe the stored energy parameter w for the elements. Then, the current-voltage-charge relations, the stored energy and the Lagrangians associated with the circuit elements are represented as [414, Chapter 3]

$$\text{Capacitor: } v_{\mathrm{c}}=\frac{q_{\mathrm{c}}}{C},\quad i_{\mathrm{c}}=\partial_t q_{\mathrm{c}}=C\partial_t v_{\mathrm{c}},\quad q_{\mathrm{c}}=Cv_{\mathrm{c}}=C\partial_t p_{\mathrm{c}}, \tag{D.3a}$$

$$w_{\mathrm{c}}=\frac{1}{2}q_{\mathrm{c}}v_{\mathrm{c}}=\frac{1}{2}\frac{q_{\mathrm{c}}^2}{C}=\frac{1}{2}Cv_{\mathrm{c}}^2=\frac{1}{2}C\left(\partial_t p_{\mathrm{c}}\right)^2, \tag{D.3b}$$

$$\mathcal{L}_{\mathrm{c}}=\frac{q_{\mathrm{c}}^2}{2C}. \tag{D.3c}$$

$$\text{Inductor: } v_{\mathrm{i}}=L\partial_t i_{\mathrm{i}},\quad p_{\mathrm{i}}=Li_{\mathrm{i}}=L\partial_t q_{\mathrm{i}},\quad \partial_t q_{\mathrm{i}}=\frac{p_{\mathrm{i}}}{L}, \tag{D.3d}$$

$$w_{\mathrm{i}} = \frac{1}{2} p_{\mathrm{i}} i_{\mathrm{i}} = \frac{1}{2} L i_{\mathrm{i}}^2 = \frac{1}{2} L \left(\partial_t q_{\mathrm{i}}\right)^2 = \frac{1}{2} \frac{p_{\mathrm{i}}^2}{L}, \tag{D.3e}$$

$$\mathcal{L}_{\mathrm{i}} = \frac{L \left(\partial_t q_{\mathrm{i}}\right)^2}{2}. \tag{D.3f}$$

$$\text{Resistor: } v_{\mathrm{r}} = R i_{\mathrm{r}}, \quad p_{\mathrm{r}} = R q_{\mathrm{r}}. \tag{D.3g}$$

Appendix E

Single LC Circuit Analysis

The circuit matrix of the single LC resonator is given by

$$\mathscr{C}_{\mathrm{LC}} = \begin{bmatrix} 0 & -1 \\ \omega_0^2 & 0 \end{bmatrix}, \quad \omega_0 = \frac{1}{\sqrt{LC}}, \tag{E.1}$$

where ω_0 is the resonance frequency of the single LC resonator. Then, the eigenvalues are expressed as $s_{1,2} = \pm \mathrm{i}\omega_0$ and the corresponding eigenvectors by assuming state vector as the stored charge in the capacitance q and its first derivative, $\Psi_{\mathrm{LC}} = [q, \dot{q}]$, are obtained as

$$\mathscr{V}_{\mathrm{LC}} = \begin{bmatrix} \frac{1}{2} & \frac{1}{2} \\ \mathrm{i}\frac{\omega_0}{2} & -\mathrm{i}\frac{\omega_0}{2} \end{bmatrix}. \tag{E.2}$$

We define impedance as a ratio between voltage (v) and current (i). Also, by using the definition of charge in the state vector which is defined based on the stored charge in the capacitance q, we calculate resonator impedance as a ratio between capacitor voltage (q/C)

and capacitor current ($\dot{q}$) as

$$Z_{1,2} = \pm\frac{1}{\mathrm{i}\omega_0 C}, \quad |Z_{1,2}| = \sqrt{\frac{L}{C}}, \tag{E.3}$$

which is defined as an impedance of single resonator.

Appendix F

CGS to SI Conversion

Table F.1 relates quantities in SI or CGS units [415]. All factors of 3 could be replaced by 2.99792458 for more precise calculations, arising from the accurate light velocity value.

Table F.1: Conversion table for given amounts of a physical quantity.

Physical Quantity	SI	CGS (Gaussian)
Length (l)	1 meter (m)	10^2 centimeters (cm)
Time (t)	1 second (s)	1 second (s)
Frequency (f)	1 hertz (Hz)	1 hertz (Hz)
Charge (q)	1 coulomb (C)	$c_{\mathrm{G}} \times 10^{-1}$ statcoulombs (FR)
Current (I)	1 ampere (A)	$c_{\mathrm{G}} \times 10^{-1}$ statamperes (FR/s)
Voltage (V)	1 volt (V)	$c_{\mathrm{G}}^{-1} \times 10^{8}$ statvolt (statV)
Capacitance (C)	1 farad (F)	$c_{\mathrm{G}}^{2} \times 10^{-9}$ cm
Inductance (L)	1 henry (H)	$c_{\mathrm{G}}^{-2} \times 10^{9}$ s^2/cm
$c_{\mathrm{SI}} = 3 \times 10^{8}$ m/s $c_{\mathrm{G}} = 3 \times 10^{10}$ cm/s		

Moreover, the parameters in the two systems of units can be converted and the conversion of equations between SI units and CGS units is provided in Table F.2.

Table F.2: Conversion table for symbols and formulas.

Quantity	Symb.	SI unit	Gaussian unit	Conversion factor
Electric charge	q	C	Fr $\left(\mathrm{cm}^{3/2}\mathrm{g}^{1/2}\mathrm{s}^{-1}\right)$	$\frac{q_\mathrm{G}}{q_\mathrm{SI}} = \frac{1}{\sqrt{4\pi\varepsilon_0}} = \frac{3\times10^9\ \mathrm{Fr}}{1\ \mathrm{C}}$
Electric current	I	A	Fr/s $\left(\mathrm{cm}^{3/2}\mathrm{g}^{1/2}\mathrm{s}^{-2}\right)$	$\frac{I_\mathrm{G}}{I_\mathrm{SI}} = \frac{1}{\sqrt{4\pi\varepsilon_0}} = \frac{3\times10^9\ \mathrm{Fr/s}}{1\ \mathrm{A}}$
Electric voltage	V	V	StatV $\left(\mathrm{cm}^{3/2}\mathrm{g}^{1/2}\mathrm{s}^{-1}\right)$	$\frac{V_\mathrm{G}}{V_\mathrm{SI}} = \sqrt{4\pi\varepsilon_0} = \frac{1\ \mathrm{StatV}}{3\times10^2\ \mathrm{V}}$
Electric field	$\mathbf{E}$	V/m	StatV/cm $\left(\mathrm{cm}^{-1/2}\mathrm{g}^{1/2}\mathrm{s}^{-1}\right)$	$\frac{\mathbf{E}_\mathrm{G}}{\mathbf{E}_\mathrm{SI}} = \sqrt{4\pi\varepsilon_0} = \frac{1\ \mathrm{StatV/cm}}{3\times10^4\ \mathrm{V/m}}$
Magnetic field	$\mathbf{H}$	A/m	Oe $\left(\mathrm{cm}^{-1/2}\mathrm{g}^{1/2}\mathrm{s}^{-1}\right)$	$\frac{\mathbf{H}_\mathrm{G}}{\mathbf{H}_\mathrm{SI}} = \sqrt{4\pi\varepsilon_0} = \frac{4\pi\times10^{-3}\ \mathrm{Oe}}{1\ \mathrm{A/m}}$
Resistance	R	Ω	s/cm	$\frac{R_\mathrm{G}}{R_\mathrm{SI}} = 4\pi\varepsilon_0 = \frac{1\ \mathrm{s/cm}}{3^2\times10^{11}\ \Omega}$
Capacitance	C	F	cm	$\frac{C_\mathrm{G}}{C_\mathrm{SI}} = \frac{1}{4\pi\varepsilon_0} = \frac{3^2\times10^{11}\ \mathrm{cm}}{1\ \mathrm{F}}$
Inductance	L	H	s^2/cm	$\frac{L_\mathrm{G}}{L_\mathrm{SI}} = 4\pi\varepsilon_0 = \frac{1\ \mathrm{s}^2/\mathrm{cm}}{3^2\times10^{11}\ \mathrm{H}}$
Cap. (p.u.l)	$\overline{C}$	F/m	$\mathrm{dim}-\mathrm{less}$	$\frac{\overline{C}_\mathrm{G}}{\overline{C}_\mathrm{SI}} = \frac{1}{4\pi\varepsilon_0} = \frac{3^2\times10^9}{1\ \mathrm{F/m}}$
Induc. (p.u.l)	$\overline{L}$	H/m	$\mathrm{s}^2/\mathrm{cm}^2$	$\frac{\overline{L}_\mathrm{G}}{\overline{L}_\mathrm{SI}} = 4\pi\varepsilon_0 = \frac{1\ \mathrm{s}^2/\mathrm{cm}^2}{3^2\times10^{13}\ \mathrm{H/m}}$
$\varepsilon_0 = 8.8541878\times10^{-12}\ \mathrm{F/m}$ $\mu_0 = 1.2566370\times10^{-6}\ \mathrm{H/m}$				

* p.u.l: per unit length
* dim-less: dimensionless

Appendix G

Translation Between the Lagrangian Model and Pierce Model Parameters

For convenience, we provide the conversion table to transform the Lagrangian model parameters to the Pierce model parameters. The list of transformations is in Table G.1.

Table G.1: Translation from Lagrangian model parameters to the Pierce model parameters.

Parameter	Lagrangian model	Pierce model
electron stream velocity	$\mathring{v}$	u_0
electron stream cross-section area	σ_{B}	A
Stream intensity	β	$\frac{I_0 u_0}{2V_0}$
Characteristic phase velocity of cold EM modes	w	$\sqrt{-\frac{\omega^2}{ZY}}$
TWT principal parameter	γ	$j\omega\frac{a^2}{Y}\frac{I_0}{2V_0}u_0$

Appendix H

Dimensionless Variables for the Lagrangian Model

We use dimensionless variables for the Lagrangian model, and the normalization factor for each parameter is defined in Table H.1.

Table H.1: List of dimensionless variables with the corresponding normalization factor.

Dimension	Normalization factor	Normalized parameters
Time	$T_{\mathrm{p}} = (2\pi) \,/\, (R_{\mathrm{sc}}\omega_{\mathrm{p}})$	$\breve{\tau}_{\mathrm{w}} = \tau_{\mathrm{w}}/T_{\mathrm{p}}$
Length	$\lambda_{\mathrm{p}} = (2\pi c) \,/\, (R_{\mathrm{sc}}\omega_{\mathrm{p}})$	$\breve{z} = z/\lambda_{\mathrm{p}}$, $\breve{\sigma}_{\mathrm{B}} = \sigma_{\mathrm{B}}/\lambda_{\mathrm{p}}^2$
Frequency	$R_{\mathrm{sc}}\omega_{\mathrm{p}} = R_{\mathrm{sc}}\sqrt{4\pi\mathring{n}e^2/m}$	$\breve{\omega} = \omega/\left(R_{\mathrm{sc}}\omega_{\mathrm{p}}\right)$, $\breve{\omega}_0 = \omega_0/\left(R_{\mathrm{sc}}\omega_{\mathrm{p}}\right)$
Velocity	$\mathring{v}$	$\breve{w} = w/\mathring{v}$, $\breve{u} = u/\mathring{v}$, $\breve{\gamma} = \gamma/\mathring{v}^2$, $\breve{\beta} = \beta/\mathring{v}^2$
Wavenumber	$k_{\mathrm{p}} = 2\pi/\lambda_{\mathrm{p}} = R_{\mathrm{sc}}\omega_{\mathrm{p}}/c$	$\breve{k} = k/k_{\mathrm{p}}$
Charge	$Q_0\left(\omega = \omega_0\right) = A\tau_{\mathrm{w}}/\left(2\sqrt{\pi}\right)$	$\breve{Q} = Q/Q_0\left(\omega = \omega_0\right)$